Advance Composites Group (ACG)
Department of Mechanical and Aerospace Engineering
Faculty of Engineering
University of Strathclyde

Additive layers to suppress delamination in composite laminates

Miguel Ubago Torres

Submitted in fulfilment of the requirements for the degree of

Doctor of Philosophy

2022

Declaration of Authenticity and Author's Rights

This thesis is the result of the author's original research. It has been composed by the author and has not been previously submitted for examination which has led to the award of a degree.

Signed: Miguel Ubago Torres

Date: 31 January 2023

Acknowledgements

Firstly, I would like to thank my supervisor Dr. Meisam Jalalvand for putting his trust in me to develop this work and for the never-ending support and guidance he provided throughout the years, the conversations and all those many weekly meetings. Then, I would like to thank my supervisor Dr. Liu Yang, whose good support came at the moments they were needed. I would also like to thank the past and present members of the Advance Composite Group, which helped me during this period. Further, I would like to thank the University of Strathclyde for the funding provided to carry out my studies.

I would like to thank Christopher Cameron for his help and support in providing me with training, advice and equipment to manufacture my experimental samples and for helping me with using the autoclave. I would also like to thank James Gillespie for his help and support in providing me with training, advice and equipment to carry out my experimental work. Moreover, I would also like to thank the Mechanical and Aerospace Department Workshop team of the University of Strathclyde, whose work for the final preparation of the testing samples was amazing and effective.

Experimental testing was supported and carried out at the Advance materials research laboratory of the University of Strathclyde. Computed Tomography scanning was supported by the National Research Facility for Lab X-ray CT (NXCT) at the μ-VIS X-ray Imaging Centre, University of Southampton, through EPSRC grant EP/T02593X/1.

I want to thank my family, who has been exceptionally supportive and understanding. Thank you to my friends, who have made the hard times easier to pass. To Sushant, who is a wonderful person and great friend. Thank you to Dio, who is always productive, helpful and funny. And last and most important, to Tara, who has been a source of help and support, and to whom I am immensely thrilled to have met.

Abstract

Delamination originating from the free edges is a common failure mechanism of composite laminates, as the free edges in composite laminates are high-stress concentration areas.

This thesis has studied a solution that could suppress delamination starting from the free edges in composite laminates in different loading scenarios. The solution consists of thin additive layers of prepreg carbon/epoxy composite material, which are added to the composite laminate's free edges to enhance the through-thickness strength of the laminate. Additionally, the risk of delamination is reduced by constraining the out-of-plane and shear movements of different plies at the free edge. The solution was explored in four different loading scenarios, which are easily encountered in the life cycle of a composite laminate, as are, composite laminates under tension, composite laminates under edge impact, composite laminates with open holes under tension, and pin-loaded composite laminates. Both numerical and experimental methods have been complementarily used in each loading case to verify the solution's effectiveness.

The use of these additive bindings for suppressing free-edge delamination was successfully proven in the case of composite laminates under tension. For example, when used to bind the edges of a $[(20_2/-20_2)_2]_s$ laminate, the tensile failure strain and load were increased by about 50%, and the failure mode changed from free-edge delamination to in-plane shear. However, it did not change the failure load and final failure mode of a substrate less susceptible to free-edge delamination as a $[(45_2/-0_2/-45_2/90_2]_s$ laminate.

The use of additive bindings in composite laminates under edge impact successfully enhanced the through-the-thickness strength of the laminates and stiffened the initial response of the laminate to the impact. As a result, higher average peak load values were observed in the specimens with bindings. Additionally, the delamination length in the perpendicular direction to the impactor displacement was reduced by about 30% for

low and medium-impact energies and by about 20% for high-impact energies. However, the damage in the parallel direction to the impactor displacement was not significantly affected, and similar delamination length occurred in specimens with binding. Therefore, further investigations are suggested to test the capabilities of additional binding configurations to enhance the damage tolerance of composite laminates under edge impact.

Additive narrow binding stripes were added to the edges of holes of composite laminates with open holes. Tensile and fatigue testing was conducted, but the results obtained were inconclusive. Further work is suggested for composite laminates with open holes. The remarkable point was that the specimens with binding had a more explosive failure and presented a smaller coefficient of variation of the strain and load values.

Last, in the case of pin-loaded laminates, narrow additive binding stripes were added at the edge of the hole of the laminate. Both quasi-static and fatigue tension-tension testing was carried out. The use of additive bindings successfully enhanced the bearing damage resistance, increasing the offset bearing strength by about 38%. In addition, additive bindings reduced the hole diameter size; hence, different diameters were used for the loading pins of the specimens without and with binding to achieve a tight fit between the pin and the hole. Smaller pin diameters in specimens with binding increased the stress concentration at the contact point, and a more defined "pear-like" shape was obtained at the deformed hole. Thus, the design of specimens with larger holes is encouraged for testing the solution in this type of specimen to avoid the effects of using different pin sizes.

List of Publications

The work presented in this PhD Thesis has produced one available publication in a journal.

Journal papers Miguel Ubago Torres and Meisam Jalalvand. Additive binding layers to suppress free-edge delamination in composite laminates under tension. *Composites Part A: Applied Science and Manufacturing*, **156**:106902, may 2022.
doi: 10.1016/j.compositesa.2022.106902

To my parents and siblings. With love.

Contents

List of Figures

List of Tables

List of Symbols and Acronyms

Acronyms

Acronym	Description
AE	Acoustic emisions
ASTM	American Society for Testing and Materials
BVID	Barely visible impact damage
CAEI	Compression after edge impact
CAI	Compression after impact
CDM	Continuum damage mechanics
CRP	Carbon fibre reinforced plastics
CSAI	Compressive stress after impact
CZD	Cohesive zone method
FM	Fracture Mechanics
FRP	Fibre reinforced plastics
GFRP	Glass fibre reinforced plastics
LEFM	Linear elastic fracture mechanics
LVI	Low velocity impact
PEEK	Polyether ether ketone
Prepreg	Pre-impregnated composites
QSC	Quadratic Stress Criterion
RTM	Resin infused mould
SCF	Stress concentration factor
SEM	Scanning electron microscopy
UD	Unidirectional

VCCT	Virtual Crack Closure Technique

Greek Symbols

Symbol	Description	Units
δ_I^0, δ_{II}^0, δ_{III}^0	CZM separation of the interface at damage onset for each crack opening mode	mm
δ_I, δ_{II}, δ_{III}	CZM separation of the interface	mm
Δa	Crack extension	m
ϵ	Axial strain	-
ϵ_c	Axial strain for delamination onset	-
η	In mixed-mode delamination BK criteria, a fitting parameter for calculating $\mathcal{G}_{equivC}$	-
γ_{xy}	Shear strain in the xy plane	-
ν_{xy}	Poisson's ratio corresponding to a contraction in direction y when an extension is applied in direction x	-
σ_I^0, σ_{II}^0, σ_{III}^0	CZM strength of the interface for each crack opening mode	N/mm^2
σ_I, σ_{II}, σ_{III}	CZM stress at the interface for each crack opening mode	N/mm^2
σ_z	Interlaminar through the thickness stress	N/mm^2
τ_{xz}	Interlaminar longitudinal shear stress	N/mm^2
τ_{yz}	Interlaminar transverse shear stress	N/mm^2
θ	Fibre orientation angle	$^\circ$

Roman Symbols

Symbol	Description	Units
$\mathcal{G}_{\mathcal{I}}$, $\mathcal{G}_{\mathcal{II}}$, $\mathcal{G}_{\mathcal{III}}$	Strain energy release rate components due to opening, in-plane shear, and out-of-plane shear crack-extension modes	N/mm
$\mathcal{G}$	Energy release rate, total, in 3D	N/mm
$\mathcal{G}_c$	Critical energy release rate or Fracture toughness, total, in 3D	N/mm
$\mathcal{G}_{equivC}$	Critical equivalent strain energy release rate for mixed-mode delamination	N/mm

$\mathcal{G}_{equiv}$	Equivalent strain energy release rate for mixed-mode delamination	N/mm
$\mathcal{G}_{Ic}$, $\mathcal{G}_{IIc}$, $\mathcal{G}_{IIIc}$	Critical energy release rate for each crack opening mode	N/mm
$\mathcal{U}$	In FM, potential energy stored in the flaw provided by the internal strain and external forces	J
$\mathcal{W}$	In FM, work required to create new surfaces	J
$\mathcal{W}_{closure}$	In VCCT, work needed for closing a crack	Nmm
Π	In FM, total internal energy	J
$\widetilde{K}_I$, $\widetilde{K}_{II}$, $\widetilde{K}_{III}$	Virgin or undamaged penalty stiffness for cohesive elements for each crack opening mode	N/mm^3
A	In FM, crack area	mm^2
a	In delamination context, crack length	mm
D_I, D_{II}, D_{III}	CZM damage variables for each crack opening mode	N/mm^3
E^*	Axial stiffnes of a laminate completely delaminated along one or more interfaces	N/mm^2
E_L	Longitudinal Young's modulus (fibre direction)	N/mm^2
E_T	Transverse Young's modulus (transverse to fibre direction)	N/mm^2
E_{lam}	Axial laminate stiffness calculated from CLT	N/mm^2
K_I, K_{II}, K_{III}	In CZM, interface stiffness or penalty stiffness for cohesive elements for each crack opening mode	N/mm^3
K_I, K_{II}, K_{III}	Stress intensity factors due to the three crack-extension modes: opening, in-plane shear, out-of-plane shear	$Pa\ m^{-1/2}$
R	Crack growth resistance, total, in 3D	N/mm
t	Laminate thickness	mm
th	Ply thickness	mm
x, y, z	Cartesian coordinates	-
ΔA	In VCCT, half area of newly created surface when crack development, ΔA=Δa x b	mm^2
Δa	In VCCT, the increase in length of the opening crack. It corresponds with the length of the element	mm
$\mathcal{G}_{max,WithoutBinding}$	In the results of the FE analysis, maximum value of energy release rate at an interface for a crack length when no additive binding is applied.	N/mm

$\mathcal{G}max$	In the results of the FE analysis, maximum value of energy release rate at an interface for a crack length.	N/mm
b	Width of a composite laminate	mm
u, v, w	In VCCT, nodal displacements	mm
X, Y, Z	In VCCT, nodal forces	N

Chapter 1

Introduction

This chapter is intended to easily position the reader on the framework of composite materials and their relevance in today's world. Adversities of the use of composite materials will be introduced, leading to the purpose of this PhD project.

1.1 Background

Composite materials have been used for a very long time. The base idea is to combine two or more materials and create new materials with the best properties of the individual materials, plus added qualities that the respective materials do not exhibit alone. A typical composite material consists of a material - known as reinforcement - with high mechanical strength and stiffness, for example, unidirectional or woven fibres, embedded in a material with lower mechanical strength and stiffness (matrix). Among known examples of these composite materials, there are mud and straw for forming adobe, steel-reinforced concrete and fibre-reinforced plastics (FRP), the latter being the most used nowadays.

In the decade of 1930s, fibre-reinforced plastics were being widely investigated. In 1936, glass fibre - commonly known as "fibreglass" - was successfully combined with a suitable polyester plastic resin to create a glass fibre reinforced plastic (GFRP) or glass fibre composite material. As a result, a composite material showed great specific strength for the first time, promising to be an excellent structural and building material. In addition to the high strength to weight properties, FRP showed good resistance to impact, fatigue and static loads. Furthermore, FRP would not corrode or rust like metals or rot like wood, which rapidly promoted their use in the naval sector. Also, GFRP was found to be transparent to radio frequencies, which led to the adaptation of composites for radar domes and other electronic equipment.

In the 1960s, a significant change occurred in the use of composite materials with the commercial introduction of the first carbon fibres to the market. Carbon fibre reinforced plastics (CFRP) improved stiffness to weight ratios even more than GFRP. This, combined with their excellent thermal properties and dimensional stability, led composites to be used more in the aerospace, automotive, sporting, and consumer goods industries. Figure 1.1 presents a chart for a better understanding of the stiffness to density and strength to toughness relations in composite materials compared with examples of different materials. The low density and high strength values of composites make composite a great option for the manufacture of structural parts of vehicles, achieving similar or higher strengths than using metals.

In the 1970s, due to the already known problem of corrosion with Aluminium and the two big energy crises - known as the "oil shocks" - that occurred in 1973 and 1979, the aerospace industry was heavily encouraged to expand the use of CFRP in both fighter aircraft and commercial airlines. As manufacturing processes and design methods improved, the use of CFRP grew enormously in the 1980s and 1990s, reaching around 20% composite weight content in fighter aircraft (*Hornet F-18*) and 15% composite weight content in commercial airlines (*Boeing 777*, *Airbus A320*, *A330*,

A340). Recently, in modern commercial aeroplanes such as A350 and B787 around 50% of the total weight is composites.

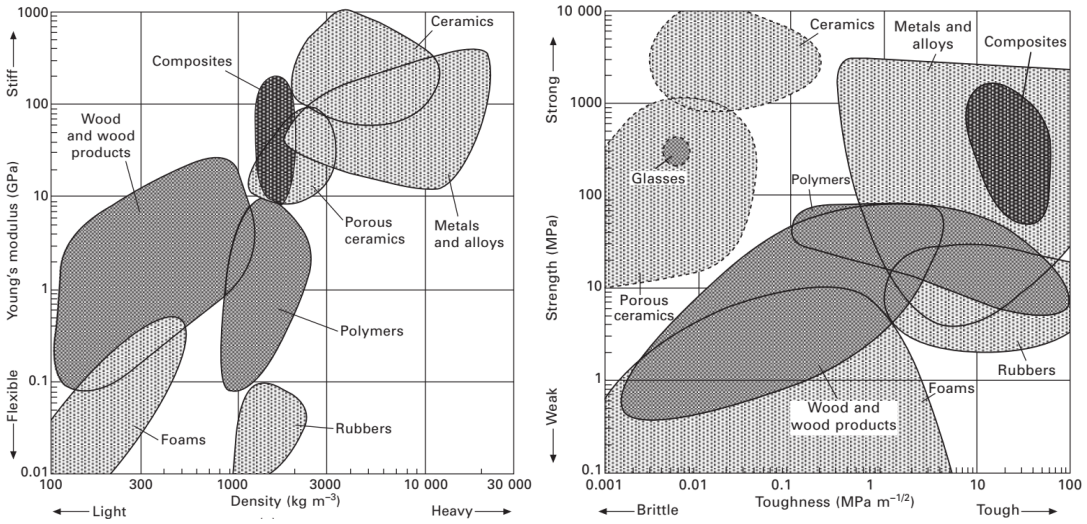

Figure 1.1: Examples of material property charts: (a) Young's modulus-density and (b) strength-toughness - Reproduced from [1].

Nowadays, a wide variety of fibre-reinforced plastics composites are commercially available. The matrix material for structural composite applications is usually a thermoset polymer, e.g., an epoxy resin, although thermoplastic composites, e.g., polyether ether ketone (PEEK), have become increasingly popular lately. Carbon, aramid or glass fibres are the most common fibres used as reinforcement. On a macroscopic scale, the fibres are embedded in the thermoset plastic, so they combine by physical rather than chemical means [2]. However, on the microscopical scale, the fibres are strongly bonded with the matrix, so the matrix transfers the load between the individual fibres. Furthermore, the fibres are protected with a coating called sizing, which enables processability through the protection of the fibre surface and ensures an excellent adhesive bond in the fibre-matrix interface [3].

Composite materials also present some disadvantages. Although continuous fibre reinforced plastics tend to give the best overall performance (compared to other types of polymer composites), they present complex fracture mechanisms and behaviour. Composite materials have low transverse properties, have brittle failure and are sensitive to moisture and high temperatures. Moreover, the mechanical analysis of composite materials is generally more difficult due to their heterogeneity and orthotropic properties. Additionally, an excellent cleanliness grade is necessary while manufacturing to avoid foreign bodies in the composite structure. Furthermore, the use of "prepregs" - fibre pre-impregnated with a resin usually for autoclave curing - requires their storage in freezers at low temperature, incurring additional equipment

and cost of production.

Despite these inconveniences, composites have gained more and more presence in the industry in the last decades, reaching a market value of $82 billion in 2016 [4]. Moreover, the trend indicates that the value of composites in the market will keep increasing to a value of $112 billion by 2027. Hence, it is also important to improve their behaviour to failure and make them more durable and easily recyclable.

1.2 Problem statement and research aims

Fibre-reinforced composite material failure mechanisms are numerous and different from those of metals. These failure mechanisms are widely influenced by diverse variables: the geometry of the specimens [5–12], the stress state on the material [13–16], the layup stacking sequence [17–21], manufacture defects as voids [22–24], and material properties [25]. These parameters are still widely investigated, and the reporting of their individual and joint influence on the failure of composite laminates is still ongoing.

Among all failure mechanisms, delamination is a critical one that has been and still is the case of the study by many [26–38]. It is caused by the combination of high interlaminar stresses and the relative weakness of the matrix of composite laminates to carry loads in the through-thickness direction. The fibres that lie in the laminate plane do not provide reinforcement through the thickness, so the composite relies on the relatively weak matrix to carry loads in that direction. This combination provokes the separation of different layers of the composite laminates. As a result, delamination induces structural integrity loss and strength reduction, leading to the ultimate laminate failure.

Delamination may occur in different circumstances, such as the presence of an embedded crack when manufacturing, as a result of an impact when handling newly produced composite parts, during the maintenance of a structure, or just as a result of the loading conditions to which the composites are subjected. In particular, free edges in FRP are interlaminar stress concentration areas and are highly probable to be where a crack or delamination starts. As a result, it is common to encounter different laminate layups that can not be adequately tested or used in composite structures because they suffer from edge delamination under certain loading conditions.

Due to the importance of this phenomenon, there have been several attempts in the past, as nowadays, to enhance the properties of composite laminates to avoid or mitigate delamination and its effects. Some of these attempts include the hybridisation [39], interleaving [40], critical ply termination [41] and stitching [42] techniques. De-

tails and more of the like solutions are better explained in section 2.2. As the nature of delamination is complex and depends on several parameters that could vary significantly, e.g., the geometry and loading conditions, finding a solution that stops delamination in all cases seems very difficult.

The research carried out in this PhD studies a method of mitigating or stopping delamination, originating from free edges of composite laminates/structures, and its effects. Of course, free edges are not the only triggers of delamination (embedded cracks, impacts, voids...), but, as mentioned, they are significant interlaminar stress concetration areas due to the presence of singular stresses, poor finishing of composite laminates/test coupons, and the unprotected regions against object impacts.

Therefore, rewriting it, in other words, the possibility of a solution that could mitigate, stop or suppress delamination originating from the edges of composite laminates/structures has been studied. The solution studied explores a design strategy for using additive composite layers [1] that could be placed over the edges of the composite laminate or edges in composite structures for suppressing delamination originating from free edges in different loading conditions and circumstances. Then, the primary aim of this PhD could be enunciated as:

> *To demonstrate how an additive binding laminate, made out of thin FRP composite layers, could be used for suppressing delamination arising from the free edges in a composite laminate/structure, and to which extent could this idea be used for different loading scenarios?*

Composites are widespread across many different industries, so the loading scenarios they are subjected to are numerous, e.g., impact, compression, traction, bending, and combinations between them, plus variations of each of them. Hence, to set boundaries and a limit to this project's scope, four different loading scenarios were decided for studying. The loading scenarios studied are as follows:

- Composite laminates under tension. Additive composite layers are used to stop free-edge delamination in composite laminates under tensile loading. This is particularly interesting for tensile test coupons and composite structures with long free edges.
- Composite laminates under edge impact. Additive composite layers are added as a reinforcement over the free edge of composite laminates subjected to blunt impacts. This reinforcement intends to hold the edge of the laminate, as delamination is the main mode of how the composite absorbs the energy of an impact.

[1] Please note that hereafter *additive layers* and *additive binding* will be used indistinctly across the whole document.

- Composite laminates with open holes. The additive composite layers are added around the edge of open holes in composite laminates under tensile load. The additive layers are added in the form of thin strips placed around the edge of the open hole.
- Bearing response of composite laminates with additive layers over the hole. In the form of thin stripes, additive composite layers are placed over the hole of composite laminates under a pin-load scenario. The addition of these stripes is studied in the enhancement of the bearing response of the composite laminate.

To summarise, this thesis aims to illustrate and describe the effect of additive composite layers as a design strategy for suppressing, avoiding or delaying delamination in composite laminates in four different loading scenarios. In this manner, four independent research questions are formulated, as follows:

1. What is the effect of using additive binding layers over the free edges of composite laminates under tension for stopping free-edge delamination?
2. What is the effect of using additive binding layers over the free edge of composite laminates under edge impact for enhancing their damage resistance?
3. What is the effect of using additive binding layers over the edge of the hole of composite laminates with open holes under tension?
4. What is the effect of using additive layers ver the edge of the hole of pin-loaded composite laminates?

The study, results and conclusions of the answers for each of these questions are to be found in their corresponding chapters: chapters 6 to 9.

1.3 Scope of the research

This thesis concentrates on studying four independent research questions that share the use of a proposed design strategy for suppressing delamination. First, a literature review was conducted to position this solution in the state of art of the actual panorama of methods for stopping delamination in composite material laminates. Composite materials failure modes knowledge is needed to understand the proposed solution's effect. An explanation and introduction to composite failure mechanisms and analysis methods were provided, focusing mainly on the virtual crack closure technique (VCCT) [43], based on fracture mechanics (FM). The VCCT was the approach used in this thesis for characterising delamination. In this manner, an exhaus-

tive explanation of damage analysis and all different composite analysis theories were out of scope.

Both numerical and experimental analyses were carried out to determine the effectiveness of the additive layers for suppressing delamination. The numerical simulation was used as a tool for designing the experiments and checking the viability of the solution in each of the loading scenarios, so they were not meant to be a high-fidelity representation of the experimental behaviour of the samples tested. Hence, the numerical models were built to keep the simulation computationally light but reliable. The VCCT was used to measure the energy release rate value ($\mathcal{G}$) at the crack tip of a pre-modelled delamination. The solution's effectiveness was measured based on the experimentally observed effects on the composite laminates' mechanical properties, its capability to stop delamination, and its influence on the failure modes (e.g., change in damage mechanisms). Hence, it was decided not to carry out progressive damage and failure finite element analysis. In this way it was possible to test different loading scenarios instead of one scenario in detail.

An exhaustive discussion of the results was done, and further works to better understand the solutions studied were proposed.

1.4 Thesis approach method

Answering one of the research questions is independent of answering any of the others, as each question can be studied separately. Hence, all the information and knowledge learnt while answering one of the questions is not directly transferable to other questions and, on some occasions, not transferable. However, to some extent, each of the questions is relevant to each other, as all four want to answer the use of additive layers for suppressing delamination in different loading scenarios. Therefore, the four distinguishable questions parted from a standard methodology particularised for each question to answer.

The procedure for studying each research question is as follows: first, a literature search and study were conducted to understand each research question's actual panorama and relevance. Second, a finite element (FE) modelling was performed based on linear elastic mechanics for measuring the value of ($\mathcal{G}$) at the crack tip of a pre-modelled delamination. Third, experimental investigations were conducted to verify the additive composite layers solution's effectiveness. Finally, both numerical and experimental analyses were compared and discussed thoroughly to verify the results of the proposed approach for each of these loading scenarios.

Due to the individual circumstances of each loading scenario, the FE models built

were specific for each of the loading scenarios. The shared part of all the FE models built is that they use the virtual crack closure technique (VCCT) [43], studying the effect of the solution on the value of the energy release rate $\mathcal{G}$. In this way, the energy release rate was a measurable variable used to study the solution's effectiveness in suppressing delamination. This value of ($\mathcal{G}$) was measured for both cases, without and then with additive layers placed over the free edge. Based on the difference obtained for the value of $\mathcal{G}$, one additive binding was chosen over the others for experimental testing.

Similarly, the experimental setup is different for each of the loading scenarios. The experiments were based on the American Society for Testing and Materials (ASTM) standards for each loading scenario. The nature of the solution studied, which is a change in the design of the specimens in itself, required modifications and considerations from the ASTM standards to take into account, as explained in chapter 4 for each of the loading scenarios.

1.5 Relevance of the research

Inmediate stakeholders of this research outputs are manufacturing companies which use composite laminates as structural components. For example, manufacturers of sailing boats could potentially benefit of stronger and more stable holes for increasing the safety of the possibility of the mast falling off. Also, companies that design fastened composite joins that could implement the solution presented as the output of the research question 4. Other manufacturing groups which could benefit are those which need to use alternative layups due to the pressence of free-edge delamination, incurring in additional weight and cost of the components.

Another immediate stakeholder of this research output is the Advanced Composite Group (ACG) of the University of Strathclyde, whose knowledge portfolio of design and analysis of composite laminates grows. Additional stakeholders are composite material groups that study the failure mode of delamination and methods for suppressing it. Other interested beneficiaries are any companies/groups/universities that want to numerically and experimentally characterise the performance of certain composite laminate layups without the happening of delamination/free-edge delamination. Further stakeholders are scientific journals that could be interested in publishing the research outputs of the four research questions or parts of them. Ultimately, other beneficiaries of the outcome of this research are my supervisors and me, as it would determine the validity of my candidature as a PhD and their capabilities for directing a PhD thesis.

The work carried out in this thesis deals directly with the improvement of composite

laminates for one of their modes of failure, delamination. The use of an innovative approach for improving the behaviour of composites is directly relevant to the sustainable development goal SDG number 9, which fosters innovation and development.

1.6 Thesis outline

This thesis is structured as follows:

Chapter 1 Introduction gives an introduction to the thesis, its background, aims, scope and stakeholders.

Chapter 2 Literature review collects the literature review conducted for the thesis. It comprises the explanation of failure mechanisms of composite materials, the theory used for understanding the work carried out, and the most present updates and findings on delamination in each of the loading scenarios at the time of the writing of this thesis. Literature on proposed solutions for stopping delamination in each of the loading scenarios is also provided.

Chapter 3 Concept of the solutions studied to suppress delamination in composite laminates introduces the idea of the additive binding and how the solution is conceptualised for the different loading scenarios.

Chapter 4 Finite element modelling deals with finite element (FE) modelling of delamination in composite materials. The background is provided on the approaches available. The VCCT is the approach used for the development of the FE modelling. The FE modelling used for each loading scenario is explained in different sections of the chapter. The chapter does not include the results obtained using the models since these are presented in the corresponding chapters to each research question.

Chapter 5 Specimens manufacture and experimental testing explains the manufacturing and testing procedures used in this research. An introduction to the manufacture of composites with prepregs is given, plus a detailed explanation of the manufacture and experimental setup for each of the specimens for the four research questions. The chapter does not include the experimental results obtained since these are presented in the corresponding chapters to each research question.

Chapter 6 Results on suppressing delamination in composite laminates under tension presents both the numerical and experimental results of the first research question based on the numerical and experimental work explained in chapters 4 and 5. The effectiveness of additive layers placed over the free edges of composite laminate tensile coupons for stopping free-edge delamination is discussed. Conclusions and possible future works are provided.

Chapter 7 Results on suppressing delamination in composite laminates under edge

impact presents both the numerical and experimental results of the second research question based on the numerical and experimental work explained in chapters 4 and 5. The effectiveness of additive layers placed over the edge of a composite laminate for stopping the advance of interlaminar delamination in composite laminates subjected to edge impact is discussed. Conclusions and possible future works are provided.

Chapter 8 Results on suppressing delamination in composite laminates with open holes presents both the numerical and experimental results of the third research question based on the numerical and experimental work explained in chapters 4 and 5. The effect of the additive composite layers placed around the free edge open holes of composite laminates is discussed. Differently from research questions, one and two, fatigue testing is also explored. Conclusions and possible future works are provided.

Chapter 9 Results on enhancing the bearing response of pin-loaded composite laminates presents both the numerical and experimental results of the fourth research question based on the numerical and experimental work explained in chapters 4 and 5. A discussion on the feasibility of additive layers for enhancing the bearing response of pin-loaded composite laminates is provided. Similar to the third research question, both quasi-static and fatigue testing have been done. Conclusions and possible future works are provided.

Chapter 10 Conclusions and future works gathers the conclusions obtained from the research carried out and provides possibilities for future works to add up with the outputs of this thesis and study better the use of additive layers for suppressing delamination.

List of References: the bibliographic references mentioned in the dissertation are presented.

Appendix A Numerical simulations additional information: in this appendix, the different finite element models are gathered. They are in the form of links to a repository containing the Python scripts used for the numerical analyses carried out in this thesis. Additionally, a detailed explanation of the functioning and operation of the Python scripts is provided.

Appendix B Specimens manufacture and testing additional information: in this appendix the complementary material of the experimental work is provided.

Chapter 2

Literature review

This chapter is intended to provide an introduction and understanding of the main failure mechanisms of fibre-reinforced plastics. Due to the significant amount of documentation available, the review presented is non-exhaustive but concise. Out of all failure mechanisms, delamination is acknowledged as one of the major failure modes in composite laminates. Its role in the four different loading scenarios studied in this thesis is exposed.

Composite laminates are made of different plies, where each ply is considered a unidirectional (UD) fibre lamina. The mechanical behaviour of a lamina is defined as transversely isotropic, while the behaviour of the composite laminate is orthotropic. Considering a single lamina or ply, the material presents high strength and stiffness in the fibre direction but has relatively poor mechanical properties when loaded transversely to the fibres, as the matrix controls the lamina properties in those cases. For facing bi-axial or multi-axial loading scenarios, several plies with different fibre orientations are bonded into a composite laminate [1]. The desired elastic properties for a composite laminate could be achieved by selecting the appropriate fibre and matrix material, the fibre volume, and the layup sequence of the plies. The fundamentals of orthotropic elasticity and laminate theory are well established [25, 32, 44–50]. Figure 2.1 schematically illustrates one single ply and the structure of a fibre-reinforced composite laminate. E_L and E_T stand for Young's modulus of the ply in both the longitudinal and transverse direction with respect to the fibre direction, respectively. Hereafter, the longitudinal direction in a ply refers to one of the fibres in a 0° layer, and the transverse direction means across the width of the ply or 90° direction.

The most common and reasonably accurate method for obtaining the elastic properties of a single ply is calculating them by a rule of mixtures (ROM) [25]. For different models for predicting ply properties, see, for example, Hyer and White [49]. The application of the ROM is based on the assumptions that one composite ply is microscopically homogeneous, linear elastic, orthotropic and in an initial stress-free state. Additionally, both the matrix and the fibre are homogeneous, linear elastic and isotropic, and the fibres are regularly well-arranged in space within the matrix. Last, the presence of imperfections as voids is neglected, and perfect coupling between the fibre and the matrix is assumed.

At the laminate level, the most commonly used theoretical framework for designing composite laminates is the classical laminate theory (CLT) [25]. The CLT assumes a plane stress condition in the laminate that converts it primarily into a two-dimensional theory. In this way, out-of-plane stress distributions are not considered. Hence, the CLT is inadequate for calculating interlaminar stresses, which might be important in the vicinity of stress concentrations as notches, holes or free edges. Nevertheless, these stress concentration fields decay rapidly with increasing the distance from the geometrical irregularity. Therefore in regions far from these stress concentration points, the CLT is assumed to be accurate. For the procedure of calculating laminate elastic properties, please visit [25] or [49].

[1] The stacking order of the various fibre-oriented plies is known as a *layup* or *stacking sequence*. Both terms are used indistinctly across the whole document.

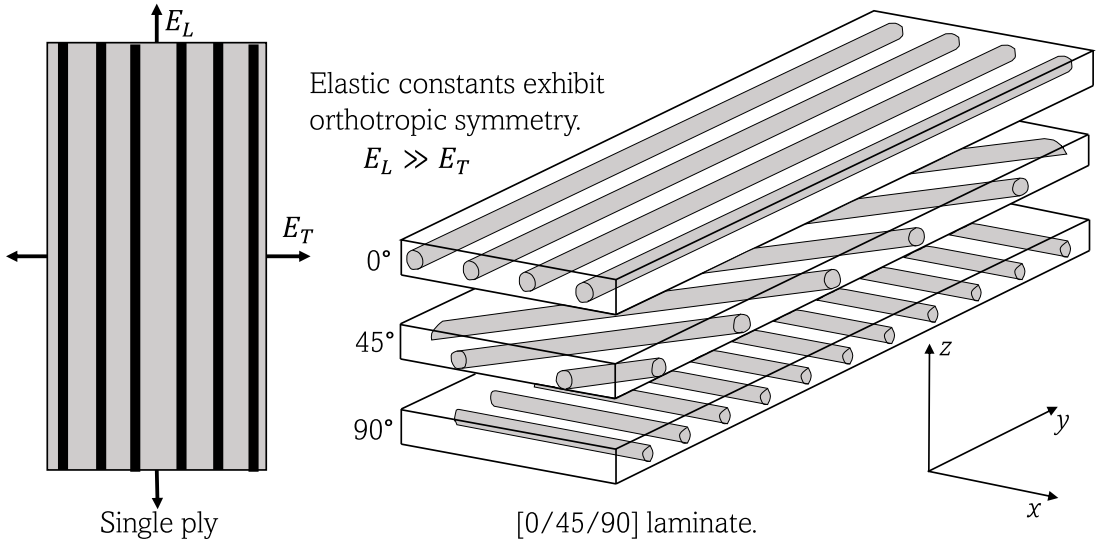

Figure 2.1: Schematic structure of fibre reinforced composites - Modified from [2].

One of the main differences between FRP and homogeneous materials is how damage originates and propagates. Although the *"damage cycle"* is similar for both metals and FRP, e.g., both begin with damage initiation, followed by damage propagation, and end in ultimate failure, the duration each of these phases is different for metals and FRP. Where metals generally propagate one crack that initiates from one specific point, the initiation of damage in an FRP is governed by a kinetic process of micro-crack accumulation, and when a critical density of micro-cracks is achieved, a macroscopic crack forms. When a crack forms in a composite laminate, the failure of the laminate seldom occurs catastrophically without warning but tends to be progressive with sub-critical damage widely dispersed through the material [2]. Also, most composites do not show any sign of plastic or ductile deformation before failure; therefore, they are usually described as brittle. However, this brittle behaviour differs from the brittleness that may occur in metals. The fracture behaviour of composites depends on their microstructure: volume fraction, strength, toughness and dimensions of the fibres, and volume fraction, strength, and ductility of the polymer matrix. Parameters such as the fibre-matrix interface are also important, and the presence of voids and defects can sometimes play a vital role in the failure mechanisms of a composite structure [51].

Many works [2, 25, 31, 32, 52, 53] have attempted to apply fracture mechanics to fibre reinforced composites to generate failure theories and predictions. However, the results from these attempts have met with mixed success. There are situations where fracture mechanics is appropriate for composites. However, the fracture of composite materials is often driven by numerous micro-cracks distributed throughout the material rather than a macroscopic crack. Thus, it is still necessary to understand the limitations of theories that were intended for homogeneous materials and that

have been adapted for composite materials [2].

Due to these variable and complex failure processes in composites, generating an accurate prediction for the failure of composites is highly challenging. Most of the work carried out for composites' failure prediction is divided into three main topics: developing accurate failure theories and acquiring comprehensive and reliable testing data sets, and developing numerical tools for the analysis of composites. All these three topics are challenging, but generating a rock-solid data set of experimental results that could be used for verifying different failure theories is depicted as the most challenging topic, as explained by Christensen in [54]. Despite the extraordinary efforts of various experimental programmes for composites characterisation as the worldwide failure exercises [55–57], there is still a lack of reliable data sets that do not satisfy some failure theories while coarsely fitting into others.

2.1 Damage mechanisms in fibre reinforced composites

The failure mechanisms of composite laminates have been classified into three main groups in the literature, e.g., *interlaminar, intralaminar and translaminar* failure mechanisms [1] [58, 59]. The interlaminar fracture mode -often referred to as interlaminar delamination or simply delamination- occurs between two adjacent plies and lies in a plane parallel to the fibres. The intralaminar fracture mode is located inside the laminate and comprises matrix cracking, matrix-fibre debonding and longitudinal splitting. Last, the translaminar fracture mode refers to the breakage of the fibres. Figure 2.2 schematically illustrates these three fracture modes. The amount of energy required for the failure to occur in each failure mechanism is different in each of them by orders of magnitude. For example, processes such as fibre-matrix debonding need about 4 to 40 times higher energies than interlaminar delamination, and events such as fibre failure or pull-out are between 20 and 600 times greater energies than the energy required for crack growth in the carbon-epoxy interlaminar direction [60].

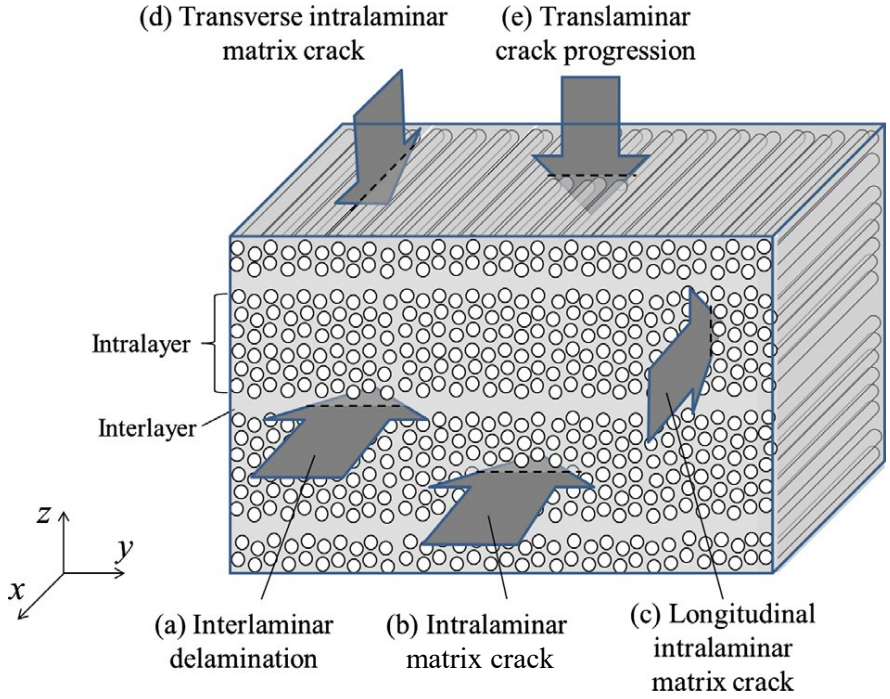

Figure 2.2: Ply-level fracture mechanisms exhibited by continuous FRP - Reproduced from [61]

Longitudinal tensile loading can produce matrix cracking, fibre bridging, fibre breakage, fibre pull-out, delamination and fibre-matrix debonding. These various failure mechanisms are illustrated in figure 2.3. The complexity of the analysis of the failure

[1] It is often found in the literature that the terms *"failure mechanisms/modes"* and *"fracture mechanisms/modes"* are interchanged. These are not to be mistaken with the *"crack extension modes"* that are illustrated in figure 2.5.

of composite materials arises as all these failure mechanisms can happen simultaneously and interact between with each other, which often means there is not a consistent sequence of damage onset. Furthermore, although, as mentioned, the propagation of failure is generally progressive and not sudden, these failure modes tend to occur in areas which are out of eyesight. Hence, advanced nondestructive inspection methods [62] are needed for damage detection, e.g., ultrasonic [63], radiographic [64], thermal [65] and optical (holography and shearography) [66] methods.

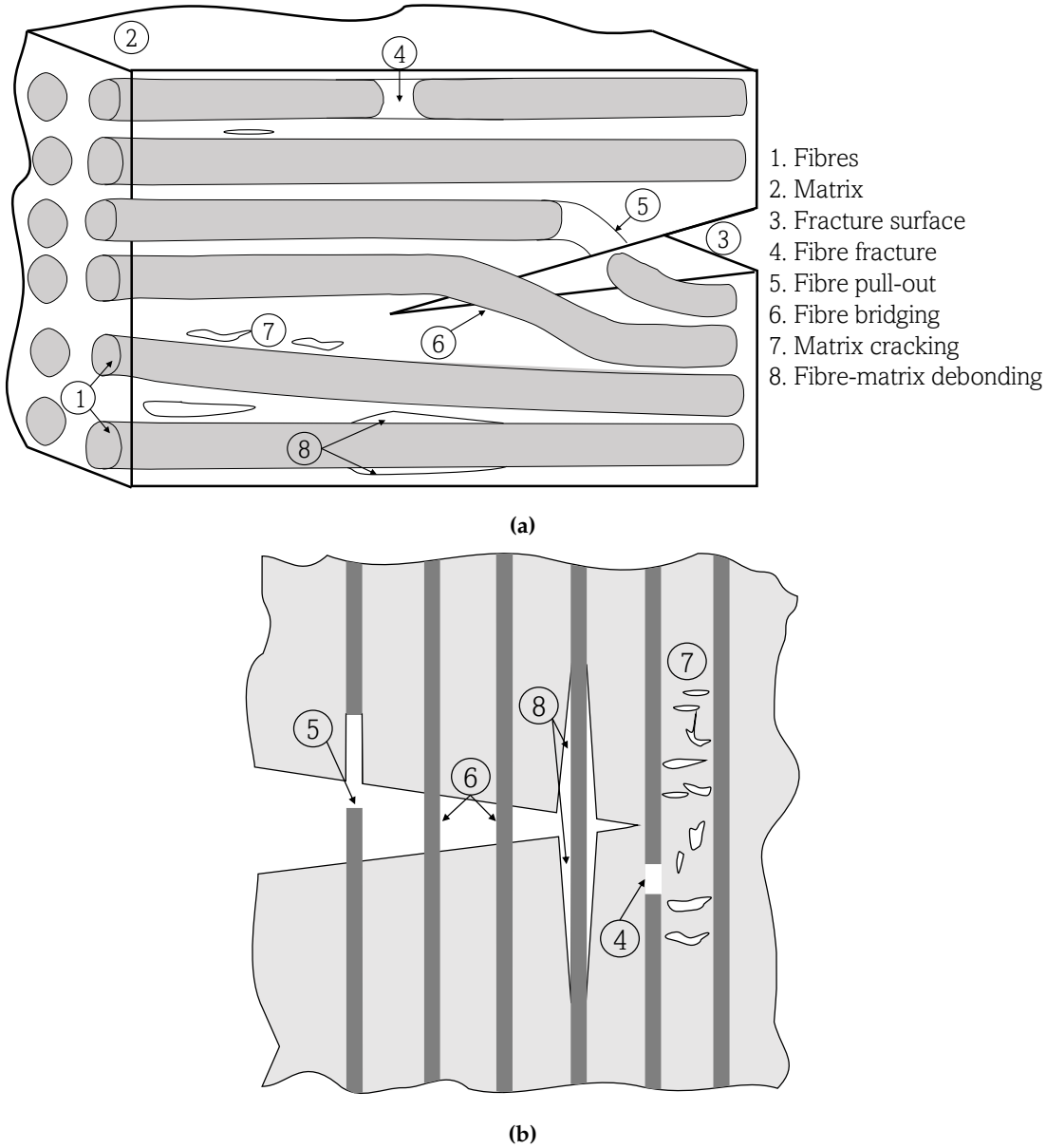

Figure 2.3: Schematic of typical damage modes of UD laminates under tensile loading. - (a) 3D view, (b) side cross-section view.

An explanation of each fracture mode's critical failure mechanisms, e.g., delamination, matrix cracking and fibre breakage, are presented in the following subsections. Nevertheless, a sufficient though a less detailed description of other failure mecha-

nisms is also provided in each of the following subsections, e.g., fibre kinking in section 2.1.3 as a fibre fracture mode.

2.1.1 Interlaminar fracture - delamination

From a macroscopic point of view, delamination is the one of the most common failure mechanism in composites. Composite laminates offer exceptional in-plane strengths. However, due to these materials' laminated structure, they suffer from relatively poor out-of-plane properties and a subsequent tendency to delaminate. Thus, delamination is a critical failure mechanism in composite laminates, not for causing the composite to break into different pieces but because it degrades the laminate to such a level that it losses its structural integrity, leading it to its final failure. Interlaminar delamination in composite structures degrades the laminate to the point that it becomes useless in service. In addition, it can lead to premature buckling of the laminate, excessive vibration, moisture intrusion, stiffness loss, and fatigue life degradation [58].

Initiation of interlaminar delaminations could arise from different sources. It could be initiated due to the impact of foreign objects (e.g., bird strike, dropping of tools or other collisions) or processing-induced defects in FRP composite parts (e.g., machining, cutting, drilling as recollected in-[67]). Residual stresses from processing and manufacturing (e.g., thermal stresses, voids, and chemical shrinkage in thermoset matrices) provide initiation sites for delamination or contribute to their propagation and growth. Moreover, stresses that lead to delamination could also result from structural sources, such as the geometry of a composite structure, e.g., two panels joined in a "T" configuration, edges, holes and ply drop-offs. However, out-of-plane stresses that lead to delamination can also arise from the mismatch in the Poisson's ratios between adjacent plies of a composite laminate. This mismatch of the Poisson's ratios results in shear stresses in the x-y plane (please see figure 2.1 for axis reference) near the ply interface. To counterpart and balance these shear stresses, a through-the-thickness stress is originated in the z-direction. If the mismatch in Poisson's ratio is big enough, substantial out-of-plane stresses occur at the edge of the panel, which can lead to the formation of a delamination crack.

In 1970 Foye and Baker [68] published a landmark report in which they observed a significant strength and failure mode dependence as a function of the stacking sequence in a laminate. This report led to the first investigation of Pagano and Pipes on the effect of the stacking sequence on laminate strength [17]. After those investigations, studies on delamination and its dependence on the laminate stacking sequence blossomed and became one of the most extensively studied phenomena in the composites literature, e.g., [29, 33, 69, 70]. These studies demonstrated that interlaminar

through-thickness stress σ_z (see figure 2.1 for sign convention) and shear stress τ_{xz} are maximum, approaching infinity, at the free-edge. In contrast, the shear stress τ_{yz} is maximum close to the edge but zero at the edge. Figure 2.4 illustrates the computation of σ_z and τ_{xz} at the interfaces of laminates under tension with different directions plies adjacent to each other. Also, the effect of the stacking sequence on delamination has not only been studied for composites under tension but also on notched composite laminates and structures [18, 71, 72], composites under impact [73] and bearing behaviour of bolted composite joints [19, 74].

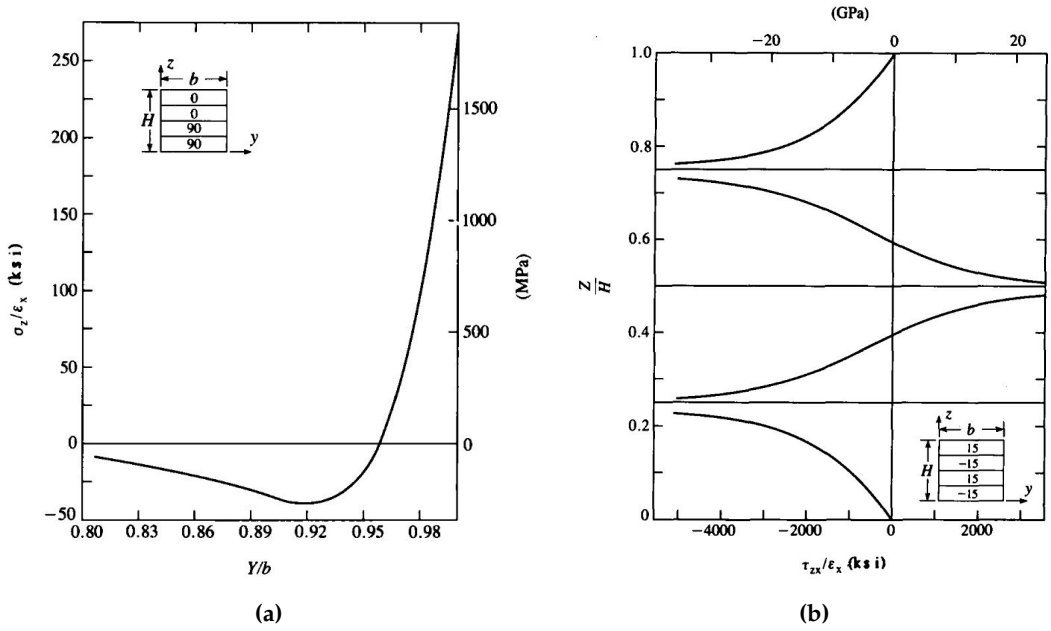

Figure 2.4: Interlaminar stresses in laminates with different fibre-orientation plies. (a) interlaminar normal stress on midplane of a $[90_2/0_2]_s$ laminate, (b) Interlaminar shear stress τ_{zx} near free edge of a $[(\pm 15)_2]s$ laminate - Reproduced from [70].

There have been a large number of works proposing criteria for the prediction and development of delamination. Two clear approaches are depicted in all of these works: one based on the strength of the material and the other based on fracture mechanics. The strength-based criteria approach involves a detailed stress analysis near the free edges used in conjunction with failure criteria [34]. These failure criteria are similar to Nuismer and Whitney's [75] average stress failure criterion. For example, Brewer and Lagace's quadratic stress criterion (QSC) [76] predicts failure based on critical values of both interlaminar shear and normal stresses (out-of-plane stresses) compared with their related strength properties. The work by Fenkse and Vizzini [77] incorporated the role of in-plane stresses into the QSC.

All in all, these criteria use combinations of the through-thickness tensile and shear parameters, in linear, quadratic or curve-fit relationships, with a small number also considering the stress in the fibre direction [78]. An exception is Wisnom et al.'s

approach [79], which is based on using principal stresses. For further reading on the different criteria proposed for characterising the initiation and development of delamination, based on strength, in composite laminates, the reader is directed to table 10 of the review carried out by Orifici et al. [80] on the methodologies for composite material modelling incorporating failure.

The other approaches to predicting the delamination propagation are based on fracture mechanics (FM). A review of different criteria based on FM can be found in table 11 of the review by Orifici [80]. Nevertheless, as the work done and explained in this thesis is based on fracture mechanics, an explanation of the basics of fracture mechanics is provided following for a better understanding of the technique used in this thesis to characterise delamination.

The FM method assumes that materials and structures always have some manufacturing defects and flaws that will cause the initiation and growth of cracks leading to structural failure. Although this assumption of a self-similar growth of a dominant crack often does not apply to the failure of composite materials, such an assumption is appropriate for delamination [2]. Thus, FM has been very successful in characterising delamination.

Fracture mechanics are based on an energy approach that states that fracture -or crack extension- occurs when the energy available for crack growth is sufficient to overcome the resistance of the material. This material resistance includes the surface energy, plastic work, or other types of energy dissipation associated with the propagation of a crack [2]. Despite being Griffith [81] the first one to propose the energy criterion, it was Irwin [82] who developed the concept for the present version of this approach: the energy release rat $\mathcal{G}$. The energy release rate is defined as the rate of change in potential energy with the crack area for a linear elastic material. In other words, the *energy release rate* is a measure of the energy available for an increment of crack extension. Based on the energy criterion, a crack can form or grow from an existing crack only if such process causes the total energy to decrease or remain constant and, thus at the moment of fracture, the energy release rate is equal to the critical energy release rate $\mathcal{G} = \mathcal{G}_c$, which is a measure of fracture toughness of the material [2]. It is to be noted that the term *rate*, as it is used in this context, does not refer to a derivative with respect to time. Instead, $\mathcal{G}$ is the rate of change in the total energy in the crack with the change in the crack area. How the area of the crack can change was defined by Irwin, who pointed out the three kinematic admissible crack-extension modes shown in figure 2.5. In this manner, these crack-extension modes can be added up to obtain any crack.

In order to quantify the crack growth in a composite structure, it is necessary to predict the conditions under which a defect or crack in the structure starts to propagate

and subsequently leads to failure. Delaminations can occur in all crack-extension modes or a combination of them. Thus delamination growth depends upon the fracture toughness of the material and the stress state of the crack tip, which is governed by the mixed-mode of the stress intensity factors K_I, K_{II} and K_{III} [1] or the strain energy release rates G_I, G_{II} and G_{III}. Not all three modes need to exist together, and generally, only one or two modes may dominate the fracture propagation [34].

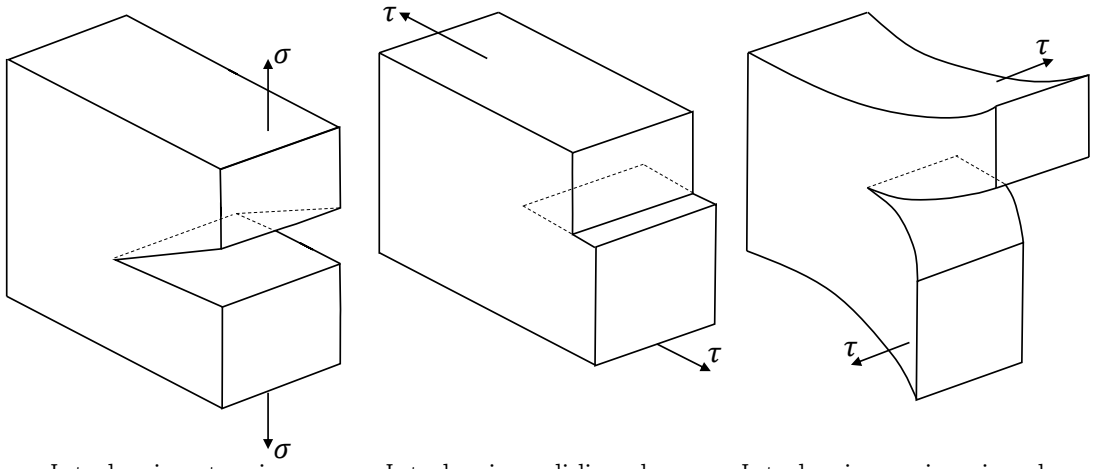

Figure 2.5: Schematic of the crack extension modes.

The procedure for calculating the energy release rate in a crack is explained as follows: If we consider an infinite plate subjected to a remote tensile stress (σ) and containing a planar flaw or crack of length $2a$, in the manner that the width of the plate is much larger than the size of the crack (width $>>$ $2a$), as seen in figure 2.6; then the energy release rate is defined as the difference between the rate of the work done, and the rate of the potential energy supplied by the internal strain energy and external forces, as the flaw area increases [82], as-is:

$$\mathcal{G} = \frac{d\Pi}{dA} = \frac{d\mathcal{W}}{dA} - \frac{d\mathcal{U}}{dA} \tag{2.1}$$

where

Π: total energy

$\mathcal{W}$: work required to create new surfaces

$\mathcal{U}$: potential energy stored in the flaw provided by the internal strain and external forces - Also known as strain energy [25, 83].

A: crack area

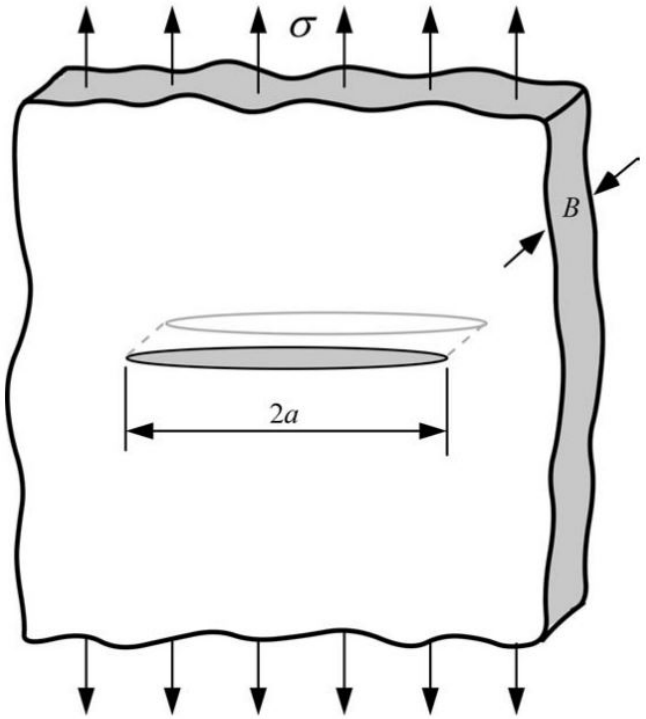

Figure 2.6: Through-thickness crack in an infinite plate subject to remote tensile stress. In practical terms, "infinite" means that the width of the plate is $>> 2a$ - Reproduced from [2].

One of the fundamental assumptions of fracture mechanics is that the fracture toughness ($\mathcal{G}_c$) -or critical energy release rate- is independent of the size and geometry of the cracked body, and it is solely dependent on the material [2]. This assumption is valid as long as the material behaviour is predominantly linear elastic.

Rybicki et al. [84] were the first to model the initiation and stable crack growth of delamination using the interlaminar energy release rate using a modified crack closure integral. Later, Rybicki et al. [85] derived the use of the energy release rate for the free-edge delamination problem (see section 2.2). They observed that the strain energy release rate value remained nearly constant during the propagation of delamination and hence determined that the critical energy release rate could be a helpful parameter for characterising the onset and growth of delamination.

Later, Wang [31] also studied the problem of delamination on the basis of fracture mechanics. He used the stress intensity factors (K_I, K_{II} and K_{III}) and the energy release rate to study the influence of fibre orientation, crack length and ply thickness on the free-edge delamination problem. He observed that the fibre orientation and ply thickness influenced the delamination behaviour (in terms of K_I, K_{II}, K_{III} and $\mathcal{G}$) significantly. Moreover, he observed that for edge delaminations at the interface of angle-ply laminates of the form of $[\pm\theta]$, the K_{II} is considerably lower than K_I

[1]The reader is referred to [2] for a deeper explanation of the stress intensity factors.

and K_{III}, and that free-edge delamination is dominated by K_{III}, (tearing mode as shown in figure 2.5). This higher magnitude of K_{III} is dependent on the ply angle (θ). However, this dominance of mode III for free-edge delamination is not a shared feature for all stacking sequences, e.g., [83] showed that the mode III contribution was negligible.

O'Brien [83] used this approach for predicting delamination based on strain energy release rate. He used a combination of energy release rate and classical laminate theory, procuring a simple yet effective method for predicting the initiation of free-edge delamination. His method is based on the stiffness loss experienced by laminates when delamination occurs, hence procuring a critical strain ϵ_c at which delamination starts.

The method proposed by O'Brien was used in this thesis for selecting the substrate laminate used for the first research question, as explained in the section section 6.1. Hence, further explanation of O'Brien's method is given in the following section section 2.2 of the literature review.

On a micro-scale, but related to delamination, one contributing factor in the composite's fracture toughness is the mechanisms of fibre bridging (schematically shown in figure 2.3 and illustrated in figure 2.7). The interlaminar fracture toughness, which in composites is usually characterised by a critical energy release rate, is mainly related to the matrix material's fracture toughness. However, the matrix and the composite's fracture toughness are not the same due to the influence of the fibres in the latter. The fibre bridging, which can take place usually between two distinct crack surfaces in composites with a low strength matrix, could lead to an overestimation of the critical energy release rate. In some instances, the crack grows around a fibre, which then bridges the crack faces and adds resistance to further crack growth. This is because it reduces the stress at the crack tip as it still transfers some stress and allows further interfacial debonding at the fibre-matrix interface. Fibre bridging is quite present in UD composites. However, the effects of fibre-bridging are reduced to almost non-existing in delamination resistance testing of FRP composites with angle-ply (non-unidirectional) layups [86]. For further reading on the fibre bridging mechanism, the reader is directed to the review carried out by Rafiullah in [87].

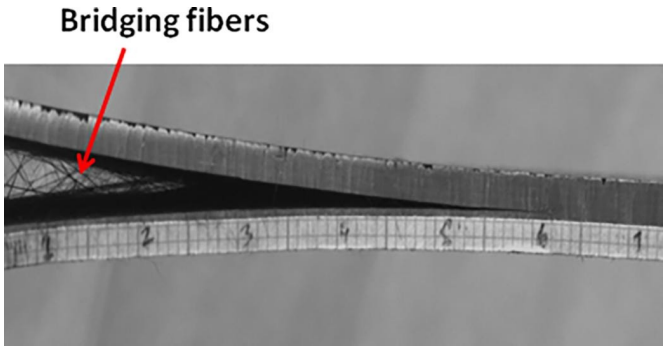

Figure 2.7: Fibre bridging in a specimen under Mode I loading - Reproduced from [87].

As it will be explained in section 2.1.2, bridging is also a key feature in the failure mechanisms of matrix cracking.

2.1.2 Intralaminar fracture - matrix cracking

Withing the failure modes that originate due to intralaminar fracture, matrix cracking is generally the most critical of them all. Matrix cracking -also known as transverse cracking when it occurs in 90° plies- is generally the first failure mode to occur. Matrix cracks can propagate between the fibres through the thickness of the laminate rather than between the plies. In addition to reducing the mechanical properties and structural integrity of composite materials, matrix cracking is the precursor of other failure modes that can be fatal for the structure or component, e.g., fibre breakage and/or delamination. The fracture mechanisms (b) intralaminar matrix crack, (c) Longitudinal intralaminar matrix crack and (d) transverse intralaminar matrix crack, as shown in figure 2.2, are all related to matrix cracking.

The initiation of matrix cracking could have different sources, e.g., voids [23] and fibre-matrix debonding in the off-axis plies [3]. These cracks, which typically initiate at defects or fibre–matrix interfaces, accumulate throughout the laminate, coalesce, and lead to failure across a critical fracture plane.

In the matter of matrix cracking developing from voids in the laminate, Liebig et al. [88] indicated that voids are located not only in the resin-rich interlayer region but also in the fibre-rich intralayer region (see figure 2.2 for reference). These voids are present between the fibre and the matrix, making the fibre one-side supported in some areas, as schematically shown in figure 2.8a. The voids lead to stress concentrations, and the bigger the void, the higher the stress concentration along the void. As a result, the voids significantly influence the load transfer between fibre and matrix [88]. Liebig et al. determined that the void length has an essential effect on the compression failure modes like shear-driven fibre failure or fibre buckling (see section 2.1.3 for an explanation of fibre failure modes) due to the only one-sided support

of the fibre. Additionally, these voids between the fibre and the matrix could derive into fibre-matrix debonding.

Paris et al. [89] studied the influence of the fibre-matrix debonding phenomenon in the case of laminate tension loading. Based on their findings, the matrix failure mechanism is associated with cracks running between fibre and matrix (fibre-matrix debonding) and interacting between them to create a zone of damage of macromechanical meaning. In this way, it is clear that the interface between the fibre and the matrix plays an essential role in the formation of cracks [89, 90]. The growth of fibre-matrix debonding, under quasi-static or fatigue loading, could develop matrix cracking that travels across different interfaces, forming a macroscopic crack visible to the naked eye. Additionally, matrix cracks in adjacent ply groups may produce stress concentrations near their intersection, which give rise to local delaminations [91]. Figure 2.8 shows an example of fibre-matrix debonding and how it could develop into a matrix crack.

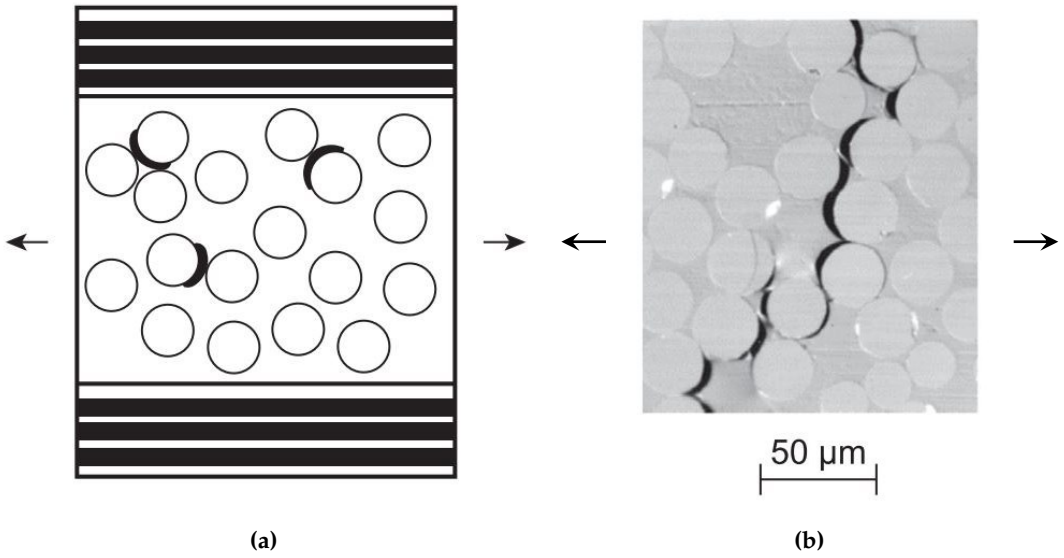

Figure 2.8: (a) Schematic of a 0/90/0 cross-ply laminate with fibre-matrix debonds developing. (b) Coalescence of fibre-matrix debonding into a crack - Reproduced from [3].

It is worth mentioning that the cracks in composite laminates are often generated and propagated within the fibre-rich "intralayer region" of the prepreg, as shown in figure 2.2(b). Matrix cracks typically extend across the thickness of the ply or plies with a common orientation (e.g., it is usual to find matrix cracking in composite laminates with groups of 90° plies when these are longitudinally loaded[1]), but do not necessarily extend across the width of the laminate [3]. This way, matrix cracks in the 90° layers can initiate short cracks in adjacent plies with other orientations, e.g., matrix cracking transfer from 90° plies to ±45° plies in quasi-isotropic laminates.

[1] As declared before figure 2.1, the longitudinal direction is that of the 0° layers.

The intralaminar matrix cracking growing across the width of through-the-thickness of the composite laminate is also known as intralaminar delaminations [61] (parallel to the lamination plane), which are different from what is usually referred to delamination or interlaminar delamination[1]. Nevertheless, matrix cracking and interlaminar delamination are intrinsically related. For example, although delamination in a free edge (as is explained in section 2.1.1 and section 2.2) is principally driven by the stresses arising from the mismatch in Poisson ratio and the sudden discontinuity of material properties, matrix cracking is almost always a necessary precursor to edge delamination [92]. Figure 2.9 shows an edge view of a $[0_2/90_2/\pm 45]_s$ CFRP laminate after fatigue loading showing matrix cracking in both the 0° and the 45° plies, as well as interlaminar delamination at the 90/45 interface.

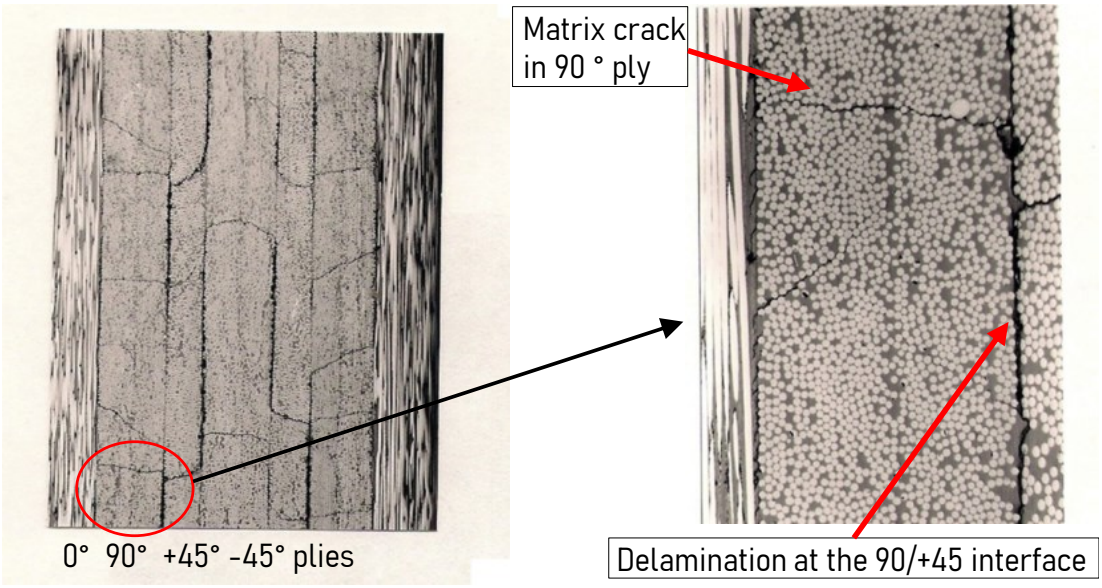

Figure 2.9: Matrix cracking and interlaminar delamination occurrence at a free edge. On the left, an edge view of a $[0_2/90_2/\pm 45]_s$ CFRP laminate after fatigue loading shows matrix cracking in both the 0° and the 45° plies, as well as interlaminar delamination at the 90/45 interface. On the right, the circle region from the left at a higher magnification - Reproduced from [3].

In the case of composite layups with 90° plies, the detection of matrix cracking onset could often be observed in stress-strain curves in the form of a non-linearity of the curve [3]. This non-linearity occurs due to two factors. First, the stiffness of the laminates decreases as a consequence of the matrix cracking in the off-axis layers (90°layers) of the load direction. Second, the "locked-in" thermal strain is released locally to the crack, allowing the compressive longitudinal thermal strains in the not 90° plies to relax, therefore lengthening the specimen. This "locked-in" thermal strain is generated on the cooling of the laminate during the manufacture (see sec-

[1]The fracture mechanism of interlaminar delamination and the approaches for quantifying and predicting it are explained thoroughly in section 2.1.1.

tion section 6.3 for reference) as a result of the mismatch in the coefficients of thermal expansion (CTE) between the 90° plies and the other different orientations plies [93]. Bailey et al. [94] observed a relationship between the thickness of the transverse plies (90° plies) and the onset strain value for the transverse intralaminar crack formation. They determined that for $[0/90/0]$ GFRP laminates with 90° plies of 0.5 mm or more, the onset longitudinal tensile strain for intralaminar transverse crack formation was independent of the thickness of the ply thickness and had a value of 0.5%. However, for 90° plies of less than 0.5 mm thickness, the strain for crack formation increased as the ply thickness decreased. This feature is exploited nowadays by the denominated "thin-ply" composites ($<$100 μm thick), which have remarkable resistance to the development of matrix cracking, and hence delamination [95].

Another type of matrix cracking is known as splitting. Splitting usually occurs when the crack runs parallel to the direction of the applied load, and it separates fibres between them as a result. For example, several studies have reported splitting of the 0° fibres in cross-ply laminates (generally $[90/0/90]$ laminates or arrangements of the sort) [3, 94, 96]. Splitting originates due to the mismatch in the poison ratio between adjacent plies and generally develops along the whole thickness of the ply. Splitting is also usually defined as a translaminar failure mechanism induced by shear-driven matrix cracking, as explained in section 2.1.3.

Wealthy literature is available for the analysis of matrix cracking and failure. All criteria developed for the matrix failure in tension assume a critical fracture plane in the transverse direction. Furthermore, apart from the maximum stress and maximum strain criteria, they generally involve an interaction between the tensile normal and in-plane shear stresses. Among the most common failure criteria, the maximum stress and maximum strain criteria are based on a comparison of the magnitudes of the individual stress and strain components with their appropriate strength and allowable strain values. After these, the most straightforward criteria proposed is that from Hashin and Rotem [97] for UD composite laminates. As mentioned in the interlaminar fracture section 2.1.1, Hashin later developed a failure criterion that included the through-thickness strength [78]. The criterion most often used over the years is the second-order tensor polynomial criterion proposed by Tsai and Wu in 1971 [45], as recollected in the historical review carried out by Herakocivh [50]. Finally, Puck's failure criterion is the most restrictive failure criterion [98], which recognises three different types of matrix failures. These correspond to the three different orientations of fracture planes relative to the reinforcing fibres. It is worth mentioning that Puck's failure criterion performed quite good in the world failure exercise, showing pretty accurate predictions [99].

A feature of longitudinal intralaminar fracture is large-scale bridging. It has been

studied that for any intralaminar failure mechanisms, the bridging of fibres in the crack region, as schematically shown in figure 2.3, has a significant influence on the intralaminar fracture toughness and crack propagation behaviour [100]. This increase in the crack propagation resistance is generally reported and studied using the fracture mechanics concept of *R-curves* [101], which depicts the crack growth resistance, $\mathcal{G}_R$, as a function of the crack extension, Δa.

2.1.3 Translaminar fracture - fibre failure

Out of all failure mechanisms in a composite laminate, fibre fracture is the most catastrophic of them all. This is because fibres are the load-carrying parts, and their collapse means the impossibility for the laminate to keep on sustaining load. In this manner, fibre failure is also the failure mode in which most energy is liberated. Typical energy values needed in the event of fibre breakage go from 20 to 60 kJ/m^2 [60]. For comparison, the energy required for interlaminar delamination development is usually between 0.1 to 1.5 kJ/m^2.

The fibres conforming composite laminates are statistically identical. This means that they are all different between them, due to different sizes of fibres (diameter), defects introduced in the fibres during the fibre manufacture or defects introduced during the composite manufacture (e.g., scratches on the fibre surface). This means that the fibres in a composite laminate will fracture at different values of the applied strain, generally producing isolated fibre fractures. At higher strains, these fractures could induce failure in adjacent fibres, leading to fibre fracture accumulation and final collapse of the laminate [3].

The presence of other failure mechanisms influences fibre failure. For example, as mentioned before in section 2.1.2, matrix cracking induced from fibre-matrix debonding could provoke the premature failure of fibres due to stress concentrations. In addition, Jamison [102] reported the presence of fibre fractures in 0° plies adjacent to matrix cracks during fatigue loading of cross-ply CFRP laminates, and hence related influence of matrix cracking on fibre fractures. This behaviour was also observed by Zangenberg et al. [103] in non-crimp fabrics and by Topal et al. [104] in 3D non-crimp orthogonal woven fabric composites.

Apart from fracture of the fibre in tension, fibres could also break in compression, e.g., kinking, splitting and compressive shear failure. Although the stresses from which failure modes arise act in the fibre direction, fibre splitting and fibre kinking are fibre failures that occur due to matrix failure, so shear-driven compression failure is the only one resulting from fibre failure. Figure 2.10 shows the different compression-driven fibre fracture modes in UD composite laminates.

Shear-driven compressive failure of fibres is originated when the compressive strength is surpassed. The fibres break cleanly, creating a clear separation at the fracture point, as shown in figure 2.10. Ewins et al. [105] observed shear-driven fibre compressive failure for the first time in composites with high tensile modulus. Later on, this phenomenon has been then well characterised in different works [106–108], that proved that the imperfections influence the compressive fibre failure in the fibre (e.g., waviness and misalignments of the fibre) and matrix cracks and delaminations that could enhance those misalignments and add rotation to the fibre within the matrix. Effendi et al. [108] suggested that the compressive strength of the composites could be improved by increasing the matrix yield stress or minimising geometric imperfections to avoid this type of failure.

Fibre kinking originates with the formation of a kink-band, as shown in figure 2.10. Kink-band formation propagates at an angle β from the fibre direction due to the initial rotation (θ_0) of the initially misaligned fibres, which induces shearing of the matrix. When the shear stress is high enough to provoke matrix failure, the fibres lose support and hence suffer additional rotation (θ), causing a twist in a portion of the fibres -known as kink width (w)-, and ultimate failure of the fibres [109].

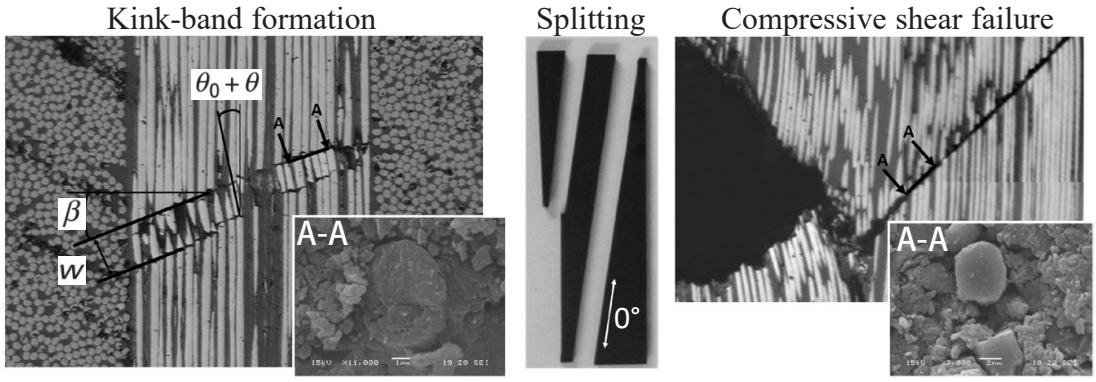

Figure 2.10: Fibre fracture modes in unidirectional composites in longitudinal compression - Reproduced from [109].

Similarly to kink-bands, and as mentioned in the previous section 2.1.2, fibre splitting is related to matrix cracking between fibres induced by shear. However, unlike fibre kinking, fibre splitting propagates through the whole specimen along the fibre-matrix interface [109], as shown in the central image of figure 2.10.

2.1.4 Summary - Failure mechanisms

Failure mechanisms in composite materials are various and complex. Due to the interaction in a mixed-mode of the different failure mechanisms, the anisotropy of composite laminates and the different loading scenarios, there have been several fail-

ure criteria and workarounds for characterising composite laminate failure. With the focus on interlaminar delamination, the approach of fracture mechanics for characterising the onset and development of a crack presented itself as a robust and straightforward method.

Literature on the role of interlaminar delamination in the different four load scenarios studied in this thesis is presented in the following sections.

2.2 Free-edge delamination in composite laminates

2.2.1 Free edge effects on the onset of delamination

As explained in section 2.1.1, delamination is a crucial failure mechanism in composite laminates. Delamination has different origins and primarily arises as a result of high interlaminar stresses. These interlaminar stresses are exceptionally high in the vicinity of free edges, as demonstrated by Pipes and Pagano in 1970 [13]. As a result, delamination at the free edges is one of the critical damage modes in composite laminates. It reduces the stiffness and strength of the laminates, leading to significant structural integrity loss and eventually laminate failure. Also, free-edge delamination is a significant problem for testing and characterising laminated composites. Unlike most final composite products, which have no or a small number of free edges, test coupons have long free edges that make them susceptible to free-edge delamination. Free-edge delamination undermines the actual load-bearing capacity of the laminate and gives non-representative test results. Figure 2.11 shows a photograph of free-edge delamination occurrence in a $[+45_4/0_4/-45_4/90_4]_s$ open-hole tensile test specimen, with the free-edge delamination happening between the -45° and 90° layers and connecting through the thickness of the 90° layer block.

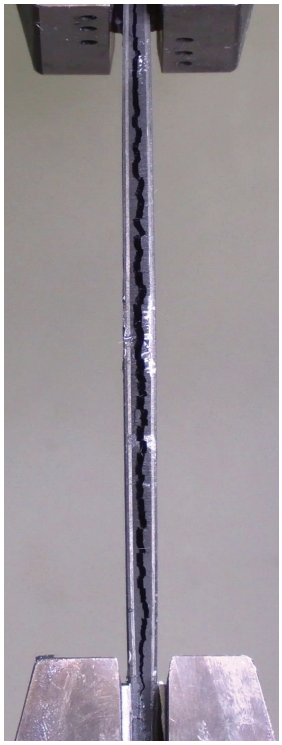

Figure 2.11: Photograph of free-edge delamination in a $[45_4/0_4/-45_4/90_4]_s$ open hole tensile test specimen.

Given its importance, free-edge delamination has been studied for decades, and rel-

atively good explanations and reliable methods to predict its development have been proposed. Pipes and Pagano [13] first gave a full three-dimensional stress distribution in composite laminates under axial extension. This work led to numerous investigations [15, 110–114] on the effect of the free-edges from a stress-based analysis. These studies demonstrated that interlaminar through-thickness stress σ_z (see figure 2.1 for sign convention) and shear stress τ_{xz} are maximum, approaching infinity, at the free-edge. In contrast, the shear stress τ_{yz} is maximum close to the edge but zero at the edge. These high interlaminar stresses near the free edge provoke edge matrix cracks, which are almost always necessary precursors for delamination to occur, and then the peel and shear stress drive the delamination [3].

The occurrence of these high stresses near the free edges is influenced by the stacking sequence of the laminate [17, 72]. In this way, there is a mismatch in engineering properties of adjacent plies in composite laminates, e.g., a mismatch in Poisson's ratio (ν_{xy}) and the coefficient of mutual influence ($\eta_{xy,x}$)[1] between layers [115]. The magnitude of these interlaminar stress depends on the value of $|\delta\nu_{xy}|$ and $|\delta\eta_{xy,x}|$, the elastic and shear moduli, stacking sequence of the laminate, mode of loading and environmental conditions as determined by Herakovich in [115]. Whereas mismatch on Poisson's ratio influences σ_z and τ_{yz} stresses, the mismatch in coefficient of mutual influence gives rise to the τ_{xz} stress near the free edge of a laminate. The mismatch in ν_{xy} and $\eta_{xy,x}$ are directly related to the orientation of the fibres in the laminate [115]. Figure 2.12 presents the dependency of ν_{xy} and $\eta_{xy,x}$ with the fibre orientation (θ) in unidirectional laminates for T300/5208 carbon-epoxy composite. As shown, the variation of ν_{xy} is symmetric about $\theta = 0$, and the variation of $\eta_{xy,x}$ is antisymmetric, based on finite element stress analysis performed by Herakovich [70].

For angle-ply laminates of the form $[\pm\theta]_s$, it could be derived that both interlaminar stresses σ_z and τ_{yz} would be negligible throughout the laminate, as ν_{xy} is an even function of θ. Hence, there is no mismatch in ν_{xy} for angle-ply laminates. The τ_{xz} shear stress would be non-zero and potentially significant, being it the leading cause of free-edge delamination in angle-ply laminates. Figure 2.13 shows the variation of $\eta_{xy,x}$ and the normalised τ_{xz} for an angle-ply laminate based on finite element stress analysis by Herakovich [70]. Based on this FE analysis, the value of τ_{xz} is maximum between 15°and 20°, varying slightly upon the elastic properties of the material.

The delamination between layers with the same Poisson's ratios and coefficients of mutual influence could still be possible, e.g., adjacent plies with the same orientation, if the interlaminar stresses caused by the neighbouring plies of different orientations or elastic properties are high enough. For instance, free-edge delamination in a laminate $[\pm 45/0/90]_s$ may occur at the through-the-thickness midplane, e.g., interface

[1] $\eta_{xy,x}$ is defined as the ratio between the shear strain γ_{xy} and the axial strain ϵ_x.

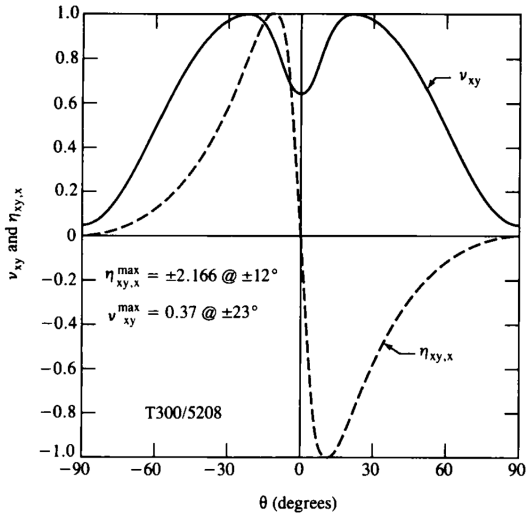

Figure 2.12: Normalised Poisson's ratio and coefficient of mutual influence as a function of fibre angle orientation in unidirectional laminates of T300/5208 carbon-epoxy composite - Reproduced from [70].

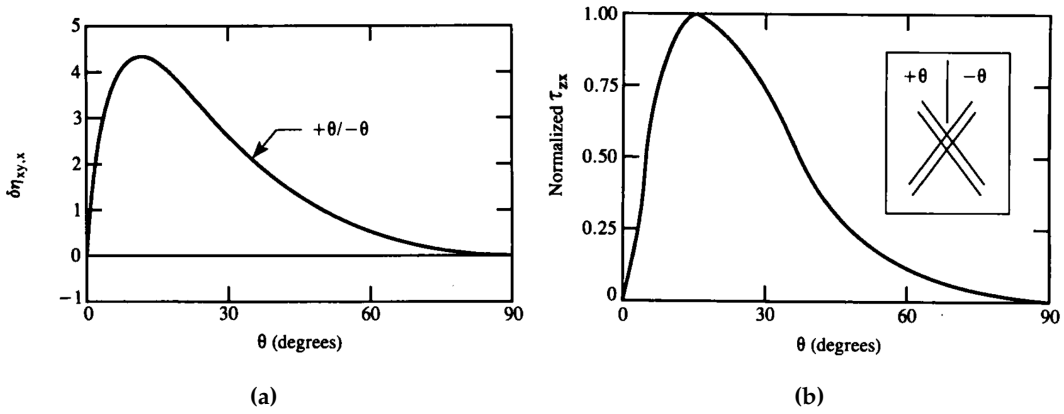

Figure 2.13: Mismatch of (a) $\eta_{xy,x}$ and (b) τ_{xz} in angle-ply laminates with the fibre angle orientation (θ) - Reproduced from [70].

$90//90$[1], where a significant value of interlaminar normal stress, σ_z develops. Figure 2.14 shows the stresses near the edge of a $[\pm 45/0/90]_s$ and its consequent delamination in the $90//90$ interface for different axial strains. For the same stacking sequence, Rodini and Eisenmann [116] experimentally demonstrated that the thicker the ply, which is stressed interlaminarly, the lowest the stress for originating free-edge delamination. This thickness effect cannot be adequately explained by a stress analysis alone and they proposed a probabilistic argument that the laminates with thick plies contain statistically more defects than laminates with thinner plies. However, this approach needs to deal with the occurrence of singular stress distributions.

[1]Hereafter the referral to a specific interface in a composite layup will be noted with a double slash while writing the composite layup, e.g., $[+45/-45/0/90//90/0/-45/45]$ for referring to the midplane interface $90//90$.

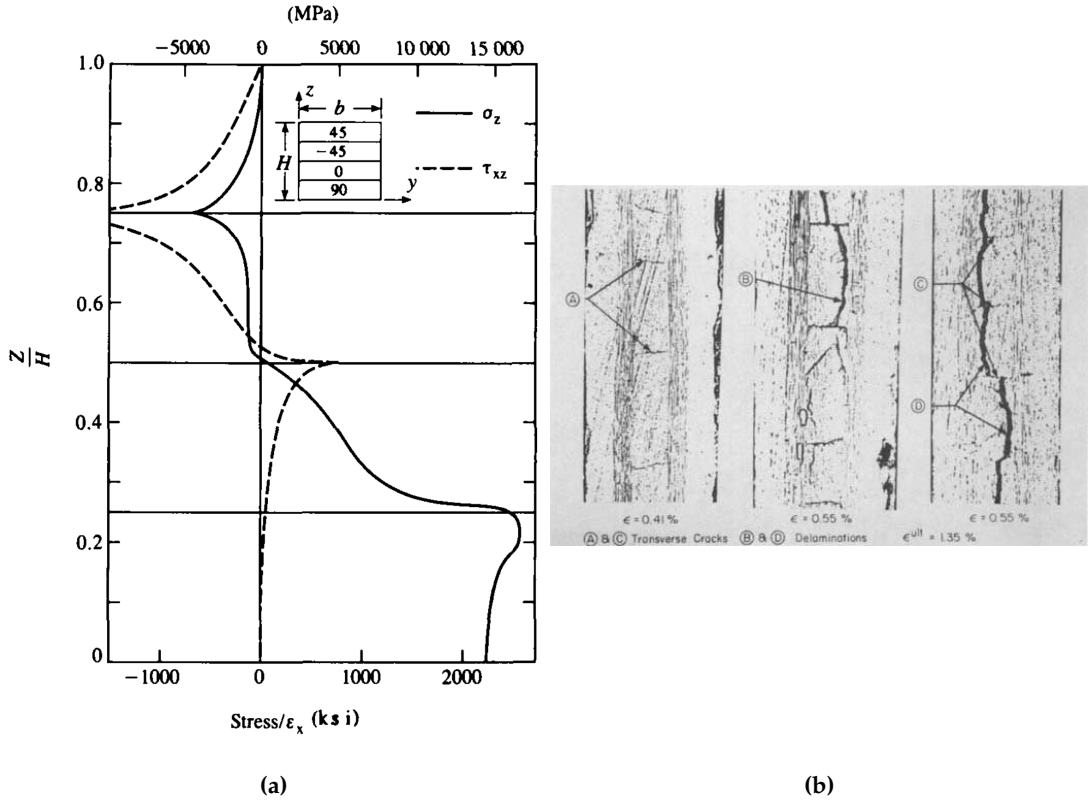

(a) (b)

Figure 2.14: (a) Stresses τ_{xz} and σ_z near the free edge of a $[\pm 45/0/90]_s$ laminate. (b) Edge damage of a $[\pm 45/0/90]_s$ laminate at different tensile strains - Reproduced from [70]

Due to such stress singularity at the edges, stress-based analyses have limitations in studying the free edge problem. Therefore, alternative methods from stress approaches for studying and predicting free-edge delamination were needed. As mentioned in section 2.1.1, fracture mechanics have been successfully used for characterising delamination and work good in the free edge problem.

Rybicki et al. [85] were the first to model the initiation and stable crack growth of delamination using the interlaminar energy release rate $\mathcal{G}$. They used a finite element analysis that did not require any special singular element or knowledge of a stress singularity in the solution. Plotting the energy release rate against the crack length, they observed that the strain energy release rate remained nearly constant during the delamination propagation. Hence, they determined that the critical energy release rate (or fracture toughness) could be a useful criterion for delamination growth. Additionally, they successfully predicted the onset of delamination in a $[\pm 30/\pm 30/90/\overline{90}]_s$ laminate.

Wang and Crossman [117] used fracture mechanics to investigate the effects of cracks in transverse plies (90°) on free-edge delamination. They used a FE formulation that used generalised plain strain for accounting for both the edge delamination and mul-

tiple transverse cracking growth processes. In the second part of their work [69], they managed to explain the effect of ply thickness on the transverse cracking and edge delamination. They assumed values of $\mathcal{G}_c = \mathcal{G}_\mathcal{I}$, but when they encountered mixed-mode cracking in one of their experiments, this equivalence was considered uncertain. The value of $\mathcal{G}_c$ for mixed-mode cracking changes from single-mode cracking. Wu and Reuter (Power law) [118], Benzeggagh-Kenane (BK law) [119], and Reeder [120, 121] have proposed different failure development criteria for calculating the value of $\mathcal{G}_c$ under mixed-mode cracking. The choice of criterion is not always clear in any given analysis, and an appropriate model is often best selected empirically. Last, Wang and Crossman praised the capabilities of the VCCT but pointed out the necessity of checking the convergence values of energy release rate with mesh refinement.

Later, Wang [122] studied the influence of fibre orientation, crack length, and ply thickness on free-edge delamination using stress intensity factors and energy release rate. As mentioned in section 2.1.1 and related to what Herakovich presented in [115], Wang showed that the mode-III stress intensity factor is one or two orders of magnitude higher than mode-I and mode-II stress intensity factors in angle-ply laminates.

O'Brien [83] used Rybicki's approach to characterise the onset and development of delamination based on the energy release rate and classical laminate theory. His method is probably one of the most important works as he obtained a simple equation (equation 2.2) for determining the critical energy release rate at which free-edge delamination would occur. Equation 2.2 is based on equation 2.1, and the loss of stiffness in a laminate after the laminate has completely delaminated. In this manner, he correctly predicted the delamination onset strain for $[\pm 30/\pm 30/90/\overline{90}]$ and $[+45_n/-45_n/0_n/90_n]_s$ (n = 1, 2, 3) laminates of T300/5208 carbon-epoxy composite. He determined that the onset strain of delamination is directly proportional to the square root of the laminate thickness. This was also reported later in other works, e.g., Crossman and Wang [123], and Schellekens [124]. Equation 2.2 is explained as follows:

Consider a symmetric composite laminate as shown in figure 2.15a. Based on O'Brien's experimental observation, a symmetric laminate of the type $[\pm 30/\pm 30/90/\overline{90}]$ would delaminate from the free edges along the two symmetric interfaces -30//90 from the midplane, as shown in figure 2.15b. The energy release rate at the free edges would be given by equation 2.2.

$$\mathcal{G} = \frac{\epsilon^2 t}{2}(E_{lam} - E^*) \tag{2.2}$$

It is necessary to mention that O'Brien developed this equation for the case of laminates which had 90° plies in the centre of the laminate. He observed that the 90°

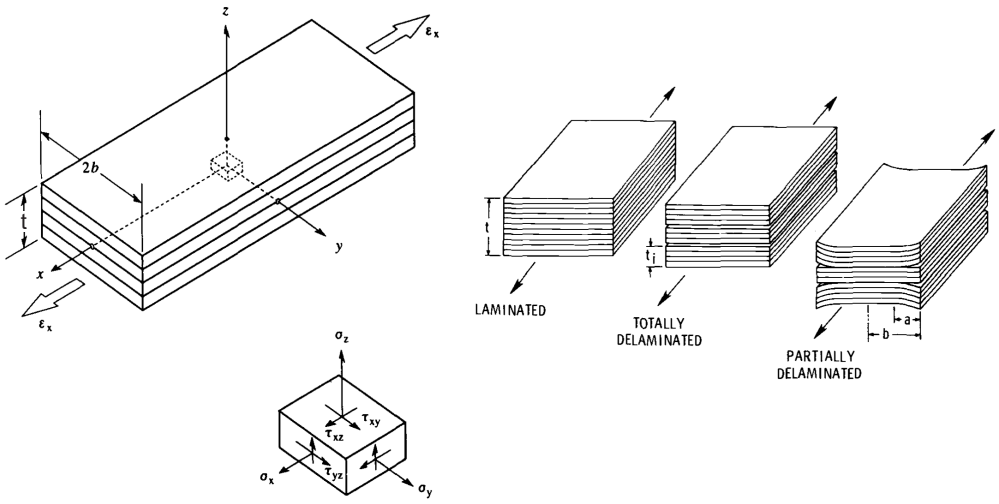

(a) **(b)**

Figure 2.15: (a) Symmetric laminated under axial strain - Reproduced from [70]. (b) Schematic of free-edge delamination in a symmetric laminate under axial loading - Reproduced from [83].

plies developed matrix cracking and zig-zag pattern that connected the delamination occurring in the -30//90 interfaces. This phenomenon also occurs in the other quasi-isotropic layup ($[+45_n/-45_n/0_n/90_n]_s$) that he tested, which is observable in the delamination profile shown in figure 2.11. In this way, instead of considering four cracks as sketched in figure 2.15b, he only considered two cracks for calculating the crack area and obtained results that agreed with his experimental observation and FE analysis. Thus, if using this equation for predicting the onset of delamination in laminates without 90° mid-layers, e.g., angle-ply laminates ($[\pm\theta]_s$), under the assumption of symmetric delamination from mid-plane as in figure 2.15b, equation 2.2 should be used with a "4" in the denominator instead of a "2". O'Brien explained this in Appendix I of his paper [83]. This appreciation is mentioned later on in section 6.1.

It is also interesting to mention that O'Brien calculated the total energy release rate ($\mathcal{G}$) as $\mathcal{G}_I + \mathcal{G}_{II}$ (as $\mathcal{G}_{III}$ was negligible) for the $[\pm 30/\pm 30/90/\overline{90}]$ layup. He assumed that the value of critical strain energy release rate ($\mathcal{G}_c$) is independent of the stacking sequence and hence used the same value of $\mathcal{G}_c$ for both layups, and successfully predicted delamination onset strain in the quasi-isotropic layup. This was possible as in both layups, the components $\mathcal{G}_I + \mathcal{G}_{II}$ are the predominant ones, with $\mathcal{G}_I$ being bigger than $\mathcal{G}_{II}$. However, this assumption might not be true always. For most resins and their composites, $\mathcal{G}_c$ may depend on time, environmental factors and crack modes. Additionally, the value of $\mathcal{G}_c$ is dependent on the mixed-mode crack opening modes [118–121].

Due to delamination, the composite laminate design seeks to avoid excessive free

edges or stress concentrators that could give way to free-edge delamination. Although delamination can not always be avoided, efforts to suppress free-edge delamination can be found in the literature. The following subsection recollects some of these solutions for suppressing free-edge delamination and compares the work done in their conceptualisation with the solution proposed for this thesis's first research question.

2.2.2 Free-edge delamination suppression concepts

Several attempts have been made to suppress the initiation and growth of free-edge delamination. Among all solutions investigated, there are two clear groups: solutions suggesting laminate modification and solutions applying local modifications at the free edges.

On the solutions suggesting laminate modification, Pagano and Pipes [17] suggested a rearrangement of the stacking sequence for reducing the interlaminar stresses that promote free-edge delamination. In this way, plies of similar orientation angle (whether θ or $-\theta$) should be separated and dispersed, looking to reduce the tensile σ_z or get compressive values of σ_z at the free edge. Figure 2.16 shows the distribution of interlaminar normal stress (σ_z) in the neighbourhood of the free edge for both adjacent plies with similar orientation angles or angle-dispersed. It is noteworthy that in Pagano and Pipes' laminates with plies interchanged in the stacking sequence, the extensional stiffness (A_{ij}) of the laminate is unaffected, whereas the bending stiffness (D_{ij}) is highly affected (please be referred to literature on CLT for better comprehension of the extensional and bending stiffness, e.g., [25, 46]). Additionally, there is a change in the values of interlaminar shear stresses. The resultant τ_{xz}, which is singular at interfaces with opposite ply orientations ($\theta//-\theta$), vanishes at the $15°//45°$ interface, while the τ_{yz} (not singular) attains a maximum at that interface [17].

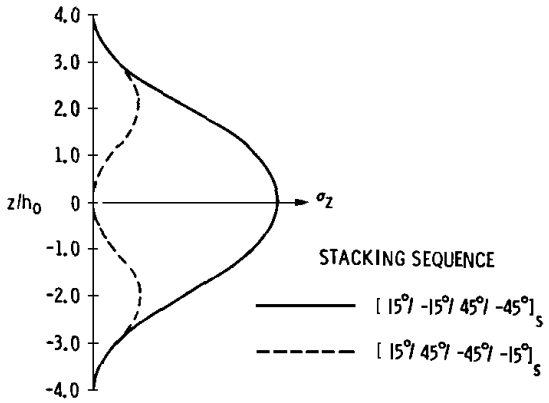

Figure 2.16: Distribution of interlaminar normal stress σ_z at the free edge - Reproduced from [17].

Herakovich [125] also added insight on the dispersion of layers with similar orientations for enhancing the strength of angle-ply laminates. He studied the influence of ply thickness in angle-ply laminates, as the thickness of the plies is an influencing parameter on the interlaminar stresses. He found out that the interlaminar shear stress τ_{xz} is about 25% higher in clustered (blocked) laminates than in alternating (dispersed) laminates. Additionally, the absolute value of τ_{xz} decreased, and it changed the sign at the layer which before had the highest value of τ_{xz}. Hence, he determined that the alternating $\pm\theta$ layer configuration provides significantly higher strength and toughness than a clustered or blocked configuration. Figure 2.17 shows a through-the-thickness interlaminar shear force and shear stress τ_{xz} distributions of different angle-ply laminates.

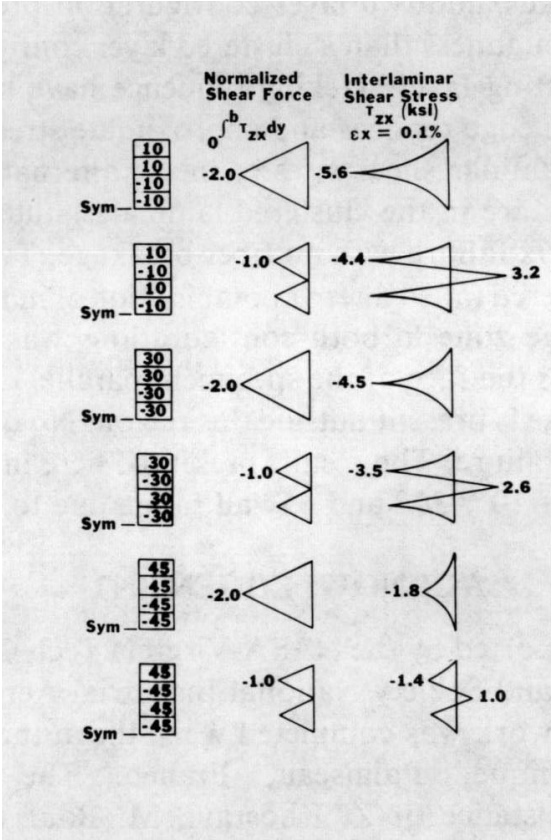

Figure 2.17: Through-the-thickness interlaminar shear stress and shear force distributions for angle-ply laminates - Reproduced from [125].

Krieger [40] used an *interleaving* technique, which places a discrete layer of tough unreinforced resin between the layers to achieve a higher interlaminar fracture toughness. In this way, introducing a ply (or interleaf) of an adhesive film with low stiffness makes it possible to reduce the shear stress concentrations at critical locations of composite structures.

Chan et al. [126] successfully suppressed delamination until final failure in $[\pm 35/0/90]_s$ and $[\pm 30_2/90/\overline{\pm 30_2}]_T$ laminates by means of adhesive layers placed between the

90°layers and the ±30° and 0° layers. In addition, they placed a thin but tough adhesive inner layer between interfaces and also only in the free edge area. They claimed that although there was no significant change in the total strain energy release rate, there was a significant decrease in the $\mathcal{G}_I$ (tension mode) percentage of the total strain energy release rate.

Similarly, Chan and Wang [39] (previously published in 1986 in [127]) studied the effect of a 90° layer when serving as the midplane layers on matrix cracking and the onset of delamination. In layups including 90° layers, the Poisson's ratio of the 90° ply relative to other ply orientations is a primary source of increased local stresses. Hence, to improve free-edge delamination resistance, Chan and Wang used a *hybridisation* approach, replacing the 90° carbon/epoxy plies in the original laminate with a lower stiffness ply. They studied using a hybridised ply of the same carbon and different resin and an S-glass/epoxy ply. This hybridisation reduced the mismatch in elastic properties of the plies. Their results showed that the hybridised laminates could withstand higher loads before the onset of laminate splitting, delamination and final failure. In this way, they concluded that the delamination and ultimate strength significantly increased when the hybridisation was done with the glass/epoxy layer.

There have been different approaches for avoiding or suppressing delamination on solutions that apply a local modification at the free edges to increase their interlaminar strength. Many of these techniques were centred and particularised for the case of laminates that presented 90° layers in the midplane of the laminate. For example, Pagano and Lackman [27] experimentally demonstrated that serrating the free edges of the laminate can reduce the chance of delamination in $[\pm 30/\pm 30/90/\overline{90}]_s$. They serrated the edges of the 90° layers and substituted the material removed with resin. Stress analysis of the serrated edges showed a reduction in the interlaminar normal stress, σ_z. Additionally, the ultimate failure stress of the laminates with the 90° serrated layers was increased by 32%. Chan and Ochoa, following the work of Chan and Wang in [127], and similarly to the edge serration done by Pagano and Lackman, conducted a prompt ply termination of the 90° layers of laminates that have a 90° layer in the midplane of the layup. This *critical ply termination* technique ends the 90° ply a small distance away from the free edges. As a result, the interlaminar stresses are reduced, and resistance to delamination is enhanced. Last, on solutions attacking the mismatch in elastic properties due to the 90° layers in the midplane of the laminate, Lee and Chan [128] studied a *discrete critical ply* technique. They proposed segmenting the 90° in the width direction, so the loading path for delamination growth is interrupted.

Mignery et al. [42] used a *stitching* technique for investigating free-edge delamination and ultimate strength in different layups of carbon/epoxy laminates and controlled

the onset and growth of delamination with X-radiography. They effectively arrested delamination, but the stitching technique had varying adverse effects on the tensile strength of the laminate. While the stitching does not cause a change in the interlaminar stress as in the previously discussed solutions, it improves the delamination resistance (fracture toughness) as the delamination crack approaches the stitch line. The stitching technique is widely used for enhancing the mechanical properties of the composite laminates [129]. Stitching, as a through-the-thickness reinforcement, influences the in-plane properties (bulk moduli and tensile strength) as well as out-of-plane properties (interlaminar properties and fracture energies). Stitches behave as bridging mechanisms (see Damage mechanisms in fibre reinforced composites for fibre bridging). See the literature review by Drake et al. [130] for further reading on the effect of stitching in out-of-plane composite properties.

Chuaqui et al. [131, 132]. They have presented an effective resin treatment on free edges to improve the short beam shear test accuracy and avoid free-edge delamination while simulating several non-standard layups in open hole laminates under tension. This technique bonds two resin blocks onto the free edges of the laminate, reducing the interlaminar stresses and delaying the onset and propagation of delamination.

Howard et al. [133, 134] presented a composite U-shaped cap as a reinforcement for free edges. A stress analysis at the edges and a qualitative semi-empirical correlation were carried out, showing a reduction of the interlaminar stresses at the free-edges of a $[\pm 30/\pm 30/90/\overline{90}]_s$ carbon/epoxy laminate. In a later study [135], it was seen that the prepreg material used for conducting the experiments had been stored for more than 10 years, and hence the results obtained in [133, 134] were different than if a fresh prepreg had been used. They tested three U-cap layup configurations, e.g., unidirectional cap (0° fibres), cross-ply cap ([0/90] fibres) and a ±45° cap, based on O'Brien's assumption [83] that the predominant failure mode for free-edge delamination is mode I delamination (delamination due to high σ_z).

Their results showed a reduction in interlaminar stresses, where the [0/90] cap reduced the most the σ_z and τ_{yz} at the 90° layers, and the ±45° reduced the most the σ_z at the ±30° layers. Although their stress predictions indicated that the ±45° cap would enhance the ultimate strength the most, their choice of material (Kevlar-epoxy) showed low strength in ±45° arrangements, hence not allowing higher carried loads. Only when three layers of these ±45° Kevlar-epoxy cloth were placed over the edge a modest increase in strength was obtained. The ply thicknesses of the materials they used for the caps are 0.137 mm for the carbon-epoxy tape and 0.084 mm for the Kevlar-epoxy cloth. In this way, they decided that the [0/90] carbon-epoxy tape was a better optimum solution that reduced the most interlaminar stresses of the laminate

they studied. Howard et al. highlighted the need for a suitable method for accounting for delamination as the stress-based method they used was mesh sensitive due to the singularity around the free edges, and the presence of delamination could not be modelled.

It is worth mentioning that although the physical concept of the solution proposed by Howard et al. [133, 134] is similar to the approach investigated as the first research question of this thesis, the approach in this thesis is quite different and more exhaustive, as it will be explained in following sections and chapters. In this thesis, an additive composite laminate made of thin-ply unidirectional prepregs is applied to the free edges of cured composite laminates to suppress free-edge delamination, as schematically shown in figure 3.1. In this thesis, these thin secondary added composite layers are referred to as "additive binding" as they are added to the primary substrate and cured in a second stage to bind the layers together at the free edges. To address the stress singularity drawback in the work by Howard et al., the effect of the additive binding is studied on the energy release rates in the presence of different delamination sizes and locations using the virtual crack closure technique (VCCT) [43]. The developed technique is used to study a wide range of additive binding layups. As will be presented, a different optimum layup is suggested as opposed to that proposed in [133, 134]. This study shows that bindings can suppress the growth of free-edge delamination as it propagates to larger sizes by reducing the energy release rates. Also, a thermal analysis has been done to study the possibility of thermal stress introduction by the binding when curing. Additionally, the recent developments in the tow spreading techniques and thin-ply technology [95, 136] have allowed the introduction of small amounts of additive secondary materials in the experiments. This provides the opportunity to suppress the free-edge delamination with a minimal alteration of the geometry, significantly less than standard ply thickness materials, e.g., those used by Howard et al.

As a brief resume of the main differences between Howard et al. work and the one presented in this thesis, there are:

- The use of thin-ply prepregs, allowing the suppression of free-edge delamination with a minimal alteration of geometry, significantly less than those that used standard ply thickness materials, e.g., Howard et al.
- The study in this thesis is done from a fracture mechanics point of view. The effectiveness of the reinforcement (additive binding) is studied on the energy release rate in the presence of different delamination sizes, and locations using the virtual crack closure technique (VCCT) [43].
- A different optimum layup is suggested as opposed to that proposed in [133,

134].

- A thermal analysis was carried out to study the possible thermal stresses that the additive binding may induce in the laminate when curing.

2.2.3 Summary - Free-edge delamination in composite laminates under tension

Free-edge delamination is one of the important damage modes in composite laminates. Free edges in composites are stress concentrators. A singular three-dimensional stress state primarily provokes this free-edge effect in the vicinity of the free edges. The presence of these singular stresses can primarily be explained by the sudden discontinuous change of the ply elastic properties, especially the Poisson's ratio and shear properties in the interface of two different-orientated layers [70]. Attempts to stop free-edge delamination found in literature could be divided into solutions suggesting laminate modification and solutions suggesting local modifications to the free edges. Most of these solutions were proposed and studied from a stress-based point of view. Due to the stress singularity at the free edges, the solution studied in this thesis is investigated by means of fracture mechanics.

All in all, the free edge problem has been studied for more than 50 years, and it is challenging to envelope all the work carried out. For a more exhaustive read on the effects of free edges in composite laminates, please refer to the literature review by Mittelstedt and Becker [137].

2.3 Composite laminates under edge impact

Composite materials are highly susceptible to impact damage. Impact events in FRP originate damage that could include indentation, matrix cracking, fibre-matrix debonding, delamination and eventually fibre breakage [138]. One major problem is the susceptibility of composite components to impact damage at low energy or low-velocity impacts (LVI), which frequently leave no visible mark, but are the source of notorious internal damage [139]. Even when no sign of impact damage is observed at the surface of impact (energies below Barely Visible Impact Damage, BVID), matrix cracking and inter-laminar failure can occur. This is because the impact energy at which visible damage is formed is much higher than the impact energy level at which substantial loss of residual properties occurs [138]. These impact-induced delaminations constitute a significant cause of compressive strength loss, and hence impacted laminates tend to buckle in the delaminated areas under compression loads. Additionally, the fatigue life of impacted composite specimens was found to be de-

termined by the compressive part of the loading and not by the tensile part [140]. For this reason, compression after impact (CAI) and compressive stress after impact (CSAI) tests were proposed in order to quantify the compressive reduction strength [138].

Most of the time, impacts are transverse or out-of-plane impacts (skin impacts). This means that the impact location is on the top or bottom surface of a composite laminate. This kind of impact gives way to the development of damage within the composite structure, degrading the structure's strength and affecting its structural capabilities for withholding load. Although skin or transverse impacts are the most common, edge-on or edge impact (in-plane impact) could also occur in specific scenarios. The edge-on impact is most commonly related to impact on the edge of a stringer on a stiffened panel [141] during manufacturing or in-service maintenance and inspection. An aeroplane's composite centre wing box is a good example of a composite structure with many free edge stringers or stiffeners inside. They are highly loaded and are designed to resist buckling to keep the structure safe, but if a tool drops on the stringer edge during the plane's maintenance, its residual properties can be drastically reduced [139, 142]. Figure 2.18 shows a FE schematic of a centre wing box of an aeroplane with the stringers. After impact, the load-carrying capability of composite structures, e.g., stringers, could be significantly affected since damage which can be introduced reduces the strength of the structure significantly [143, 144].

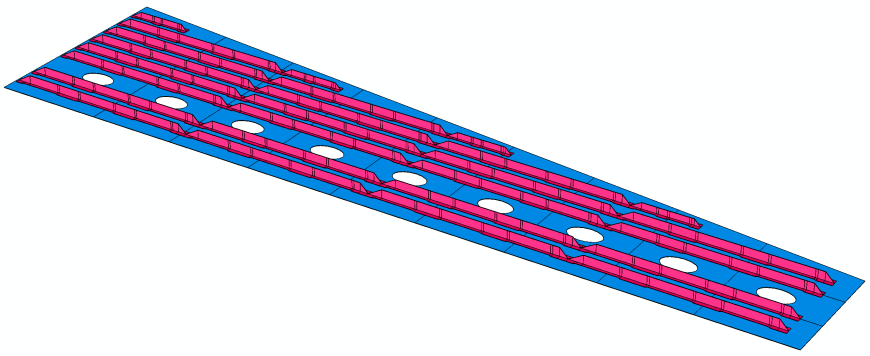

Figure 2.18: FE schematic model of stringers on a composite wingbox skin.

A wealthy literature could be found about testing and simulation of ou-of-plane impact-induced damage, e.g [73, 140, 144–162], and even industry standards (ASTM D7136 and ASTM 7137, etc.) have been developed. However, the edge-on impact or in-plane impact-induced damage has been considerably less studied [139, 142, 163–165], where the work by Ostre et al. is one of the most complete ones [166–169]. Figure 2.19 shows an schematic of the principle of edge-on impact.

Malhotra [139] experimentally studied the effect of impact position for low-velocity

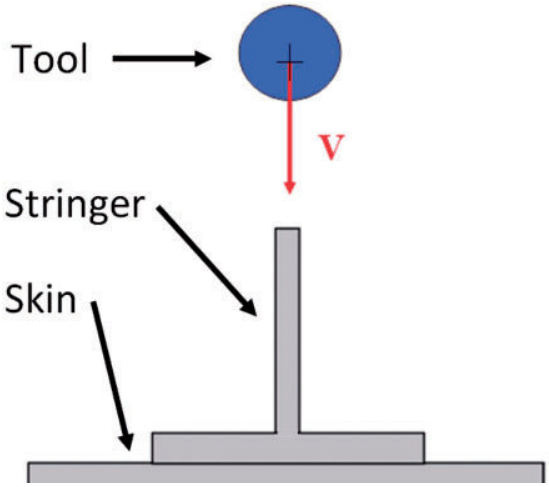

Figure 2.19: Edge impact principle - Reproduced from [166].

impacts and its correlation with residual strength. Rhead et al. [142] presented a semi-analytical fracture mechanics model for studying the compressive strength of composite laminates following edge impact. They assumed the final failure of impacted laminates is caused by delamination buckling, which leads to propagation of damage away from the original site. Ostre et al. developed a three-dimensional model for capturing the edge impact [167] and compression after impact [169] response of composite laminates. The model is a discrete 3D impact model using Abaqus explicit solver and a user-defined Vumat subroutine. Their model is based on the one developed by Rivillant, Bouvet and Hongkarnjanaku in [170] and validated for different stacking sequences in [73]. They used cohesive elements to model the interlaminar delamination and intralaminar matrix cracking. The fibre failure is implemented by conventional continuum damage mechanics (see for example [171] for more information in continuum damage mechanics, CDM) but with original formulation between the integration points of the element to produce a constant energy release rate per unit area. More recently, Thorsson et al. [172] used a shell-based FE modelling technique for capturing the response of a laminate subjected to low-velocity edge impact and compressive strength after impact. They managed to predict with a sufficient level of agreement the damage caused by impact energies that produce barely visible impact damage.

In this thesis, the in-plane, edge-on or edge impact is the case of study, as is one loading scenario in which the additive binding solution could be of use for enhancing the damage tolerance of composite laminates against impact-induced damage. Hence, edge impact-induced damage is explained in the following subsection. The damage events succession in a composite laminate's edge impact scenario is explained.

2.3.1 Damage caused by edge impact in composite laminates

The impact damage scenario is susceptible to the material properties, the stacking sequence of the laminate and the impact energy. The damage mechanisms generated after an edge impact are similar to those developed during classical out-of-plane or skin impact testing (delamination, matrix cracking and fibre breakage). However, edge impact events present distinct features from skin impacts, such as a semi-elliptical damaged area with non-symmetrical delamination occurrence about the midplane [142] (usually at all interfaces [166]), and wedge effects and multiple matrix cracks along the length direction [166]. In previous studies, [141, 164, 166, 168] it was shown that typically the edge impact response of composite laminates is more similar to a progressive crushing process of the edge rather than a skin impact scenario. This is noted due to the occurrence of some phenomena like compressive fibre failure and wedge effects, which are of minor importance during skin impact, but become important in edge impact events, as well as in edge crushing [167].

In this way, the typical mechanical response of composites under edge impact is similar to that observed in progressive crushing of composite laminates [141, 164, 166, 168]. An initial peak force is observed at the impact moment, related to the stiffness of the laminate in the impact direction, followed by a progressive stage (plateau) of approximately constant force with eventual oscillations, in which matrix cracking and delamination develop [141, 166, 168]. Figure 2.20a shows the typical load-displacement curve of composite laminate under progressive edge crushing. Hull [173] classified the crushing process into two main failure modes. The first one is the one referred to as splaying (figure 2.20b), in which bundles of bending delaminated lamina splay on both sides of the main crack, and the broken matrix and fibres trapped at the crushing zone could lead to the formation of debris wedge on the surface of the crushing area [166]. The second degradation mode is known as fragmentation (figure 2.20c) and consists of the multiple short-length fractures of the plies due to pure compression, transverse shearing and sharp bending, forming small fragments on the crush zone [166]. These two failure modes are observed during edge impact as shown in figure 2.21.

Ostre et al. [166] were the first to propose the degradation modes and their chronology in the event of composite laminate's edge impacts. They proposed that the formation of kink bands and wedge effects have a leading role, followed by a crushing phenomenon. This description is similar to that of the crushing test curve (figure 2.20a), whereas the wedge effect could be compared to the splaying effect (figure 2.20b), and the kink band formation could be compared to the fragmentation mode (figure 2.20c). From the initial contact between the impactor and the edge until the moment that the maximum load is reached, the contact surface between the impactor

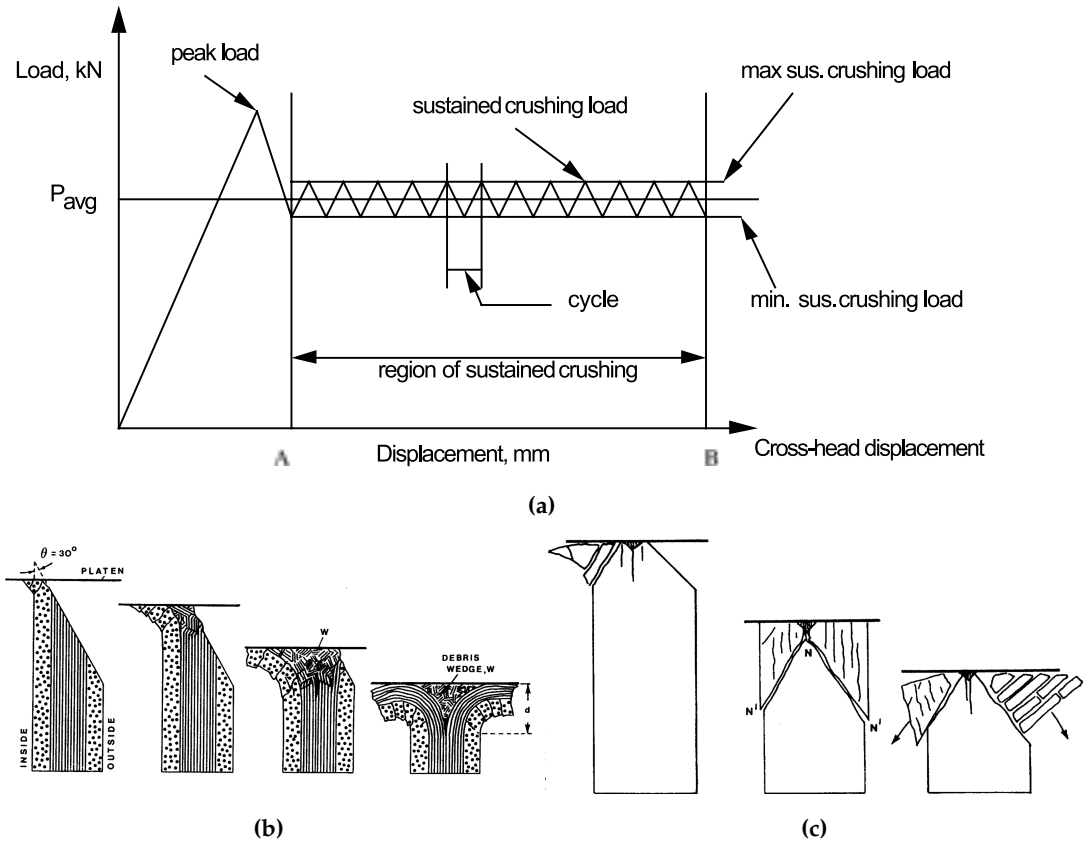

Figure 2.20: Composite laminate crushing process - (a) Typical load displacement curve for crushing test (reproduced from [174]) , and the two main degradation modes: (b) splaying of the edge, (c) fragmentation of the edge (reproduced from [173]).

tip and the specimen grows. During those moments, kink bands appear in the plies parallel to the impact direction. After the maximum force has been reached, it falls rapidly until the plateau force value due to crushing and the appearance of wedge effects, developing matrix cracks that propagate through neighbouring plies of different orientations. As the force reaches a plateau, interlaminar delamination starts to develop. Interlaminar delamination is the most energy-absorbing failure mechanism present; this is easily checked when observing the load-displacement curve, as the energy dissipated during the development of delaminations would be the area under the curve for the plateau region. As this crushing plateau progresses, the cracks advance from the middle of the thickness of the laminate, or point of impact, to the outer plies and a swelling effect appears. The remaining debris under the impactor help push the outer plies, and the swelling contributes to delamination spreading below the impact area [165]. Last, when all energy has been liberated, the discharge begins. The impactor displacement changes way, and hence there is a gradual drop in the stress value observed. Usually, a permanent indentation and an out-of-plane swelling footprint remain at the impact location after the impactor rebound, as seen

in figure 2.21. For more detail on the edge impact chronology description, please be referred to [166, 168]

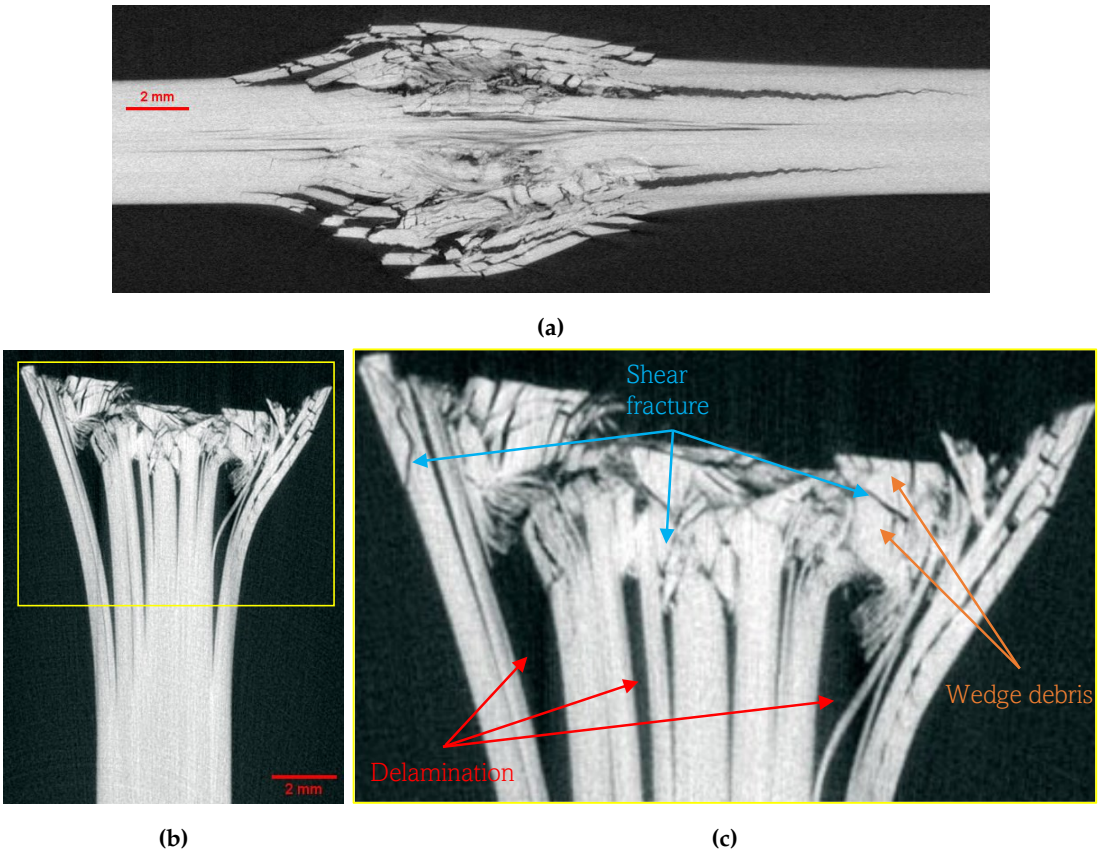

Figure 2.21: XCT images from a $[45_2/0_2/-45_2/0_4/90_2]_s$ composite laminate impacted on the edge with a cylindrical tup and an energy of 10J. (a) Top view, (b) cross-sectional view at the centre of the impact, (c) detail of the cross-sectional view pointing out delamination, shear fracture and wedge debris areas.

It is interesting to note that as the impact energy increases, the peak load and impact duration increase, while the crushing plateau load remains relatively constant [141, 166], and larger permanent indentations and out-of-plane swellings are obtained. Additionally, it was experimentally and numerically observed that the load at the plateau is apparently independent of the stacking sequence [166, 168]. Nevertheless, despite this independence of the crushing load with the stacking sequence, the damage extent is somewhat different [141, 166], hence affecting the subsequent CAEI response [165].

2.3.2 Low velocity impact damage tolerance enhancement

Impact events are challenging to solve or prevent. Hence, as previously mentioned, many efforts have been dedicated to understanding and predicting the damage tol-

erance of composite laminates under the events of skin or edge impact [1]. Several studies have been conducted on the influence of the stacking sequence of the laminate on the damage tolerance and how modifications of the layup could help to enhance the damage tolerance. Most of these studies have been dedicated to the cases of skin impacts [149, 158, 176–181], and, in contrast, not so many layups have been studied for the case of edge impacts. For example, Ostre et al. studied four different quasi-isotropic layups [166], and Arteiro et al. added two quasi-isotropic layups more [165].

A particular method for stacking sequence modification is the helicoidal or Boulingand-inspired architectures. These architectures are inspired by the shell of crustaceans and have gotten relatively good attention lately [182–189]. These helicoidal stacking sequences have been studied in the case of skin impacts showing an improvement in impact damage tolerance. Impacted helicoidal structures develop several cracks that remain parallel to the local fibre orientation, mainly by matrix cracking. In this way, the fibres are left almost undamaged [190]. This accumulation of the highly diffused sub-critical damage allows the bio-inspired Bouligand structures to withstand impacts while retaining more of their undamaged mechanical properties [191]. However, due to the difficulty in manufacturing and the research knowledge associated with the performance of twisted composite architectures [185].

Apart from varying the stacking sequence of the laminate, the use of different materials is also an important aspect to consider. Fotouhi et al. [192] reported the better potential of the glass laminates for energy absorption purposes compared to the carbon laminates. The S-glass/8552 epoxy laminates sustained higher deflections prior to failure than the IM7-carbon/epoxy laminates, while both materials experienced similar load levels. Additionally, the energy absorption of the glass laminates was almost two times higher than that of the carbon, hence the potential of glass laminates for use in applications susceptible to impact damage events. Moreover, using hybrid composite laminates has shown better performance than using only one composite system.

Saka and Harding [193] carried out in-plane tensile impact studies on woven hybrid composites. They observed that the tensile strength was higher at the impact strain rate than at the quasi-static strain rate. Their experimental studies showed that the tensile strength of woven glass/carbon hybrid composites was more than that of only-carbon or only-glass composites. Furthermore, Hosur et al. [178] studied the low-velocity impact response of hybrid composites made of plain woven S2-glass and twill woven carbon-glass fabrics. They reported a considerable improvement

[1] In case the reader is interested in solutions once impact event has happened, Hall et al. [175] have presented a study on the effectiveness of patch repairs for impacted composite laminates.

in the load-carrying capability of hybrid laminates compared to carbon-epoxy laminates with a reduction in stiffness [194]. Other studies similarly concluded that hybrid glass-carbon/epoxy composites give higher CAI and better load-bearing capacity than only-carbon or only-glass composites [195, 196].

In addition to these layup modifications, better matrix systems have also been suggested for enhancing the damage response. For example, Soutis [177] pointed out that materials with tougher (more ductile) resins suffer minor impact damage and show better strength retention in CAI than the standard resin systems. Moreover, Cartié and Irving [197] determined that resin toughness has a much more critical role than fibre strength and stiffness, influencing the CAI performance in quasi-isotropic CFRP laminates.

Similarly to the case for stopping free-edge delamination, Sharma and Sankar [198] used stitching to investigate its effect on the impact tolerance damage and the interlaminar properties of carbon-epoxy composite laminates under skin impact. They concluded that in this loading scenario, the stitching technique did not appreciably affected the damage resistance of the laminates. However, the damage tolerance improves significantly, and so does the CSAI. Additionally, they proposed a manufacturing method for the high-volume production of stitched laminates using the resin-infused mould (RTM) technique.

It is worth mentioning that, to the author's knowledge, no technique similar to the one present in this thesis for enhancing the damage tolerance of composite laminates under edge impact has been found in the literature. Using a thin-ply composite binding to protect the edge of composite laminates against edge impact is a solution that adds a neglectable amount of weight to the whole mass of the composite structure. However, small additions of these thin-ply layers have been proven to strengthen composite laminates in some scenarios, as in the case of free-edge delamination [199]. The concept of the solution proposed for the second research question in this thesis is depicted and explained in section Additive binding layers to enhance damage tolerance and response of composite laminates under edge impact of the chapter Concept of the solutions studied to suppress delamination in composite laminates

2.3.3 Summary - Composite laminates under impact

Literature on impact damage and impact response in composite laminates has been reviewed. The chronology of the damage development has been explained based on the work by Ostre et al. [166]. Most of the studies conducted have been for the case of skin impacts, and little literature can be found on the edge impact scenario. Due to the nature of the applications of composite structures in the transport industry,

weight is an essential factor. Hence, the addition of protections for avoiding impact damage is typically forbidding. In this way, much research has been carried out to understand the role of the layup on the impact damage tolerance, as the stacking sequence is something that can be varied easily without incurring in addition of weight. Hence, the use of additive layers for enhancing the damage tolerance of composite laminates under edge impact could be a potential tool due to its small weight addition to the composite structure.

2.4 Composite laminates with open holes

2.4.1 Considerations for fracture criteria of notched laminates

The presence of discontinuities as open holes in composite laminates means the occurrence of stress concentrations. In essence, open holes present free edges. Hence, the same problem as in the case of free-edge delamination occurs, where high interlaminar stresses arise due to the presence of open holes [71].

The problem of high stresses in the vicinity of open holes in plates has been studied for a very long time now [200]. It has been found that in the case of composite laminates, the strength of the system is a function of the absolute dimension of the cutout (hole) [201]. Furthermore, in composite materials with relatively brittle matrices and significantly orthotropic, the hole size effect is more pronounced [201].

Waddoups et al. [52] used linear elastic fracture mechanics (LEFM) concepts to explain the hole size effect. They pointed out that the value of critical stress due to the presence of open holes depends on the hole size. For hole sizes larger than one inch (25.4 mm), the ratio between the stress carried without a flaw or damage (σ_0) and the stress with the flaw (σ_c) was constant, while for diameters less than one inch, the tensile stress clearly varied with the hole size. The ratio between the stress at the hole tip (maximum stress at the hole) and the stress in the laminate without a hole is also called the stress concentration factor (SCF). Figure 2.22 shows the dependency of the stress concentration factor with the size of the hole based on the model by Waddoups et al. However, this model presented limitations. Due to the necessary development by Bowie [200], it could only be used for isotropic materials. In addition, the characteristic dimension (a) they used for characterising σ_c/σ_0 was not constant for all hole sizes, and they did not provide any physical interpretation for this dimension [71].

To characterise the strength of composite laminates with open holes, the works of Cruse [202] and Whitney and Nuismer [75, 203] were the first ones proposed. While Cruse [202] used a method based on LEFM with the critical stress intensity factors (K_c) for the material to determine the strength of notched laminates, Whitney and

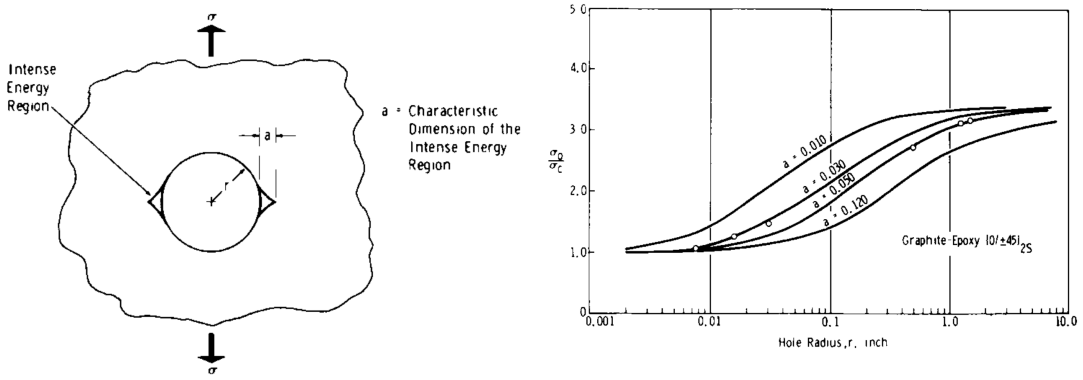

(a) **(b)**

Figure 2.22: Dependence of the stress concentration factor with the hole diameter by Waddoups et al. - Reproduced from [52]

Nuismer [75] focused on the finite state of stress near the boundary of the hole. Whitney and Nuismer used two different approaches that led to two two-parameter criteria that predicted the hole size effects without using LEFM. These two models [75] are known as the point stress and average stress models. The point stress model assumes that the final failure occurs when the stress at a characteristic distance from the hole reaches the unnotched strength of the laminate. In the average stress model, the failure is assumed to occur when the laminate stress averaged over a characteristic distance (d_0) is equal to the unnotched strength of the laminate. However, these two models presented limitations. As they fixed the value of d_0 to be constant for all notch sizes, their formulation yielded a two-parameter model, which was essentially equivalent to the LEFM models. For the laminates they studied, they observed a direct relationship between the Mode I fracture toughness and the unnotched laminate strength. For this reason, Whitney and Nuismer also ventured that the characteristic lengths a_0 and d_0 they used for their models are constant parameters for various laminates, discontinuity geometries and material systems. It is interesting to note that these stresses in the vicinity of an open hole are generally between three and four times the value of stress in the laminate without the hole [52, 71].

Pipes, Wetherhold and Gillespie [201] proposed a three-parameter strength model. Their model took into account several parameters that influence the notched strength of composite laminates, e.g., fibre-matrix interfacial bonding, matrix properties, fibre properties, fibre orientation and laminate stacking sequence. All these parameters were represented using two material properties they defined as ”notch sensitivity factor” and an exponential parameter ”m” that would be inherent to the material. They achieved excellent agreement between their model and experimental data from different stacking sequence laminates.

Vaidya et al. [204] proposed a fracture criterion for notched composite laminates containing 0° layers. The criterion is based on the experimental observation that the 0° layers govern the laminate strength. This is also in agreement with the failure mechanisms and failure chronology described by Hallet et al. [205], as the final failure of laminates with open holes under tension ultimately occurs when their 0° layers fail. Vaidya et al. introduced the fracture toughness of fibre breakage as an effective material parameter. In this way, the parameter is layup independent and can be used to predict the strength of any laminate configuration, which suffices the requisite of containing 0° layers in its stacking sequence. Additionally, later, Vaidya et al. [206] studied the effect of ply thickness on notched laminates, which present fibre-dominated strength (layers with 0° layers). They showed that ply block thickness significantly affects the notched strength of cross-ply and quasi-isotropic laminates, being less pronounced in the latter ones. As in the case of free-edge delamination, the amount of delamination increases with the thickness of the laminates. Furthermore, in the quasi-isotropic laminates, the failure mode changed from fibre failure to delamination failure when the thickness of the ply blocks was of four or more plies blocked together.

Camanho et al. [207] proposed a finite fracture mechanics model for predicting the open-hole strength of composite laminates. Their models are based on both a strength-based criterion (equivalent to the average stress criterion [75]) and fracture mechanics. As an improvement over other methods, the strength prediction method is based on independently measured material properties. There is no need for calibration for different hole sizes and specimen widths. The model only needs the ply elastic constants and two additional independent material properties: the unnotched strength of the laminate and the fracture toughness of the laminate. Additionally, the model is useful for assessing the brittleness of a given material/geometry combination based on the fracture toughness of the material. As a drawback, it should be noted that the finite fracture mechanics model is only applicable to notched laminates that exhibit pull-out or brittle failure modes (see section 2.4.2 for an explanation of failure modes of notched composites). In this manner, the model proposed is not valid for laminates which present delamination as failure mode, as appropriate numerical finite element analysis is required for predicting the strength in these cases [207]

All of these fracture criteria need to deal with the so-called ”size effects” in laminated composites [5, 10]. Size effects in composite laminates occur at different material and structural levels. For example, at the mesoscale, the tensile and in-plane shear strengths of a ply constrained by sublaminates depend on the ply thickness [208]. This phenomenon is also known as the ”in situ effect” and was initially detected by Parvizi in [208] when testing cross-ply glass fibre laminates under tension. This in

situ effect represents how, when plies constrain a ply with different fibre orientations in a laminate, their transverse tensile and in-plane shear strengths are higher than the strength of the same ply in a unidirectional laminate. The in situ effect is influenced by the number of plies stacked together and the fibre orientation of these constraining plies. Figure 2.23 illustrates the in situ effect for the relation between the in situ transverse tensile strength experimentally measured and the thickness of 90° layers in three different layups for T300/944 carbon/epoxy composite laminates. To predict the strength of notched laminates subjected to in-plane shear and transverse tensile stresses, a failure criterion should be established as a function of the in situ strengths [209].

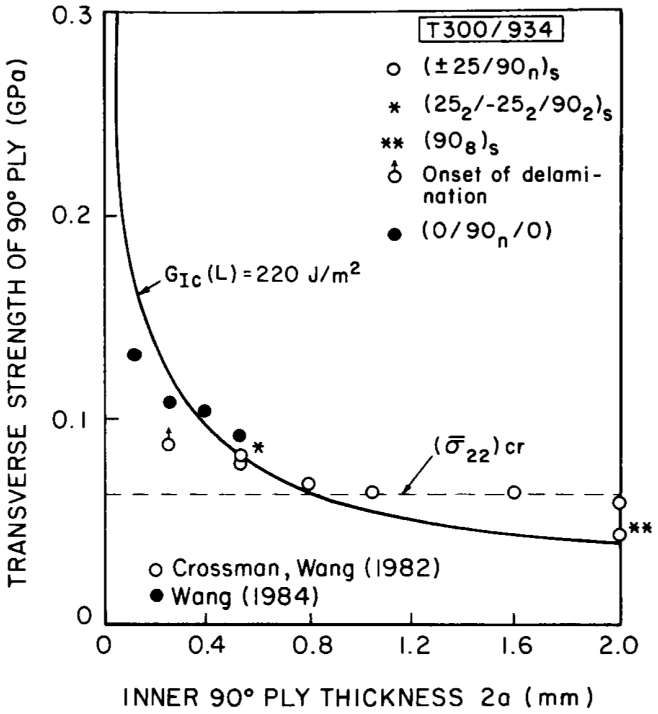

Figure 2.23: In situ effect in laminated composites - Reproduced from [210]

The size effect or in situ effect phenomenon has been studied particularly for composite laminates with open holes, e.g., [8, 11, 12, 211, 212], as different hole sizes give great variations in notched strength of the composite laminate. This effect, usually known as the ”hole size effect”, is caused by the development and propagation of non-critical ply-level damage mechanisms that occur in the vicinity of the hole before the final collapse of the laminate [8]. The nature of the non-critical damage mechanisms is known and has been reported, e.g., [211, 213]. However, The hole size effect is not the only geometrical parameter affecting the strength of notched laminates. For example, as in the case of unnotched laminates, the thickness of the laminate has an important role, especially in the case of ply-blocked laminates. Figure 2.24 shows the effect of thickness on open-hole tensile strength for 3.175 mm diameter holes in a

$[45_m/90_m/-45_m/0_m]_{ns}$ laminate, (with $m, n = 1, 2, 3...$). The subscripts m and n refer to the number of plies of each orientation, representing two different ways of increasing the thickness of the laminate. When m is increase, it is known as ply scaling, and when n is increased, it is known as sublaminate scaling.

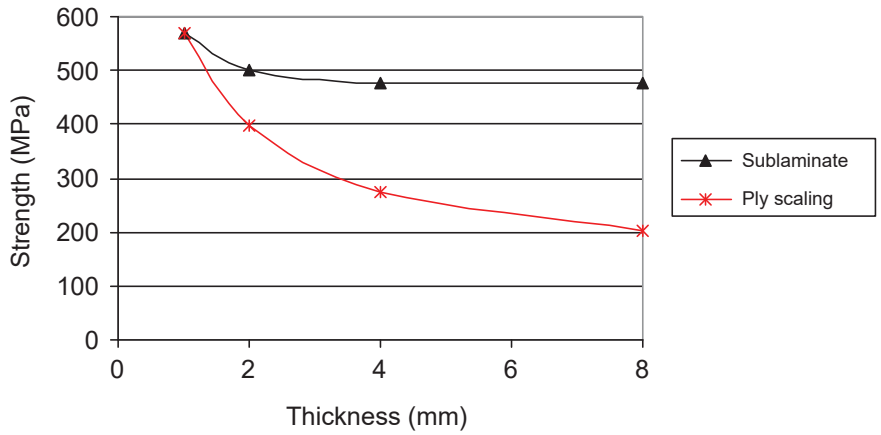

Figure 2.24: Effect of thickness on open-hole tensile strength for a $[45_m/90_m/-45_m/0_m]_{ns}$ laminate with a hole diameter of 3.175 mm. - Reproduced from [212]

Additionally to the hole size effect, as it happens in the case of free-edge delamination, the stacking sequence of the laminate influences the strength of the laminate due to interlaminar edge effects [71]. Lagace [214] studied the notch strength varying the stacking sequence and the hole diameter. He found that for $[0/90_2]_s$ laminates, the damage mechanisms that provoked the failure changed from fibre-dominated to matrix-dominated fracture as the hole size decreased. This failure mechanism change from fibre-dominated to matrix-dominated fracture was accompanied by an increase in delamination and a considerable less change in strength with hole size than expected on the basis of analytical fracture criteria as the Whitney–Nuismer [75] fracture criteria model.

The hole size effect also influences the change in failure mechanisms in laminates with open holes. Generally, the strength of notched multidirectional laminates tends to decrease with the hole size. However, Green et al. [211] observed a different trend for the case of ply-blocked laminates (ply-level scaling). A quasi-isotropic laminate with plies of the same directions stacked together, as $[45_4/90_4/-45_2/0_4]_s$ and laminate thickness of 4 mm, showed an increase in its strength with increasing the size of the hole, as represented in figure 2.25. In this way, while an increase in the thickness at constant hole diameter of the laminate led to a decrease in failure stress, an increase in the hole diameter at constant thickness[1] led to an increase in failure stress. Figure 2.25 shows the variation in failure stress of both ply-scaled

[1]The dimensions of notched tensile coupon specimens are designed in a way that there is a scaled proportion between all their in-plane parameters as defined by the ASTM D5766 [215]. This is later explained in the chapter 5 under the section 5.4.

and sublaminate-scaled (or ply dispersed) and their corresponding analytical predictions with the average stress criterion [75], with the hole diameter for the case of a $[45_4/90_4/-45_4/0_4]_s$ laminate. Green et al. [211] attributed this finding to the formation of delaminations at the free edge of the hole. In combination with all the other scaling testing they performed, they observed that the effect of increasing the thickness on ply-level scaled specimens is predominant over the effect of increasing the in-plane dimensions. As previously mentioned, the energy available for delamination to propagate grows when increasing the thickness of the laminate [206].

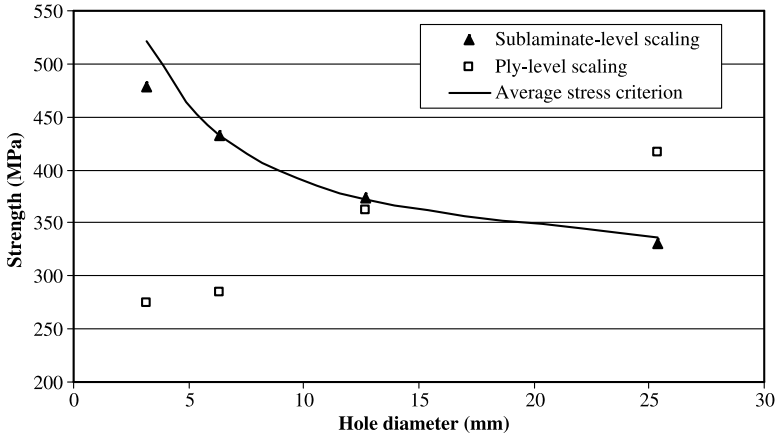

Figure 2.25: Experimental vs analytical notched strength with respect to hole diameter for a $[45_4/90_4/-45_2/0_4]_s$ laminate. - Reproduced from [211]

The ply thickness controls the size of the delaminations occurring at the free edges [211]. These delaminations are relatively large for small hole diameters and hence form and grow instantaneously to form extensive delaminations towards the edges of the laminate. For larger hole diameters (and assuming the same laminate thickness), the delamination is relatively smaller, and the delamination around the hole grows in a more stable trend. As delamination from the edges and the hole grow towards each other, the easiness for these two delamination fronts to join is directly controlled by the width of the laminate [216].

As a result of the difficulties in accounting for accurate predictions of the notched strength of composite laminates, several numerical models have been proposed for this purpose [11, 205, 213, 217–219]. However, these models still need extensive experimental data to determine their effectiveness under different scenarios, e.g., layup, specimen dimensions, and loading conditions. Furthermore, Hallet et al. [220] acknowledge that even if the FE models are capable of capturing variations, both in terms of the failure mechanisms and the absolute strength values in notched composite laminates, these simulations could be extremely computationally expensive. For these reasons, they put the challenge on implementing these approaches in a simplified form which can model components at an industrially relevant scale. These

kind of approaches have met success in Virtual Test Laboratories (VTL), as the one introduced by Falco et al. in [221, 222]. Chuaqui et al. [132], based on the VTL introduced by Falco et al. [222], have studied the effects of ply angle (fibre orientation) and blocking (ply block thickness) on open-hole tensile strength of composite laminates. They studied an extensive set of what they called standard and non-standard stacking sequences, as they used standard $(0, \pm 45, 90)$-degree angles and non-standard angles with non-orthogonal ply orientations. They used a high fidelity three-dimensional mesoscale FE model in Abaqus Explicit, obtaining a maximum 5% relative difference between the model predictions and experimental strength results. Additionally, the failure morphology between the FE predictions and the "post-morten" C-scans found very good agreement. Additional information on the relevant FE models is provided in chapter Chapter 4 under section 4.4.

2.4.2 Damage mechanisms in composite laminates with open holes

The damage chronology and mechanisms in composite laminates with open holes are complicated and vary on different parameters, e.g., laminate thickness, hole diameter, and laminate's layup, among others., as explained in the previous section 2.4.1. In an extensive characterisation campaign at University of Bristol [21, 205, 211, 212, 216], they explained the damage mechanisms and size effects in ply-level and sublaminate scaling laminates of layup $[45_m/90_m/-45_m/0_m]_{ns}$, (with $m, n = 1, 2, 3...$). Figure 2.26 illustrates the difference between ply-level and sublaminate-level scaling. They divided their study cases into "1D scaling", where in-plane dimensions were kept constant, and the thickness was scaled, "2D scaling", where the in-plane dimensions were scaled and the thickness was kept constant, and "3D scaling", where all three dimensions (thickness, width and hole diameter) were scaled. Three different failure modes are identified as the cause of laminate failure depending on the scaling level of the laminate dimensions. These failure modes are delamination, pull-out and brittle failure. The failure mechanisms in this laminate stacking sequence could be used as a reference in other quasi-isotropic laminates $(0, \pm 45, 90$ degree plies) under tension due to their similarities.

The results of the test campaign of notched strength of quasi-isotropic laminates of Hexcel IM7/8552 carbon/epoxy prepreg with layup $[45_m/90_m/-45_m/0_m]_{ns}$, being $0°$ the direction of the applied load, are summarised in figure 2.28 as of recollected in [216]. The parameters "D", "W", "t" and "t_{ply}" represent hole diameter, the width of the specimen, laminate thickness and ply thickness, respectively. It was seen that in the case of blocked plies (ply scaling), extensive delamination occurred first, and the failure mode was defined as such. On the other hand, in the case of dispersed plies (sublaminate scaling), fibre failure occurred first, with extensive pull-out on

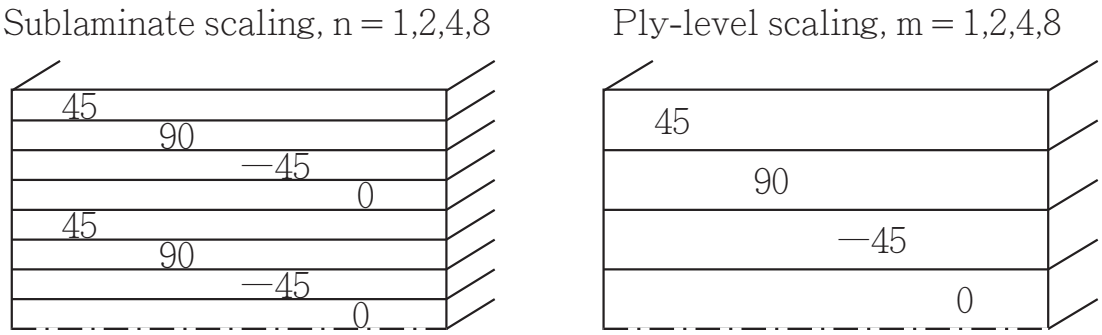

Figure 2.26: Thickness scaling approaches for $[45_m/90_m/-45_m/0_m]_{ns}$ laminates. - Reproduced from [212]

the smaller specimens (small hole diameters and narrower specimens) and a cleaner brittle fracture in larger specimens [211]. Hence three failure mechanisms were defined: pull-out (fibre-dominated failure with extensive subcritical damage), brittle (fibre-dominated failure with minor subcritical damage) and delamination (matrix-dominated failure). These three failure modes are shown in figure 2.27.

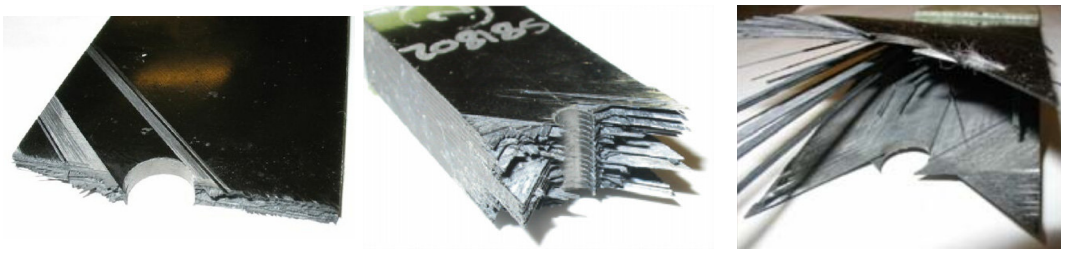

(a) **(b)** **(c)**

Figure 2.27: Different failure mechanisms in open hole tension tests: (a) brittle, (b) pull-out, (c) delamination - Reproduced from [212]

The pull-out failure mode is caused by fibre failure of the 0° layers. This fibre breakage is accompanied by delamination between the off-axis layers, which tend to fail due to matrix cracking. Green et al. [211] observed that the pull-out occurred across the whole width of the specimens, with splitting failure into the off-axis layers that propagated from the hole and roughly occurred at the tangent point of the fibres of the off-axis layers with the hole. The load-displacement curve for this type of failure is linear initially and has extensive non-linearity prior to its failure. This non-linearity was assumed to be due to the damage occurring prior to failure, e.g., splitting, delamination of the off-axis layers and matrix cracking of the 90° layers at the hole.

In the same way as a pull-out failure, the brittle failure is fibre-dominated. However, when laminates break brittlely, they presented slight delamination or splitting of the off-axis layers. For this type of failure, the damage is localised in the area of the hole, and every ply of the laminate failed at the same thickness-width fracture plane by fibre failure in the 0° 45° and -45° layers and by matrix cracking in the 90° layers.

W/D	N° Blocked plies, m	N° Sub-laminates, n	t_{ply} (mm)	t (mm)	Hole diameter, D (mm)					
					1.6	3.175	6.35	12.7	25.4	50.8
Results from Green et al.										
5	1	4	0.125	4		478 (3.1)	433 (2.0)	374 (1.0)	331 (3.0)	
5	2	1	0.25	2		396 (5.2)				
5	4	1	0.5	4		275 (5.6)	285 (5.2)	362 (2.6)	417 (4.1)	
5	8	1	1	8		202 (7.9)			232 (1.9)	
Results from Green.										
5	2	2	0.25	4		469 (2.5)	463 (2.8)	457 (1.9)	375 (3.0)	
Results from Görlich.										
5	2	2	0.25	4	448 (5.5)	463 (3.6)	461 (5.7)			
5	4	1	0.5	4	264 (3.7)					427 (-)
Results from Cheung and Hallet.										
5	2	1	0.25	2		448 (5.3)				
10	2	1	0.25	2		605 (5.0)				
Failure mode:		Delamination		Pull-out		Brittle				

Figure 2.28: Gross failure stresses, MPa, (coefficient of variation, %) for open hole tension of $[45_m/90_m/-45_m/0_m]_{ns}$ laminates. Results from Green et al. [211], Green [223], Görlich [224] and Cheung and Hallet [225]. - Modified from [216]

Last, the delamination failure consisted of extensive delamination between the -45° and 0° layers. Apart from this delamination, extensive splitting happened in the 45° and -45° layers, so the off-axis layers failed in a similar way to that of the pull-out failure case (cracks and delamination originating from the hole) [211]. Failure initiated from transverse cracks on the surface of the 45° plies, which led to delamination of the 45/90 interface. These transverse cracks initiated first at the hole and then at the free edge. In this manner, the 45/90 interface delamination joined through the width of the specimens. When the damage joined up, it moved down through the 90° plies, hence delaminating the 90/-45 interface. The damage kept further through the thickness of the -45° ply and originated the delamination of the -45/0 interface. The 0° plies suffered splitting with the -45/0 interface delamination, and two ligaments on either side of the hole were left to carry the load. These failure mechanisms were illustrated by Wisnom et al. [216], as shown in figure 2.29. The delamination of the -45/0 interface was accompanied by a sudden sharp load drop, and later the load recovered as the 0° kept withholding the load until their final, fatal breakage.

Differently from the pull-out and brittle force-displacement graphs, the delamination curves showed a load drop at the time of the -45/0 interface delamination. After this sudden load drop, the laminate kept on withholding load to even higher values of the load than the load drop. In the last moments prior to failure, the 0° plies were

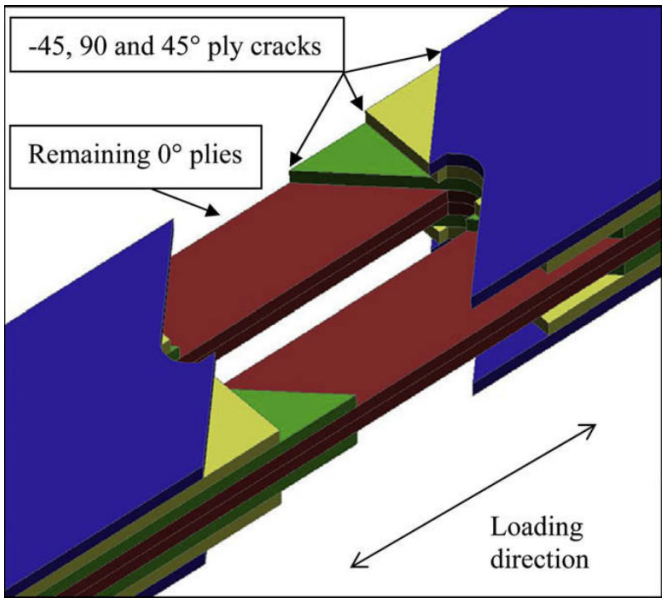

Figure 2.29: Schematic illustration of the mechanisms of outer 45/90/-45 plies separating from the 0° plies - Reproduced from [216]

the only ones holding the load, and when they collapsed, the laminate failed entirely. Until the point of -45/0 interface delamination, substantial damage had occurred in the specimens already. Hence, the failure point of the laminate is defined as the first load drop point, even though the laminates were still capable of carrying load after the first load drop. It is also common to observe not only one significant load drop but smaller several of them, obtaining a "serrated" profile of the graph. These smaller load drops correspond to events of transverse cracking in the 90° layers, 45/90 interface delamination and -45/0 interface delamination.

As to the chronology described, the damage propagates throughout all the laminate after the delaminations started at the hole, and the free edges join together in the 45/90 interface. Hence, in the case of laminates with bigger diameter holes and consequently wider, the 45/90 interface delamination takes longer to join from the hole to the edge. In this manner, inversely to the case of thinner ply blocks or sublaminate scaling, the notched strength in thick ply-blocked laminates increases with the size of the hole as shown in figure 2.25.

Wisnom et al. [216] compared the values of notched strength for a ply-blocked laminate of the form of m=4 and n=1 ($[45_4/90_4/-45_4/0_4]_s$), and ply thickness of 0.125 mm, with the values of the same unnotched laminate. As the hole diameter and consequently the width of the laminate increase, the notched strength reached an asymptote value equal to that of the unnotched strength of a 32 mm wide laminate (W/D = 5). They observed that the transverse cracks in the 45° top ply originated triangular delaminations at the intersection of the ply and the free edge. Moreover,

they observed that the moment at which these triangular delaminations grew across the whole width of the specimen was when delamination was able to step down to the -45/0 interface and propagate along the length of the specimen, causing a load drop. In this way, Wisnom et al. ventured that it would be expected that if the specimens were very narrow, these triangular delaminations would join through the width faster, leading to an earlier onset of full delamination. They demonstrated this feature by testing an unnotched laminate of the same layup and width of 4 mm. These 4 mm wide specimens failed very close to the notched strength values for small hole diameters. Thus, they concluded that the width to ply block thickness is the critical parameter affecting the laminates with an open hole which fails due to delamination. Figure 2.30 shows the effect of hole size on delamination stress (failure stress) of $[45_4/90_4/-45_4/0_4]_s$ laminates.

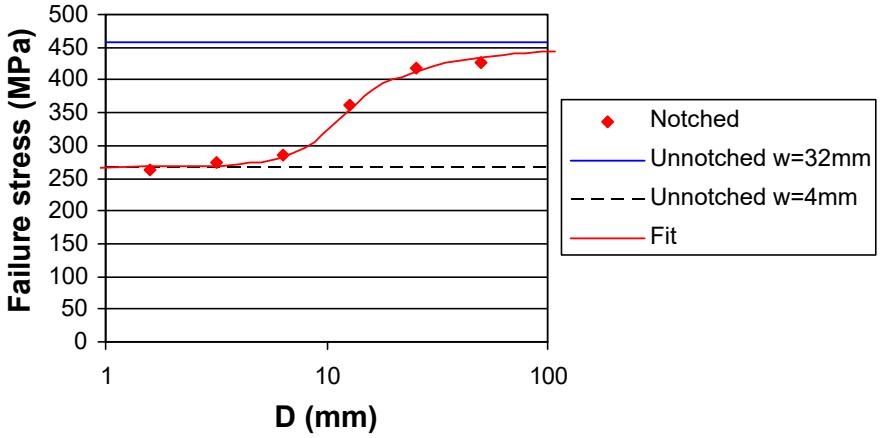

Figure 2.30: Effect of hole size on delamination stress of $[45_4/90_4/-45_4/0_4]_s$ laminates. - Reproduced from [216]

For the case of the laminates which did not fail due to delamination, e.g., m=1 and n=4, there was the presence of localised delamination visible at the hole edge starting at matrix cracks [211], which affected the stress concentration. These delaminations extended through the thickness locally, similarly to the effect observed in unnotched specimens or specimens whose overall failure mode is delamination. Additionally, splinting of the 0° layers also occurred, blunting the notch and hence allowing the specimens to support stresses higher than the value of the unnotched strength divided by the stress concentrator factor. In this way, as the hole size increases in the case of m=1 and n=4, it becomes more difficult for these local delaminations to join up and splitting to occur. Hence, the failure mode changes from pull-out (extensive subcritical damage) to brittle (minor subcritical damage), achieving lower values of ultimate failure stress. In this manner, the hole size to ply thickness ratio becomes an important parameter for the fibre failure cases, causing a reduction in the failure stress as damage (splitting and local delamination) is inhibited.

2.4.3 Summary - Composite laminates with open holes

Open holes in composite laminates mean the presence of stress concentrators. The failure mechanisms of laminates with open holes are difficult and change with different layups. For the quasi-isotropic laminates studied in the testing campaign by the University of Bristol, in the cases where the laminate failure is due to fibre failure, the inhibition of delamination or intra-ply damage (local delamination at the hole and splitting) provokes the reduction in notched strength of the laminate, as this damage blunts the hole and consequently the stress concentration factor of it, allowing higher loads than the strength of the unnotched laminate divided by the SCF. On the other hand, in the case of failure by overall delamination, the increase in the size of the specimen provokes an increase in notched strength.

Wisnom et al. [216] determined that the different hole size effects as a function of ply thickness can be explained in terms of delamination and also demonstrated it numerically [205]. In this manner, delamination has a crucial role in the in-plane strength, failure mechanism and hole size effect in open hole tension of quasi-isotropic laminates. Delamination can lead to premature failure, especially for small holes and thick ply blocks.

No particular solutions have been found in the literature for suppressing delamination in composite laminates with open holes apart from varying the geometrical dimensions for obtaining a brittle or pull-out failure. However, as shown in figure 2.28, the fact that delamination failure occurred with only 0.25 mm thick ply blocks is of concern, as 0.125 mm ply thickness is a standard prepreg ply thickness [216].

2.5 Pin-loaded composite laminates

Mechanically fastened joints are widely used in many applications (e.g., the aerospace industry) to secure highly loaded FRP components or structures to other FRP or metallic parts. However, in bolted composite structures, stress concentrations develop around the holes, severely reducing the strength of the structure [226]. Furthermore, due to the presence of a hole, which is a stress concentration point (see section 2.4), and the interaction between the laminate and the fastener, the load-carrying ability of the laminate has been found to be reduced significantly due to damage initiation, and accumulation within the laminate from the early stage of loading [227].

2.5.1 Bearing strength of pin-loaded composite laminates

The large number of parameters involved complicates the characterisation of bearing failure in bolted composite laminates. Geometric parameters have been shown to have a relative impact on the bearing strength [228]. While the bearing strength decreases with an increased diameter-to-thickness ratio (D/t), the width-to-diameter (W/D) and edge distance-to-diameter (e/D) do not influence the bearing failure stress but determine the mode in which failure occurs (see figures 2.31 and 2.32 for an understanding of the geometrical parameters). Several studies [226, 229–232] have demonstrated that the bearing strength is strongly affected by the presence and value of lateral constraint on the top and bottom surfaces of the material surrounding the hole. The bearing strength increases with increasing the clamping-applied force, as well as with increasing the constrained lateral area, e.g., by increasing the washer outside diameter [228]. Figure 2.31 illustrates a schematic of how the lateral constraint is applied to the experimental testing of bearing strength of composite laminates for pin joint configurations (double shear specimens as of ASTM D5961). Application of a lateral clamping load produces a shift from bearing to net-section failure mode [232] (see figure 2.33 for failure modes in composite bolted joints). Additionally, the ultimate bearing strength has been shown to increase more than 100% by applying a lateral clamping load [232].

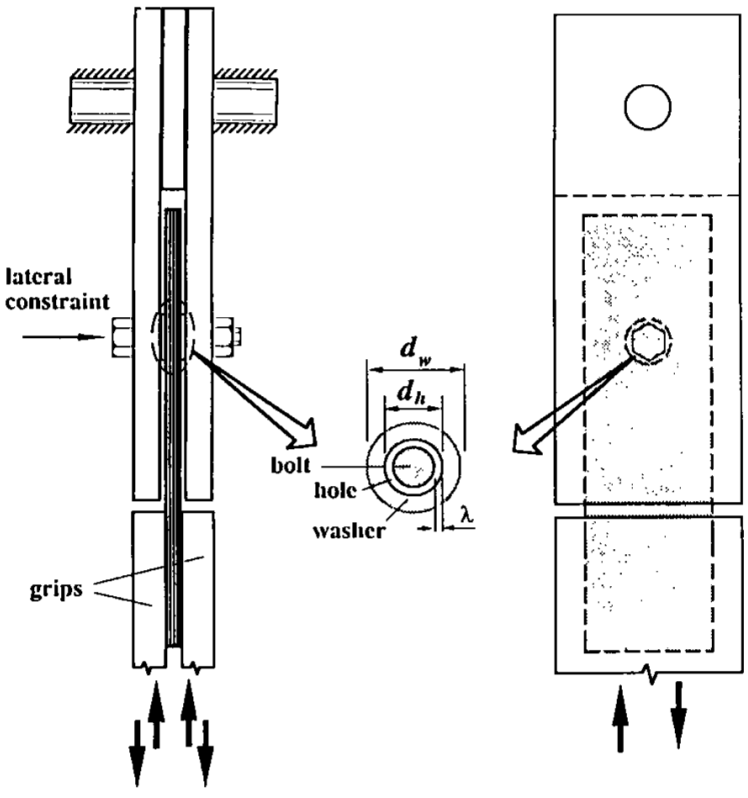

Figure 2.31: Schematic of loading fixture. - Reproduced from [226]

Quinn and Matthews [233] studied the effect of the stacking sequence on the bearing strength of GFRP laminates. In the case of quasi-isotropic laminates with 0° ±45° and 90° plies, they reported that placing the 90° layers at or next to the surface increases the bearing strength. Additionally, they found that the failure mode was linked to the stacking sequence. Smith and Pascoe [19] studied the bearing strength depending on the stacking sequence of eight quasi-isotropic stacking sequences of CFRP laminates. They found that it appeared to be less of a stacking sequence effect for CFRP than for the GFRP tested in [233]. They reported that the effect of the stacking sequence has a minor influence on the determination of the bearing strength of a CFRP composite laminate. Despite that, Aktas and Dirikolu [74] studied the bearing strength of $[0/45/-45/90]_s$ and $[90/45/-45/0]_s$ CFRP laminates and found similar behaviour from that showed in [19] for GFRP laminates. They reported a 12% and 20% improvement in the safe and maximum bearing strengths when the 90° plies were located at the surface.

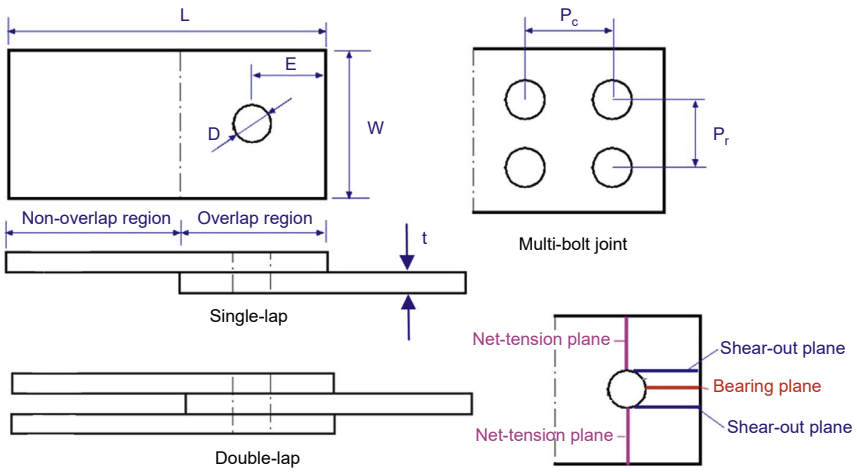

Figure 2.32: Definition of joint geometric design parameters. - Reproduced from [234]

Figure 2.32 shows an illustration of some commonly used joint geometric design parameters. Failure modes are generally associated with failure planes. These planes are referred to as the bearing plane, the net-tension plane and the shear-out plane, as shown in figure 2.32. At a testing specimen level, there are four ways in which a composite bolted joint can fail when the laminate is the failing part[1]. These are bearing, net-tension, shear-out and mixed or cleavage failure. Figure 2.33 shows a schematic representation of these failure modes. The bearing failure mode is a progressive failure mechanism which occurs when the laminate cannot withstand load anymore. Bearing is a non-catastrophic failure mode where non-linearities in the load-displacement relation appear before the final failure. On the other hand, shear-out and net-tension occur catastrophically and present lower strength [235].

[1]When the failure occurs due to the bolt, there are two additional ways in which the joint could fail.

Therefore, it is an unwanted failure mode. In the case of this thesis, the bearing failure is the one studied.

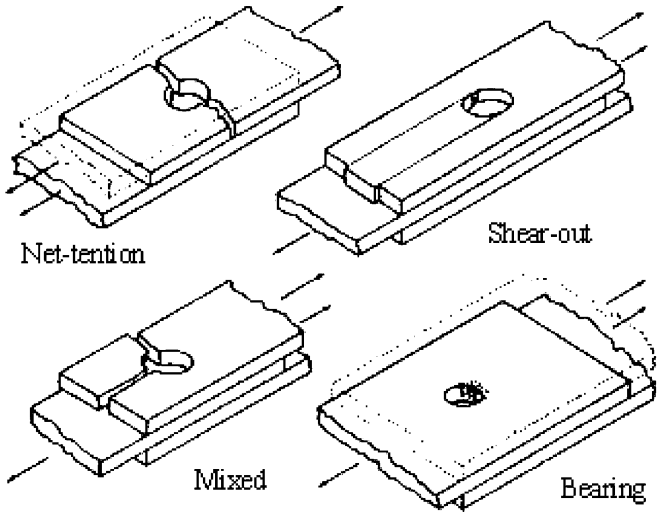

Figure 2.33: Typical failure modes in composite bolted joints: net-tension, shear-out, mixed or cleavage, and bearing failure. - Reproduced from [74]

One very studied parameter on the strength of bolted composite laminates is the effect of bolt clearance [232, 234, 236–242]. Depending on the loading mode, according to the ASTM D5961, it has been reported that the influence of the bolt-hole clearance has different importance. The bolt-hole clearance is defined as the difference between the hole and pin diameter in μm, but it is also often referred in terms of percentage.

Pierron et al. [240] investigated, both numerically and experimentally, the pin-hole clearance in $\pm 45°$ single GFRP plates loaded in pin joint (double shear test specimen as of in ASTM D5961). They studied clearances of up to 12.5% for a pin diameter of 16 mm. They reported a decrease in load failure of up to 30% for specimens with 12.5% clearance (2 mm clearance in their study). Finally, they concluded that the joint stiffness did not vary much with bolt-hole clearance but did not quantify this affirmation. However, as pointed out by McCarthy et al. [241], the load-deflection curves of Pierron et al. [240] experiments would indicate a stiffness loss between 15% and 20%, which is quite substantial. It is worth mentioning that such big clearances would certainly incur strength and joint stiffness loss, as the size of the pin diameter would be taking a leading role [243]. As the diameter decreases, the bearing strength drops due to the fact that the stress concentration factor of the bolt-hole contact intensifies [234]. Kelly and Hallström [232] found that for reasonable clearances of no more than 3.05%, for CFRP laminates, the effect of the bolt-hole clearance was important with regard to the 2% offset strength (see the ASTM D5961 [244] for the definition of offset strength). However, the ultimate bearing strength was not significantly affected by these clearances. Kashaba et al. [242] reported the same findings for GFRP laminates.

However, they did show an effect on the ultimate bearing strength, where there was a reduction of up to 15.3% when the clearance was 300 μmm. They reported that although specimens with pin-hole aerospace tolerances (clearance of 50 μm) had lower values of ultimate strength compared to neat-fit specimens, they presented higher failure displacement. Furthermore, in this manner, these specimens showed higher energy absorption, which could play an important role in delaying catastrophic failure [242]. Hyer, Klang and Cooper [237] studied not only the effect of the bolt-hole clearance but also the effect of the elasticity of the pin and the friction between the pin and the hole surface. They concluded that both the friction and the clearance significantly influence the stress distribution at the hole and the maximum value of the stresses around it. While the clearance affects the location, direction and magnitude of the maximum stresses, the friction reduces the bearing stress at the 0° plies, shifting the peak stress away from the 0° plies. Regarding the pin elasticity, they concluded that it is not a parameter as crucial as bolt-hole clearance and friction and that pin elasticity reduces the peak stresses. However, this peak stress reduction is not drastic if using a rigid pin.

Single-bolt/single-lap joints (single shear specimen as of in ASTM D5961) result in significant stress concentrations in the thickness direction and lower bearing strengths than pin joint configurations [245]. McCarthy et al. [241] studied the effects of bolt-hole clearance in single-lap composite joints by means of an extensive experimental programme. They reported that for reasonable clearances in single-bolt/single-lap joints, the 2% offset strength (see [244]) is not significantly affected by the bolt-hole clearance, with a maximum of 7.5% strength drop for clearance of 3% for finger-tight joints (lateral constraint is clamped with a "finger-tight" force) with protruding-head bolts. They did not observe bearing strength drop for countersunk and fully clamped joints. They expressed that a dependency of offset bearing strength would be expected for higher clearances, as in the case of DiNicola and Fantle [238] or Pierron et al. [240], who use large clearance values. Additionally, they reported a dependency of joint stiffness with the bolt-hole clearance.

Additionally, the radial clearance between washers, which provides the lateral constraint at the edge of the hole, and the bolt/pin has been studied. Herrington and Sabbaghian [246] studied the variation of bearing strength with respect to the clearance between the bolt diameter and the inside diameter of the washer. They found that the bolt-to-washer diameter ratio was a significant parameter for the bearing strength of bolted composite joints. A tight fit was found to present the maximum bearing strength. Large clearances between the washer and the bolt were reported to have the same strength as the pin-loaded case (without lateral constraint), even for relatively large clamping forces.

All in all, it has been seen that although the bolt-hole clearance is important for the bearing strength value of composite bolted joints, other parameters such as the lateral constraint or bolt-washer clearance have a stronger influence on the bearing strength.

2.5.2 Failure mechanisms in pin-loaded composite laminates

Camanho et al. [235] conducted an experimental investigation to determine the damage mechanisms in the bearing, shear-out and net-tension failure modes in bolted CFRP laminates. They used a Hexcel T300/914 carbon/epoxy composite material with a laminate stacking sequence of $[0/90/45/-45]_{2s}$. They reported that, while for the specimens that failed by bearing, the damage onset started around 80% of the failure load, for the net-tension and shear-out specimens, no damage was visible until 90% of the failure load. In the case of bearing specimens, extensive delamination and crushing occur. Additionally, the damage tends to follow a $\pm 45°$ direction with respect to the loading direction for both the bearing and shear-out specimens. Damage on the bearing plane follows similar trends in all failure modes. First, there is localised delamination between the 0° and 90° plies at the hole edge. As the load increases, matrix cracking develops through the thickness between the 90° and 45° plies. That matrix cracking further develops into delamination in the 45/-45 interface. The 45/-45 interface delamination leads to matrix cracking of the -45° plies and fibre micro-buckling, as also observed by Naik and Crew [247]. For the bearing specimens, these damage mechanisms lead to shear cracks under the washer surface. These failure mechanisms stop being present at a 2 mm distance from the hole boundary. At this distance from the hole edge and in bearing planes of $\theta = 42°$ fibre microbucling occurs. For the shear-out specimens, delamination on the 45/-45 and 0/90 interfaces and matrix cracking in the off-axis plies occur. For the net-tension specimens, no damage occurs until 90% of the failure load. Delamination on the 90/45, to a lesser extent, on the 45/-45 interfaces occurs at this load. Additionally, matrix cracking in the off-axis plies also happens.

Thus, Camanho et al. [235] concluded that mechanically bolted joints fail in a CRFP laminate due to damage accumulation. Additionally, they indicated that due to the three-dimensional effects present at the hole edge, a three-dimensional failure criterion should be used to predict non-critical damage mechanisms that occur prior to final failure. In this manner, they also pointed out the necessity of accounting delamination in any failure criterion used for bearing strength of pin-loaded laminates.

Xiao and Ishikawa [248] conducted an experimental investigation to study the strength and failure of mechanically fastened composites in IM7/PIXA and IM600/Q133 carbon/epoxy composite materials with $[45/0/-45/90]_{2s}$ stacking sequence. They studied the failure process by means of acoustic emissions (AE) and proposed a

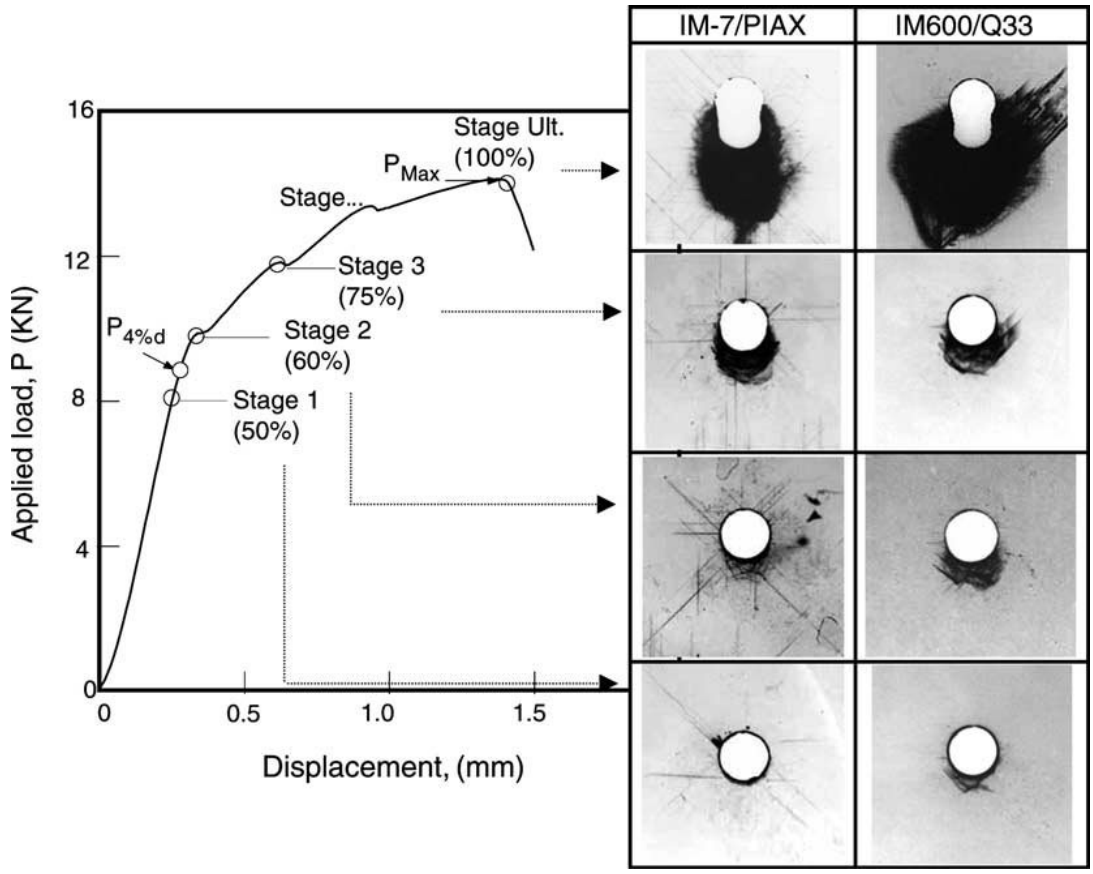

Figure 2.34: X-ray radiographs of bearing damage tested at four load levels for both IM7/PIAX and IM600/Q33 composite laminates with stacking sequence of $[45/0/-45/90]_{2s}$. - Reproduced from [248]

non-contact electro-optical extensometer to measure the hole elongation. Similarly to Camanho et al. [235] they observed that the bearing failure could be outlined as a process of compressive damage accumulation, dividing it into four stages: damage onset, damage growth, local fracture and structural fracture or failure. Figure 2.34 illustrates a typical bearing load-displacement curve with the four stages marked and X-ray images corresponding to the damage accumulated at each stage for the two material systems they tested. They suggested that different sound frequencies could be assigned to different failure mechanisms to measure the damage development with acoustic emissions. They hypothesised that low or middle amplitude AE correspond to fibre micro-buckling and high amplitude signals to delamination or out-of-plane shear cracking. Based on the X-ray images they obtained from the different load stages, they described the failure as follows: at stage 1, there is the main phenomenon of crushing in the contact area between the bolt and the hole. The main damage mechanism during stage 2 is accumulated compressive damage in the inside-washer region. Additionally, kink band formation was observed at the load level of 60%. Xiao and Ishikawa [248] observed that this fibre kinking seemed to cause shear

cracking and delamination in the $\pm 45°$ plies. Where the kink bands were pronounced in the IM7/PIXA specimens at this loading stage, the IM600/Q133 presented both kink bands and local delamination. At load stage 3, through-the-thickness shear cracking developed. The kink bands in the $0°$ plies moved to the $\pm 45°$ plies and induced shear cracks and delamination, and subsequently, these damages interacted and coupled with each other. Moreover, as the inside-washer region reached a saturation state in damage, large-scale delaminations and shear cracks formed under the washer area leading to a rapid decrease in joint response and final failure at stage 4 (please be referred to Xiao's and Ishikawa's work [248] for better understanding with the aid of scanning electron microscopy images). Figure 2.35 shows the damage state at maximum load. In conclusion, for this damage chronology, the damage progress was defined as an intermittently accumulated process by multiple through-thickness shear cracks. If no lateral constraint is provided, such damages will spread rapidly around the circular hole.

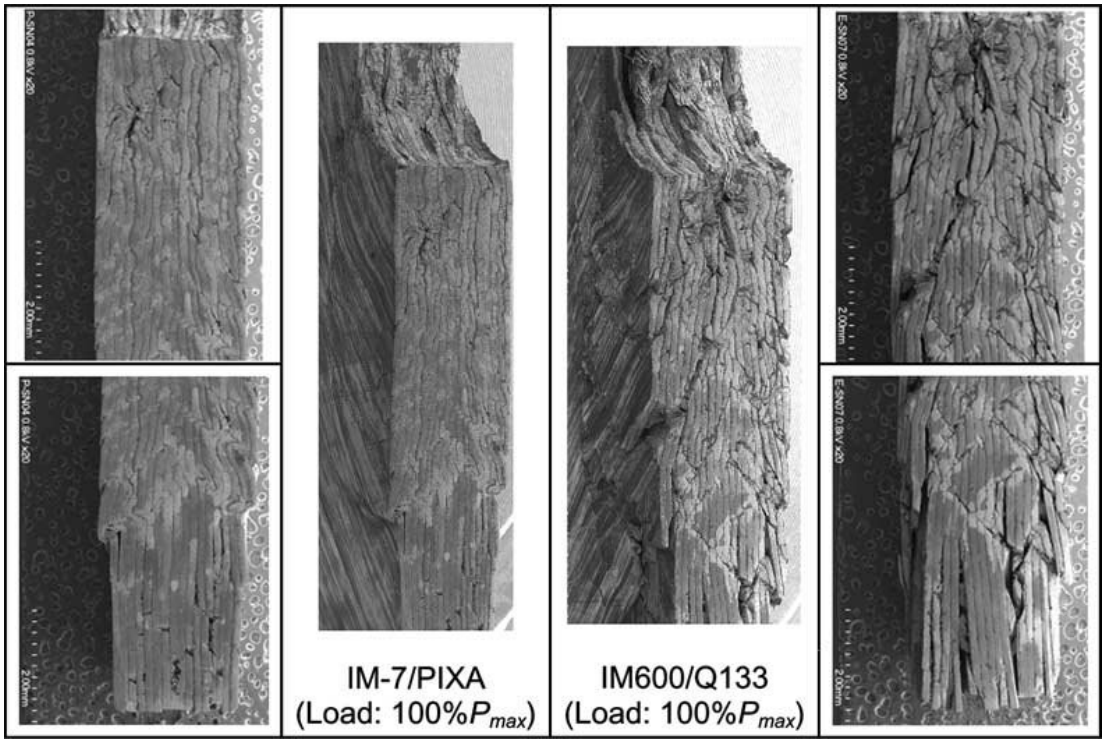

Figure 2.35: Scanning electron microscopy (SEM) images of through-the-thickness bearing damage at failure point (stage 4) for both IM7/PIAX and IM600/Q33 composite laminates with stacking sequence of $[45/0/-45/90]_{2s}$. - Reproduced from [248]

Cao et al. [249] have recently conducted a detailed experimental investigation on the failure mechanisms and chronology of damage in bolted thin-ply composite laminates. In particular, they have studied the bearing behaviour and failure mechanism under pin-joint or double-lap bolted joint configurations. They studied the progress of the damage at four different load points, equivalent to the four stage points in

figure 2.34: (A) where the first small stiffness loss appears (stage 1 in figure 2.34), (B) peak force at the metal-like yield stage (stage 2 in figure 2.34), (C) slow dropping of the stress with the increase of displacement (stage 3 in figure 2.34), and (D) sudden load drop (stage 4 in figure 2.34). Figure 2.36 shows a schematic and X-ray images of the damage chronology summary they reported. They reported the following damage accumulation and failure chronology: only a small hole crushing and matrix micro-cracking are observed during damage initiation. As the bearing load increases, great amount of micro-damage (matrix cracking and fibre bearing fracture) develops in the area around the hole accumulating debris in the fracture area. Fibre kinking occurs in the bearing failure plane (0° direction) and net-tension plane (90° direction) and induces out-of-plane shear cracking. At the moment of the first load drop (stage 2 in figure 2.34), extensive shear matrix cracking and fibre fracture were observed in the bearing plane area. Fibre kinking and fragmentation of the 0° plies promotes a wedge effect matrix cracking in the through-the-thickness direction towards the $\pm 45°$ plies, similarly to the one explained in section 2.3.1 for the case of edge impact. They concluded that the progressive bearing failure of thin-ply laminates was the result of multiple interacting failure modes (bearing fracture, fibre kinking, matrix cracking and fibre/matrix debonding), which ultimately produced the permanent deformation of the fastener and subsequent extensive hole crushing. However, due to the improved in-situ transverse tensile and in-plane shear strength common to thin-ply laminates, the propagation of intralaminar and interlaminar cracks in the form of delamination was not observable.

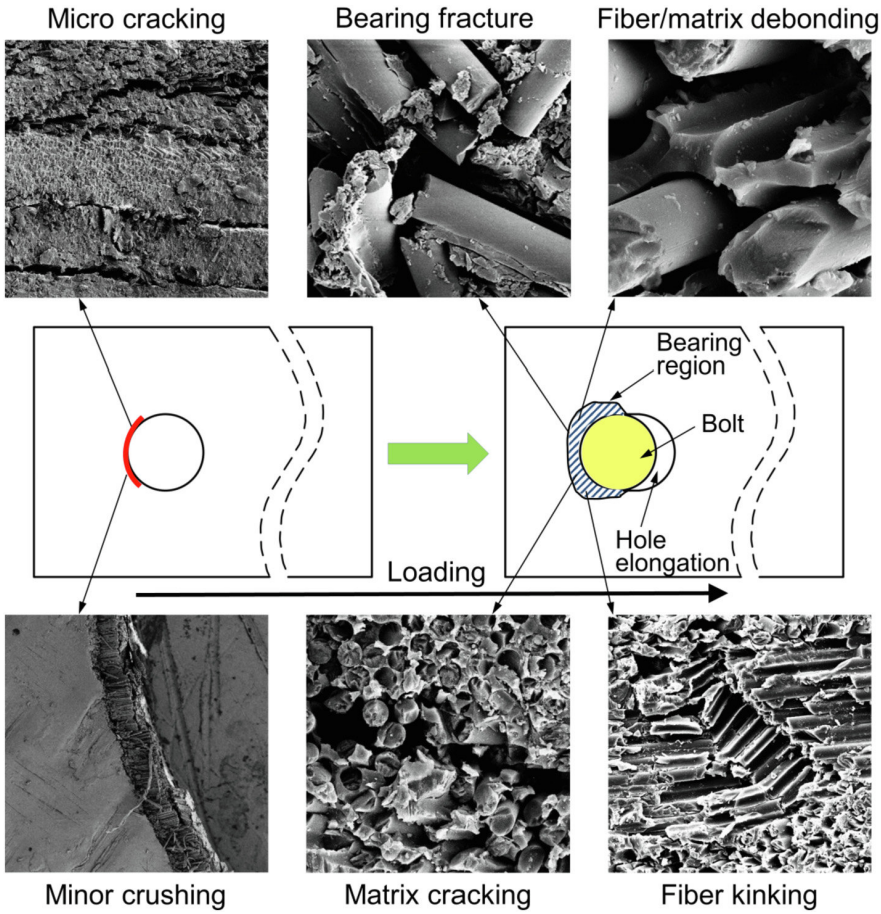

Figure 2.36: Schematic showing the bearing failure of thin-py laminates around a bolted hole during the initiation and propagation of damage. - Reproduced from [249]

2.5.3 Bearing strength enhancement strategies of pin-loaded composite laminates

The bearing strength is usually the most limiting parameter in composite fastener joints. It is especially critical for single-row bolted, lug, and shear-loaded joints [250]. Hence, bolted joint regions in composite laminates are expected to be thicker than the rest of the laminate, incurring additional weight on the whole structure. Looking to avoid these weak structure points, different methods for improving the bearing capabilities of bolted joints in composites have been explored in the literature.

Similarly to the other loading scenarios already explained (free-edge delamination, edge impact and laminates with open holes), layup rearrangements or modifications have been suggested for higher bearing strengths of bolted composite laminates. For example, Aktas and Dirikolu [74] pointed out that placing the 90° plies of quasi-isotropic laminates near the surface gave higher failure stress than placing them in the centre of the laminate.

Other methods propose a more localised solution, as reinforcement of the area around

the hole [250–255].

Hole reinforcements in the form of metallic inserts have been explored for enhancing the bearing response of composite joints. Local embedding of thin titanium layers into the composite laminate in the coupling region results in a considerable improvement in structural efficiency of bolted and riveted joints in CFRP structures [252]. Kolesnikov et al. [252] reported a great potential increase of specific bearing strength when using titanium hybridisation. Fink et al. [256] demonstrated the use of this technique in three-row bolted joints. They obtained an increase of 32% in specific bearing strength compared with a pure CFRP laminate when using about 20% titanium content in the hybridised region. Camanho et al. [253] studied experimentally and numerically the local hybridisation of the composite around the hole with titanium plies. They studied the effect of the number of titanium plies substituting carbon plies on the bearing strength. They concluded that increasing the titanium content increased the bearing strength but also increased the weight. With up to 50% titanium, they observed a remarkable 29% specific bearing strength improvement. Additionally, they observed a 31% joint stiffness increase when the titanium content was increased from 0% to 50%. This technique was later assessed by Fink et al. [254] for implementing it to a spacecraft payload adaptor. They suggested that the possibility of using this technique could potentially save weight with the reduction of bolt rows, fasteners, edge and pitch distances and overlap lengths.

Akbarpour and Hallström [255] have explored a similar idea to that of Fink et al. [250, 252–254], but implementing the metal reinforcement in the form of stacked patches around the holes. They used stainless steel patches instead of titanium. Akbarpour and Hallström reported these metal inserts to suppose a penalty weight of only 5 g and could achieve up to a 60% improvement in the bearing strength. They pointed out that this reinforcement technique seemed to give a higher bearing strength reinforcement than for a corresponding lamella coupling concept [252].

Troschitz et al. [257] studied the viability of embedding metallic inserts in continuous carbon fibre reinforce thermoplastics while using compression moulding. They used a method for pre-forming the hole and placing the metallic insert without breaking or disrupting the fibres of the composite. By means of computed tomography (CT) imaging analyses, they reported that the final material structure around the insert resulted in inhomogeneous three-dimensional fibre orientation and local variation of fibre content. In this way, the resulting mechanical behaviour of the insert was very dependent on this complex geometry originating in the embedding process. In a theoretical manner, Jones and Platts [251] numerically experimented with the possibility of having different internal fibre geometry near the hole area and, in this way, procuring reinforcement to the hole. Although this option would be better than

metal inserts from a specific strength point of view, manufacturing such patterns is highly difficult.

Additionally, the use of thin-ply laminates has shown a better bearing response than standard ply thickness laminates [249, 258]. The use of thin plies improves the load-carrying capabilities of pin-loaded composite laminates [249, 258]. The more homogeneous microstructures distribution of the fibre and matrix in thin-ply composites aid in minimising the number of voids and resin-rich areas thin-ply in composite laminates, enhancing the initial damage stress. Thus, pin-loaded thin-ply composite laminates have higher bearing strength and damage tolerance.

2.5.4 Summary - Pin-loaded composite laminates

Bolted joints in composite laminates are vulnerable points for the strength of composite structures. For this reason, regions where bolted joints are present, tend to be over-dimensioned with respect to the rest of the composite structure. Composite bolted joints could fail in four different manners when the composite laminate is the failing part: net-tension, shear-out, bearing and mixed failure. The bearing failure mode is a non-catastrophic failure, in which the join fails gradually, contrary to the net-tension and shear-out failure modes. Additionally, bearing failure occurs for higher loads than the net-tension and shear-out failure modes. The failure occurring in a bolted joint has been summarised as the accumulation of crushing damage that develops in fibre fracture (fibre kinking), matrix cracking, delamination and ultimate failure when the joint can not withhold any more load.

The failure mechanisms in composite bolted joints are various and complex. Different proposals have been made to enhance the load-bearing capabilities of bolted joints. Among the most promising methods are those of hybridising the composite laminate with metal layers, such as titanium plies, for example. In this way, the mechanical properties of the laminate are enhanced around the hole and the specific strength of the joint increases. As far as the literature review conducted in this thesis, the use of additive layers for enhancing the bearing strength of pin-loaded composite laminates has not been done. As a potential benefit, additive layers add much less weight and material, compared with solutions that use metallic inserts or metallic hybridised plies.

Chapter 3

Concept of the solutions studied to suppress delamination in composite laminates

This chapter presents the ideas of the visioned solutions for each of the research questions enunciated at the end of chapter 1. The physical meaning and the conceptualisation of the solutions are presented, so the reader can easily locate how the idea presented is addressed in the following chapters. The actual manufacture and final form of the ideas will be shown in chapter chapter 5, where details of the specifically tailored design of each of the conceptualised ideas presented in this chapter have been put in place.

3.1 Additive binding layers to suppress free-edge delamination in composite laminates under tension

Due to the low strength of the polymer matrices, interlaminar cracks known as delamination can develop between the layers, as illustrated in figure 3.1a. For the purpose of suppressing free-edge delamination, the idea of using additive layers has been explored in this thesis. The concept of it is based on an additive composite laminate made out of thin-ply unidirectional prepreg. This thin-ply laminate is applied to the free edges of cured composite laminates to suppress free-edge delamination, as schematically shown in figure 3.1b. As mentioned in 2.2.2, throughout this thesis, these thin secondary added composite layers are referred to as "additive binding" as they are added to the main substrate and cured in a second stage to bind the layers together at the free edges. In this way, this secondary added laminate acts as a binding, providing constraint and holding the plies of the substrate together, as illustrated in figure 3.1b. The binding can introduce fibre reinforcement in the thickness direction at the free edges, and therefore, it enhances the interlaminar strength of the laminate around the free edges. It also constrains relative out-of-plane and shear movements of different plies at the free edge, reducing the risk of delamination.

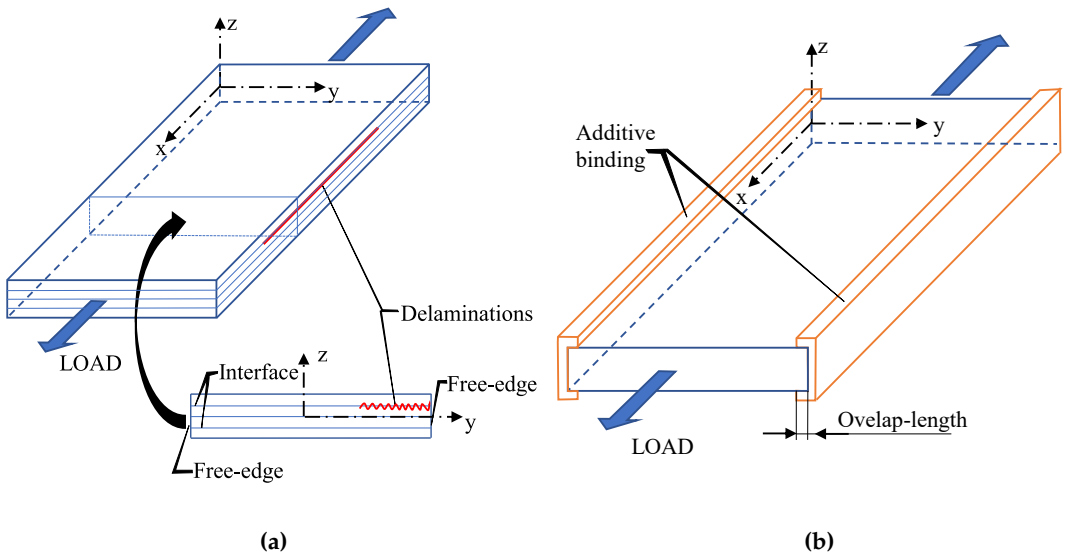

Figure 3.1: A composite laminate subjected to axial load. a) No binding applied with free-edge delamination, b) additive binding applied at the free edges

It will be shown that this solution can achieve more realistic and precise composite strength characterisation results by eliminating the free-edge delamination where this damage mode causes premature failure. Additionally, this solution can efficiently improve the composite strength by suppressing or delaying delamination in industrial applications with free edges.

3.2 Additive binding layers to enhance damage tolerance and response of composite laminates under edge impact

Composite structures are highly vulnerable to the impact of foreign objects. Due to the low strength of the polymer matrices and the brittleness of the fibres, foreign object impacts can generate internal damage that reduces the strength of the structure significantly. This internal damage is a combination of interlaminar delaminations, fibre breakage, fibre kinking and matrix crushing and cracking. Figure 3.2a schematically shows the interlaminar (delaminations) damage originated from the edge impact of a composite stiffener or stringer. An important part of the energy of the impact is dissipated through interlaminar delamination, debilitating the strength of the composite laminate. The idea of using additive layers has been explored to enhance the damage tolerance of composite laminates under edge impact. These additive binding is intended to reduce the extent of delamination or delaminated area on edge impacted laminates.

The concept of it is based on an additive composite laminate made out of thin-ply unidirectional prepreg. This thin-ply laminate is applied to the free edge of composite stiffeners, which are susceptible to suffer edge impacts. Figure 3.2b schematically shows how the additive binding is applied over the free edge of a composite stiffener, similar to the free-edge delamination tensile coupons. The addition of this thin-ply laminate provides initial protection against the direct impact on the free edges of the different plies of the laminate. Additionally, the additive binding provides through-the-thickness constraint, helping to stop the advance of delamination through the composite laminate.

It will be shown to which extent delamination could be stopped by using the additive binding in composite laminates under edge impact. Additionally, the solution does not excessively compromise the weight of the structure, hence barely modifying the specific strength of the structure.

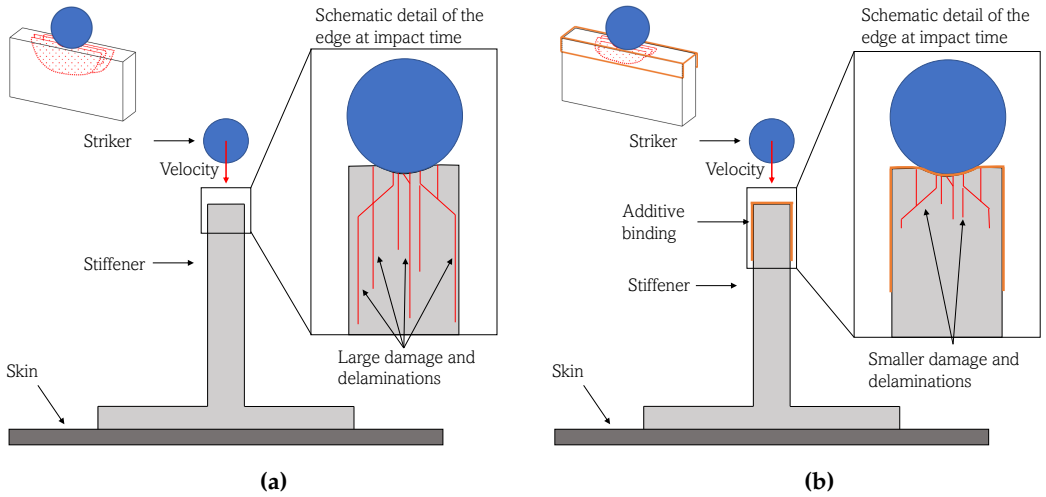

Figure 3.2: Schematic of a composite stringer impacted on the edge with a free-falling striker. a) No binding applied with interlaminar delamination, b) additive binding applied at the free edges reducing the delaminated area after impact.

3.3 Additive binding layers to suppress free-edge delamination in composite laminates under tension with open holes

Open holes in composite laminates are stress concentration points which reduce the overall strength of composite structures. However, they are usually needed to pass wires and pipes through the structure. As explained in section 2.4.2, interlaminar delamination in composite laminates with open holes delays the final failure point of the composite laminate (when the laminate can not withstand any more load). It is taken as a general practice to define the actual failure of the laminate as the point at which the first load drop is detected in the force-displacement graphs. This load drop is associated with the moment at which the delamination originated from the hole edge and the laminate edges join up through the width of the laminate. Figure 3.3a schematically shows delaminations growing from the open hole of a composite laminate under tension.

Stopping or delaying the spread of these interlaminar delaminations could delay the moment at which the first drop in force occurs. For this reason, the idea of using additive layers has been explored to delay or reduce the extent of the delamination originating from the hole edge. The concept of the solution is based on an additive composite laminate made out of thin-ply unidirectional prepreg. This thin-ply laminate is added to the edge of the hole, as schematically shown in figure 3.3b. These additive layers are intended to suppress the initiation of delamination and then hold the extent of delamination arising from the edge of the hole. In this way, it will be explored to which extent this additive binding could enhance the mechanical prop-

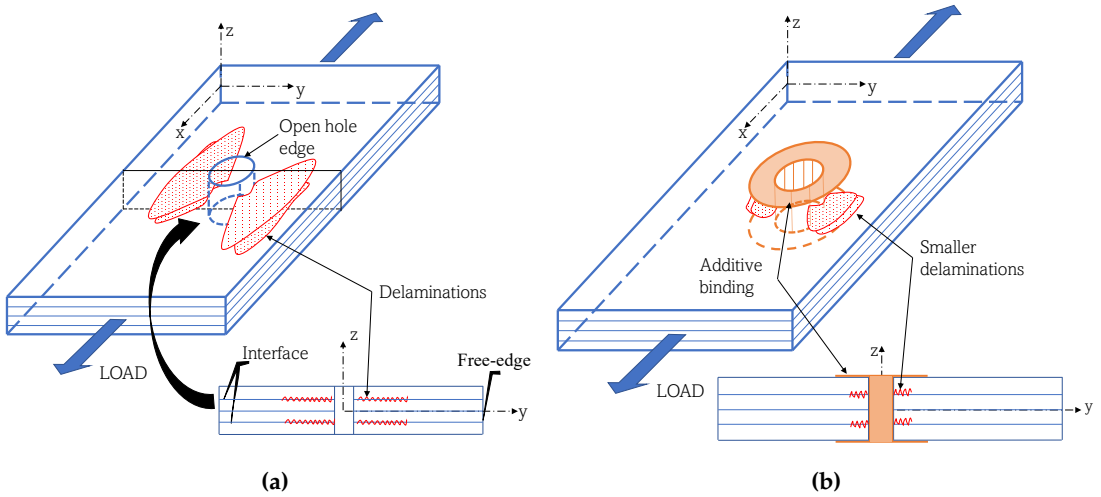

Figure 3.3: Schematic of a composite laminate with an open hole under tensile load. a) No binding is applied with interlaminar delamination, b) additive binding is applied around the edge of the hole, reducing the delaminated area.

erties of composite laminates with open holes, plus to which extent delamination is being arrested.

3.4 Additive binding layers for enhancing the bearing response of pin-loaded composite laminates

Bolted joints are one of the weakest areas of a composite structure. For this reason, the composite laminate is thicker around the bolted areas. Holes are stress concentration points, where the stress values reach up to three or four times the stress in points of the composite far from holes. Additionally, as explained in section 2.5.1, the bolt or fastener in composite bolted joints induces a crushing effect on the surface of the hole. This crushing of the hole develops fibre breakage plus small matrix cracking, which induces delamination and the final failure of the joint. Figure 3.4a schematically shows a bearing test specimen with delamination arising from the edge of the hole.

It has been shown in section 2.5.3 that increasing the stiffness of the laminate around the hole under crushing effects with metallic inserts increases the bearing strength of composite bolted joints significantly. In this thesis, the enhancement of the bearing strength of composite laminates has been explored by employing additive composite layers. The concept of the solution is based on an additive composite laminate made out of thin-ply unidirectional prepreg. This thin-ply laminate is added to the edge of the hole, as schematically shown in figure 3.4b. It will be shown to which extent the additive binding can enhance the bearing strength of bolted composite laminates.

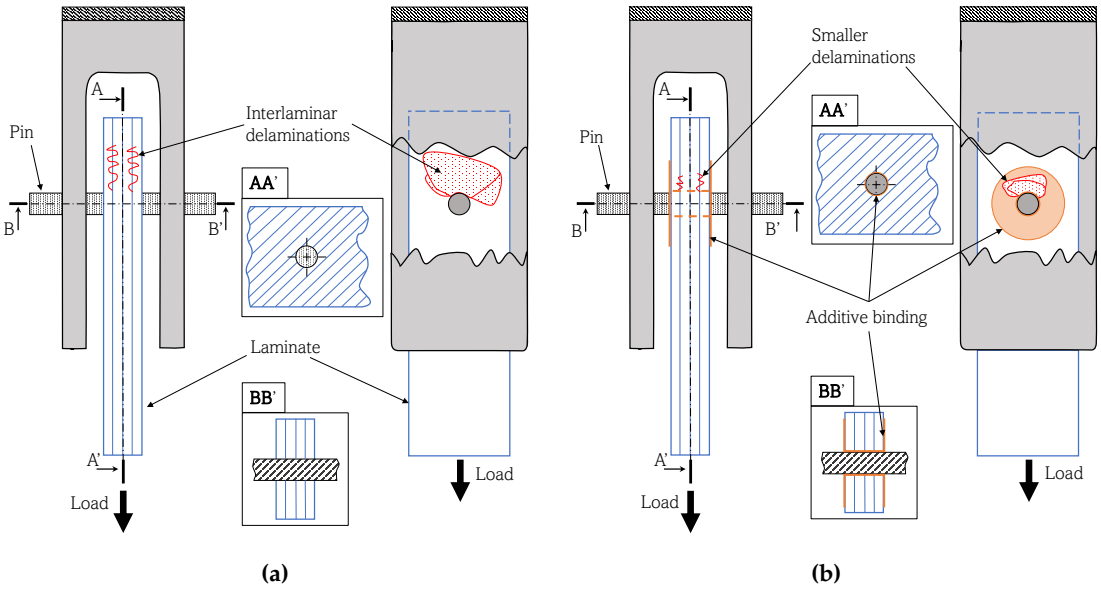

Figure 3.4: Schematic of a pin-loaded composite laminate in a bearing strength testing setup. a) No binding is applied with interlaminar delamination, and b) additive binding is applied between the hole and the pin around the edge of the hole, reducing the delaminated area.

Chapter 4

Finite element modelling

Numerical simulations have been used in this thesis as a tool to assess the effectiveness of the proposed solutions for each research question. A high-fidelity modelling strategy has been avoided, as that was not the purpose intended for the FEA in this thesis. This way, computationally light models have been produced for studying and analysing proposed solutions. This chapter presents the strategy for determining the most suitable additive binding stacking sequence and geometry. An explanation of existing modelling techniques developed for computationally analysing composite materials is given. Thus, the advantages and disadvantages of the technique chosen for this thesis are presented. Additionally, different sections of the chapter are dedicated to explaining how delamination has been modelled for each particular loading scenario.

4.1 Modelling delamination in composite materials

Delaminations in composite laminates are constrained to develop in their own plane (interlaminar), as the toughness of the interface is relatively low in comparison with that of the adjoining material [259]. At the time of analysing delamination utilising finite element models, there are two clearly defined approaches[1]. Delaminations can be analysed by using *cohesive damage models* (section 4.1.1) and *the virtual crack closure technique* (section 4.1.2).

Cohesive damage models implement constitutive interfacial laws defined in terms of damage variables and a damage evolution law. These constitutive laws and variables take form in cohesive damage elements, which are generally inserted between solid elements [261–264] or beam/shell elements [264].

The fracture mechanics approach has already been mentioned and explained in section 2.1.1. Fracture mechanics allows for predicting the growth of an existing crack. The most extended technique for modelling delamination with FM is the virtual crack closure technique (VCCT) [43, 259].

The procedures for defining and using both techniques are more or less standardised, but nomenclature and definitions sometimes vary depending on the software used. For the numerical analysis done in this thesis, the software Abaqus by DS Simulia has been used. The Abaqus version is Abaqus 2019, with FOX version 1.0 and Python version 2.7.3.

4.1.1 Cohesive zone method

The cohesive zone method (CZM) is based on the assumption that the stress transfer capacity between the two separating faces of delamination is not entirely lost at damage initiation but instead is a progressive event governed by progressive stiffness reduction of the interface between the two faces separating. Figure 4.1 displays a schematic of the crack propagation concept using the cohesive zone method. This approach replaces the engineering stress-strain concept with a traction-separation concept. Cohesive zone model elements can be modelled with zero-thickness elements. Hence, the initial thickness of the element cannot be used as per the definition of strain. Instead, deformation is measured by the separation δ between the faces of the plies connected through the CZM element. In this way, the damage

[1] It is to be noted that this chapter is written taking into account that the reader is knowledgeable and understands the principles of FE modelling. In case needing further information than the one given in this thesis, the reader can be referred to the book of Barbero [259] and the documentation available of Abaqus [260]

initiation is related to the interfacial strength, e.g., the maximum traction on the traction-displacement jump relation. When the area under the traction-displacement jump relation equals the fracture toughness, the traction is reduced to zero, and new crack surfaces are formed. The major advantage of cohesive zone modelling is that it allows for accounting delamination of existing cracks but also allows for the creation of new ones, contrary to the VCCT approach.

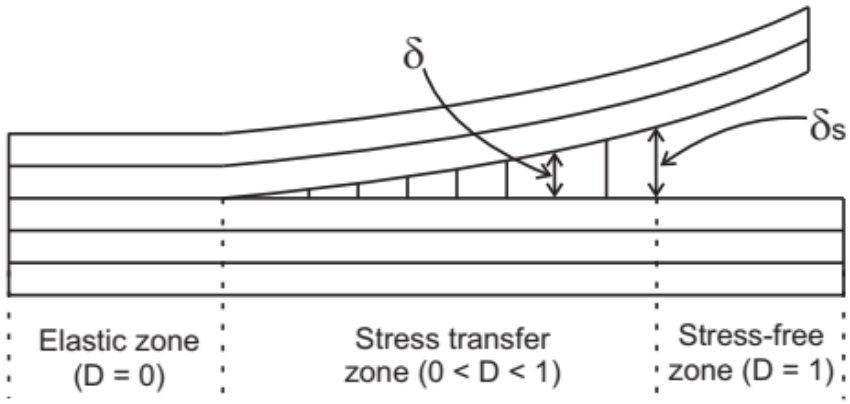

Figure 4.1: Schematic of the basis for cohesive zone method to simulate crack propagation. - Reproduced from [259]

The interface between the two possible separating faces of the composite laminate is modelled with cohesive elements [265]. These cohesive elements can be modelled as zero-thickness elements (defining coincident opposite nodes of the cohesive element) or finite-thickness elements. The faces of the adjacent plies of the composite laminate are, therefore, to be regarded as connected to each other through the stiffness of the cohesive element [259]. Thus, during the deformation of the laminate, the resulting separation of the plies would be proportional to the stiffness of the cohesive element. The CZM element is not formulated as usual by integration over the volume of the element because the initial volume of the element is zero. The CZM element can be visualised as a spring between the initially coincident nodes of the element. The nodes of the cohesive element will open (mode I: opening) or slide (mode II: shear and III: tearing) relative to each other, as shown in figure 2.5.

When formulating the CZM, several researchers have developed different approaches in terms of how to account for the coupling of the three crack propagation modes. A single-mode deformation cohesive model, which assumes that the three crack propagation modes are uncoupled (even if they are active simultaneously), is explained in this thesis. Hence, the formulation presented in this section works only for pure modes I, II, or III. For further reading on formulations for mixed-mode cohesive models, the reader is directed to the relevant book [259], the book chapter [266], and articles [262, 267–271] on the matter. The work by Turon et al. [268] is particularly

interesting as they introduced a damage model for variable mixed-modes. Additionally, they introduced a new criterion for the onset of delamination based on an energy approach, which stems from the expression of the critical energy release rate proposed by Benzeggagh and Kenane [119].

In a single-mode cohesive model, the formulation for any of the three crack modes is similar. The surface tractions at the interface are σ_i, with $i = I, II, III$ denoting the three crack propagation modes. The corresponding separations between the opposite faces of the CZM element are denoted as δ_i. Finally, the through-the-thickness interface stiffness (referred to as *penalty stiffness* in Abaqus) is denoted as K_i. In this way, the stress, displacement and the cohesive behaviour of the stiffness is described in terms of a traction-separation law, represented by equation 4.1. Figure 4.2 represents how the stress is transferred in terms of the traction-separation law for the cohesive zone model. The selection of the value of K_i is an additional part of the modelling preparation. Although there is no defined way to obtain the interface stiffness *Ki* value, there are approximations and experimentally-based discussions on how to choose numerical values for K_i, as provided in [272].

$$\sigma_i = K_i \delta_i \tag{4.1}$$

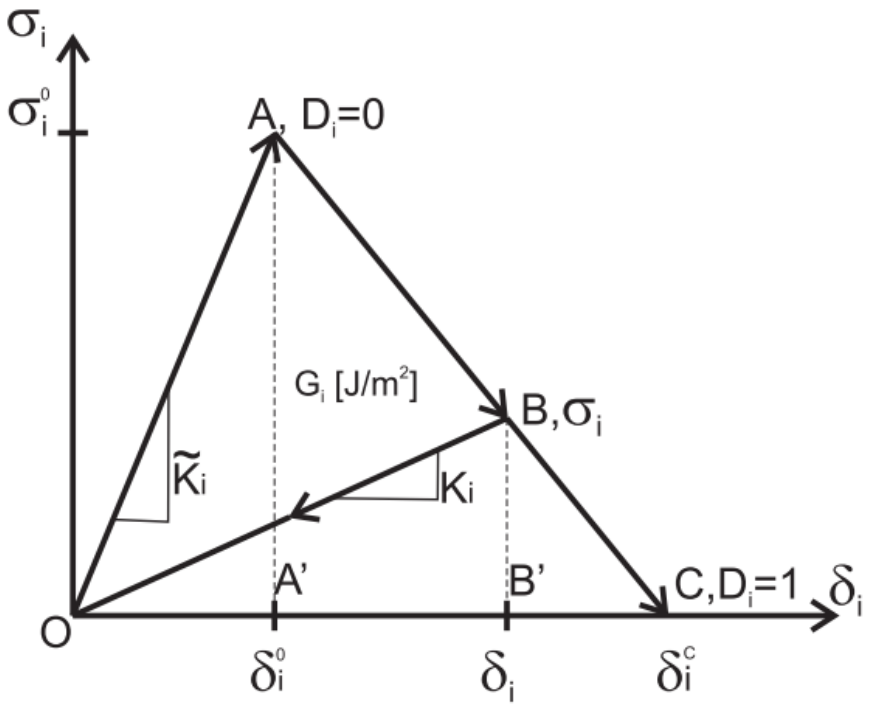

Figure 4.2: Stress transfer model for cohesive zone model. - Reproduced from [259].

Initially, the material is subjected to a low tensile load in a linear elastic behaviour up to the onset of damage, represented by the $\overline{OA}$ line in figure 4.2. During $\overline{OA}$, the material presents an undamaged interface stiffness $\widetilde{K}_i$ ($[N/mm^3]$). Point A, D_i =

0 (equation 4.2), represents the onset of damage. At this point, the stress is equal to the interlaminar strength of the material, σ_i^0 (corresponding with δ_i^0). So the damage initiation criteria is $\sigma_i = \sigma_i^0$. At this point, σ_i^0 represents the strength of the interface, with one strength value for each crack opening mode, σ_I^0, σ_{II}^0, σ_{III}^0. In CZM, these modes are named "damage modes", as CZM does not evaluate FM. In its place, CZM replaces the FM problem by a continuum damage mechanics (CDM) problem [259]. At damage onset, the two plies do not separate completely into a physical crack; rather, the interface starts losing its stiffness. Thus, as the relative displacement increases, the interface accumulates damage, starts losing its stiffness and the stress goes lower than the strength (point B).

The CZM elements use an assumption of elastic damage behaviour [259]. Hence, if the material would be unloaded before the total failure of the interface (point C in figure 4.2), e.g., at point B, the stress-separation would unload to the origin (point O), as shown in figure 4.2. Due to the damage accumulated, the next time the material is loaded, the elastic period would present a K_i stiffness (slope between points O and B in, as shown in figure 4.2). Consequently, the stress-separation law needs to account for the D_i damage variables, representing the damage absorbed by the material while loaded. There are as many damage variables as damage modes D_I, D_{II}, D_{III}, which are state variables to be determined during the analysis as a function of the relative separation between the faces of the laminate, δ_i, which are provided by the FE solution, and the values δ_i^0 and δ_i^c, calculated from equations 4.1 and 4.3. The physical interpretation of D_i is a measurement of the degradation of the stiffness. Equation 4.2 defines the relationship between the interface stiffness of the undamaged material ($\widetilde{K}_i$) and the interface stiffness K_i. The undamaged stiffness values $\widetilde{K}_i$ are additional material properties needed for the CZM model, which are different from the Young's modulus (E), or the shear modulus (G).

$$K_i = (1 - D_i)\widetilde{K}_i \tag{4.2}$$

The energy release rate at point B is the area enclosed in the triangle OAB. Eventually, there will be a point for a displacement value in which there will be a total fracture of the cohesive bond (point C in figure 4.2). At this point, the stiffness of the element is reduced to zero. Additionally, this point corresponds with the critical energy release rate value, G_{ic}, with $i = I, II, III$. So the area of the triangle OAC equals the value of fracture toughness or the critical energy release rate of the interface. In this way, the separation distance at fracture δ_i^c can be calculated as per equation 4.3.

$$\delta_i^c = \frac{2G_{ic}}{\sigma_i^0} \tag{4.3}$$

As shown, CZM modelling needs nine experimental material values for its working, e.g., $\widetilde{K}_I$, $\widetilde{K}_{II}$, $\widetilde{K}_{III}$, σ_I^0, σ_{II}^0, σ_{III}^0, $\mathcal{G}_{\mathcal{I}}$,$\mathcal{G}_{\mathcal{II}}$ and $\mathcal{G}_{\mathcal{III}}$. On the other hand, the VCCT requires only the three values of critical energy release rate (fracture toughness) to predict the onset and evolution of delamination. Additionally, CZM is generally computationally costlier than VCCT.

4.1.2 Virtual crack closure technique

The virtual crack closure technique (VCCT) is a method based on fracture mechanics that allows for predicting the onset and development of cracks based on the presence of preliminary imperfections, flaws or cracks. According to the VCCT, the strain energy release rate can be evaluated starting from the assumption that for an infinitesimal crack opening, the strain released is equal to the amount of work required to close the crack. Hence, the energy required to form or propagate a crack is equal to the elastic energy released by the solid during the crack formation. So, the energy released is the difference between the elastic strain energy available before and after the crack is formed. Based on this definition, the energy release rate can be written based on the strain energy before and after the crack, as in equation 4.4

$$\mathcal{G} = \frac{-\Delta\mathcal{U}}{\Delta A} \tag{4.4}$$

where A is one-half of the surface created, and $\mathcal{U}$ is the internal elastic strain energy. In other words, as shown in figure 4.3, the energy $\mathcal{G}$ released when the crack is extended by Δa from a to $a + \Delta a$ is identical to the energy required to close the crack between the points l and i (see figure 4.3).

Additionally, this crack extension of Δa from $a + \Delta a$ (node i) to $a + 2\Delta a$ (node k), does not significantly alter the state at the crack tip. This means that the displacements of the nodes just behind the crack tip are approximately equal to the displacements of the nodes in the previous crack extension. Based on figure 4.3, when the crack tip is located at node k, the displacements behind the crack tip at node i are approximately equal to the displacements behind node l when the crack tip is located at node i. It is to be noted that the nodes l, i and k, represented in figure 4.3, are referring to the nodes at the top surface of the crack, and they have their respective coincident but not merged nodes on the bottom surface of the crack. These nodes in the lower surface are denoted with an * (asterisk). Based on the Griffith energy approach [81], the crack progresses as the energy available $\mathcal{G}$ is higher than the material energy necessary for fracture, $\mathcal{G}_c$, as shown in equation 4.5.

$$\mathcal{G} \geqslant \mathcal{G}_c \tag{4.5}$$

The elastic strain energy released during crack propagation $\Delta\mathcal{U}$, and therefore to create the new surface area, can be calculated as the work required to close the crack $\mathcal{W}_{closure}$, i.e.,

$$\Delta\mathcal{U} = \mathcal{W}_{closure} \tag{4.6}$$

In this way, based on the definition of energy release rate given in equation 4.4, and on that, the change in strain energy $\Delta\mathcal{U}$ is considered to be equal to the work required for crack closure $\mathcal{W}_{closure}$ (equation 4.6), the calculation of the crack closure work provides the base for the VCCT. The crack closure work can be calculated from the FE nodal displacements and forces, as illustrated in figure 4.3.

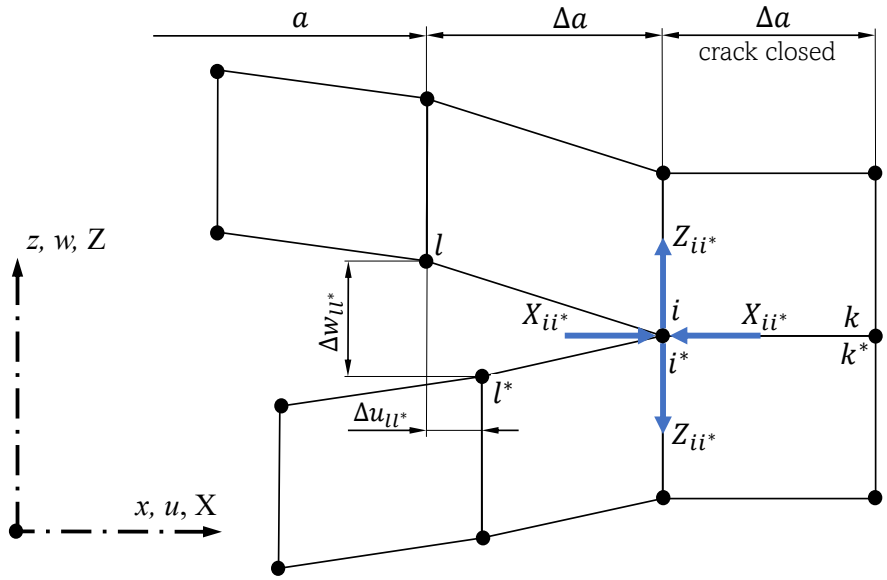

Figure 4.3: Two-dimensional principle of the virtual crack closure technique.

Initially, the crack surfaces are rigidly bonded. The nodal forces (X, Z) and displacements (u, w) at the coincident nodes i and i^* are calculated from the FE solution. The software Abaqus [273] uses the hypothesis of "self-similar crack propagation", which enounces that during crack propagation, the crack configuration between the nodes i-k-k^*-i^* will be similar to the crack configuration between nodes l-i-i^*-l^*. Hence, the separation between i and i^* will be equal to the separation between nodes l-l^* before crack propagation. This implies that $\Delta w_{ii^*} = \Delta w_{ll^*} = w_l - w_{l^*}$ and $\Delta u_{ii^*} = \Delta u_{ll^*} = u_l - u_{l^*}$.

In the suppose of single mode deformation, e.g., pure mode I (opening mode), if $\mathcal{G}_I > \mathcal{G}_{Ic}$ (crack propagation) and the nodes i-i^* open, the elastic work needed for closing the crack is given by equation 4.7

$$\mathcal{W}_{closure,modeI} = \frac{1}{2}[Z_{ii^*}\Delta w_{ii^*}] = \frac{1}{2}[Z_{ii^*}\Delta w_{ll^*}] \tag{4.7}$$

On the other hand, if the single mode deformation is mode II (shear mode), and if $\mathcal{G}_{II} > \mathcal{G}_{IIc}$ and the nodes i-i^* open, the elastic work needed for closing the crack is

$$\mathcal{W}_{closure,modeII} = \frac{1}{2}[X_{ii^*}\Delta u_{ll^*}] \tag{4.8}$$

where X_{ii^*} and Z_{ii^*} are the shear and opening forces at the nodal points i and i^*, and Δu_{ll^*} and Δw_{ll^*} are the shear and opening displacements at nodes l and l^*.

The components of the energy release rate can be calculated then as $\mathcal{W}_{closure}/\Delta A$, as shown in equations 4.9 and 4.10, where ΔA is one-half of the crack surface created. This area of the newly created crack is ΔA = Δa x b, where b is the width of the crack. For a two-dimensional model, it is assumed that it has unit width, and hence ΔA = Δa x 1.

$$\mathcal{G}_{\mathcal{I}} = \frac{\mathcal{W}_{closure,modeI}}{\Delta a} = \frac{1}{2\Delta a}[Z_{ii^*}\Delta w_{ll^*}] \tag{4.9}$$

$$\mathcal{G}_{\mathcal{II}} = \frac{\mathcal{W}_{closure,modeII}}{\Delta a} = \frac{1}{2\Delta a}[X_{ii^*}\Delta u_{ll^*}] \tag{4.10}$$

The VCCT method works similarly for mode III by considering the corresponding components of the separation and nodal forces. A three-dimensional VCCT model is presented in figure 4.4 where the nodal forces of the lower surface corresponding to node i^* have not been represented in figure 4.4a for clarity of the drawing. The new created surface area for a node is calculated as ΔA = Δa x b. The width is calculated from half of the distance from the node to its adjacent nodes in the crack tip, as shown in figure 4.4. For this reason, when Krueger [43] proposed corrections for elements with different lengths or widths at the crack tip. For elements which present the same crack opening length Δa and width b at the crack tip, the energy release rate can be calculated as

$$\mathcal{G}_{\mathcal{I}} = \frac{1}{2\Delta A}Z_{ii^*}(w_l - w_{l^*}) \tag{4.11}$$

$$\mathcal{G}_{\mathcal{II}} = \frac{1}{2\Delta A}X_{ii^*}(u_l - u_{l^*}) \tag{4.12}$$

$$\mathcal{G}_{\mathcal{II}} = \frac{1}{2\Delta A}Y_{ii^*}(v_l - v_{l^*}) \tag{4.13}$$

For a pure single mode crack propagation, the condition for crack propagation (equation 4.5) becomes

$$\frac{\mathcal{G}_i}{\mathcal{G}_{ic}} \geqslant 1 \tag{4.14}$$

where $i = I, II, III$, so $\mathcal{G}_i$ is the corresponding opening mode strain energy release rate and $\mathcal{G}_{ic}$ is the corresponding critical energy release rate for that opening mode.

For mixed-mode loading, the single-mode crack criterion needs to be replaced with a mixed-mode criterion, which is based on experimental data for acquiring fitting parameters [118–121]. These criteria make use of an equivalent strain energy release rate $\mathcal{G}_{equiv}$ calculated via VCCT and a critical equivalent strain energy release rate $\mathcal{G}_{equivC}$, which is calculated based on the mixed-mode criterion defined and the bond strength of the interface. So the crack propagation criterion is expressed as

$$\frac{\mathcal{G}_{equiv}}{\mathcal{G}_{equivC}} \geqslant 1 \tag{4.15}$$

For example, the BK law [119] is expressed as

$$\frac{\mathcal{G}_{equiv}}{\mathcal{G}_{equivC}} = \frac{\mathcal{G}_I + \mathcal{G}_{II} + \mathcal{G}_{III}}{\mathcal{G}_{Ic} + (\mathcal{G}_{IIc} - \mathcal{G}_{Ic})(\frac{\mathcal{G}_{II}+\mathcal{G}_{III}}{\mathcal{G}_I+\mathcal{G}_{II}+\mathcal{G}_{III}})^\eta} \geqslant 1 \tag{4.16}$$

where η is an experimental fitting parameter which depends on the material and the mixed-mode ratio. For further reading of the different mixed-mode criteria, the reader is directed to the proper articles where they were presented [118–121] and the Abaqus documentation for learning how Abaqus implements the criteria [273]. Abaqus standard 2019 provides three of these common mixed-mode formulae for computing the VCCT crack propagation analysis, the BK law [119], the power law [118], and the Reeder law [121] models.

As shown, the VCCT is a straightforward method for evaluating the opening and development of delaminations. This thesis aims to provide insight into the use of additive bindings for stopping and delaying delamination. Hence, the FE analysis is used as a tool for designing the most appropriate additive binding for stopping delamination. Hence, to model several different additive bindings and find the optimum one, the VCCT offers a few advantages over other techniques, e.g., progressive damage modelling using cohesive elements: (i) it is fast and numerically efficient, (ii) it directly provides values of $\mathcal{G}$, so makes comparing the efficiency of different bindings straightforward.

The VCCT modelling uses what is called ”bonded nodes” in the Abaqus environment. These nodes indicate to the program where the defined pre-crack is. The

contact definition of the different plies is made with surface-to-surface interactions, in which the "bonded nodes" need to be defined. Then, these bonded nodes extend across all the interfaces of the plies, which are not part of the pre-crack. Thus, as the simulations which have been carried out in this thesis do not model the propagation of delamination by defining very high values of fracture toughness, these nodes bonding the interfaces will not separate despite the high interlaminar stresses arising at the free edges.

Moreover, the prior definition of the crack tip, via Python scripting, eases the preparation of the FEA for developing post-processing subroutines, accelerating data acquisition from the FE model. Therefore, even if more rough in some aspects, the VCCT continues to attract the attention of researchers due to the simplicity of its theory and its suitability for implementation in post-processing subroutines. This post-processing subroutines are particularly useful when high volume of simulations are to be run, as is the case in this thesis.

The validation of the effectiveness and design of the additive binding was based on its ability to reduce the value of the energy release rate, so increasing the load for delamination initiation. Hence, the VCCT was the method selected for simulating delamination in all four research questions FE modelling, as the calculation of $\mathcal{G}$ is straightforward. Particular explanations on how these FE models have been built are given following. All of these FE models have been built via Python scripts, which allow a rapid change in parameters while building the models, e.g., width, thickness and length of the model, delamination-related parameters and mesh options. As a result, coincident mesh nodes could be built accurately for smoother VCCT operation. Additionally, building the models with a Python script makes it easier to define "interesting points" as the nodes of the crack tip, the displacements and forces application points and other particular elements. Thus, the results data collection is accelerated, and it is possible to automatise it for several simulations changing different parameters. The Python scripts used for each of the cases explained in the following sections are available in a digital repository which is presented in Appendix A Numerical simulations additional information. Additionally, all these Python scripts are commented on for easy guidance on building the models and explanation of secondary decisions and assumptions taken for the proper working of the simulations.

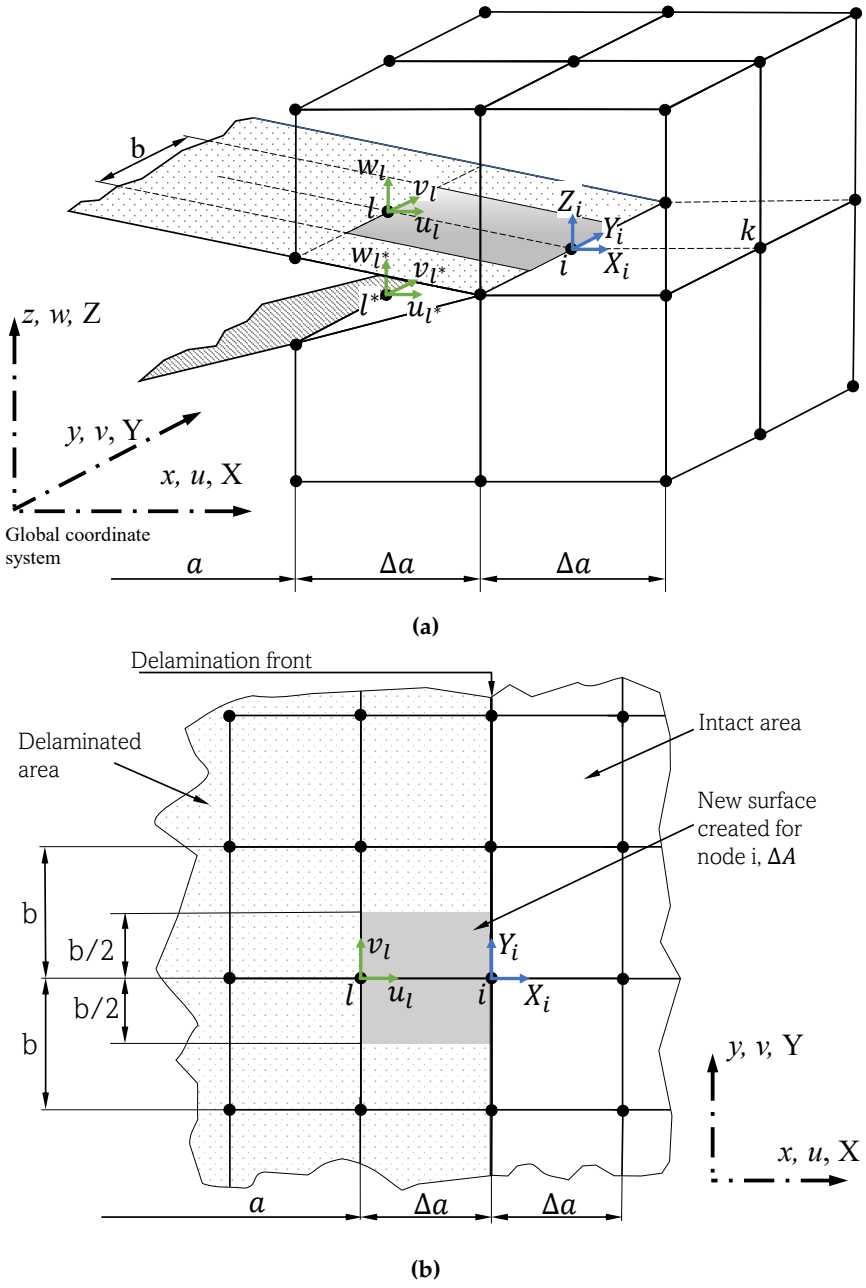

Figure 4.4: Virtual crack closure technique for four-noded plate/shell and eight-noded solid elements. (a) 3D view (lower surface forces are omitted for clarity) and (b) top view of the upper surface (lower surface terms omitted for clarity).

4.2 Modelling of additive bindings for suppressing free-edge delamination in composite laminates under tension

Composite laminates with large free edges under tension, e.g., tensile coupons, are susceptible to free-edge delamination. The effectiveness of additive bindings for suppressing free-edge delamination in composite laminates under tension was studied using Abaqus 2019. The effectiveness of the solution is measured with the change in the value of the energy release rate at a crack tip. The model built assumes the presence of a delamination crack at the free edges of a tensile coupon, so the value of $\mathcal{G}$ can be calculated at the crack tip using VCCT. A Python code[1] was developed for Abaqus 2019 for building simulations and acquiring the data for post-processing of the simulation. The code was built for using the VCCT to calculate the energy release rate values at the crack tip in a substrate laminate when subjected to axial strain.

Simulations were conducted for the different substrate laminate layups explored to study the effect of the length and position (interface number) of the interlaminar crack on the energy release rate. In each layup, the interfaces with the highest energy release rate values are those assumed to fail before the others and are referred to as critical interfaces. The energy release rates at the critical interfaces of the models with and without bindings are compared to study the effect of the additive bindings to suppress delamination. The values of the energy release rate were obtained for each crack opening mode from the simulation. Finally, an equivalent or total energy release rate was calculated as per the definition of $\mathcal{G}_{equiv}$ in equation 4.16, e.g.,

$$\mathcal{G}_{equiv} = \mathcal{G}_I + \mathcal{G}_{II} + \mathcal{G}_{III} \tag{4.17}$$

The finite element model presented is applicable to any layup, independent of its ply thickness, width, ply orientation, etc. In laminates under axial strain, the stress field does not vary along the length of the specimen at a point distant from the end-tabs. This is also applicable for the FE modelling case, and therefore, the use of a generalised plane strain condition is applicable, as explained by Pipes and Pagano in [13]. Using a generalised plane strain condition gives accurate stress and strain field at points in the middle of the sample while significantly reducing the computational cost. A slice model, as proposed by Jiang [274], based on the generalised plane strain condition, was used instead of a full tensile sample model, as shown schematically in figure 4.5a. The generalised plane strain aims to mimic the displacement field far away from the end-tabs, where the displacement field is constant in the x-axis

[1] All Python codes for running the simulations for all the cases mentioned in this thesis can be found in Appendix A Numerical simulations additional information

at different sections. Free-edge delamination is assumed to be perpendicular to y-z plane but independent of the x-axis. Therefore, the $y-z$ plane may warp under load, giving rise to the use of generalised plane strain condition. It is worth mentioning that variation of displacement across a section is expected away from the tabs, and the slice in figure 4.5b is correctly seen to be slightly deformed out of the plane. However, this displacement field stays the same for different slices far from the end-tabs.

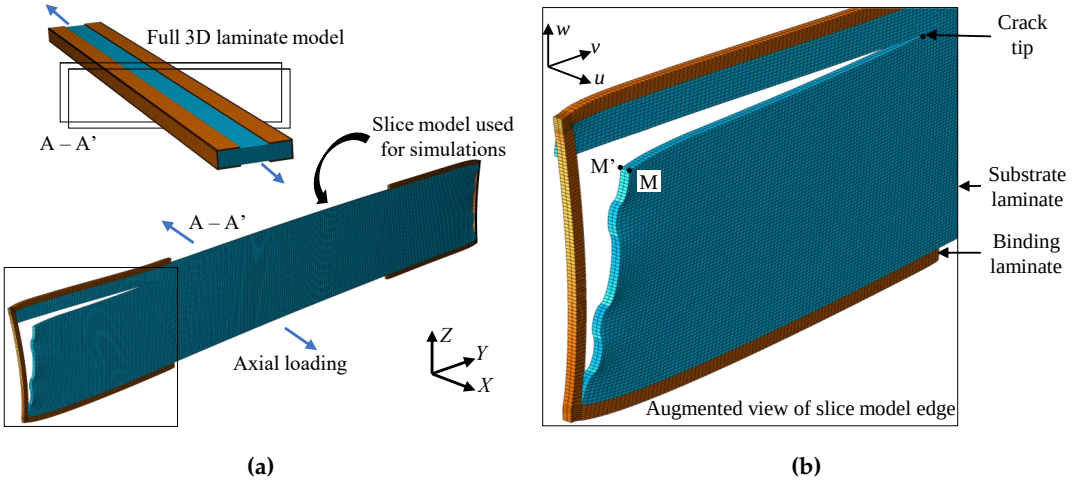

Figure 4.5: Slice model based on generalised plane strain condition with an additive binding. (a) A figure of the slice model used for the simulation, taken from the centre of a full 3D model representation (not used in the simulations), (b) details of a free-edge delamination model with an additive binding.

The finite element model of the composite substrate was built using individual layers meshed with 3D-8noded brick elements (C3D8I). Each layer of the substrate and additive binding had a mesh size of 0.05 mm in the width (y) direction (see figure 4.5). Also, two elements per ply thickness were used for both the substrate and the binding and two elements in the length (x) direction. Only one crack on one side of the layup was modelled, making the slice model asymmetrical. This is because the interlaminar cracks on both edges are independent of each other, and the lack of delamination on one side does not change the $\mathcal{G}$ values on the other side. Figure 4.5b shows the slice finite element model with the additive binding applied. The substrate laminate slice represented in figure 4.5b is 20 mm wide, 0.07 mm long, and 2.08 mm thick and shows a 4.5 mm long edge-delamination. The binding shown in figure 4.5b is 0.12 mm thick and has an overlap length of 5 mm (see figure 3.1b for reference on overlap length).

The generalised plane strain condition is achieved by applying equation-type restrictions to node pairs with equal y and z coordinates on either side of the slice. All nodes on one face of the slice are constrained to have the same displacements, in the transverse (v) and thickness (w) directions, as that of their equivalent nodes on the

opposite face. For example, points M and M', opposite nodes on the front and back faces, as shown in figure 4.5b, are constrained as below

$$v_M - v_{M'} = 0 \tag{4.18}$$

$$w_M - w_{M'} = 0 \tag{4.19}$$

Another constraint should be applied to guarantee uniform longitudinal strain on the loading direction. This is achieved by fixing the distance between the corresponding nodes, e.g., M and M', proportional to the applied extension, ϵ=1%, and the slice length L in the loading direction as shown below

$$u_M - u_{M'} = \epsilon L \tag{4.20}$$

Where u represents the movement of each node in the loading direction, as shown in figure 4.5b. A minimum of two elements in the loading direction is required to avoid any interference of the constraining equations or reaction forces on the back and front faces with the nodal forces used in VCCT. This will allow the node at the midplane of the slice model not to be directly constrained by equations (4.18) to (4.20) and be used to calculate the energy release rate values at the crack tip. The layers of the substrate laminate were constrained together using the tie function in Abaqus. The layers adjacent to the pre-crack were constrained together with a surface-to-surface contact interaction with a small sliding formulation and surface-to-surface discretisation[1]. Arbitrary high fracture toughness values equal to $9 \cdot 10^{34}$ N/mm were applied to avoid crack growth simulation. Delamination growth is not aimed to be modelled, as this study focuses on comparing the impact of the additive binding on the energy release rate at different interfaces and crack lengths.

The free edges of the substrate laminate were not tied to the internal surface of the binding laminates, as seen in figure 4.5b. This is to consider the possibility of unbonded additive binding layers to the free edges of the substrate and obtain conservative upper limit energy release rates for the cases with additive binding. Furthermore, to study the possibility of a crack occurring between the top/bottom surface of the binding and the substrate, models with initial cracks were simulated[2]. The value

[1]The formulation definition for surface-to-surface contact interaction in Abaqus is referred to as discretisation or enforcement indistinctively in this thesis. The choice between node-to-surface and surface-to-surface depends on the type of analysis done and the experimental trial for the best fit to the type of simulation. The discretisation definitions chosen in this thesis are for optimising and speeding the simulations for each model.

[2]The Python code for this model can be found with the rest in Appendix A Numerical simulations additional information.

of $\mathcal{G}$ at the crack between the binding and the substrate laminate was found to be insignificant, less than 2.5% of the maximum value of $\mathcal{G}$ at the critical interface of the same substrate. Therefore, no delamination is expected between the binding and the substrate, and the additive bindings were tie-constrained to the substrate's top and bottom surfaces and tie-constrained among themselves. In this way, no cracks were considered between the top and bottom surfaces of the substrate laminate and the additive binding.

Different crack lengths at different interfaces between layers with different fibre orientations were modelled, as will be explained in section 6.1. Due to the symmetry of the laminates, only half of the interfaces needed to be modelled. The run time for each simulation was approximately 5 minutes for each delamination length. This short simulation time along with the applied fine element size were possible as the slice modelling technique was used.

4.3 Modelling delamination extent in composite laminates under edge impact

The damage morphology and interaction in composite laminates under edge impact is complex and challenging, as explained in section 2.3. Due to the dynamic nature of impacts, most of the FE frameworks proposed for simulating edge-on impacts use explicit formulation, CZM modelling and user-defined subroutines for defining the damage mechanisms. As a result, these kinds of simulations tend to be computationally costly. In this thesis, the simulation of the whole failure process in an edge impact scenario was out of scope, and only delamination was modelled, as $\mathcal{G}$ was the parameter used for determining the effectiveness of the additive binding. Hence, similar to the case of free-edge delamination, the VCCT was used to calculate $\mathcal{G}$.

The VCCT was not designed for dynamic simulations in which parts deform excessively, and elements are deleted in the development of the simulation (as by common practice in explicit impact simulations) when they become debris to the simulation and are not in contact with any other part of the model anymore. As mentioned in section 2.3, it has been demonstrated that the damage scenario of the edge impact test shows similarities with a crushing damage scenario [167]. In this way, the FE modelling carried out in this thesis consisted of a quasi-static crushing of a stiff impactor on the edge of a composite laminate, as shown in figure 4.6. Since only delamination was being modelled in a crushing damage scenario, the definition of contact interactions, element sizes and boundary conditions were adapted accordingly to avoid excessive element distortion or rotation in the model.

Simulations were conducted for the substrate laminate layup studied to analyse the effect of the additive binding. The model built assumes the presence of delamination cracks, using VCCT, at each of the interfaces of the laminate. Equally long cracks were simulated in all of the interfaces. As mentioned in the case of free-edge delamination, the presence of cracks in one interface does not impede the development of cracks in other interfaces. In the case of the free-edge delamination modelling, only one crack was simulated for simplicity and to speed up the simulation. However, in the case of edge impact/crushing, it was clear, after several simulations, that modelling the presence of a crack in all interfaces generated a faster convergence than only simulating one crack. This faster convergence is due to the happening of excessive distortions when only one crack is simulated using VCCT. Both simulations with single cracks at different interfaces and cracks at all interfaces were carried out for comparison. The value of $\mathcal{G}$ at each interface when only modelling one crack were found to be equal to the value of $\mathcal{G}$ at each interface when cracks were modelled at all interfaces. In this way it was concluded that the value of $\mathcal{G}$ is not affected if modelling more than one crack for the simulations carried out. The values of the energy release rate of the models with and without bindings were compared to study the effect of the additive bindings to suppress delamination. The values of the energy release rate were obtained for each crack opening mode from the simulation. Finally, an equivalent or total energy release rate was calculated as per equation 4.17.

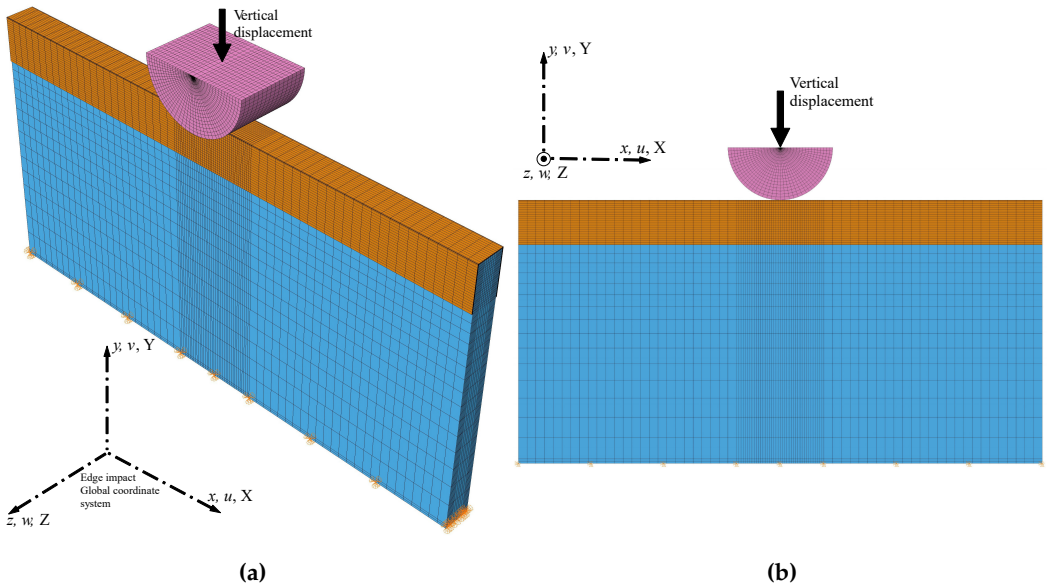

Figure 4.6: FE setup of a $[45_2/0_2/-45_2/0_4/90_2]_s$ composite laminate under edge crushing. (a) 3D view of the model, (b) front view of the model.

The FE model presented is applicable to any layup, independent of its ply thickness, width, ply orientation, etc. The finite element model of the composite substrate was

built using individual layers with 3D-8noded brick elements (C3D8). When there is more than one ply of the same fibre orientation stacked together, they are modelled as a thicker ply, e.g., a laminate of $[90_2/0_2]_s$ stacking sequence would be modelled with three plies and two interfaces. The thickness of the eight laid-up plies when manufacturing is accounted within the three plies modelled. As visible in figure 4.6, the meshing strategy of the substrate laminate involved creating a finer element mesh around the area of crushing so the elements which are in direct contact with the impactor, or in the vicinity, do not deform excessively. This area extends 5 mm to each side from the centre of the impactor in the x direction and 5 mm down from the impact point in the y direction (see figure 4.6 for axis reference). Figure 4.7 shows a schematic of the dimensions used for building the model and a detail of the fine mesh area. Each layer of the substrate laminate had two elements per ply thickness. The mesh size in the fine mesh region was 0.25 mm in the x and y directions. In the side areas, the mesh was 1 mm long in the x direction and had a single biased element size in the y direction, from an element size of 0.5 mm at the contact point with the fine mesh region to an element size of 2.5 mm at the bottom of the laminate. The lower part of the laminate was fixed with displacement constraints to simulate it being fixed in the rig used for the experimental testing. Hence, $u = v = w = 0$, and the rotations $\gamma_{xy}, \gamma_{xz}, \gamma_{yz}$ were not set.

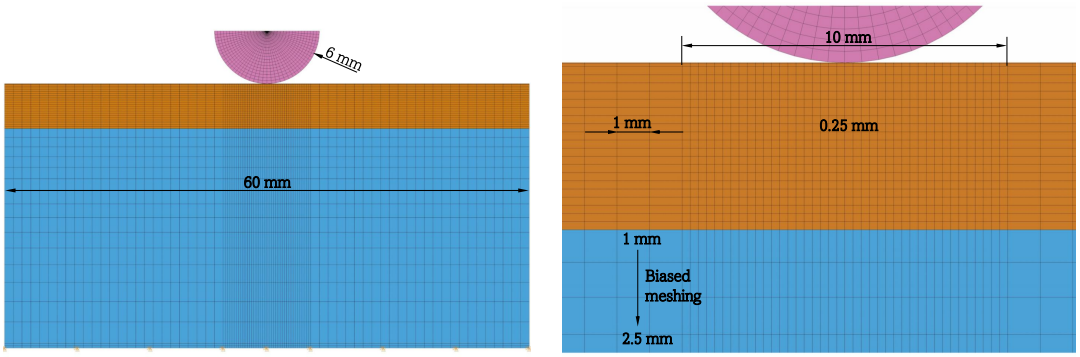

Figure 4.7: Close view of dimensions and meshing of edge impact FE models. (a) Whole front view of the laminate, (b) close-up view of the fine mesh region of the model.

All the layers of the substrate laminate were constrained between them with a surface-to-surface contact interaction with node-to-surface enforcement/discretisation and a small sliding formulation. In the case of free-edge delamination, surface-to-surface discretisation was used. It is worth mentioning that both node-to-surface and surface-to-surface discretisation methods work equally suitable for the models built in this thesis, as the meshes built are coincident. This means that the nodes of each substrate and additive binding layer are coincident, and both discretisation methods work. In addition, arbitrary high fracture toughness values equal to $9x10^{34}$ N/mm

were applied to avoid crack propagation. Similar to the free-edge delamination case, delamination growth is not aimed to be modelled, as the focus of this study is to compare the impact of the additive binding on the energy release rate at different interfaces and crack lengths.

Similar to the FE models of unnotched specimens under tension, as shown in the detail of figure 4.5b, the free edges of the substrate laminate were not tied to the internal surface of the binding laminates. This is due to the fact that at the moment of impact, the material is generally damaged. Additionally, it accounts for the possibility of an imperfect bonding between the binding and the substrate during the manufacturing process. Based on the results obtained for the free-edge delamination simulations, no cracks were modelled between the additive binding and the substrate laminate top and bottom layers. Hence, the additive bindings were tie-constrained to the substrate's top and bottom surfaces and tie-constrained among themselves.

A steel cylindrical-shaped impactor was modelled similarly to the one used in the experiments. A vertical displacement of 0.5 mm was applied to the impactor, and the energy release rates at the different interfaces were compared. For the simulations without binding, the run time was approximately 1 hour for small delamination lengths (0.25-0.5 mm). However, the behaviour observed was that as the pre-crack length increased, so did the simulation time, and the run time for a delamination length of 2.0 mm took about 2 hours and 30 minutes to complete. This increment in the simulation time is explained in section A.4 of the Appendix A Numerical simulations additional information. For the cases with binding, the run time was about 1 hour and 40 minutes for the smaller delamination lengths modelled and up to 2 hours and 30 minutes for the larger delamination lengths analysed. The mesh size can be changed easily within the python script for more accurate energy release rate values. However, finer sizes of mesh incremented the simulation time significantly. This is due to the fact of the increment of degrees of freedom with the increment of the number of elements and the convergence difficulties that arise due to the contact interaction.

The main points of the model have been presented in this section. Nevertheless, the reader is encouraged to read the Python scripts used and run them in Abaqus for building up the models for a better explanation and understanding of secondary decisions taken for the proper working of the model. Additionally, a section with lessons learned on the simulation of these models is included in the FE analysis Appendix A Numerical simulations additional information.

4.4 Modelling additive bindings in the delamination extent of composite laminates with open holes

Similar to the case of edge impact modelling, composite laminates with open holes are generally found to be modelled with CZM models and user subroutines for characterising the composite damage. However, as in the previous two cases, the simulations performed in this thesis were carried out with the VCCT. The VCCT was chosen as CZM is much more computationally expensive and takes more time to run. Additionally, the aim of the simulations was not to model the damage progressively but to run several simulations for different delamination lengths. Furthermore, due to the presence of free edges along the composite laminate, free-edge delamination could arise when the focus of the analysis is on the hole edges and not on the exterior long free edges. Thus, some modelling techniques that use the CZM need to incorporate a "fictional" supplemental part along the free edges to which the free edges are tied to avoid free-edge delamination while modelling the delamination arising from the edge of the open-hole [132]. However, this free-edge delamination is easier to model when using the VCCT.

The modelling strategy followed for the FE analysis in the case of composite laminates with open holes is similar to that one in the case of free-edge delamination. The model assumes the presence of a delamination crack at one interface initiating from the edge of the open hole, so the delamination had a circular shape. Hence one delamination length at one interface was modelled at a time. The open hole is modelled in the centre of the laminate. The energy release rate values were calculated as per equation 4.17 and then compared for each interface and crack length. Contrary to the case of unnotched laminates under tension (research question one), a generalised plane strain and slice model technique did not apply to the model for speeding up the simulation time. For this reason, each simulation for the cases without binding took around 45 minutes, and all in all, no simulation without binding took longer than one hour to complete. For the simulations of the laminates with binding applied, each simulation took an average of about one hour to complete, whereas no simulation took more than one hour and a half[1].

Unlike the cases of unnotched laminates under tension and edge impact (research questions one and two), the binding design is different from a continuous additive binding, as the additive binding needed to be applied to the edge of the hole. As will be explained in section 5.4, the additive binding was built out of thin-ply prepreg stripes, so being a discontinuous stripe-like additive binding, and hence the simu-

[1]See Appendix A Numerical simulations additional information for information on the computer specifications on which simulations were run.

lations were adapted to such manufacturing technique. Figure 4.8 presents the FE models used for both the cases without and with binding. The simulations performed for the cases without binding were automatised for the building, analysis and acquisition of data, as for the free-edge delamination and edge impact cases. As shown in figure 4.8b the additive binding stripes had their shape adapted to fit with the curvature of the hole. This geometry of the binding stripes was more challenging to build than the continuous laminate additive binding shape used for the free-edge delamination and edge impact cases. For this reason, the automatisation for building, analysing and acquiring the data was divided into different steps.

The substrate laminates of the simulations with binding were built with the same Python code as for the cases without binding (figure 4.8a). The additive binding stripes were modelled independently in the CAE environment of Abaqus, saved as "Step files" (.stp or .step files), and then imported to the model with the substrate laminates, which already had all the interactions, boundary conditions and node-sets defined. The additive binding parts were included in the assembly of the model, and interactions were applied between the additive bindings and substrate laminate. Following the definition of the interactions, the simulation was set to perform the analysis, and once finished, the results were asked from the ODB file with another Python script. This last Python script is uniquely used for acquiring the data of the simulations of laminates with open holes and additive binding applied. The code is similar that can be found in the Python script for the case without binding.

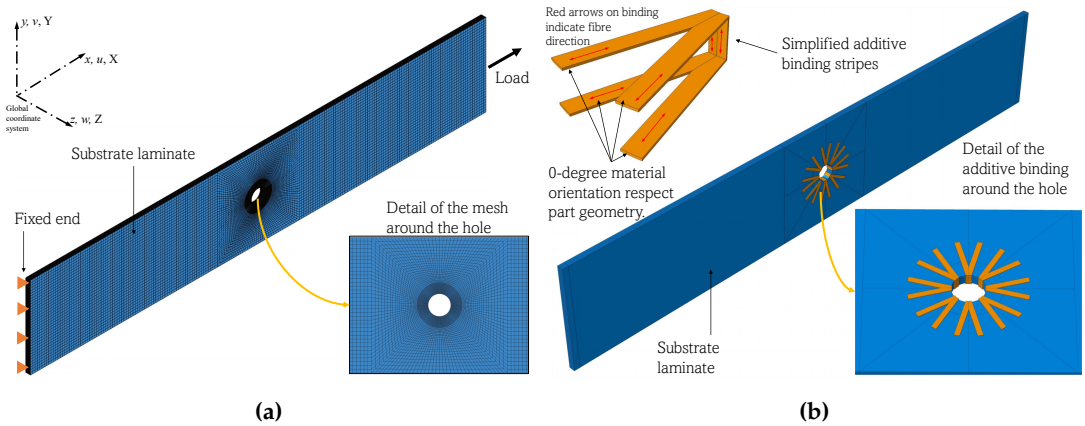

Figure 4.8: FE setup of a $[45_2/0_2/-45_2/90_2]_s$ composite laminate with an open hole under tensile load (a) 3D view of the model without binding, (b) 3D view of the model with binding and a detail view of the approximated binding around the open hole.

It is to be noted that the additive binding shown in figure 4.8b is an approximation of the actual additive bindings manufactured as will be explained in section 5.4. The binding is intended to have a $[\pm\theta]_s$ layup made out of thin stripes. This is achieved by this discontinuous thin stripe-like binding part used as an approximate binding in

the simulations. A more realistic additive binding as shown in section 4.5, similar to the one manufactured was also modelled. It is to be noted that additional simulations with a more realistic shape approximation of the additive binding (see figure 4.10b showing the binding modelled in the pin load simulations) were also carried out in for the open-hole case. The numerical results for using both bindings are presented in section 8.2.1.

The FE open hole model presented is applicable to any layup, independent of its ply thickness, width, ply orientation, hole size, etc. The only constraint is that if the thickness of the substrate laminate or the size of the hole change, the additive binding parts would need to be sized accordingly. This is a straightforward action, as the parts are provided as ".step" files which can be escalated in any CAD program, e.g., SolidWorks.

The FE open hole model of the composite substrate was built using individual layers with 3D-8noded brick elements (C3D8). Each layer of the substrate laminate was modelled with two elements in the thickness (z axis as in figure 4.8a). As shown in figure 4.8, the area around the hole has a mesh with a fine element size which is organised in a radial form. Around the open hole, there is an external circumference which acts as a boundary to the fine mesh area. Between the open hole edge and the fine mesh circumference boundary, an element size of 0.125 mm is modelled. As distance increases from the fine mesh boundary circumference, a biased element size is modelled from a size of 0.125 mm to 0.5 mm. The biased meshing area extends along the width of the substrate in the y direction and an equal width distance, half in each side of the hole, in the x direction. Outside the central area of the substrate laminate, a mesh size of 0.5 mm is set. The Additive bindings were meshed with two elements per ply thickness and a seed mesh size of 0.12 mm. Figure 4.9 shows a close detail of the modelled mesh dimensions.

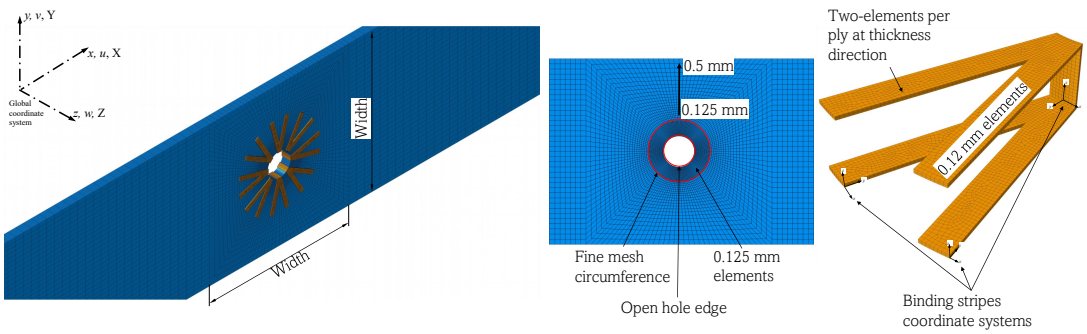

Figure 4.9: FE open hole model mesh details (a) 3D view of the model with binding, (b) front view of the substrate laminate with fine mesh area dimensions and meshed additive binding.

Only one crack was modelled at a time, making the model asymmetrical. This is because, as explained in previous subsections 4.2, the interlaminar cracks on different interfaces are independent of each other, and the lack of delamination in one interface does not change the $\mathcal{G}$ values on the other interfaces. There is the possibility of building a symmetric model from the through-the-thickness mid-plane of the substrate laminate, modelling two cracks by symmetry boundary conditions. This analysis would be only valid for the modelling cases without additive binding, as no symmetry condition can be applied to the additive bindings. Furthermore, analysing a half model with symmetry boundary conditions would give slightly different energy release rate values at the crack tip (although in the same scale and order of magnitude) due to simulation adjustments. As explained in the case of unnotched laminates under tension, when modelling with symmetry, two cracks are being simulated but no significant change in $\mathcal{G}$ is observed as the development of a delamination does not influence the other. Thus, it was decided to perform simulations of the whole substrate laminate for the case without binding, albeit with an increase in computational cost.

The layers adjacent to the pre-crack were constrained together with a surface-to-surface contact interaction with a small sliding formulation and node-to-surface discretisation. Arbitrary high fracture toughness values equal to $9x10^{34}$ N/mm were selected for the crack interface to avoid crack growth simulation. Delamination growth is not aimed to be modelled, as this study focuses on comparing the impact of the additive binding on the energy release rate at different interfaces and crack lengths. All the layers which were not adjacent to the crack were tie-constrained between them with a surface-to-surface enforcement. The internal surfaces of the discontinuous stripe-like additive bindings were tie constrained to the top and bottom surfaces of the substrate laminate. However, the open hole free edges of the substrate laminate plies were not tied to the internal through-the-thickness surface of the "V-shaped" bindings. This is for achieving conservative results, which account for the possibility that the additive binding is not well-bonded to the through-the-thickness open-hole edge.

The load was applied as displacement control. A strain of 1% was used for all simulations and was applied through a "dummy node" to which one end of the substrate laminate was coupled with equation constraints. In this way, the displacements applied to the "dummy node" are applied homogeneously to the coupled-constrained end of the substrate laminate, and no load gradients are generated. The other end of the laminate was fixed with encastre boundary conditions. It is worth mentioning that for tensile simulations, such as the ones performed for free-edge delamination, open-hole and pin load, it is a better practice to apply displacements and forces with equations, rigid body, tie and coupling interactions rather than directly to one only

node, edge or surface of the model. This is due to the fact of possible involuntary deformations of the mesh, which increments the load in one node or edge, experiencing numerical errors or imprecisions. Additionally, defining one ”dummy” or ”extra” node to which displacement and load will be applied simplifies the acquisition of data related to the loading displacements and forces. Hence, postprocessing is easier and faster.

4.5 Modelling additive bindings in the delamination extent of pin-loaded composite laminates

The FE modelling of delamination in pin-loaded composite laminates had similarities to both the edge impact and open-hole simulations. Similar to the edge impact models, the pin load models presumed the presence of delaminations in all the interfaces of the substrate laminate. This is due to convergence speed issues related to the contact interaction between the pin and the substrate laminate hole edge. In similarity with the open hole simulations, the pin load models presented a fine mesh definition around the hole edge, which is similar to the one used in the open hole simulations. The values of energy release rate at the crack tip were calculated for each crack opening mode, and then the $\mathcal{G}_{equiv}$ was calculated as per equation 4.17 and compared for each crack length.

The design of the additive binding is the same as in the case of the laminates with open holes under tension. The additive binding was applied in the form of thin stripes of thin-ply composite prepreg, which was placed around the edge of the hole. Figure 4.10 presents the FE pin-loaded models used for both the cases without and with binding. Similarly, as in the case of the open hole simulations, the simulations performed for the cases without binding were totally automatised for the building, analysis and acquisition of the data of the model. Figure 4.10b shows the additive binding stripes modelled and how their shape was adapted to fit the curvature of the hole. Additionally, the stripes shown in figure 4.10b are a more realistic approximation of the stripes placed in the manufactured specimens[1]. Unlike the binding shown in figure 4.8b, the realistic additive binding is modelled with two parts for achieving the correct curvature of the stripes around the hole edge and better represents the manufactured pin-loaded specimens with binding. The geometry of the bindings modelled made it very challenging to automate the building of the model. Hence, the building, analysing and acquisition of the data were divided into different steps.

The substrate laminates of the simulations with binding were built with the same

[1]It is to be noted that the open hole model was analysed with both types of stripes, the simplified ones (figure 4.8b) and the more realistic ones (figure 4.10b).

Python code as for the cases without binding (figure 4.10a). The additive binding stripes were modelled independently in the CAE environment of Abaqus, saved as "Step files" (.stp or .step files), and then imported to the model with the substrate laminates, which already had all the interactions, boundary conditions and node-sets defined. The additive binding parts were included in the assembly model, and interactions were applied between the additive bindings and the substrate laminate. Following the definition of the interactions, the simulation was set to perform the analysis, and once finished, the results were asked from the ODB file with another Python script. This last Python script is uniquely used for acquiring the data of the simulations of laminates with open holes and additive binding applied. The code is the same that can be found in the postprocessing part of the Python script for the case without binding.

The pin used for loading the model was defined as a discrete rigid shell. A tensile axial displacement which was equivalent to a 1% extension was applied. The displacement was applied through a "dummy node" at the opposite end of the substrate laminate from where the pin is located. For fixing the model, the pin displacements and rotations were set to zero. The final dimensions of the models are explained in section 9.1. The distance of the hole from the nearest edge is defined by the letter "e" and is known as the "hole edge distance", as shown in figure 4.11a.

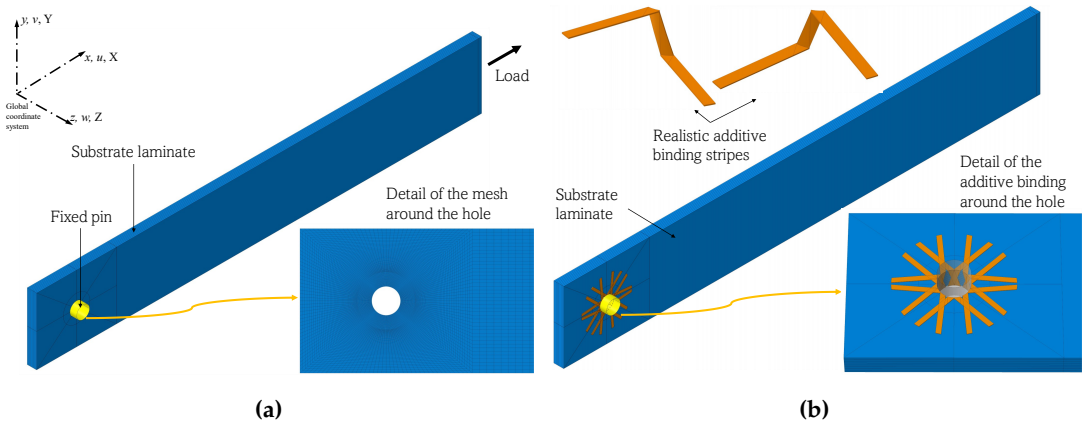

Figure 4.10: FE setup of a $[45_2/0_2/-45_2/90_2]_s$ pin-loaded composite laminate (a) 3D view of the model without binding, (b) 3D view of the model with binding and a detail view of the approximated binding around the open hole.

It is worth mentioning that the additive binding shown in figure 4.10b is a realistic approximation of the actual manufactured additive binding as explained in 5.5. The binding is intended to have a $[\pm\theta]_s$ layup made out of thin stripes. This is achieved in the model by the 3D "Z"-shaped folded UD stripes of the binding, as shown in figure 4.10b. Both positive and negative contributions ($\pm\theta$) of the additive binding are represented with two different additive binding stripe parts. Additionally, it is

worth mentioning that substrate laminates shown in figure 4.10 are longer than the ones simulated for obtaining results. The models simulated were 60 mm long, and additional simulations for few pre-crack lengths were performed to verify that this specimen's modelled length would give the same values of $\mathcal{G}$ as a length of 200 mm. The representation shown in figure 4.10 is done to better understand the model.

The FE pin-loaded model presented is applicable to any layup, independent of its ply thickness, width, ply orientation, etc. As in the case of the open hole simulations, the only constraint is that if the thickness of the substrate laminate or the size of the hole change, the additive binding parts would need to be sized accordingly. This task can be done with any CAD program, e.g., SolidWorks, scaling the "Step" file provided in Appendix A Numerical simulations additional information.

The FE pin-loaded model of the composite substrate was built using individual layers with 3D-8noded brick elements (C3D8). Each layer of the substrate laminate was modelled with two elements per ply thickness (z axis as in figure 4.10a). As shown in figure 4.11, the area around the hole has a mesh with a fine element mesh area. Between the open hole and the fine mesh boundary circumference, an element size of 0.125 mm is modelled. As the distance increases from the fine mesh boundary circumference, a biased element size is modelled from a size of 0.125 mm to 0.75 mm. The biased meshing area extends along the width (y axis) of the substrate and distance of double the hole edge distance (e) from the end of the substrate laminate in the length direction (x axis) of the substrate laminate, as shown in figure 4.11b. Outside the hole area of the substrate laminate, a mesh size of 1.5 mm long per 0.75 mm wide is set. The additive bindings were meshed with two elements per ply thickness. A free meshing technique with an element size of 0.12 mm was applied to the bindings, as it was not possible to use a structured mesh due to its curved shape.

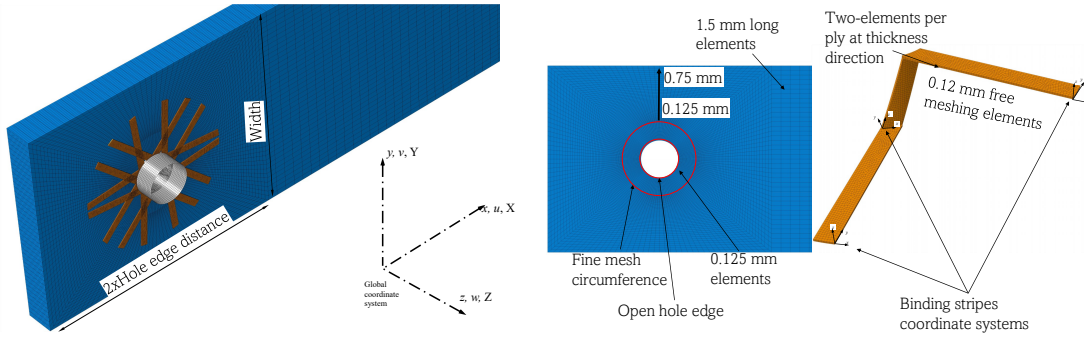

Figure 4.11: FE pin load model mesh details (a) 3D view of the model with binding, (b) front view of the substrate laminate with fine mesh area dimensions and meshed additive binding.

As in the edge impact case, all the layers of the substrate laminate were constrained with a surface-to-surface contact interaction with node-to-surface discretisation and a small sliding formulation. Arbitrary high fracture toughness values equal to $9x10^{34}$ N/mm were selected for the crack interfaces to avoid crack growth simulation. Delamination growth is not aimed to be modelled, as this study aims to compare the impact of the additive binding on the energy release rate for different delamination lengths. The internal surfaces of the additive bindings were tie-constrained to the top and bottom surfaces of the substrate laminate. However, the internal through-the-thickness surfaces of the additive bindings were not constrained to the hole edges of the substrate laminate plies. This was for achieving conservative results, assuming the possibility that the additive binding and the substrate laminate are not correctly bonded at the edge of the through-the-thickness hole edge.

Contrary to the case of the open hole models, the pin load specimens without binding were modelled with symmetry boundary conditions applied, through-the-thickness, at the middle layer of the substrate laminate. In this manner, only half of the model from the middle of the thickness was modelled. This decision was made to make the simulations computationally lighter, as the simulations with the whole model (no symmetry) took more than 6 hours to complete. It was verified that the energy release rate values were not noticeably affected by this decision and were still comparable to the case with binding. The models with binding were modelled whole (without symmetry from the middle layer of the substrate laminate)

4.6 Summary

The simulations carried out in this thesis have the objective of determining the effectiveness of the additive binding on reducing the value of energy release rate at a crack tip of different composite substrate laminates. Also, the numerical models are used to determine the best design for the additive binding. All the simulations are based on the VCCT and hence are maintained simple but robust, reliable and computationally economical.

The four different models created for analysing the effect of the additive binding on the energy release rate at the crack tips of composite laminates in the four different loading scenarios have been presented. Additionally, to these base models, further variations of the models have been used for estimating the effect of single parameters on the energy release rate, e.g., the influence of the through-the-thickness transverse shear modulus on $\mathcal{G}$, as explained in section A.3.

All the models were built with a Python script written for each of the loading scenarios to simulate. These Python scripts plus the ".step" files for the additive bindings,

in the case of the open hole and pin load simulations, are provided in the Appendix A Numerical simulations additional information.

Chapter 5

Specimens manufacture and experimental testing

This chapter explains in detail the manufacturing process of each specimen experimentally tested. All substrate laminates had a similar manufacturing process based on a typical vacuum bag autoclaved setup, and then they were tailored to their particular testing environment. The definition of the testing procedure followed for each loading scenario is also given.

5.1 Materials

The material used for the substrate laminate manufacturing was Hexply IM7/913 prepreg, provided by Hexcel, with a fibre areal weight of 130 g/m^2. This composite system is an intermediate tensile modulus carbon fibre [275], with a versatile epoxy resin which presents great environmental resistance [276]. This material is mostly used in aerospace for primary aircraft structures and helicopter blades. For the binding, thin-ply prepreg manufactured by SK Chemicals with the commercial name of Skyflex USN020 [277] was used. "U", "S", "N", and "020" denote unidirectional (UD) prepreg type, no scrim and the fibre areal weight (FAW) in $[g/m^2]$, respectively. This composite comprises Tairyfil TC33 high strength, standard modulus carbon fibres manufactured by Formosa Plastics [278]. The resin system used is a standard grade epoxy named Skyflex K51 [279], manufactured by SK Chemicals. Both resin systems (Hexcel 913 and Skyflex K51) were cured at 125 °C according to their curing cycle provided by the manufacturers. The material properties for the applied prepregs are shown in table 5.1.

Table 5.1: UD prepreg properties for IM7/913 and TC33/K51.

Ply property	IM7/913	TC33/K51
E_{11} (GPa)	159.87[a]	95.3[c]
$E_{22} = E_{33}$ (GPa)	11.38[b]	6.1[c]
$\nu_{12} = \nu_{13}$	0.32[b]	0.3[c]
ν_{23}	0.45[b]	0.45[c]
$G_{12} = G_{13}$ (GPa)	5.2[b]	2.47[c]
G_{23} (GPa)	3.9[b]	3.9[d]
Strain to failure ϵ_{11^*} (%)	1.6[a]	1.5[c]
v_f (%)	57.4[a]	39[c]

[a] Data by the manufacturer. E_{11} calculated using the rule of mixtures.

[b] Assumed to be equal to that of IM7/913 found in [280].

[c] From [281].

[d] Assumed to be equal to that of IM7/913. See section A.3 of chapter A, for an explanation on the effect of G_{23} on $\mathcal{G}$.

5.2 Manufacture of unnotched tensile specimens and placement of additive binding

The specimens manufactured and tested were parallel-edge end-tabbed tensile specimens.

The manufacture of the substrate laminates was similar to the conventional process for curing standard prepregs. First, 300 mm by 300 mm IM7/913 composite plates were cured in an autoclave at the recommended temperature and pressure cycle for the Hexcel 913 epoxy resin, 60 min at 125 °C and 7 bars. Figure 5.1 shows the prepreg curing cycle diagram for Hexcel 913 epoxy resin, as per manufacturer's indications. After the plates were cured, the specimens were cut from the plates using a water-jet bench tool. Next, end-tabs were bonded to the substrate laminate using a two-component Araldite 2014-2 glue and were let to cure at room temperature for at least 24 hours. The substrate laminate dimensions were 200 mm long with 120 mm free length from end-tabs, 20 mm wide, and an average measured cured ply thickness of 0.13 mm, equal to the nominal thickness reported by the manufacturer.

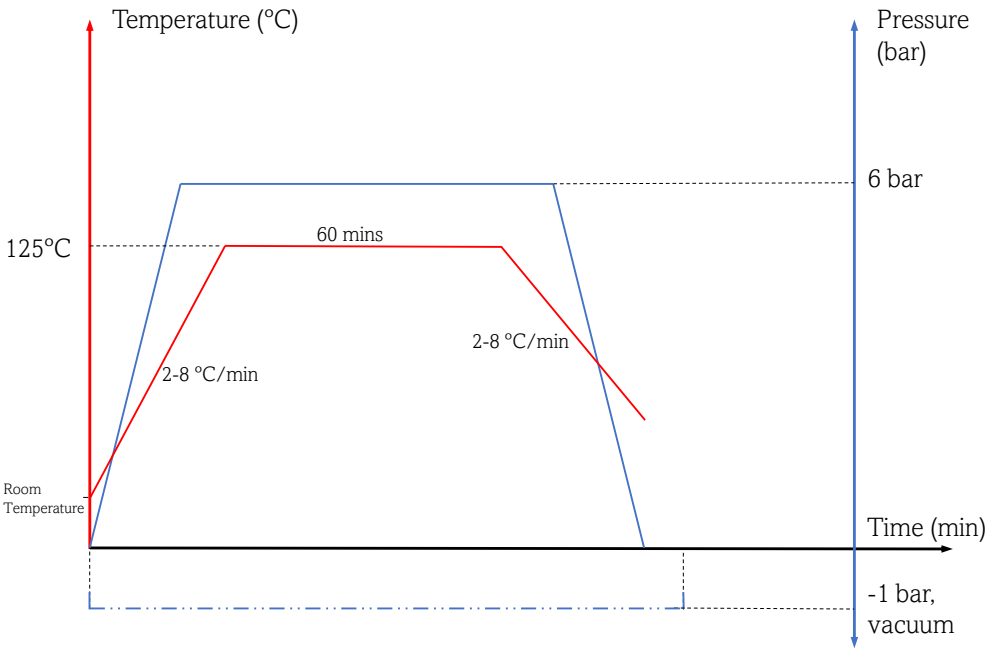

Figure 5.1: Pressure and temperature cycle recommended by the manufacturer for the Hexcel IM7/913 carbon/epoxy prepreg material

After the tensile samples were end-tabbed, additive bindings were applied to the edge of the substrates and then cured following the K51 epoxy resin curing cycle, 30 minutes dwell at 80 °C and 90 minutes at 125 °C with a pressure of 6 bars. Figure 5.2 shows the prepreg diagram cure cycle for Skyflex K51 epoxy resin, as per the manufacturer's indications.

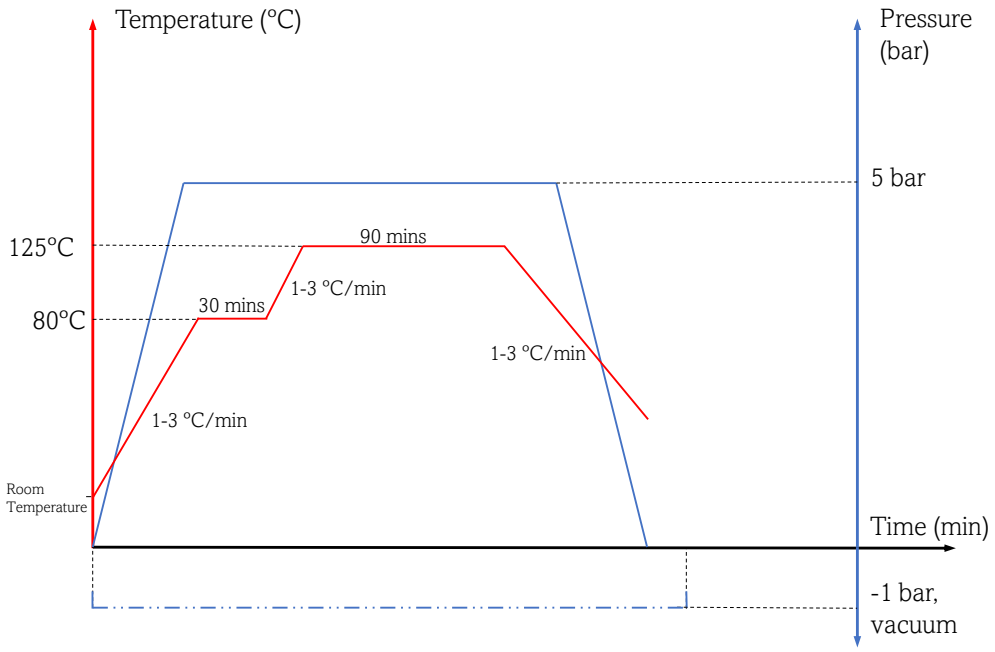

Figure 5.2: Pressure and temperature cycle recommended by the manufacturer for the Skyflex TC33/K51 carbon/epoxy prepreg material

The binding plies were cut from a flat, uncured prepreg roll and stacked up to build a 120 mm long and 12 mm wide laminate. The nominal ply thickness for this material is 0.03 mm [281]. The 12 mm width was selected so that the overlap-length on both top and bottom surfaces is 5 mm, considering approximately 2 mm for the substrate laminate thickness (see 6.1 for layup selected for total substrate laminate thickness).

The manufacture, placement and vacuum bagging of the bindings are schematically shown in figure 5.3 and explained following. Additionally, figure 5.4 shows the experimental arrangement for manufacturing the specimens.

i Additive plies were laid upon a flat plate to build the stacking sequences depending on the applied binding layup (see section 6.2.1 for the layups manufactured and tested).

ii The middle of each binding was placed along the substrate mid-plane at the free edges and then folded carefully over the substrate's top and bottom surfaces, as illustrated in figure 5.3a.

iii A plastic release film was wrapped around the free length of the substrate laminate, as shown in figure 5.3b.

iv Batches of 7 or 8 specimens were placed in a fully sealed vacuum bag. A breather cloth was used between the vacuum bag and the samples to ensure the vacuum applied an evenly distributed pressure to the free length of all substrates. Fig-

ure 5.3c shows schematically the specimens prepared for the second autoclave curing stage.

v The vacuum bag containing the batch of specimens was put in an autoclave and the bindings were cured according to the binding prepreg curing cycle.

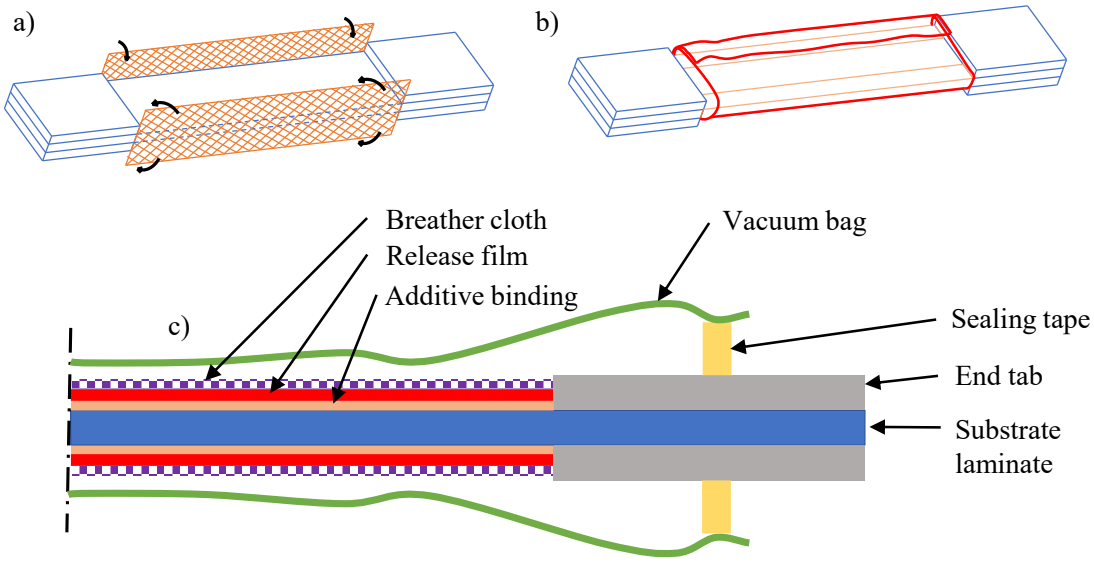

Figure 5.3: Binding manufacture and application to the substrate's laminate free edges, (a) folding the binding laminate over the free edge of the substrate, (b) wrapping the release film around the binding and substrate laminates, (c) the substrate with the binding inside the vacuum bag.

The curing temperature of the substrate laminate and the binding were the same (125 °C). Hence, it is not expected that a second curing cycle on the substrate laminates with bindings would have a significant impact on the samples substrate[1].

As it will be explained in the discussion of the experimental results, section 6.5, the manufacturing method used for samples with binding, indicates that placing the additive binding after end-tabbing the specimens could propitiate stress concentration at the end-tabs. Therefore, alternative manufacturing steps are given in section 6.5 for possibly avoiding these stress concentration points.

Additional information relating to the lessons learned while manufacturing of the coupons is recollected in Appendix B Specimens manufacture and testing additional information

[1]This applies to all cases later explained. Hence, in none of the specimens manufactured for all four different loading scenarios, the second curing cycle is expected to impact significantly the samples

(a) (b)

Figure 5.4: Substrate laminates with the binding inside the vacuum bag. (a) specimens before curing, (b) specimens after curing.

5.3 Manufacture of edge impact specimens and placement of additive binding

The specimens manufactured and tested were rectangular-shaped laminates. The manufacturing procedure for the substrate laminate is similar to the one explained in section 5.2, only varying the dimensions of the laminate. The substrate laminate dimensions were 130 mm long (length) by 60 mm wide (height), and an average measured cured ply thickness of 0.13 mm. After the samples were cut, additive bindings were applied to one of the edges of the substrate laminate, where the impact would occur.

The binding plies were cut from a flat, uncured prepreg roll and stacked up to build a 130 mm long and 13 mm wide laminate. The nominal ply thickness for this material is 0.03 mm [281]. The 13 mm width was selected so that the overlap-length on both top and bottom surfaces is 5 mm, considering approximately 3 mm for the substrate laminate thickness (see 6.1 for layup selected for total substrate laminate thickness).

The manufacture, placement and vacuum bagging of the bindings are schematically shown in figure 5.5 and explained following. Figure 5.6 shows the experimental arrangement and steps for manufacturing the specimens.

i Additive binding plies were laid upon a flat plate to build the stacking sequences depending on the applied binding layup (see section 7.1.1 for the layups manufactured and tested).

ii The middle of the binding was placed along the substrate mid-plane at the free edge and then folded carefully over the substrate's top and bottom surfaces, as illustrated in figure 5.5a.

iii A plastic release film was wrapped around half of the substrate laminate, covering the free edge with the additive binding, as shown in figure 5.5b. The release film was fixed in place with thermal tape.

iv All the specimens were packed together to cure all of them simultaneously. First, the specimens were stacked together, so the free edges, which had the additive binding wrapped in release film, were next to each other. Figure 5.5c shows how the specimens were all stacked together.

v The specimens were placed in a fully sealed vacuum bag. A breather cloth was used between the vacuum bag and the samples to ensure the vacuum was applied evenly over the top and bottom specimens of the stack. The breather cloth was wrapped around the specimen's block but not covering the area where the binding was applied. In this way, the vacuum bag was in direct contact with the release film touching the binding. Figure 5.5d shows schematically the specimens prepared for the second autoclave curing stage. A support part made of aluminium was placed at the bottom edge of the specimens (opposite to the edge with the binding) to create a support for when the vacuum bag would compress the edges with the binding, hence obtaining a flat-ended surface of the binding at the edge. Figure 5.6a shows the experimental equivalent setup depicted in the schematic of figure 5.5d. Figure 5.6d shows some details of the specimens with binding.

vi The vacuum bag containing the batch of specimens was put in an autoclave and the bindings were cured according to the binding prepreg curing cycle.

It is worth mentioning that using an auxiliary or support part inside the vacuum bag, as shown in figure 5.5d, was crucial for obtaining a good finishing of the binding at the edge of the specimen. The support acts as a stopping point for the specimens to not move and not misalign at the additive binding edge, so the vacuum bag applied pressure over all the edges. If the support part was not to be used, some specimens might slide over each other while applying the vacuum, and no proper pressure would be applied over the edge with the binding by the vacuum bag. Thus, a "belly" or gap could potentially appear between the additive binding and the through-the-thickness part of the edge of the substrate laminate.

It is to be noted that the release film applied over the edge of the specimens should be long enough to ensure that the excess flowed K51 resin does not bond the different

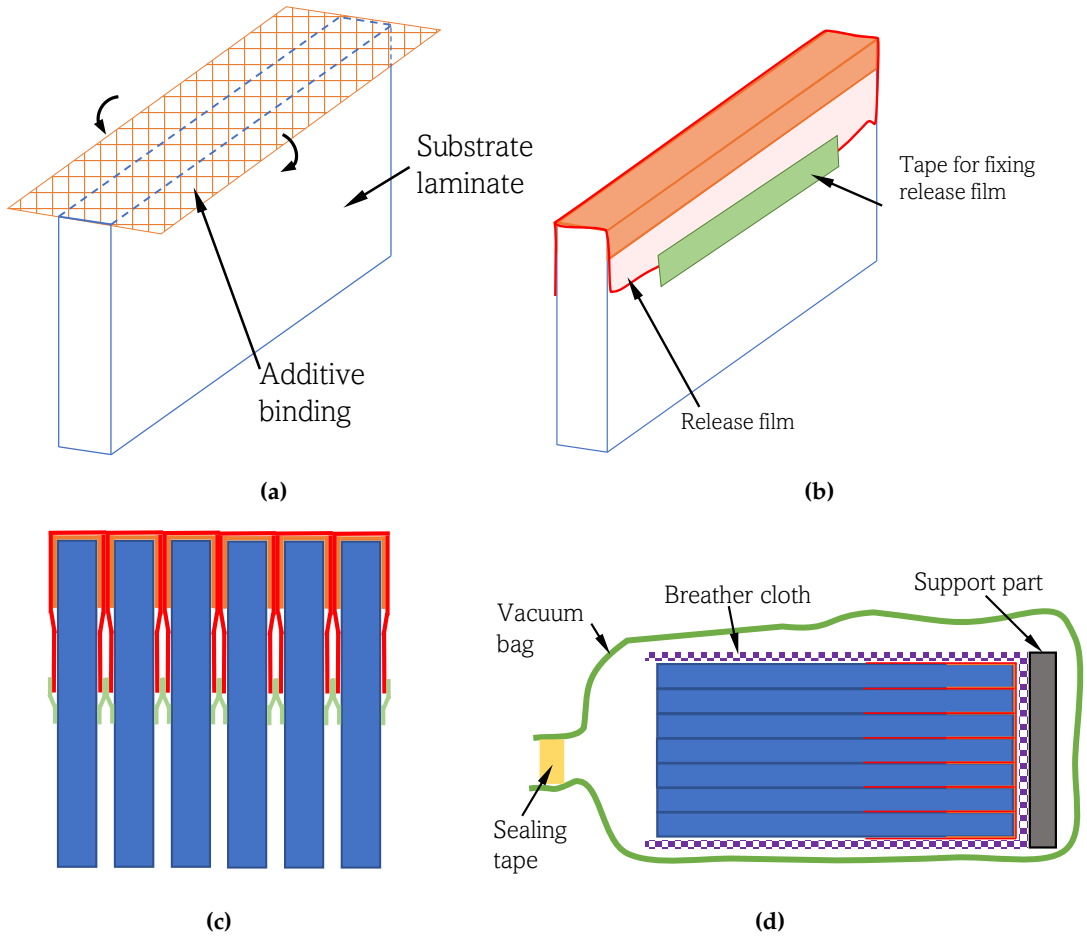

Figure 5.5: Binding manufacture and application to the substrate laminate's free edges, (a) folding the binding laminate over the free edge of the substrate, (b) wrapping the release film around the binding and substrate laminates, (c) stacking of the substrate laminates with the additive bindings in place, (d) the substrate with the binding inside the vacuum bag.

specimens during the second curing. Figure 5.6c shows how the release film at least covers half of the width of the samples and how excess resin ridges under the release film.

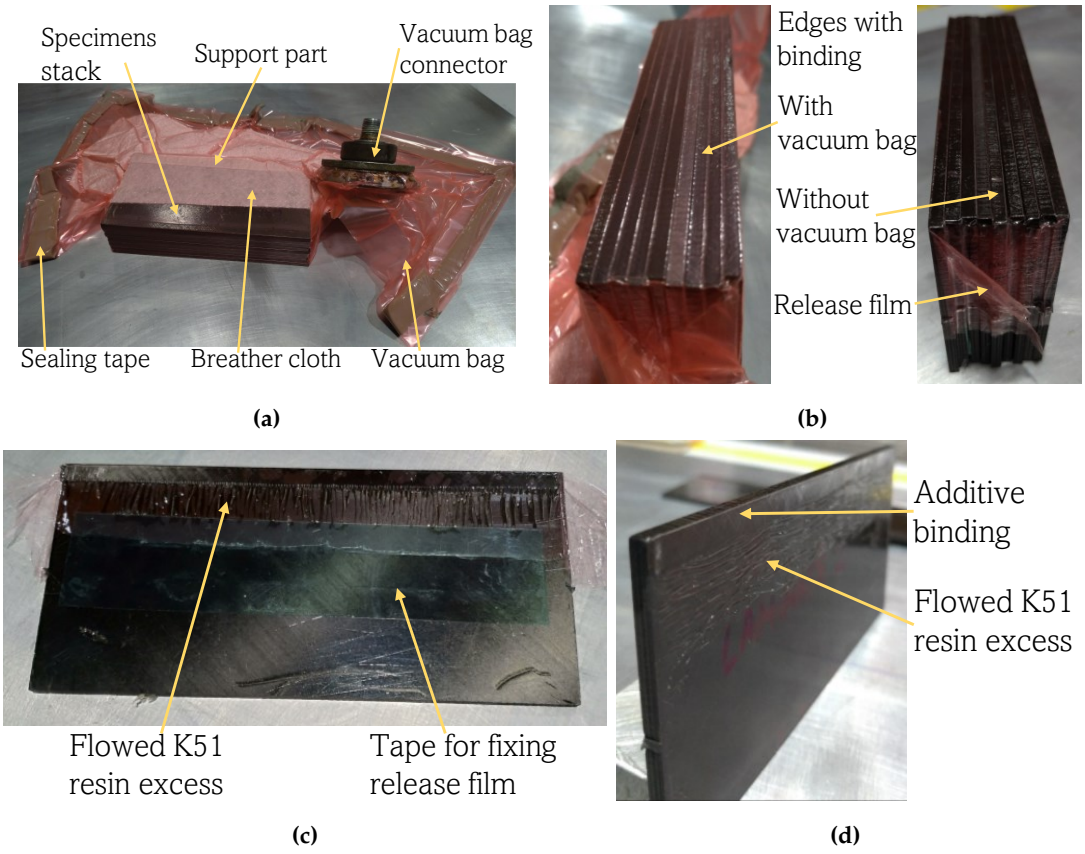

Figure 5.6: Binding manufacture and application to the substrate laminate's free edges, (a) Stack of specimens after curing, just taken out of autoclave. The support part is covered with the breather cloth, (b) finishing of the edge with the additive binding, pictures with and without vacuum bag, both with release film, (c) picture showing the flow of excess K51 resin after the curing.

5.4 Manufacture of open hole specimens and placement of additive binding

The specimens manufactured and tested were parallel-edge end-tabbed tensile specimens with open holes in the centre of the laminate. IM7/913 prepreg was used to manufacture the substrate laminate, and TC33/K51 prepreg was used to confect the additive bindings. The manufacturing procedure for the substrate laminate of the open hole specimens is equal to the one explained in sections 5.2 and 5.3, until the drilling of the hole and placement of the additive bindings.

The substrate laminate dimensions were based on the ASTM D5766/D5766M-11 [215], as shown in figure 5.7. The hole was 6 mm in diameter, so the dimensions of the substrate laminates manufactured were 200 mm long with 120 mm free length from end-tabs, 30 mm wide, and an average measured cured ply thickness of 0.13 mm. Also, additional specimens with the same geometry previously given but dif-

ferent hole diameters were manufactured and tested, as will be explained in 8.3.

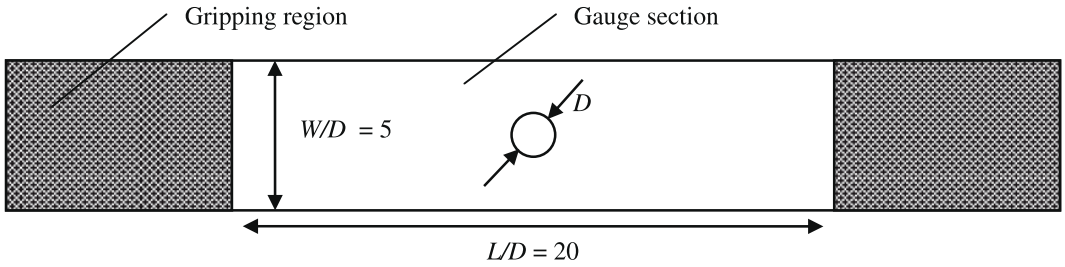

Figure 5.7: Open hole specimen geometry. - Reproduced from [216].

Once the tensile samples were cut into 200 mm x 30 mm specimens, the hole was drilled. For drilling the holes, a sacrificial part was used on the bottom surface of the substrate laminate. The sample was compressed over the sacrificial wooden part, so pressure was applied over the bottom surface. In this way, the delamination originating from the exit of the drill bit was reduced. In addition, two different drill diameters were used to reduce the delamination that originated from the entry of the drill. One drill bit of 3 mm was used for the first drilling, and a drill bit with the final desired diameter was used for the second drilling. Figure 5.8 schematically shows how the holes were drilled.

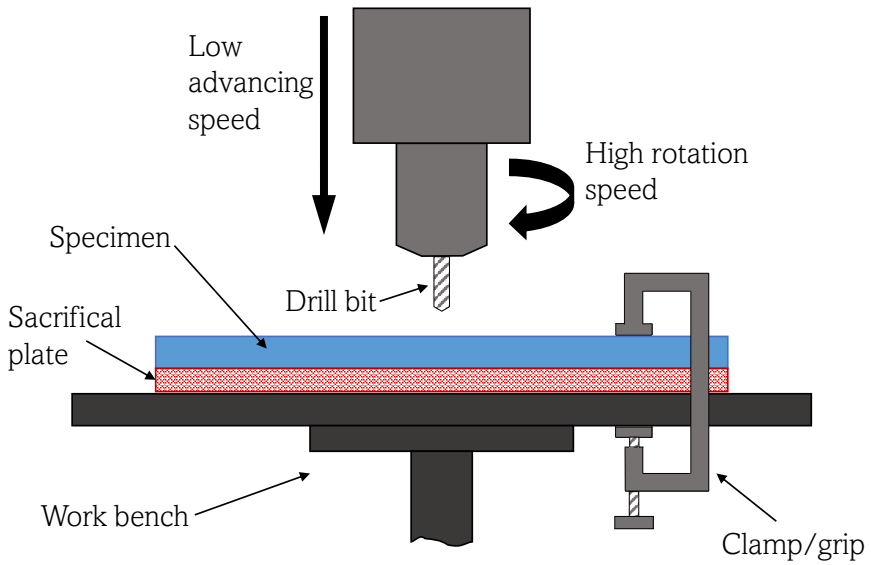

Figure 5.8: Schematic of the setup for drilling the holes in the substrate laminate.

After the samples were drilled, they were end-tabbed using a two-component Araldite 2014-2 glue and were let to cure at room temperature for at least 24 hours. Then, additive bindings were applied to the edge of the open hole in the form of thin stripes. The specimens were then cured following the K51 epoxy resin curing cycle, 30 minutes dwell at 80°C and 90 minutes at 125°C with a pressure of 6 bars, as displayed in

figure 5.2.

The binding plies were cut from a flat, uncured prepreg roll and stacked up with a $[0]_4$ layup from which cutting the thin additive binding stripes. In this way, the stripes are made of very narrow unidirectional laminates, which are bent over the edge of the hole of the substrate laminate. The binding stripes' dimensions were approximately 60 mm long by 2 mm wide, and a cured ply thickness of 0.03 mm. The manufacture, placement and vacuum bagging of the bindings are schematically shown in figure 5.9 and explained following. It is to be noted that the dimensions of the drawings are schematic and that the proportions have been exaggerated for a clearer demonstration of the drawing. Additionally, figure 5.10 shows the experimental arrangement for manufacturing the specimens. Manufacturing the open-hole specimens was very challenging, and as advice for trying to replicate the work, it would have been recommended that the diameter of the hole would be bigger for ease of manufacturing.

i Additive binding plies were laid upon a flat plate in a $[0]_4$ layup and cut into narrow stripes. These stripes were threaded through the hole of the substrate laminate and folded over the top and bottom surfaces of the substrate laminate. Figure 5.9a shows a schematic of one stripe being folded over the top surface of the substrate laminate after the bottom flap had already been laid down.

ii Once all the binding stripes had been threaded in place, a thermal silicon button was introduced in the hole for generating pressure over the additive binding. In this way, the binding would bond better with the through-the-thickness part of the hole edge. The silicon buttons were punched out of a thermal silicon sheet and submerged in a release agent, so they did not get bonded to the additive bindings. Figure 5.9b shows a schematic of a silicon button being pushed through the hole and a cut view of the substrate laminate with the silicon button in place.

iii The specimens are then wrapped around the centre with a release film and placed over an aluminium support part. The bottom support part, as indicated in figure 5.9c is needed, so the free length between end-tabs is not unsupported. A second top aluminium support part is then placed over the specimens for applying pressure over the additive binding, which lays on the top part of the specimens.

iv The specimens are then covered with a breather clot for applying homogeneous pressure, and the vacuum bag is put in place and sealed with sealing tape (tacky tape). Figure 5.9c shows a schematic of the profile of the specimens prior to being introduced in the autoclave.

v The vacuum bag containing the batch of specimens was put in an autoclave and the bindings were cured according to the binding prepreg curing cycle.

It is worth mentioning that if the bottom support part is not put in place, the free length between end-tabs would be unsupported. For this reason, when the specimens were inside the autoclave, the pressure and the vacuum would provoke a bending of the free length, obtaining a final curved specimen after the second curing. In this way, the bottom part shall be taken so its thickness plus the additive binding and release film thickness are equal to the thickness of the end-tab, as shown in figure 5.9.

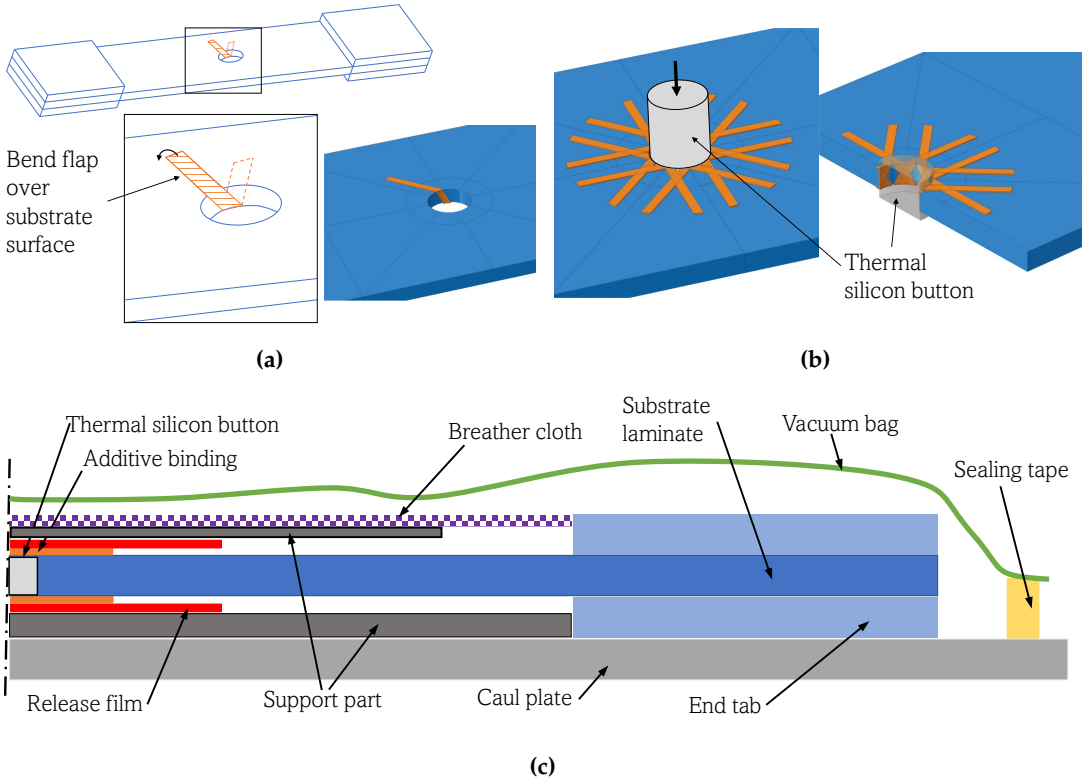

Figure 5.9: Binding manufacture and application to the substrate laminate's hole edge, (a) Additive binding stripe being threaded and folded. (b) A thermal silicon button is pushed through the hole to apply pressure on the additive binding at the interior of the hole. (c) Profile of a specimen before introducing it in the autoclave, it is to be noted the need for support parts to apply pressure over the bottom and top surfaces of the free length between end-tabs of the substrate laminate.

It is important to note that the placement of the binding around the edge of the open hole slightly reduces the total diameter of the hole. The possible effects of that slight reduction in the experimental results are explained in chapter 8.

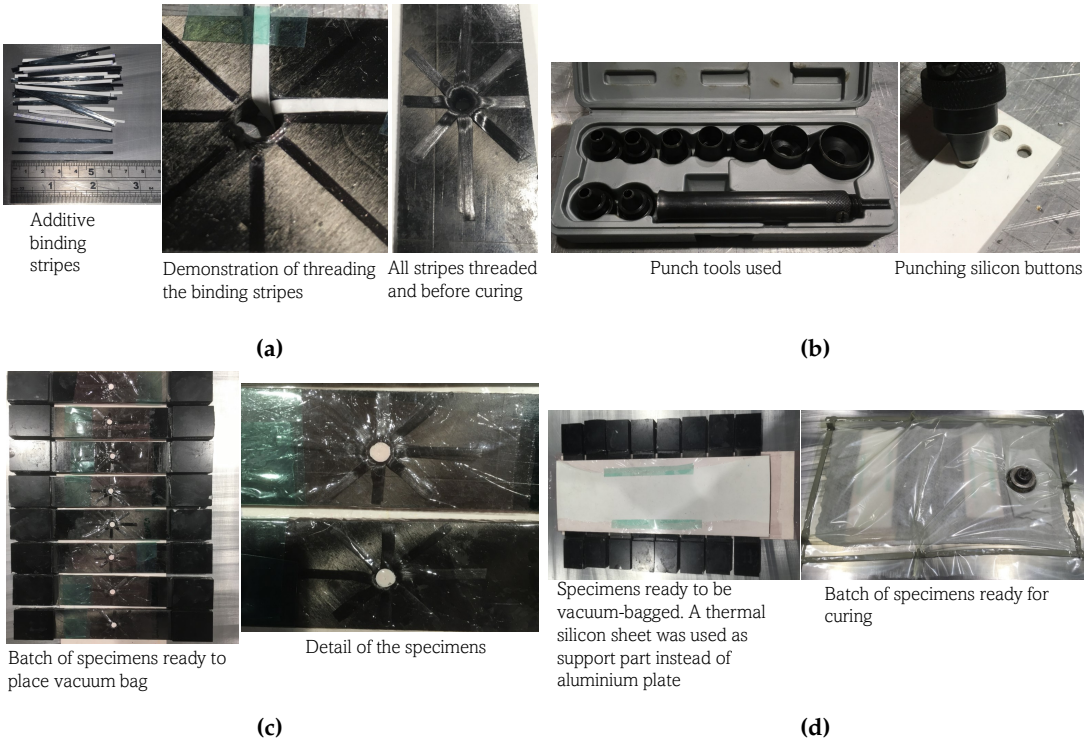

Figure 5.10: Binding manufacture and application to the substrate laminate's hole edge, (a) Additive binding stripes being threaded and folded. (b) Thermal silicon button punching. (c) A batch of specimens with the silicon buttons in the hole wrapped in release film and placed over the caul plate. (d) Specimens are ready to be introduced in the autoclave for curing.

5.5 Manufacture of pin load specimens and placement of additive binding

The manufacture of pin load specimens was carried out at the same time as the open hole specimens due to the similarity of the process. The specimens manufactured and tested were parallel-edge specimens, end-tabbed only in one of their ends and with a hole on the other. The manufacturing procedure of the substrate laminate of the pin load specimens is equal to the one explained in sections 5.2 and 5.3, until the drilling of the hole and the placement of the additive binding, which was similar to the procedure explained in section 5.4.

The substrate laminate dimensions were based on the ASTM D 5961/D 5961M–01 [244] double-shear specimen, as shown in figure 5.11. The hole diameter was 6 mm, and the dimensions of the substrate laminates manufactured were 200 mm long with 160 mm free length from the end-tab to the extreme, 30 mm wide, and an average measured cured ply thickness of 0.13 mm. The distance from the specimen's end to the centre of the hole was 18 mm. Additionally, as will be explained in 9.3, additional

specimens with the same geometry previously given but different hole diameters were manufactured and tested.

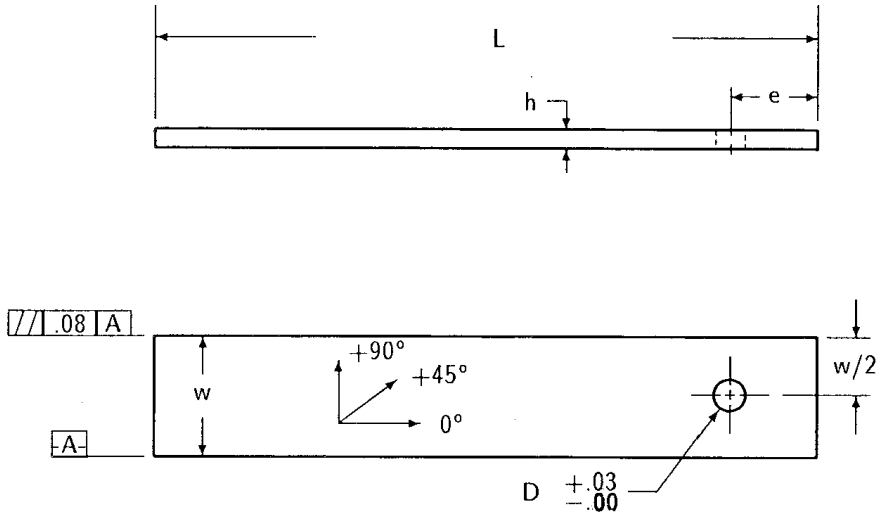

Figure 5.11: Double-shear specimen geometrical definition. - Reproduced from [244]

After the double-shear specimens were cut into 200 mm x 30 mm samples, the hole was drilled. The procedure for drilling the hole was equal to the one for the open hole specimens, as explained in section 5.4 and schematically shown in figure 5.8. After the holes were drilled, the specimens were end-tabbed using a two-component Araldite 2014-2 glue and were let to cure at room temperature for at least 24 hours. Afterwards, additive bindings were applied to the edge of the open hole in the form of stripes, as shown in figure 5.9a. The specimens were then cured following the K51 epoxy resin curing cycle, 30 minutes dwell at 80°C and 90 minutes at 125°C with a pressure of 6 bars, as shown in figure 5.2.

The narrow binding plies stripes were cut from a flat, uncured prepreg roll and stacked with a $[0]_4$ layup. This means that the additive binding stripes are very narrow unidirectional laminates which are bent over the edge of the hole of the substrate laminate. The additive binding stripes' dimensions were approximately 60 mm long by 2 mm wide, and a cured ply thickness of 0.03 mm. The manufacture, placement, and vacuum bagging of the pin load specimens were the same as the one described for the open-hole specimens. Figure 5.9 showing the schematics for the manufacture of open hole specimens with additive binding is valid for the manufacture of the pin load specimens with binding. It is to be noted that the dimensions of the drawings are schematic, and the geometrical proportions have been exaggerated for a better understanding of the drawing. Figure 5.12 shows the pin load specimens with additive binding before being placed in the autoclave for curing.

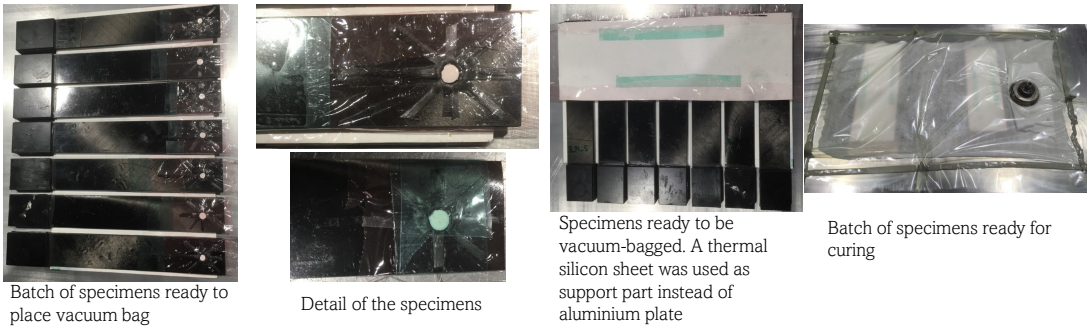

Batch of specimens ready to place vacuum bag

Detail of the specimens

Specimens ready to be vacuum-bagged. A thermal silicon sheet was used as support part instead of aluminium plate

Batch of specimens ready for curing

(a) **(b)**

Figure 5.12: Pin load specimens with binding ready to be cured in the autoclave. (a) Additive binding stripes had been threaded in the hole of the pin load specimens, silicon buttons were in place inside the hole, and the substrate laminates were wrapped in release film. (b) Specimens are ready to be introduced in the autoclave for curing.

5.6 Quasi-static tensile testing

5.6.1 Tensile test of unnotched laminates

The testing of the tensile specimens for the first research question was conducted based on the ASTM D3039/D3039M testing standard [282]. The mechanical testing was conducted under quasi-static displacement-control tensile loading at a 1 mm per minute (mm/min) rate. A computer-controlled Instron Electromechanical 5969 50 kN universal testing machine with mechanical wedge grips was used to apply the load. Figure 5.13 shows the Instron Electromechanical 5969 test machine. The axial extension of the specimens was measured by means of an Instron 2663-821 video extensometer system. Guide points were marked on the surface of the specimens for the video extensometer to follow. Only axial extension was measured.

At least five repetition samples per layup configuration were tested until failure to ensure the reproducibility and repeatability of the results.

Measurements of force, displacement and axial extension were recorded for later data processing.

Figure 5.13: Instron 5969 machine and Instron 2663-821 video extensometer system used for tensile experiments of the free-edge delamination specimens. - Reproduced from [283]

5.6.2 Tensile test of laminates with open holes

The testing of the tensile specimens for the third research question was conducted based on the ASTM D7615/D7615M testing standard [215]. The mechanical testing was performed under quasi-static displacement-control tensile loading at a 1 mm per minute (mm/min) rate. A computer-controlled Instron Servo-hydraulic 8801 $\pm$100 kN universal testing machine with hydraulic wedge grips was used to apply the load. Figure 5.14 shows the Instron Servo-hydraulic 8801 test machine. As will be explained in chapter 8, the open-hole specimens tested were thicker than the free-edge delamination specimens, so the failure load was higher than 50 kN, and a tester with a higher load range was needed.

The axial extension was measured with the axial cross-head displacement of the grips. The possible uncertainties from the machine in the measurement that could be in place for using the axial displacement of the grips for calculating the cross-head displacement are present in both sets of experiments, without and with binding, and hence the results are comparable. Figure 5.15 shows a specimen with open hole under tensile loading in the Instron Servo-hydraulic 8801, and free-edge delamination is appreciable.

At least five repetition samples per layup configuration were tested until failure to ensure the reproducibility and repeatability of the results.

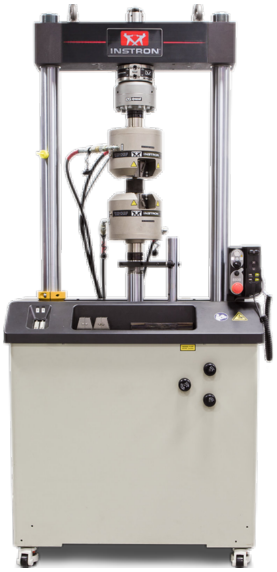

Figure 5.14: Instron 8801 machine used for tensile and fatigue tension-tension experiments of open hole and pin-loaded specimens. - Reproduced from [284]

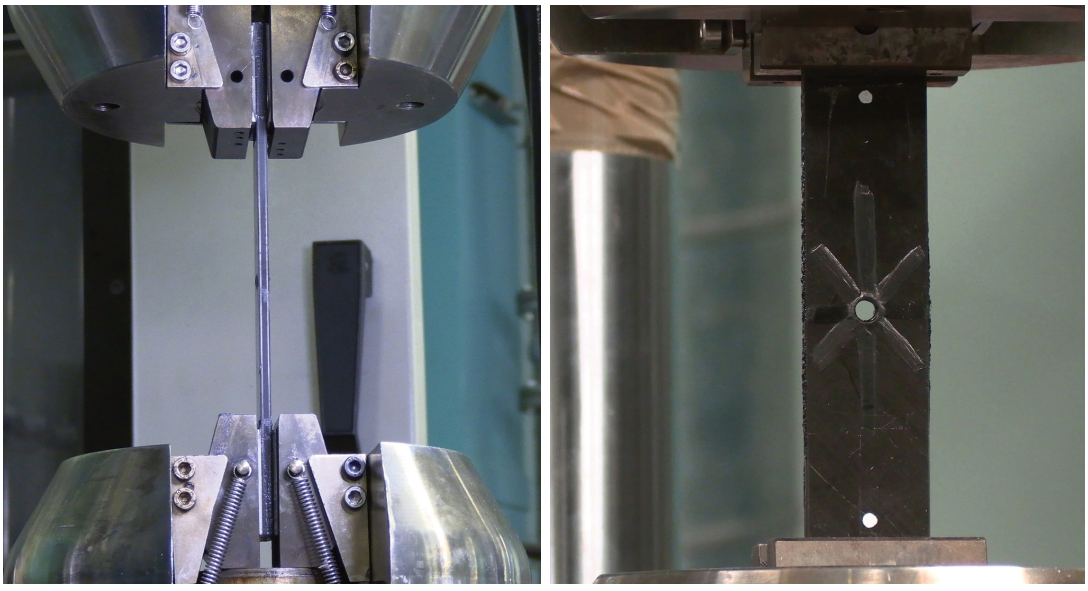

(a) **(b)**

Figure 5.15: Open hole specimen under tension in an Instron Servo-hydraulic 8801 tester. a) Side view, b) front/top view.

5.7 Edge impact testing

The aim of an experimental impact machine is to produce representative damage of what actually originates during the service life of the composite parts. Experimental impact tests were conducted at a low speed with the help of a drop-weight impact machine. As of the moment of writing this thesis, and as per the author's knowledge, no particular experimental setup and standard exist for composite edge-on impacts, and hence a tailored setup similar to the one used in [166] was built.

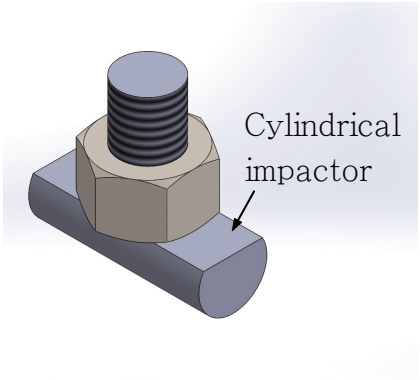

Figure 5.16: Cylindrical-shaped impactor manufactured for the testing.

Mechanical testing of the specimens was carried out in a Rosand Instrumented Falling Weight Impact Tester type 5. The tests were carried out with an in-house manufactured cylindrical-shaped tup, striker, or impactor. Better repeatability of the damage morphology could be achieved using a cylindrical impactor shape than when using a hemispherical tup [142]. Figure 5.16 shows the schematic of the cylindrical impactor which was used for testing[1]. All tests were performed with the same cylindrical-shaped impactor. The impactor used was 5.76 kg of weight and had a diameter of 12 mm and 30 mm in length. In this manner, the impactor clearly impacted at the edge of the specimen, albeit with small misalignments that could have been in place between the vertical movement of the impactor line and the height of the specimen. Figure 5.17 shows the free drop weight tester used.

Results of force, time and displacement were extracted from the experiments for later processing. First, the striking mass was moved up and down to achieve the desired impact energy. Next, the force was taken from the load cell. An optical light gate was used for measuring the velocity of the impactor just before the impact. The optical light gate needed to be calibrated prior to the development of the experiments. Then, the displacement was automatically calculated via energy conservation equations. The specimens were clamped in a specifically designed edge impact rig, as shown

[1]Further drawings and details of the cylindrical impactor are presented in Appendix B Specimens manufacture and testing additional information

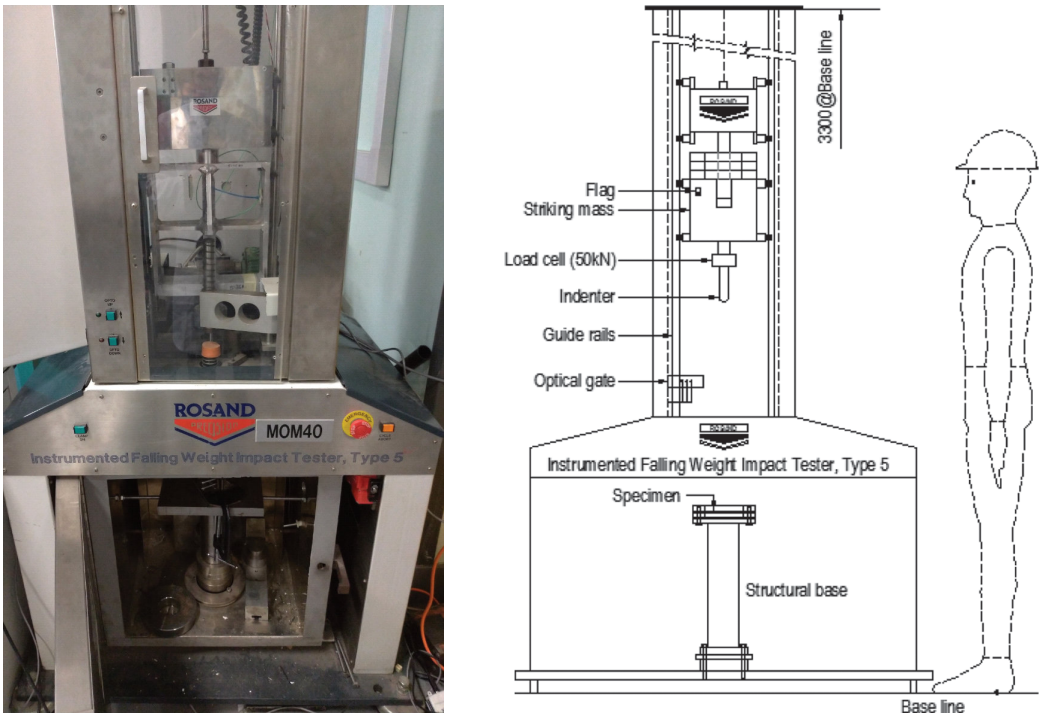

(a) **(b)**

Figure 5.17: Fully instrumented Rosand IFW5 falling weight machine - Reproduced from [285].

in figure 5.18. The rig dimensions were particularised for the specimens tested, so half of the specimen's width was locked, and the other half was free, as shown in figure 5.18b. The edge impact rig was composed of a steel support and a shim for holding the specimen constrained under uniform pressure. As explained in [166], this rig type does not allow for out-of-plane bending, which is generally observed in a wing-box stiffener. However, the out-of-plane bending restriction happens for both specimens without and with binding, and hence the results obtained are comparable. Figure 5.19 shows an edge impact specimen prior to and after impact with the cylindrical impactor. It is visible that despite the slight misalignment of the impactor vertical falling line with the edge of the specimen, the tup impacted correctly and did not miss the edge of the specimen.

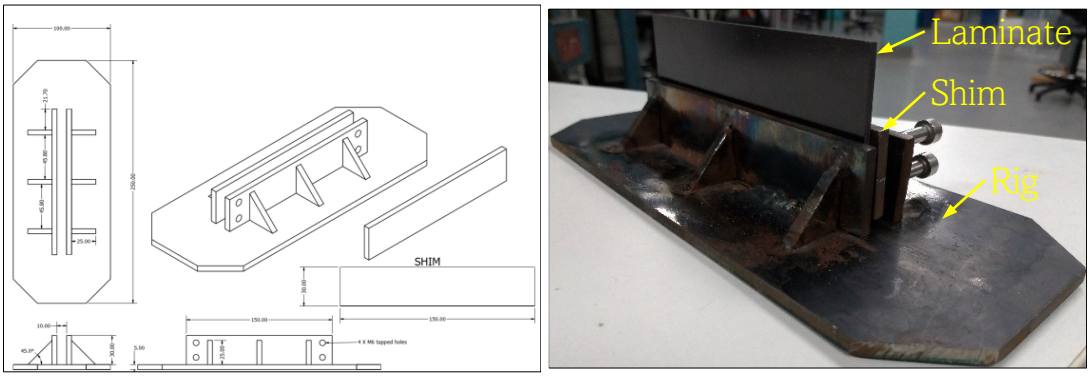

(a) (b)

Figure 5.18: Edge impact test rig manufactured for conducting the experimental testing. (a) rig drawings with measurements reproduced from [286]. (b) Edge impact specimen in the testing rig.

(a) (b)

Figure 5.19: Edge impact specimen in the testing rig and inside the impact chamber. (a) prior to impact, and (b) impacted.

5.8 Quasi-static bearing test of pin-loaded composite laminates

The pin-load specimens manufactured were tested according to the ASTM D5961/D5961M-01 standard [244]. Mechanical testing of the pin load specimens was performed under quasi-static displacement-controlled tensile loading at a 1 mm per minute (mm/min) rate. The same computer-controlled Instron Servo-hydraulic 8801 testing machine used for the open-hole specimens was used for the pin load specimens. Hydraulic wedge grips were used to fix the specimens and apply the load. Figure 5.14 shows the Instron Servo-hydraulic 8801 test machine.

The axial extension was measured with the axial cross-head displacement of the

grips, as in the open hole specimens case. The load was applied as shown in figure 5.20. One of the tensile tester grips was closed around a steel rig manufactured for the pin load tests carried out. The rig was connected to the specimens through a pin which, being doubly supported, threaded the specimen. This way, the pin would pull from the hole of the specimen.

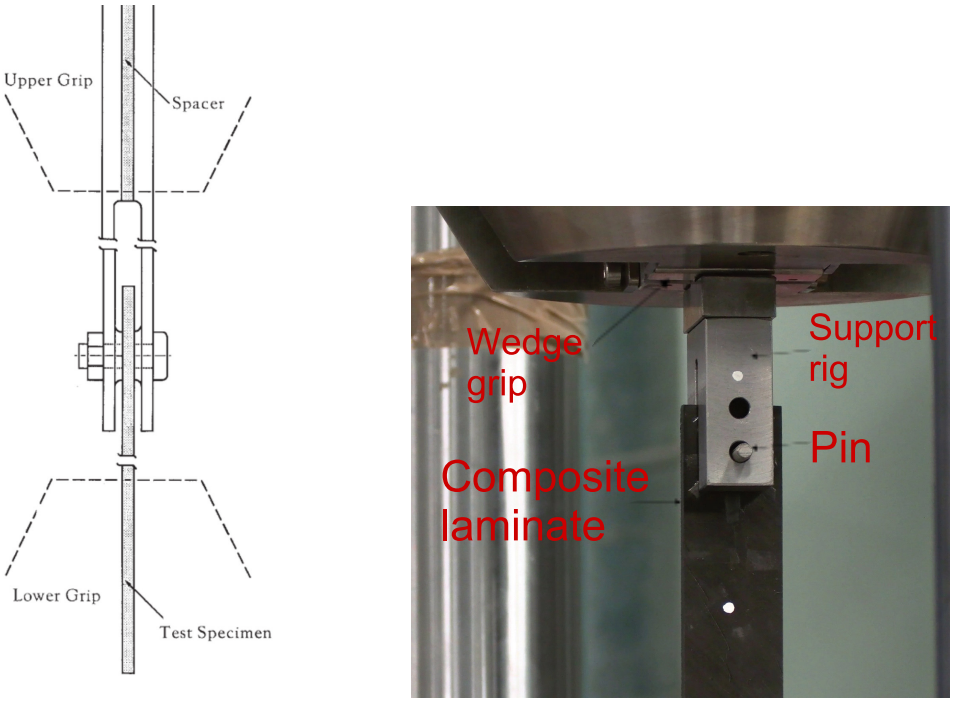

Figure 5.20: Pin load test setup. (a) schematic of the test with the rig for holding the pin and the specimen. (b) Image of the rig, pin and laminate assembly in a test.

5.9 Fatigue testing

5.9.1 Fatigue test of laminates with open holes

Fatigue tension-tension (T-T) testing was carried out for tensile specimens with open-hole. The testing was conducted under the guidance of the ASTMD7615 standard [287]. The procedure is modified from the previously quasi-static tensile test to include repetitive constant amplitude force cycles at a specified frequency. Although all efforts were made to keep the test as standard as possible, deviations from the standard occurred. These deviations are reported in section 8.3.

Fatigue tests of composite laminates with open holes report the stiffness and strength reduction of the specimen for a determined number of cycles (load and unload) and loading rate. The change in stiffness due to fatigue damage could be obtained cyclicly

for all the loading and unloading cycles. Additionally, the new stiffness could be obtained by interrupting the cyclic loading after a certain number of fatigue cycles, N, and performing a quasi-static tensile test using the static test method [215]. However, caution must be observed when using this latter method for measuring the strength, as a higher loading force than the one being used for the fatigue test could trigger the failure of the laminate.

The results of the fatigue tests are susceptible to the loading ratio (R-ratio) and the value of the maximum force to which the specimens are loaded. The R-ratio or loading ratio is the relation between the minimum and maximum load applied in the loading cycle. The tests were run with a 65% severity, this meaning that the maximum force used for the fatigue testing was 65% of the failure load of the quasi-static specimens without binding. All the open-hole fatigue testings were conducted in the same Instron 8801 tensile tester as the quasi-static specimens. In this way, the axial extension was measured with the axial cross-head displacement of the grips. Each test was run in load control using a constant amplitude and an R-ratio of 0.1, meaning that if the maximum force was 40 kN, the minimum force would be 4 kN. The testing frequency was set to 5 repetitions per second (5 Hz), as per standard practice [287, 288] for not incurring in a risk of increasing the temperature of the sample. Each test was left to run to 10^5 cycles unless failure, defined as a 15% loss of stiffness, occurred before reaching that limit. 10^5 number of cycles is commonly used in the aerospace industry and is appropriate for the number of load cycles experienced during the useful life of an aircraft [288].

5.9.2 Fatigue bearing test of pin-loaded composite laminates

Fatigue tension-tension (T-T) testing was carried out for pin load specimens. The testing was carried out under the indications of the ASM D6873-03 standard [289]. This procedure is modified from the previously described static bearing test method [244] to include repetitive constant amplitude force (stress) cycles at a specified frequency. The results obtained from a fatigue bearing test are the elongation of the hole and the loss of bearing strength. The elongation of the hole can be measured with the change in displacement amplitude of the grips of the tester. The loss of bearing strength due to fatigue damage could be obtained from each loading cycle for all the loading and unloading cycles. Additionally, the bearing strength can be obtained by discontinuing the cyclic loading after a certain number of fatigue cycles, N, and performing a static bearing test using the static test method [244], similar as in the fatigue tests of laminates with open holes.

The selection of R-ratio affects the bearing fatigue response of the mechanically fastened composite joints. Each test was run under load control using a constant am-

plitude and an R-ratio of 0.1, as in the open-hole fatigue tests. However, it is worth mentioning that the most critical force ratio in pin-loaded composites, is the reversed load ratio (R = -1) because specimens that are loaded under reversed load ratio exhibit bearing damage on both sides of the bolt-hole [290]. The test procedure does not specify other factors that influence the fatigue response, such as fastener selection, fastener preload/torque, fastener bolt-hole clearance, and environmental conditions. Specimen geometry, support fixtures and test configuration are similar to those used for the quasi-static specimens. As it will be explained in chapter 9, different pin sizes and materials were used for the fatigue testing of the specimens.

All fatigue bearing tests were conducted in the same Instron 8801 tensile tester as the quasi-static bearing tests, and same methods as for the fatigue tests of laminates with open holes were used.

5.10 Summary

The manufacture and testing of the specimens experimentally analysed in this thesis have been presented. Although the manufacturing of the different samples kept similarities between them, the time and effort of the manufacture was considerably different. The edge impact specimens were the fastest to make, and the pin-load ones were the slowest, as the threading of the thin discontinuous stripes through the holes of the specimens was laborious and time consuming to ensure repeatability on the testing. quite difficult.

Chapter 6

Results on suppressing delamination in composite laminates under tension

This chapter presents the numerical and experimental results for the first research question. A great number of simulations have been performed to choose the adequate additive binding layup. Then, experimental testing as described in section 5.6 was carried out to study the effectiveness of the solution. The use of additive bindings for suppressing delamination in composite laminates under tension is exposed, discussed, and finally, conclusions are drawn.

6.1 Substrate laminate selection

A layup susceptible to free-edge delamination, when subjected to axial loading, was sought to study the effectiveness of the additive binding solution. The substrate laminate was chosen to be balanced and symmetric to avoid coupling effects. Different stacking sequences of $[\pm\theta]_s$, with θ between 0 to 90 degrees were studied. Equation 6.1 presented in Appendix I of O'Brien's paper [83] was used to find the energy release rate at the free edges for different laminates. As explained in section 2.2.1, it is worth mentioning that O'Brien provides another version of this equation (equation 2.2) in the same paper, with 2 in the denominator instead of 4 and justifies that for laminates with matrix cracking in central 90-degree layers and a zig-zag shape of the delamination. As there is no 90° layer in the assumed $[\pm\theta]_s$ laminates to link the delaminations at different interfaces equation 6.1 is deemed to be more accurate, and as will be shown in section 6.2 and explained in section 6.5.1, this version of the equation gives relatively close results to the Finite Element (FE) predictions.

$$\mathcal{G} = \frac{\epsilon^2 t}{4}(E_{lam} - E^*) \tag{6.1}$$

Where $\mathcal{G}$ is the strain energy release rate, ϵ is the nominal applied strain, t is the total thickness of the laminate, E_{lam} is the axial stiffness of the laminate, and E^* is the axial stiffness of the laminate completely delaminated along one or more interfaces. Figure 6.1 displays the variation of the energy release rate for the $[\pm\theta]_s$ layups versus θ using equation 6.1. The material properties used for the laminate are those presented in table 5.1 for IM7/913 carbon/epoxy composite. The nominal ply thickness used was 0.13 mm, and the applied strain was $\epsilon = 1\%$.

As per the values of mechanical properties used, the value of $\mathcal{G}$ is maximum for values of θ around 16°. For this thesis, θ was selected to be equal to 20°. This angle-ply layup still gives a high $\mathcal{G}$ value, and its susceptibility to free-edge delamination has been studied and reported by Xu and Wisnom in [291]. Additionally, we know that the energy release rate is proportional to the ply block thickness. Therefore, the stacking sequence $[(20_2/-20_2)_2]_s$ was selected as a substrate laminate susceptible to free-edge delamination. A quasi-isotropic laminate with the stacking sequence of $[45_2/0_2/-45_2/90_2]_s$ was also selected to study the effect of the additive binding on laminates not so sensitive to free-edge delamination. This layup is similar to the one studied by O'Brien in [292], so it is expected to indicate matrix cracking in the off-axis layers followed by local free edge delamination before the final failure due to failure of the 0° layers.

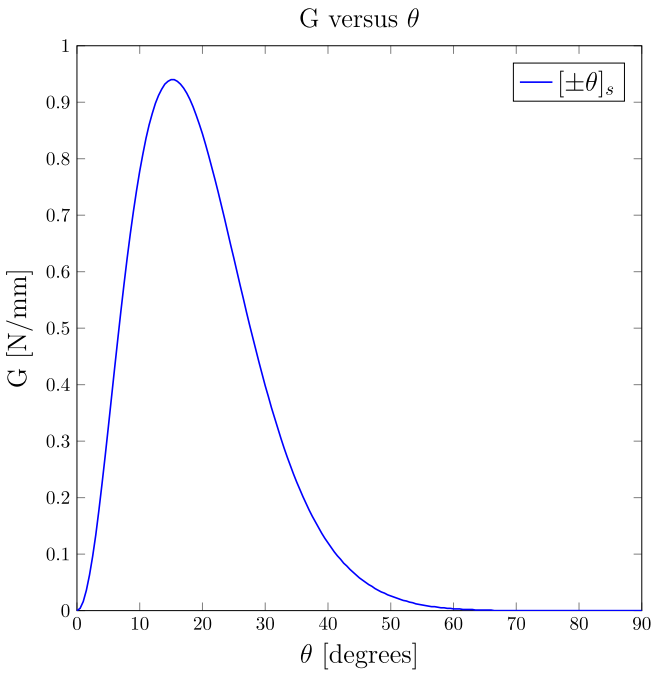

Figure 6.1: Variation of energy release rate $\mathcal{G}$ for free edge delamination in $[\pm\theta]_s$ angle-ply layups versus θ using equation 6.1

6.2 FE results

Different crack lengths at three interfaces between layer blocks with different fibre orientations were modelled due to the symmetry of the laminates. Figure 6.2 shows the total energy release rate ($\mathcal{G}$) variation for different pre-crack lengths for the AP and QI laminates obtained from the slice FE model. For the AP laminate, the critical interface is interface 1, as defined in figure 6.2. In the QI laminate case, the critical interface is interface 3. Therefore, these interfaces are most likely to delaminate at the free edges.

Figure 6.2 also shows the $\mathcal{G}$ values calculated using equation 6.1 for the critical interfaces. The material properties used are those in table 5.1. E^* were calculated assuming AP laminates totally delaminate at interfaces 1 and its symmetric equivalent. Similarly, QI laminates were assumed to be totally delaminated at interface three and its symmetric equivalent when calculating E^* (see figure 6.2 for interface numbers reference). Equation 6.1, proposed by O'Brien, seems to have a relatively acceptable agreement with the asymptote of the FE results, given its simplicity and ease of application.

As shown in figure 6.2, the longest crack length simulated is 5.5 mm, which is a relatively big crack size for a total laminate width of 20 mm. As the crack length increases, the stiffness of the substrate and, consequently, the $\mathcal{G}$ value can reduce (see

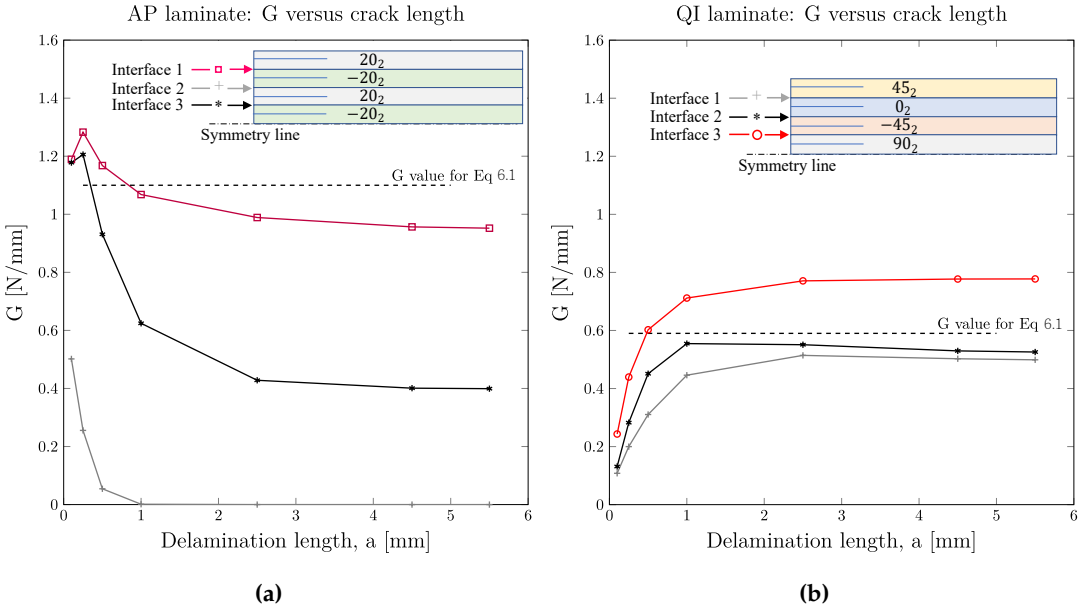

Figure 6.2: Energy release rate for interlaminar cracks at different crack lengths and interfaces for an applied strain of 1%. (a) AP laminate, (b) QI laminate

equation 6.1). The change in the stiffness is only 2.5% from a 0.1 mm crack length to a 5.5 mm crack length in the AP laminate. Therefore, applying a constant strain (displacement control) rather than constant stress (load control) is not expected to affect the results shown above. Additionally, similar stiffness reduction occurs in the model with the binding, so both models with and without binding under displacement control are directly comparable, and the stiffness reduction due to increased crack length does not compromise such comparison. The FE model is linear-elastic, and for ease of analysis and comparison, all simulations are performed with 1% applied strain. The energy release rate at different strains is quadratically proportional and can be calculated straight away.

6.2.1 Binding design

When the uncured flat binding laminate made out of thin-ply unidirectional prepreg is bent over the substrate laminate edges (see section 5.2 for the specimen's manufacture method), its fibre orientation in the top part (see figure 6.3b for reference) inverts in the binding bottom part. In other words, each layer orientation of the binding in the top part is mirrored in the bottom part. Figure 6.3 shows a schematic representation of the binding's layup and its stacking sequence on the top and bottom parts. It was decided to have a symmetrical and balanced additive binding layup to minimise any coupling effects between the in-plane tension and other deformation modes. While the whole binding is not perfectly symmetric versus the substrate mid-plane,

it is relatively close to being symmetric. Hence, given its small dimensions compared to the main substrate, the bending-tension coupling is expected to be negligible.

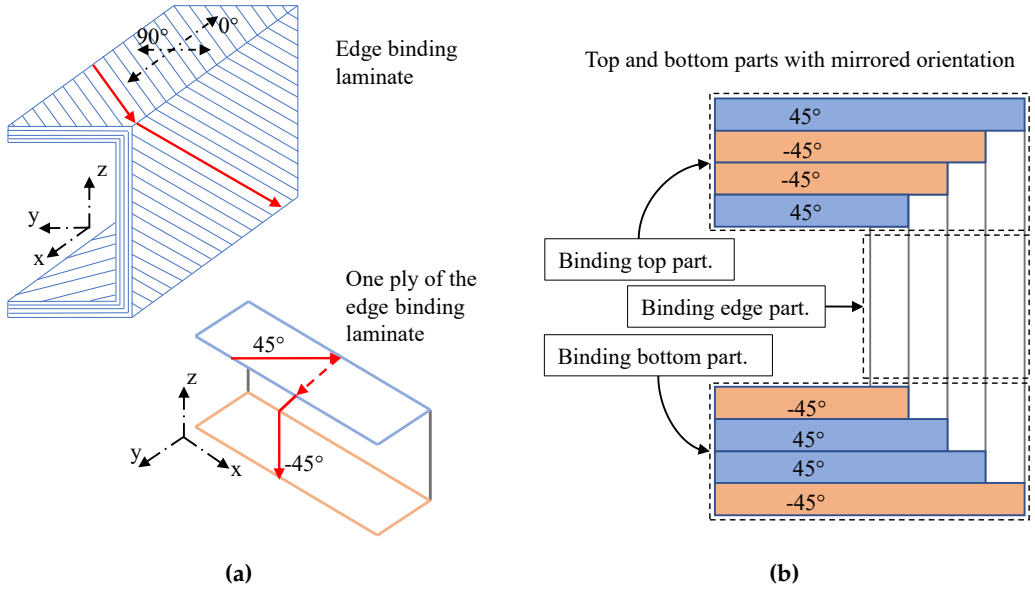

Figure 6.3: Change of the fibre orientation in the binding. (a) Fibre direction in a multi-layer edge binding and in one of the edge binding plies, (b) top and bottom parts of the binding with mirrored orientation.

A large number of simulations were performed to find the best binding layup. Different additive binding layups were tried for minimising the energy release rate at the critical interfaces using numerical analysis explained in section 4.1. Both AP and QI laminates are symmetric and therefore have two critical interfaces symmetric against the mid-plane. For the AP laminate, the critical interfaces are interface number 1 and 7, indicated by // in the layup $[20_2//-20_2/20_2/-20_2/-20_2/20_2/-20_2//20_2]$. In the case of the QI laminate, interfaces 3 and 5 are the critical interfaces in the layup $[45_2/0_2/-45_2//90_2/90_2//-45_2/0_2/45_2]$. As shown in figure 6.2, in both AP and QI cases, after delamination lengths of about 4 mm, the energy release rate values follow a constant asymptotic value. Therefore, a pre-crack of 4.5 mm was modelled at the critical interface of the AP and QI substrate laminates. Different additive bindings with stacking sequence of $[\pm\theta]_s$, $[\theta]_4$ and $[\theta/\phi]_s$ were numerically analysed, with ϕ changing from 0 to 90 degrees with 15 degrees intervals, and θ changing from -90 to 90 degrees with 15 degrees intervals for each ϕ angle. The total energy release rate ($\mathcal{G}$) results of these simulations are presented in figure 6.4. For each layup, the presence of the 4.5 mm pre-crack at either of the critical interfaces of the AP and QI laminates was studied, and the higher value is reported in figure 6.4, so the effect of the binding asymmetry is considered in the results.

According to the results shown in figure 6.4, the $[\pm45]_s$ layup is the optimum binding

layup that gives the minimum energy release rate for the AP substrate. This binding layup reduces the energy release rate value by around 70%, from 0.94 to 0.28 N/mm.

Different binding layups for the QI substrate laminate have a minor impact on reducing the total energy release rate value. For comparison with the AP substrate laminate, a $[\pm 45]_s$ binding layup was chosen for the QI laminate experiments. This layup reduces the energy release rate by 19%, from 0.78 to 0.63 N/mm. Different binding layups give similar $\mathcal{G}$ values. The $[0]_4$ and $[90]_4$ binding layups only have one fibre orientation, making them easier to manufacture. The $[0]_4$ gives the $\mathcal{G}$ value of 0.63 N/mm for the QI laminate case, which reduces 22% compared with the substrate without binding, and it is lower than the value of G given by $[90]_4$ binding layup. Hence, the $[0]_4$ binding layup was also selected for additional testing on the effectiveness of the additive bindings. The comparison of the energy release rate values for different delamination lengths at the critical interfaces with a $[\pm 45]_s$ binding against laminates without binding is shown in figure 6.5a and figure 6.5b for the AP and QI substrates, respectively.

The AP laminate with a $[\pm 45]_s$ additive binding still presents high $\mathcal{G}$ values for small edge delaminations, as shown in figure 6.5a. However, as the delamination grows, the value of $\mathcal{G}$ reduces rapidly, indicating that the crack propagation would be suppressed by the binding. For the QI laminate with a $[\pm 45]_s$ binding, shown in figure 6.5b, the value of $\mathcal{G}$ is less reduced and stays just under the $\mathcal{G}$ values for QI laminate without binding for different delamination lengths.

Separate simulations were carried out to determine the effect of the binding overlap-length over the substrate laminate width (see figure 4.5b for the definition of overlap length). Figure 6.6 indicates the variation of energy release rate versus the binding overlap-length for a $[\pm 45]_s$ additive binding layup, with different delamination lengths at interface 1 of the AP laminate. Numerically, small binding overlap-length have a similar effect to those bindings with longer overlap-length. This is because the binding overlapping part does not significantly contribute to load transfer and the constraining of the delamination. Therefore, for the experiments, the binding overlap-length was decided to be 5 mm, allowing repeatability in the manual manufacture process of the laminate with binding (see section 5.2 for the procedure of samples manufacturing and placement of the additive binding).

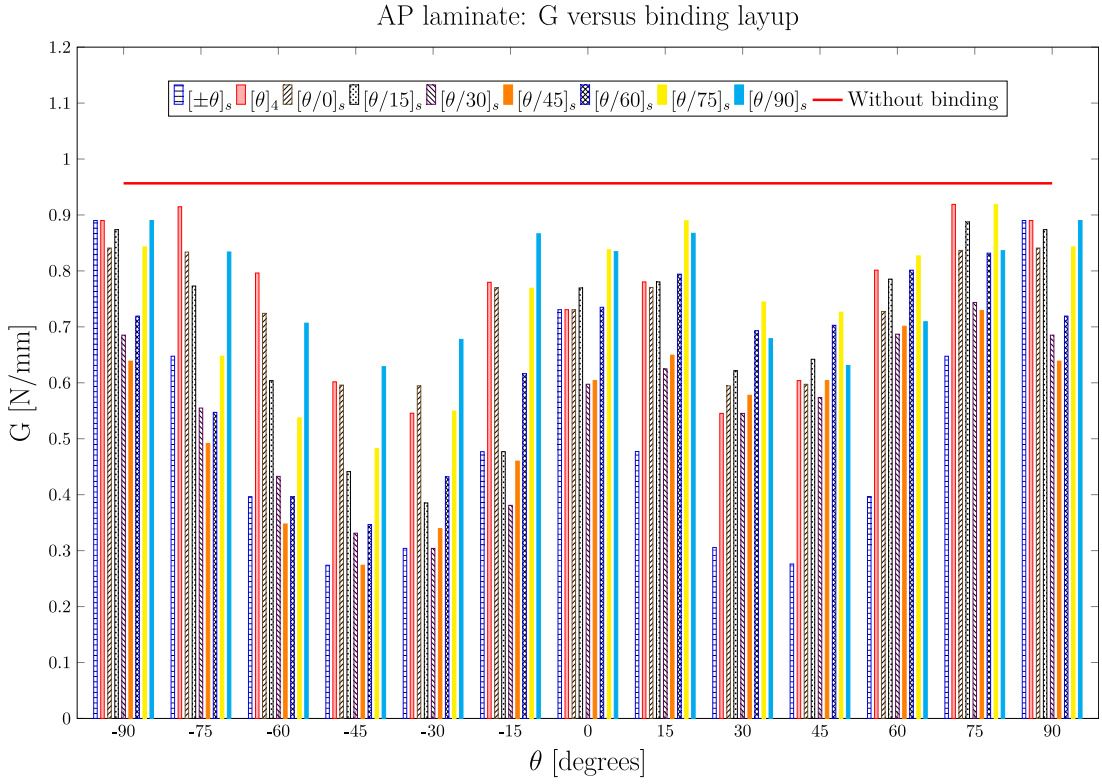

(a)

(b)

Figure 6.4: Highest energy release rate values of the AP and QI substrates treated with different binding layups of $[\pm\theta]_s$, $[\theta]_4$ and $[\theta/\phi]_s$ at their critical interfaces compared against the energy release rate of the substrates with no binding. (a) AP substrate with a pre-crack of 4.5 mm at interface 1 or 7. (b) QI substrate with a pre-crack of 4.5 mm at interface 3 or 5.

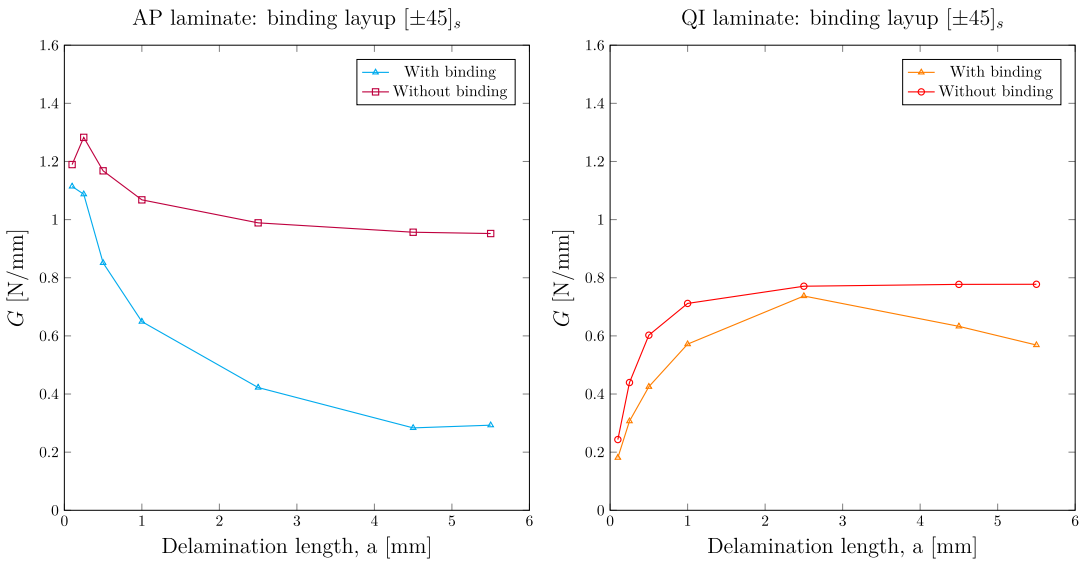

(a) **(b)**

Figure 6.5: Energy release rate versus crack length for laminates with and without additive binding. (a) AP laminate with delamination at interface 1, (b) QI laminate with delamination at interface 3.

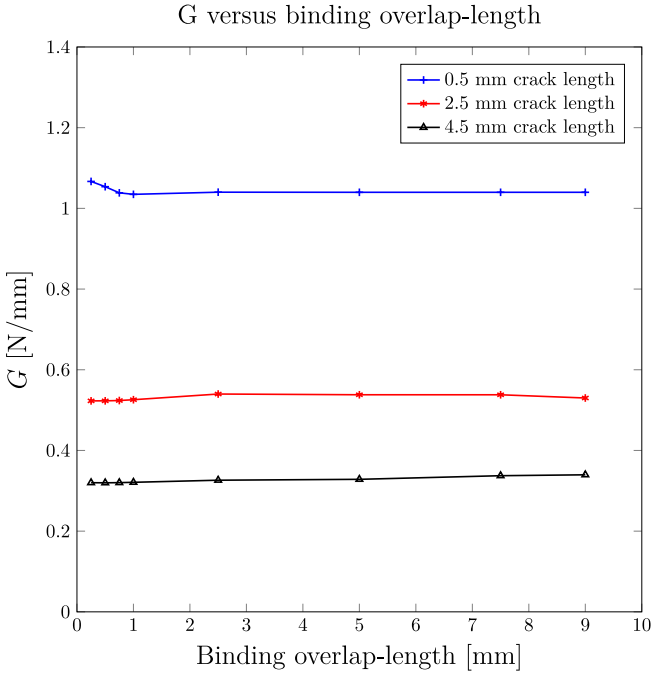

Figure 6.6: Energy release rate versus the overlap-length of a $[\pm 45]_s$ additive binding applied to the AP substrate laminate with 0.5, 2.5 and 4.5 mm delamination lengths at the critical interface.

6.3 Thermal analysis

Residual thermal stresses could have a negative impact on the distribution and concentration of stresses in composite laminates. For that reason, a FE analysis was carried out to determine the magnitude of possible residual thermal stresses in the laminates once the additive binding has been placed and cured in the specimens. It will be shown that, although there are residual stresses from the curing of the additive binding, these residual stresses induced by the binding will not have a negative impact on the free-edges stresses state in both layups. Additionally, the bindings will introduce a small compressive through-thickness direction residual stresses to the substrate laminate, which can have a small positive impact on suppressing delamination.

Coefficients of thermal expansion used for IM7/913 are $\alpha_1 = -9x10^{-7}\ K^{-1}$ and $\alpha_2 = \alpha_3 = 2.88x10^{-5}\ K^{-1}$ taken from [293]. For TC33/K51, the estimated thermal expansion coefficients from [281], are $\alpha_1 = -110^{-6}\ K^{-1}$ and $\alpha_2 = \alpha_3 = 410^{-5}\ K^{-1}$. A room temperature of 20 °C was considered, giving a 105 °C temperature drop from the 125 °C curing and glass transition temperature.

A FE analysis similar to the one explained in section 4.1 was used to calculate the residual thermal stresses at the free edge of the substrate laminate when no binding is applied and when a $[\pm 45]_s$ binding is applied. Figure 9 shows the numerical results obtained for the through-thickness stresses S_{33} and S_{13} in global coordinates (x, y, z) at the free edge of the substrate laminate.

As shown in figure 6.7, the application of the $[\pm 45]_s$ additive binding is not affecting the S_{13} stress in either AP or QI laminate. However, the binding applies some compressive stress in the z-direction, reaching about -22 MPa at the top and bottom surfaces of the free edges.

This indicates that the binding layers are not only constraining the relative movement of the layers by introducing through-thickness constraints but also providing small compressive stress, which may further suppress any potential free-edge delamination.

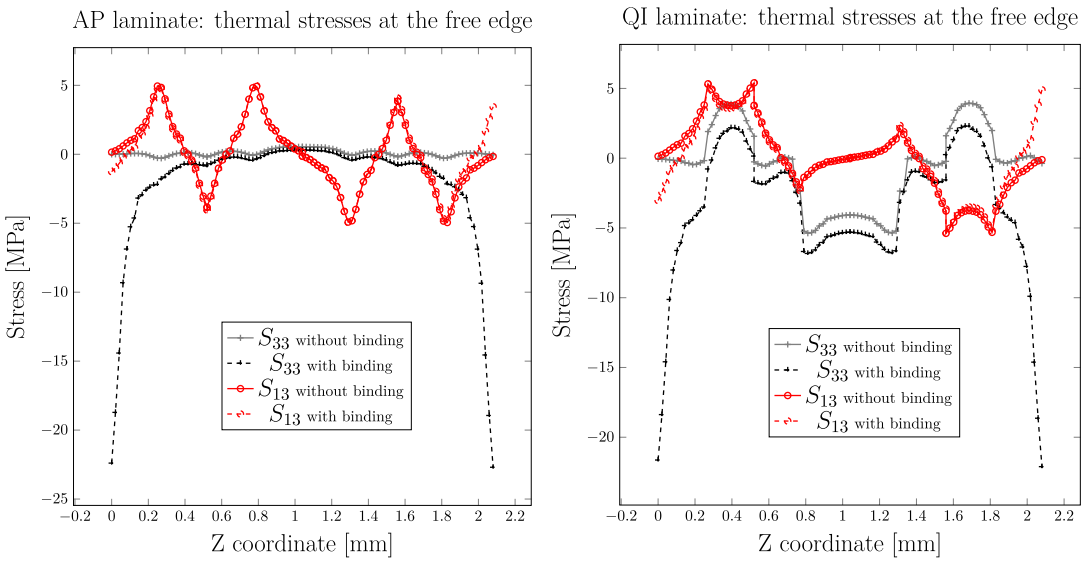

Figure 6.7: Thermal stresses S_{33} and S_{13} in global coordinates at the free edges of the substrate laminates without and then with a $[\pm 45]_s$ binding applied. (a) AP laminate, (b) QI laminate

6.4 Experimental results

The mechanical testing was conducted as explained in section 5.6.1. For calculating the average applied stress to the specimens without binding, the force measured by the load cell was divided by the cross-section area of each specimen. The width of all specimens was measured separately at 3 points along the length and then averaged. The nominal ply thickness of 0.13 mm was used for calculating the total thickness of the substrate laminates.

Two cross-sectional areas were used to calculate the stress in the samples with binding, and two stress values were calculated: (1) substrate cross-sectional area, as explained above, plus binding's nominal cross-sectional area, and (2) substrate cross-sectional only. It is believed that both stress definitions provide useful information. This is because a different binding overlap length does not affect the value of $\mathcal{G}$ and, consequently, would not change the failure load as shown in figure 6.6, i.e. a binding with 2 mm overlap-length would have the same failure force with a smaller binding cross-section area. Hence, it is valuable to show the stresses only based on the substrates' cross-sectional area. Furthermore, the cross-section of the binding is less than 7% of the substrate's cross-sectional area and would not change the graphs significantly.

The stress-extension results for samples with and without binding are shown in figures 6.8, 6.9, and 6.10 for the AP laminates and the QI laminates with $[\pm 45]_s$ and

$[0]_4$ bindings, respectively. To make the comparison clearer, the cases with binding and including the binding cross-sectional area for calculating the stress are plotted with an offset of 0.5% strain. The cases with binding and calculated only with the cross-sectional area of the substrate are plotted with an offset of 1% strain. Table 6.1 presents the load direction engineering modulus, maximum force, stress-based only on substrate cross-section area, and strain at failure of the AP and QI laminates with and without binding.

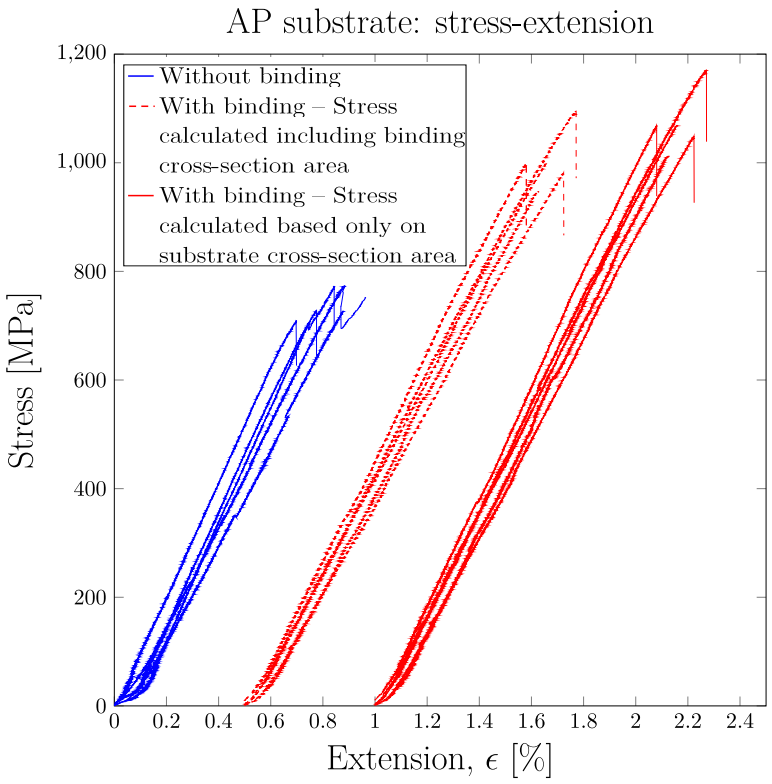

Figure 6.8: Stress-extension experimental results for the AP substrates without any binding and with $[\pm 45]_s$ binding

The strain and force at failure are taken as the points where the first significant drop of the load is seen, defining the point when the laminate cannot withhold the load anymore. For the case without binding, the AP laminates show an average value of 0.8%, 733.21 MPa and 30.78 kN for strain, stress, and load at the failure point, respectively. The QI laminates show similar average values of 721.59 MPa and 30.36 kN for stress and load at failure, but due to lower axial stiffness, the failure strain is 1.49%, almost double that of the AP laminates.

The AP laminates with $[\pm 45]_s$ additive bindings show a significant increase in their strain, stress, and force at failure. The average strain at failure was 1.19%, indicating a significant 49% increase compared to the 0.80% failure strain of the AP laminates without binding. A similar 47% increase is observed in the average maximum force, from 30.78 to 45.21 kN. On the contrary, the QI laminates show a slight reduction

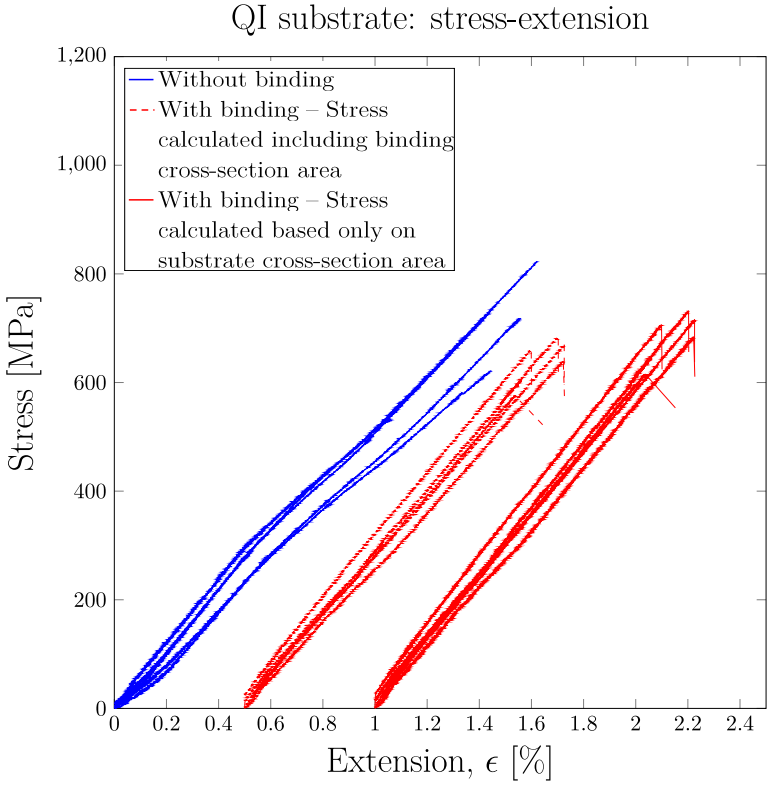

Figure 6.9: Stress-extension experimental results for the QI substrates without any binding and with $[\pm 45]_s$ binding.

of about 4% in the average values of failure stress and force and a small increase in the stiffness of the laminate when $[\pm 45]_s$ bindings are applied, reducing the strain at failure 22% from 1.49% strain to 1.16% strain. The $[0]_4$ bindings applied to the QI substrate seem to cause more noticeable reductions in the failure stress and force, although it increased the stiffness of the laminates too, reducing the strain at failure 29% from 1.49% strain to 1.05% strain. The obtained experimental results are discussed in the next section.

For calculating the engineering modulus of the laminates, the slope of a straight line between two points on the stress-extension graphs at 0.2% and 0.4% extension were used for each specimen and then averaged for each group.

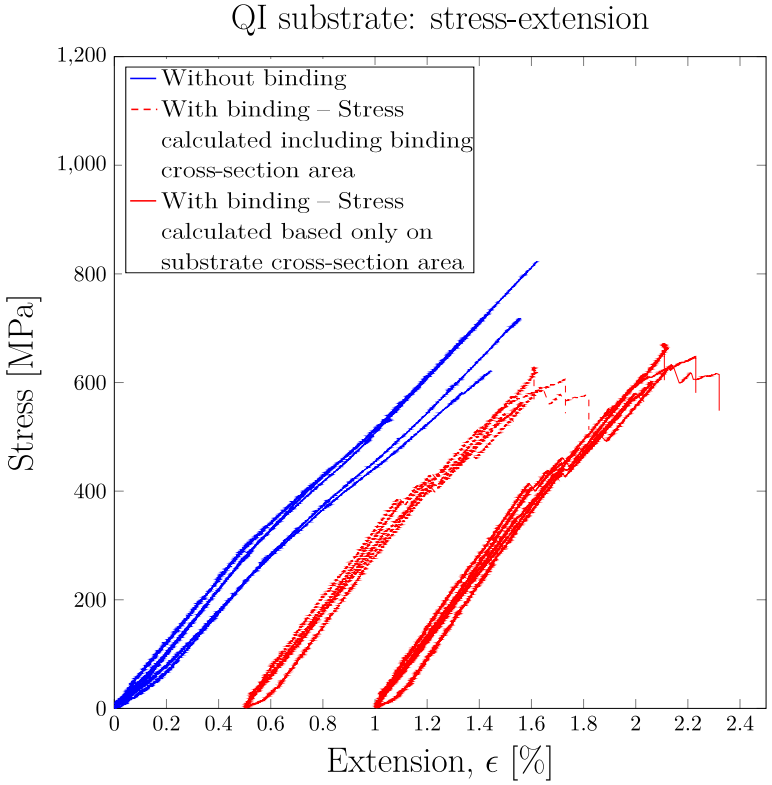

Figure 6.10: Stress-extension experimental results for the QI substrates without any binding and with $[0]_4$ binding.

Table 6.1: Maximum force, stress and strain at failure for AP and QI laminates.

Specimen	Load direction engineering modulus [GPa] (CV%)	Maximum force [kN] (CV%)	Failure stress [MPa] (CV%)	Failure strain [abs.%] (CV%)
AP laminate without binding	100.47 (8.23)	30.78 (3.39)	733.21 (3.25)	0.80 (9.76)
AP laminate with $[\pm 45]_s$ binding	95.6 (5.04)	45.21 (5.00)	1077.21 (4.95)	1.19 (6.85)
QI laminate without binding	56.07 (6.61)	30.36 (9.72)	721.59 (9.85)	1.49 (6.04)
QI laminate with $[\pm 45]_s$ binding	57.82 (6.51)	29.03 (6.55)	690.37 (6.54)	1.16 (7.33)
QI laminate with $[0]_4$ binding	66.70 (3.30)	26.35 (6.00)	627.03 (5.77)	1.05 (15.75)

It is interesting to note that after inspection of all failed specimens, no debond be-

tween the binding and the substrate was identified at points away from the main failure points, e.g., figures 6.11, 6.12 and 6.13. Hence, it was concluded that the additive binding does not tend to debond from the substrate laminate. This is aligned with the very low energy release rate values calculated for assumed cracks between the binding and the substrate, as explained in section 4.2. However, the binding did break as a result of the laminate failure as shown in figures 6.11, 6.12 and 6.13.

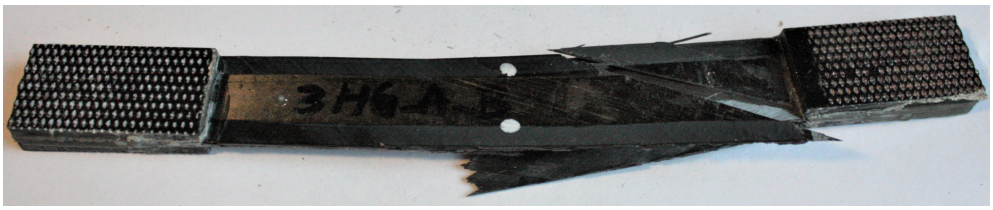

(a)

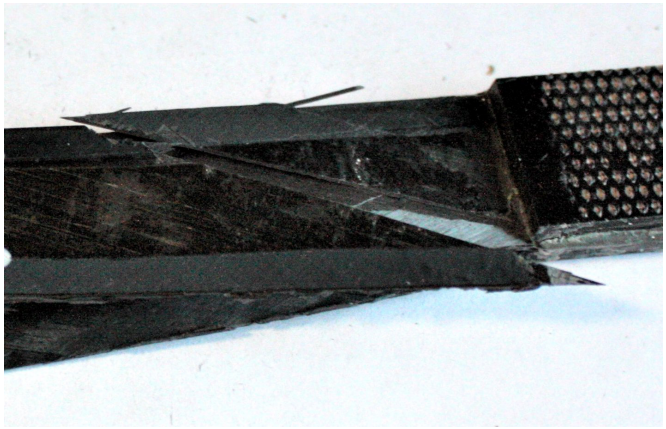

(b)

Figure 6.11: Failed AP laminate with a $[\pm 45]_s$ binding showing that the additive binding is not debonding from the substrate laminate. (a) Whole laminate. (b) Close view of the point of failure at the point where the additive binding and the end-tab meet.

(a)

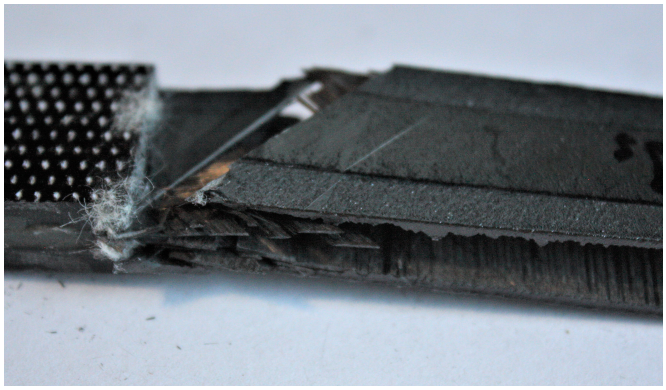

(b)

Figure 6.12: Failed QI laminate with a $[\pm 45]_s$ binding showing that the additive binding is not debonding from the substrate laminate. (a) Whole laminate. (b) Close view of the point of failure at the point where the additive binding and the end-tab meet.

(a)

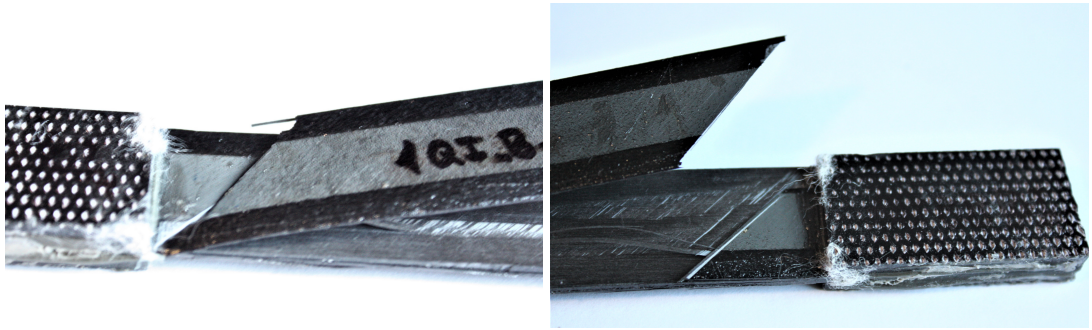

(b) **(c)**

Figure 6.13: Failed QI laminate with a $[0]_4$ binding showing that the additive binding is not debonding from the substrate laminate. (a) Whole laminate. (b), (c) Close view of the point of failure at the point where the additive binding and the end-tab meet.

6.5 Discussion

This section aims to explain how the binding suppressed the damage modes triggered by the free-edges, e.g. free-edge delamination and matrix cracking, whereas other failure modes are not significantly affected.

6.5.1 Failure analysis of the Angle-ply substrate

Xu and Wisnom showed that $[(20_2/-20_2)_2]_s$ AP laminates under tension fail shortly after initiation of the free-edge delamination [291]. Equation 6.1 and the FE slice modelling results can be used to find the free-edge delamination onset strain of the AP laminates. From the FE analysis, the mixed-mode ratio is found to be equal to one, $(\mathcal{G}_{II}+\mathcal{G}_{III})/(\mathcal{G}_{I}+\mathcal{G}_{II}+\mathcal{G}_{III})=1$, for the AP laminates. Therefore, the fracture toughness, $\mathcal{G}_c$, is assumed to be equal to pure mode II fracture toughness. No data was found for the fracture toughness values of the IM7/913, so the value of fracture toughness $\mathcal{G}_{Ic}$ and $\mathcal{G}_{IIc}$, which are known to be mostly matrix dependant, were taken as $\mathcal{G}_{Ic}$=0.25 N/mm and $\mathcal{G}_{IIc}$=1.08 N/mm, estimated from E-Glass/913 prepreg in [267]. Additionally, $\mathcal{G}_{IIIc}$ was assumed equal to $\mathcal{G}_{IIc}$ as per the common practice [280]. Introducing this $\mathcal{G}_c$ value in equation 6.1, the free-edge delamination onset strain in the AP laminates is calculated to be 0.98%. For calculating E^* in equation 6.1, two complete and symmetrical delaminations are assumed between the outer 20_2 layers and the inner layers. The FE analysis provides a free-edge delamination onset strain of 0.92%, calculated with a pre-crack length of 0.25 mm as the value of $\mathcal{G}$ is maximum at this delamination length as shown in figure 6.5a.

The analytical and FE free-edge delamination onset strain predictions are higher than the observed average failure strain of 0.8% for the AP laminates without binding. This could be partially explained as AP laminates do not fail only by free-edge delamination but due to an interaction between free-edge delamination and splitting of the plies. When those splits and delaminations propagated, they joined through the thickness, and the surface ply peeled off, as clearly shown in figure 6.14a and described by Xu and Wisnom in [291]. Similarly, as described in section 6.1, O'Brien observed that the experimental onset strain of free-edge delamination occurs at strains lower than the strain values predicted in equation 6.1 and, therefore, proposed an empirical modification to the same equation to include 2 in the denominator of the equation rather than 4 [83]. He justified this change based on the presence of zig-zag and asymmetric delamination in reality.

The possibility of failure modes other than free-edge delamination was studied using Classical Laminate Theory. The fibre, transverse, and shear direction stresses in all

±20 layers at 0.80% applied axial strain are calculated to be equal to 907.5, -75.0 and ±62.1 MPa, respectively. All these values are significantly lower than the material's estimated tensile strength in fibre direction (2723 MPa) [275], transverse compression strength (286 MPa) [294], as well as shear strength (88.3 MPa), estimated from the E-glass/913 shear strength in [295]. This indicates that the free-edge delamination initiated the failure process of the AP laminates without binding. This is also confirmed by examining the failed specimens shown in figure 6.14, where a red circle indicates extensive free-edge delamination and separation of the layers.

For the AP laminates with binding, the failure strain is increased by 49%, from 0.8% for those without binding to 1.19%. As the laminate is treated with the binding, O'Brien's analytical technique is not applicable to calculate the free-edge delamination onset strain. The FE results presented in figure 6.5a indicate a significant reduction in the energy release rate for delamination growth, suggesting that the delamination growth would be stable, unlike the AP laminates without binding. For delamination lengths of about 4 mm, the energy release rate is estimated to be 0.42 N/mm at 1.19% strain, where the $\mathcal{G}$ approaches an asymptote. This value is significantly lower than the mode II fracture toughness, and therefore, no catastrophic free-edge delamination growth is expected.

The fibre, transverse and shear direction stress values in all ±20 layers at 1.19% axial strain are calculated to be equal to 1350, -111.6 and ±92.4 MPa, respectively. While fibre and transverse direction stresses are far below the strength values, the shear direction stress is above the shear strength value of 88.3 MPa. This suggests that ±20 layers are most likely to break due to shear at this axial strain. In the absence of other layers in this substrate, e.g. 0° layers, failure of the ±20 layers leads to the whole laminate final failure. Figure 6.14b indicates one of the AP samples after its failure point. No edge delamination is detectable, and the failure is relatively localised (highlighted with a red arrow) with cracks along the fibre, suggesting a shear failure mode.

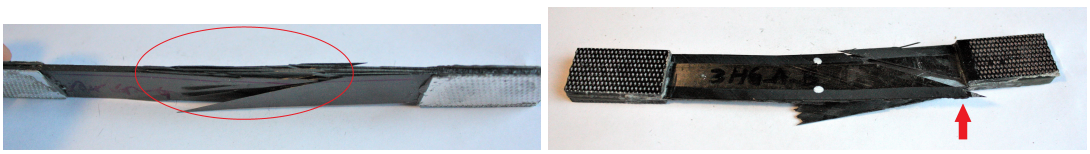

(a) **(b)**

Figure 6.14: AP laminates after failure. (a) without binding, (b) with binding.

It is to be noted that the selection of a $[\pm 45]_s$ binding layup indicated by the FE modelling did stop the free-edge delamination. This shows the capabilities of the FE modelling approach for choosing an appropriate binding layup. Further experiments on other binding layups can help to build a richer set of experimental results and are

suggested by the authors as interesting future research.

6.5.2 Failure analysis of the Quasi-isotropic substrate

From the detailed experiments in [35], we know that the final failure of the QI laminates occurs when the 0 layers fail due to fibre failure. Therefore, the final failure process of the QI laminates without binding is not controlled by free-edge delamination. Nonetheless, free-edge delamination and matrix cracking can cause stiffness reduction.

From the FE analysis, the mixed-mode ratio for the free-edge delamination in the QI laminates is found to be $(\mathcal{G}_{II} + \mathcal{G}_{III})/(\mathcal{G}_I + \mathcal{G}_{II} + \mathcal{G}_{III}) = 0.6$. Using the BK-law [36] with an exponent value 1, the fracture toughness, $\mathcal{G}_c$, is estimated to be equal to 0.748 N/mm, using $\mathcal{G}_{Ic}$=0.25 N/mm and $\mathcal{G}_{IIc} = \mathcal{G}_{IIIc}$=1.08 N/mm from [31].The free-edge delamination onset strain is calculated to be 1.12% using Equation 1, whereas E^* was calculated assuming that QI laminates completely and symmetrically delaminate at the two critical interfaces. The $\mathcal{G}$ values from FE analysis shown in Fig 7 b, for the case without binding, are small for short delamination lengths and increase gradually to an asymptotic value by which the free-edge delamination onset strain is calculated to be 0.98%. Predictions from both Equation 1 and FE are significantly higher than 0.55% extension around which the slope of the initial linear elastic stress-extension graphs changes indicating stiffness reduction. This suggests the possibility of initiation of other failure modes, e.g. matrix cracking in the off-axis 90 and $\pm$45 layers as the first mode of damage in the QI layup.

Based on Classical Laminate Theory, 90° layers transverse direction stress at a strain of 0.63% is higher than their transverse strength (88.3 MPa). This is close to 0.55% axial strain at which the stress-extension curves of the QI laminates without binding start to deviate from the linear-elastic response. This indicates that matrix cracking is likely to initiate first and induce free-edge delamination at higher strains. Figure 6.15 shows both QI samples without binding after failure. Transverse cracks in the off-axis layers and delamination are evident. Introduction of the $[\pm 45]_s$ bindings to the QI laminates resulted in a slight 4% reduction in their final failure load and a 22% reduction in the final failure strain. The similarity in the failure load is mainly because the final failure process of the QI laminates is not dominated by free-edge delamination, and introducing the bindings does not have a significant impact on the 0° layers fibre failure load. The reduction in the failure strain is caused by a 23% increase in the secant load direction modulus of the laminates between the origin and the final failure point. The binding suppresses the in-plane transverse and interlaminar damage arising from the free edges, and no change of slope is distinguishable in the stress-extension graph. Comparing the stress-extension graphs in figure 6.9 indicates

that the laminates with binding show an almost perfect linear elastic response up to their final failure point. Those without binding show some non-linearity caused by possible matrix cracking and free-edge delamination. The slight 4% reduction in the final load failure is believed to be due to the stress concentration caused by the bindings at the end-tabs, as shown in figure 6.15b with a red arrow. It is expected that this reduction of failure load could be avoided if the binding was first applied to the entire length of the QI substrates without end-tabs, and then end-tabs were bonded to the binding. The results obtained from $[0]_4$ bindings show a reduction of 12% in the load-bearing capacity of the laminate and a 30% reduction in the failure strain. Similar to the $[\pm 45]_s$ bindings, the reduction in the failure load is assumed to be due to stress concentration caused by the binding at the end tab, as $[0]_4$ laminate has higher stiffness along the load direction. This has caused higher stress concentration at the end tabs and resulted in a lower failure load. Also, the reduction in the failure strain is due to a 17% increase in the secant engineering modulus of the samples between the origin and the final failure point. Additionally, the load-extension graphs of the QI specimens with $[0]_4$ bindings showed a clear sign of damage and non-linearity around 0.6% to 0.8% extension, suggesting this binding laminate was not successful in suppressing the damages initiating from the free edges

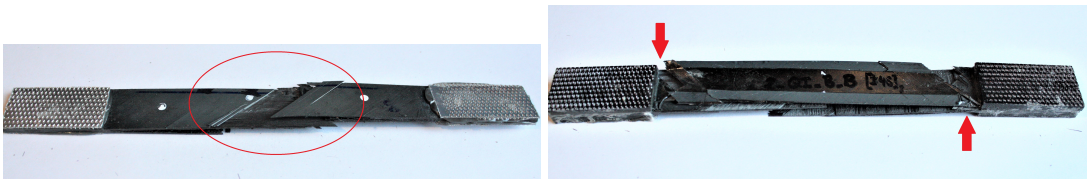

(a) **(b)**

Figure 6.15: QI laminates after failure. (a) without binding, (b) with binding.

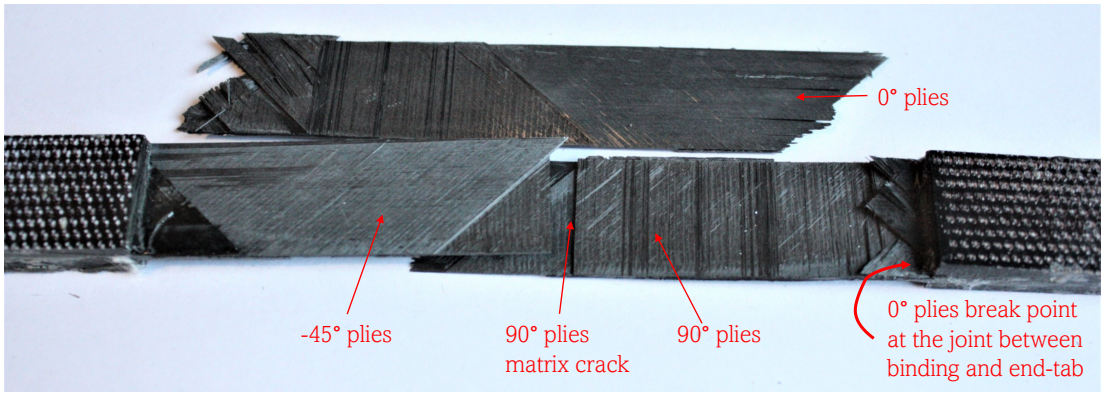

Figure 6.16: QI laminate with $[\pm 45]_s$ binding, totally delaminated between the 0//-45 (interface 2) and -45//90 (interface 3) interfaces. It is visible that 0° plies broke next to the end-tabs, and the 90° plies broke at the centre of the specimen.

6.6 Conclusion

The idea of using additive bindings as an effective technique to suppress free-edge delamination is presented. Finally, the concluding points of this study are mentioned below:

- Using additive bindings at the free edges on laminates susceptible to free-edge delamination under axial loading can significantly enhance their failure load and strain. For example, in the angle-ply laminate $[(20_2/-20_2)_2]_s$ studied in this paper, the failure load and strain were increased by 47% and 49%, respectively.

- The use of this technique can suppress other modes of damage arising at the free edges, e.g. matrix cracking. For example, in the quasi-isotropic layup studied in this paper, the non-linearity of the stress-extension curve was eliminated with the use of $[\pm 45]_s$ additive bindings, indicating that the matrix cracking and free-edge delamination in the off-axis layers were successfully suppressed.

- The $[\pm 45]_s$ additive bindings do not affect other failure modes. This is deemed to be because of their small quantity compared to the main substrate and relatively low stiffness in the load direction. For instance, the final failure stress stayed almost unchanged in the quasi-isotropic substrate, indicating that the final failure process dominated by 0-degree layer fibre failure was not affected by the bindings. This is particularly good news for testing and characterisation purposes, suggesting that binding mainly eliminates the damages initiated by the free-edges, and other failure modes are not affected.

- It is to be noted that the selection of a $[\pm 45]_s$ binding layup indicated by the FE modelling did stop the free-edge delamination. This shows the capabilities of the FE modelling approach for choosing an appropriate binding layup. Further experiments on other binding layups can help to build a richer set of experimental results and are suggested by the authors as interesting future research. Additionally, the FE modelling allows for a better informed choosing on the binding material. For this thesis only one material was studied, but the effect of the Young modulus of the fibre could have a great impact.

- Improvement of the binding manufacturing methods could be further explored to avoid introducing stress concentration at the binding termination point. For example, longer bindings covered by the end-tab could potentially resolve this issue.

- This technique could be used to suppress free-edge delamination in real structures or composite laminate coupon samples for material characterisation testing.

Chapter 7

Results on suppressing delamination in composite laminates under edge impact

This chapter presents the numerical and experimental results for the second research question. Numerical results indicate that the constraint that the additive binding places at the edge of the substrate laminate enhances the damage tolerance of the substrate laminate, reducing the delamination after crushing or impact at the edge. Experimental testing as described in section 5.7 was carried out to study the effectiveness of the solution. Some experimental specimens were X-ray scanned (XCT), and clear damage profiles after impact were shown. The use of additive bindings at the edge of substrate laminates under edge impact helped to reduce the delamination. The results are exposed, discussed, and finally, conclusions are drawn.

7.1 Laminate selection

A stacking sequence which presents serious delamination damage after edge-on impact was sought to study the effectiveness of the additive binding solution. Additionally, the layup of the substrate laminate was desired to comply with industry-standard layups for aircraft stiffeners. In this way, a $[45_2/0_2/-45_2/0_4/90_2]_s$ layup was selected. This layup is the same one corresponding to the stacking sequence number 3, "Stacking 3", studied in [166]. It was shown by Ostre et al. [166] that this layup presented similar maximum delamination crack lengths to other layups studied, but the delaminated area grew more than other layups for the same energy impact levels or permanent indentations. Figure 7.1 shows the experimental results obtained in [166] for maximum delamination crack length versus impact energy and delaminated area versus permanent dent for different stacking sequences studied.

The layup presents 50% of its plies oriented in 0° and limits the numbers of different orientation interfaces when using 0°, ±45° and 90°. Additionally, positioning the 45° layers at the top and bottom surfaces gives better resistance to buckling than other layups of similar design [165].

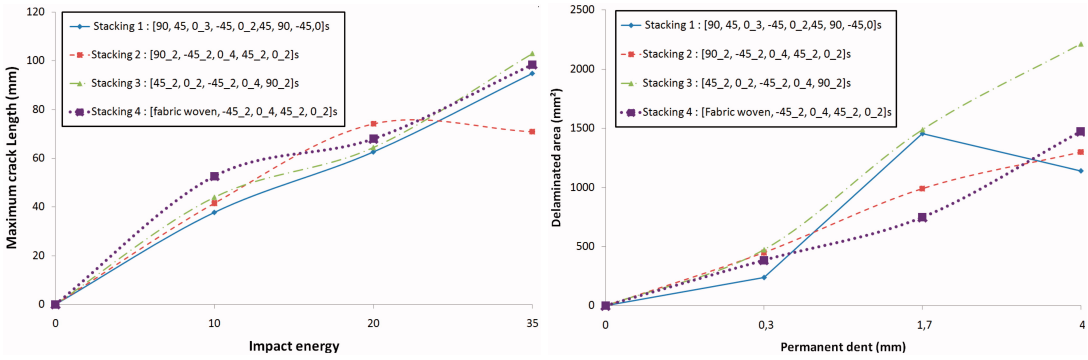

(a) **(b)**

Figure 7.1: Crack extension comparison for different composite laminates under edge impact. (a) Maximum crack length against different impact energies. (b) Delaminated area for different permanent indentation markings - Reproduced from [166].

7.1.1 Binding design

Similarly to the case of the free-edge delamination specimens, the additive binding placed over the edge of the impact specimens presented a $[+\theta/-\theta]_s$ layup on one surface of the substrate laminate and a $[-\theta/+\theta]_s$ layup on the opposite surface of the substrate laminate (see section 6.2.1 for further information).

Unlike the free-edge delamination specimens, the numerical simulations of the edge impact specimens took a long time to complete. In this way, it was decided to run less

simulations, and hence, based on the results obtained of the free-edge delamination case, an additive binding of $[\pm 45]_s$ was selected and numerically studied.

7.2 FE results

Different crack lengths at all interfaces between layer blocks with different fibre orientations were modelled. As explained in section 4.3, a fine mesh was modelled around the impact area, and hence the results of the energy release rate shown following are comprised of the nodes in this fine mesh area. The energy release rate values obtained are plotted against the x crack coordinate of the node at the crack tip. Figure 7.2 shows the general definition of the crack tip nodes and how the x coordinate is measured. The substrate laminate modelled dimensions were 60 mm long (x direction), 30 mm wide (y direction) and single cured ply thickness of 0.13 mm. The fine mesh area (0.25 mm element size) was modelled with a length of 10 mm as shown in figure 7.2.

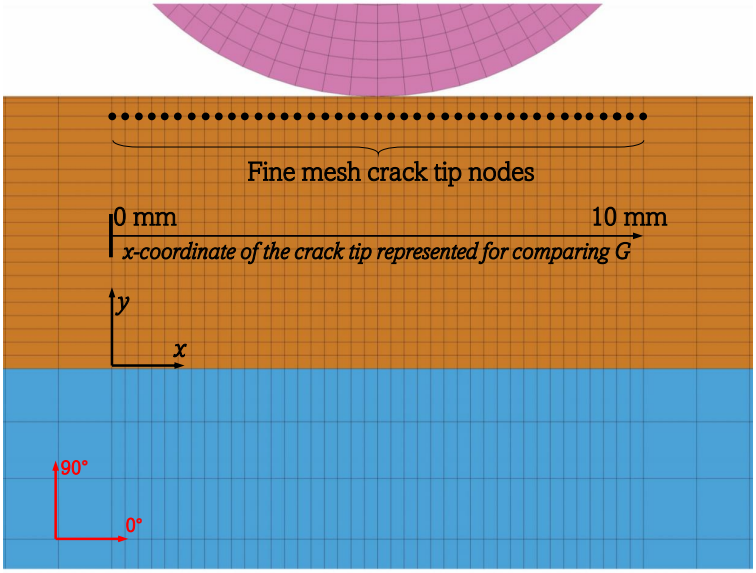

Figure 7.2: Definition of the crack tip nodes between interfaces at the fine mesh area, and x coordinate of the impact zone.

It is worth mentioning that values of $\mathcal{G}$ are obtained through all the interfaces of the substrate laminate (60x30 mm), as the bonded nodes of the interface define the crack tip. However, only the values of the energy release rate around the fine mesh were represented, as shown in figures 7.3 and 7.5. This is because the value of $\mathcal{G}$ outside the fine mesh area was very small compared to the values of $\mathcal{G}$ at the impact area or were zero. Figure 7.3 displays the value of $\mathcal{G}$ for edge impacted laminates without binding at different interfaces for different delamination lengths when a vertical impactor displacement of 0.5 mm is applied. The values of $\mathcal{G}$ are normalised

with the maximum value of energy release rate ($\mathcal{G}_{max}$), which occurs at interface 1 for a crack length of 0.25 mm (see figure 7.3d for interface numbering).

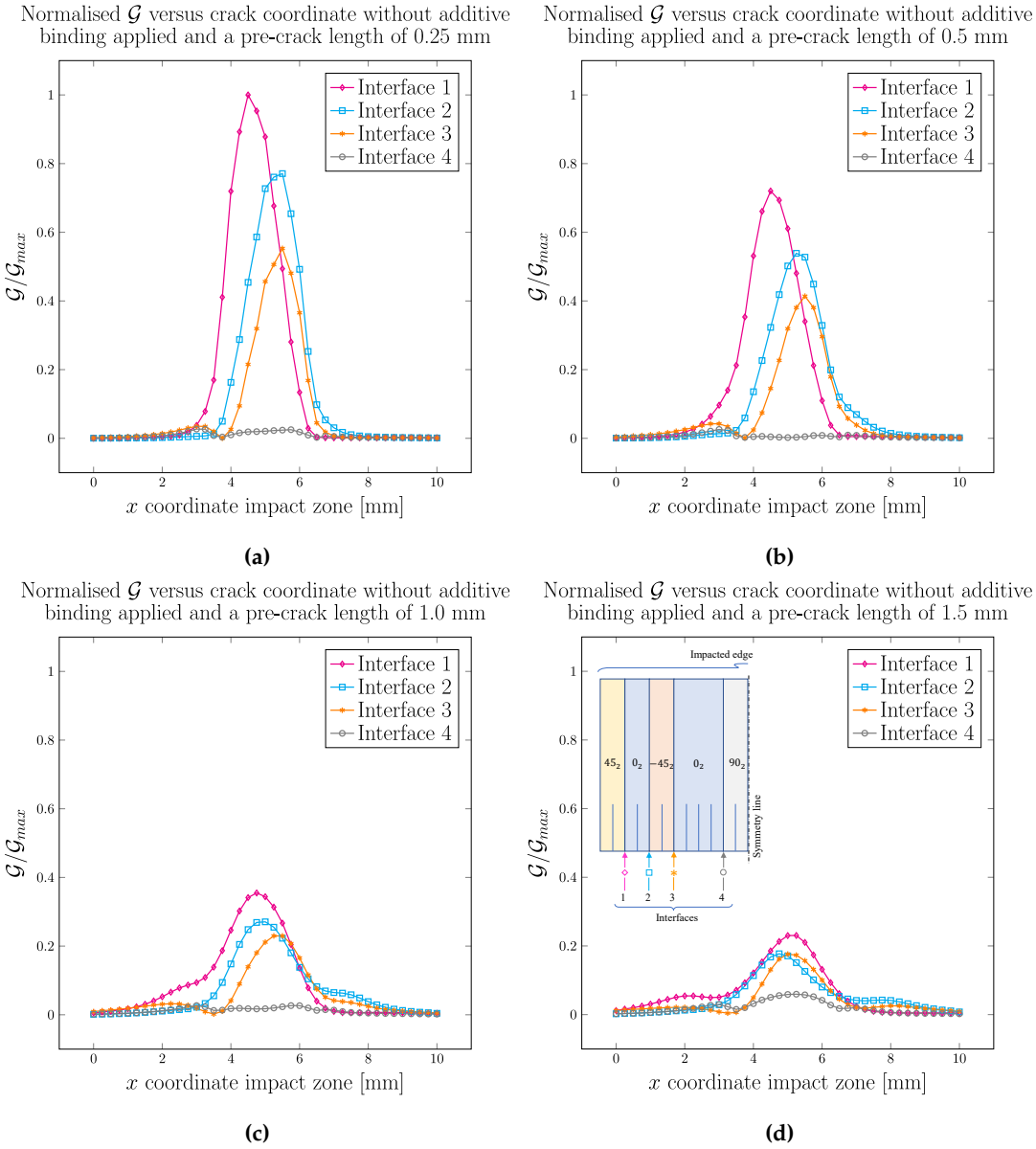

Figure 7.3: Normalised energy release rate for interlaminar cracks at different crack lengths and interfaces $\mathcal{G}$, with the maximum energy release rate $\mathcal{G}_{max}$, for an applied impactor vertical displacement of 0.5 mm. The $\mathcal{G}_{max}$ occurs for a crack length of 0.25 mm at interface 1 in laminates without binding. Case without binding results. (a) $\mathcal{G}/\mathcal{G}_{max}$ for a crack length of 0.25 mm. (b) $\mathcal{G}/\mathcal{G}_{max}$ for a crack length of 0.5 mm. (c) $\mathcal{G}/\mathcal{G}_{max}$ for a crack length of 1.0 mm. (d) $\mathcal{G}/\mathcal{G}_{max}$ for a crack length of 1.5 mm with leged for interface numbering.

As shown in figure 7.3, the biggest delamination length simulated is 1.5 mm, as when larger crack lengths were simulated, the simulation time increased, as explained in section 7.2. Hence it was decided not to simulate larger delaminations. The highest value of energy release rate is achieved for a delamination length of 0.25 mm at inter-

face 1 and interface 8 ($[45_2//0_2/-45/0_4/90_4/0_4/-45_2/0_2//45_2]$), as the substrate laminate is symmetrical. The values of energy release rate were normalised as the values obtained from the FE analysis are not realistic values of energy release rate, as the simulations are performed without crack development. For reference, the value of the energy release rate at interface 1 for a crack of 0.25 mm calculated from the FE analysis is 70.54 N/mm.

Figure 7.4 shows the maximum values of energy release rate at different interfaces for different crack lengths when no binding is applied. The values are normalised with the maximum value of energy release rate (70.54 N/mm).

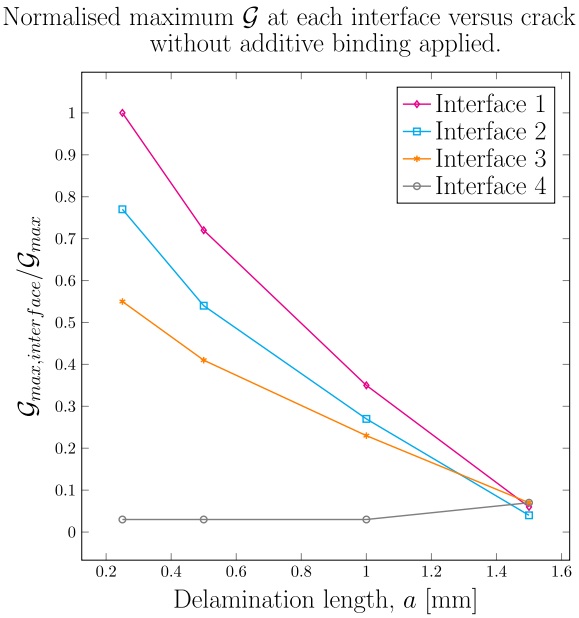

Figure 7.4: Maximum energy release rate at each interface ($\mathcal{G}_{max,interface}$), normalised with the maximum value of energy release rate ($\mathcal{G}_{max}$) for different crack lengths. The $\mathcal{G}_{max}$ occurs for a crack length of 0.25 mm at interface 1 in laminates without binding. Case without binding.

As in the case of samples under tension with free-edge delamination, the value of the energy release rate also decreases in the edge impact specimens as the crack length increases. The presence of the highest values of energy release rate at interface 1 is in agreement with the experimentally observed results. As shown in the XCT scans displayed in section 7.3, interfaces 1 and 8 present large delaminations that extend lengthy along the length direction (x direction).

Figure 7.5 presents the values of $\mathcal{G}$ at the different interfaces for different crack lengths when a $[\pm 45]_s$ additive binding is applied to the substrate laminate. A vertical impactor displacement of 0.5 mm is applied. The values of $\mathcal{G}$ are normalised with the maximum value of energy release rate $\mathcal{G}_{max}$ for the case without binding, which occurs at interface 1 for a crack length of 0.25 mm (70.54 N/mm).

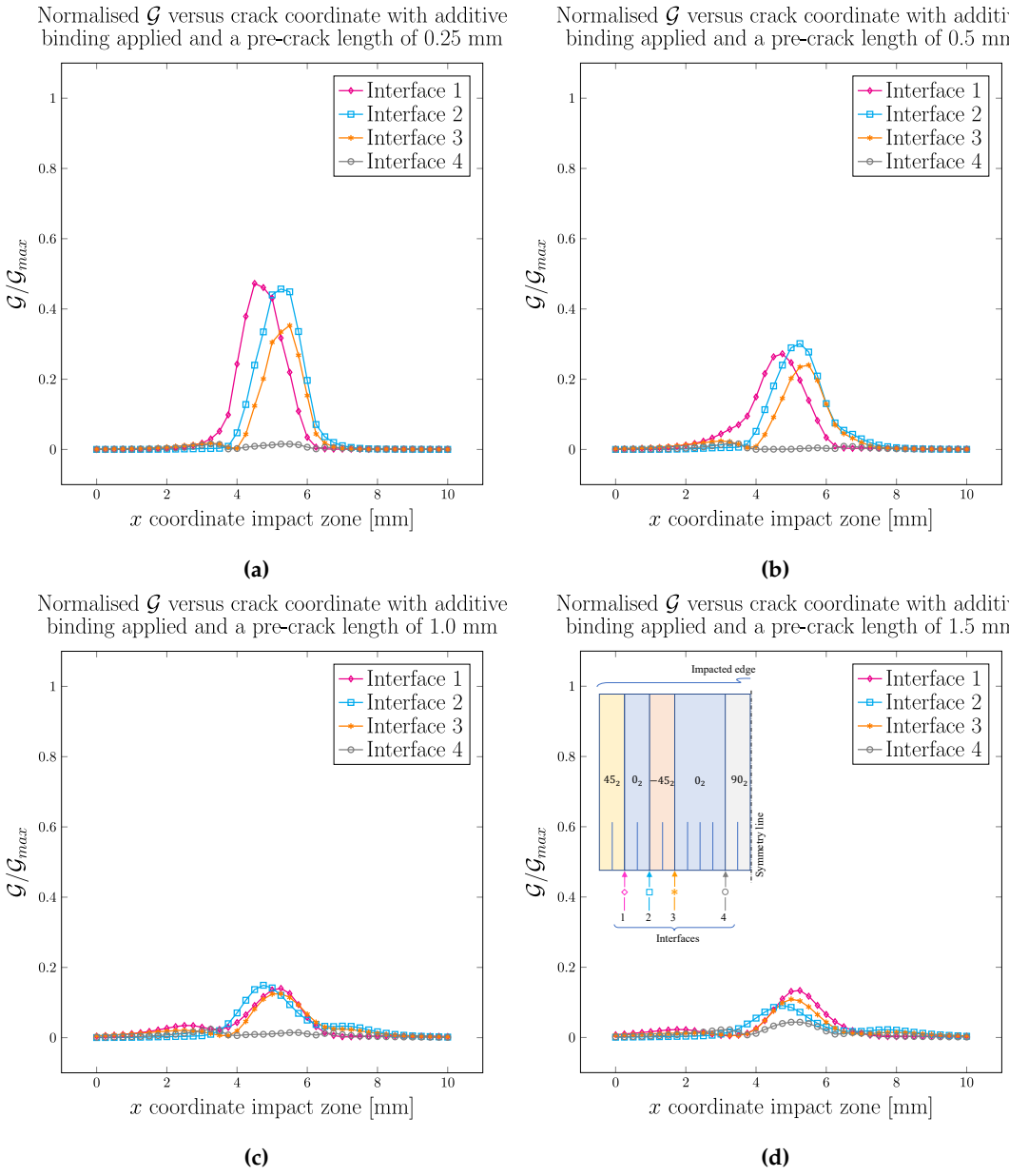

Figure 7.5: Normalised energy release rate for interlaminar cracks at different crack lengths and interfaces $\mathcal{G}$, with the maximum energy release rate $\mathcal{G}_{max}$, for an applied impactor vertical displacement of 0.5 mm. The $\mathcal{G}_{max}$ occurs for a crack length of 0.25 mm at interface 1 in laminates without binding. Case with binding results. (a) $\mathcal{G}/\mathcal{G}_{max}$ for a crack length of 0.25 mm. (b) $\mathcal{G}/\mathcal{G}_{max}$ for a crack length of 0.5 mm. (c) $\mathcal{G}/\mathcal{G}_{max}$ for a crack length of 1.0 mm. (d) $\mathcal{G}/\mathcal{G}_{max}$ for a crack length of 1.5 mm with leged for interface numbering.

As shown in figure 7.5, the value of $\mathcal{G}$ reduces significantly when the $[\pm 45]_s$ additive binding is in place. The maximum value of $\mathcal{G}$ for the case with binding also occurs at interface 1 for a delamination length of 0.25 mm. However, the value of $\mathcal{G}$ calculated is less than 50% of the value of $\mathcal{G}$ for the case without binding, in particular, a reduction of 53%. For reference, the value of $\mathcal{G}$ at interface 1 for a crack length of 0.25 mm when

a $[\pm 45]_s$ binding is applied is 33.34 N/mm.

Figure 7.6 shows the maximum values of energy release rate at different interfaces for different crack lengths when a $[\pm 45]_s$ binding is applied. The values are normalised with the maximum value of energy release rate (70.54 N/mm). It is visible that when the additive binding is applied, the values of $\mathcal{G}$ at interface 1 reduce to values near values of $\mathcal{G}$ at interface 2. Moreover, for at delamination lengths of 1.5 mm, the value of $\mathcal{G}$ of interfaces 2 and 3 is higher than at interface 1.

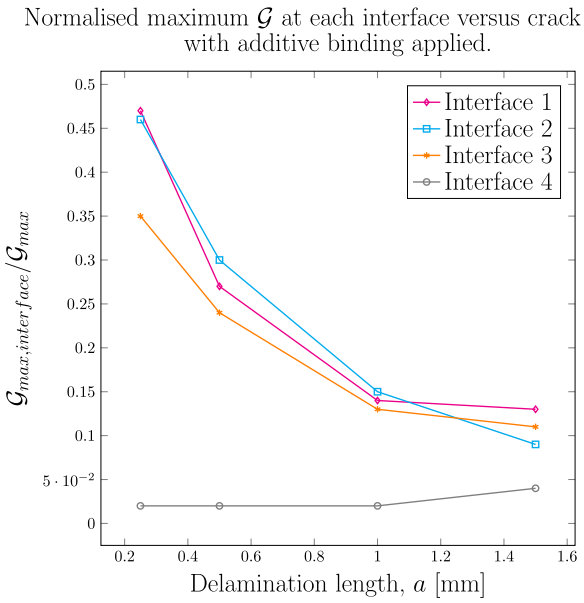

Figure 7.6: Maximum energy release rate at each interface $\mathcal{G}_{max,interface}$, normalised with the maximum value of energy release rate $\mathcal{G}_{max}$ for different crack lengths. The $\mathcal{G}_{max}$ occurs for a crack length of 0.25 mm at interface 1 in laminates without binding. Case with binding.

It is worth mentioning that despite the significant reduction of $\mathcal{G}$ for the simulated cases with additive binding, delamination would still be occurring under the loading conditions simulated, as the $\mathcal{G}$ values for the cases with additive binding are still much larger than the fracture toughness values of the material. For example, the value of $\mathcal{G}$ at interface 2 for a crack length of 0.5 mm is 21.26 N/mm, which is much larger than the values of fracture toughness $\mathcal{G}_{Ic}$=0.25 N/mm and $\mathcal{G}_{IIc}$=$\mathcal{G}_{IIIc}$=1.08 N/mm for IM7/913 prepreg (see section 6.5 for the source of fracture toughness values). Nevertheless, the use of an additive binding significantly reduced the values of $\mathcal{G}$ for the loading condition simulated. This could indicate that for different loading scenarios, e.g., smaller impactor vertical displacements, delamination still could occur in cases without binding, whereas in cases with binding, the delamination could be stopped or reduced.

Figure 7.7 shows a comparison of the energy release rate values at interface 1 ($[45_2//0_2/-$

$45_2/0_4/90_2]_s$) for when no binding is applied and when the binding is applied. The values of $\mathcal{G}$ are normalised with the maximum value of $\mathcal{G}$ (70.54 N/mm).

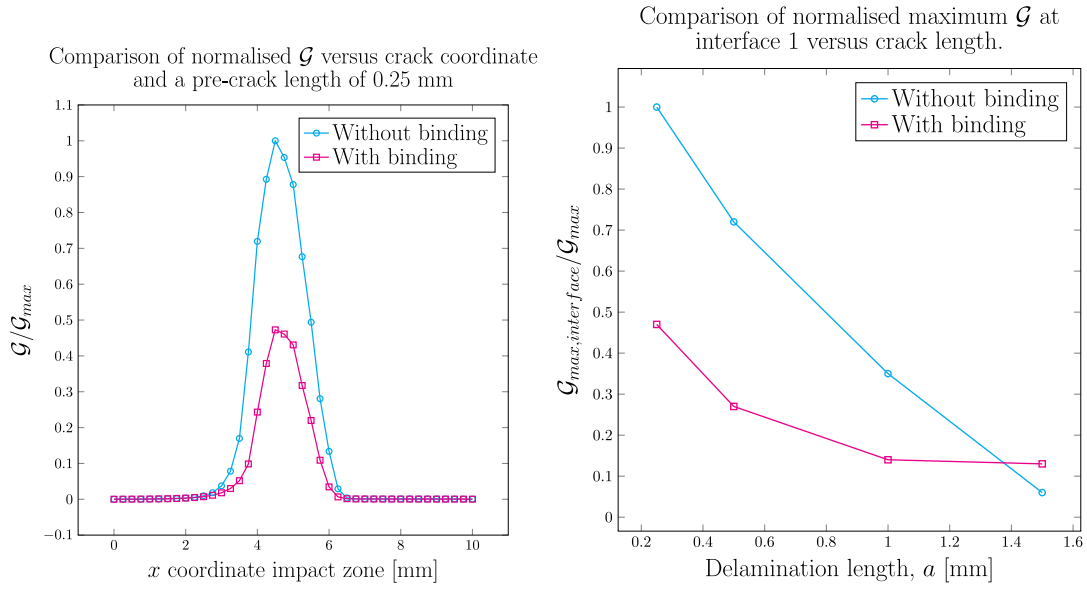

(a) **(b)**

Figure 7.7: Comparison of normalised energy release rate at interface 1 for a impactor vertical displacement of 0.5 mm. (a) $\mathcal{G}/\mathcal{G}_{max}$ versus crack coordinate.(b) $\mathcal{G}_{max,interface}/\mathcal{G}_{max}$ versus crack length.

A reduction of 53% in the maximum value of $\mathcal{G}$ at the crack tip is achieved from the case without binding to the case with binding. The maximum value of $\mathcal{G}$ does not occur under the precise point of contact between the edge of the substrate laminate and the impactor but is a bit displaced due to the 45° orientation of the top layers. This is because the 45° generates a high crack mode III. In particular, the maximum value of $\mathcal{G}$ occurs at x coordinate 4.5 mm.

7.3 Experimental results

The mechanical testing was conducted in a Rosand Instrumented Falling Weight Impact Tester type 5 as explained in section 5.7. Three different levels of energy impact were tested, e.g., 5 J, 10 J and 15 J. At least three repetition samples per configuration were tested. For setting up the impact energy, the weight drop height was modified according to the mass of the impactor plus the mass of the cylindrical impactor, the combination of the two masses was a total weight of 5.76 kg.

7.3.1 Edge impact weight drop tester results

The results of the force-displacement, force-time and dissipated energy-time graph were obtained from all the tests, and are presented in figures 7.9 to 7.11. The behaviour observed was similar for all the tests. First, the force climbed sharply, and a maximum or peak force was reached, after which it fell rapidly into a middle region and in which it stabilised around an average force value for all three impact energies tested. This average force value for the different specimens resembles a plateau from which the force increases and decreases until the impact event finalises with the ultimate dropping of force. It is deemed that during the plateau area, crushing, delamination and fibre breakage occurred. However, after the load decreased completely, a permanent indentation remains at the impacted edge. Figure 7.8 shows the permanent indentation at the edge of the specimens impacted with the three levels of energy, e.g., 5 J, 10 J and 15 J. Figures 7.9 to 7.11 present the force-displacement, force-time and energy-time graphs obtained from the experimental testing for the 5 J, 10 J and 15 J, respectively.

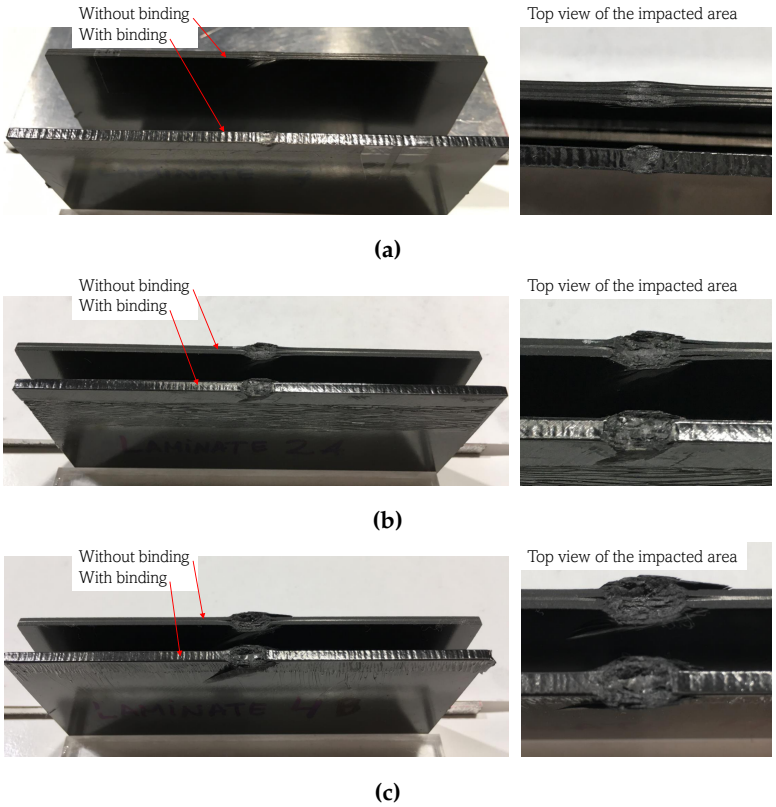

Figure 7.8: edge impacted specimens permanent indentation after impact. (a) 5 J energy impact, (b) 10 J energy impact and (c) 15 J energy impact.

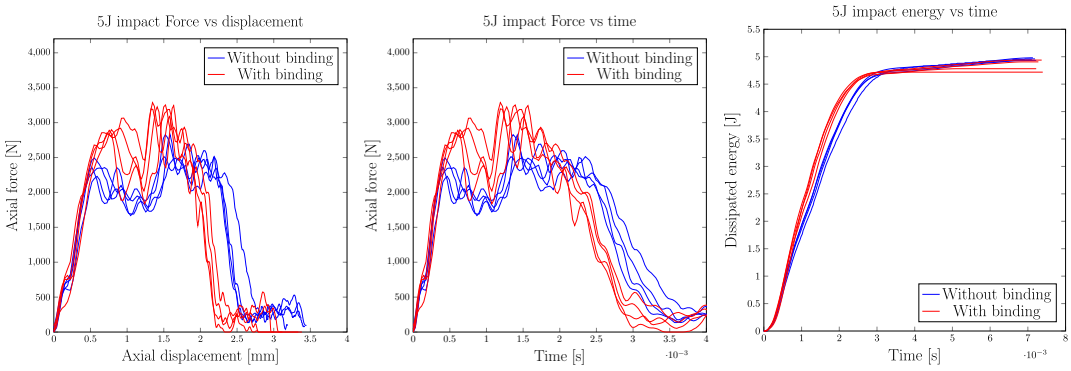

(a) **(b)** **(c)**

Figure 7.9: Experimental results for 5 J energy edge impact tests. (a) Vertical axial impact force versus vertical axial displacement. (b) Vertical axial impact force versus time. (c) Dissipated energy versus impact time.

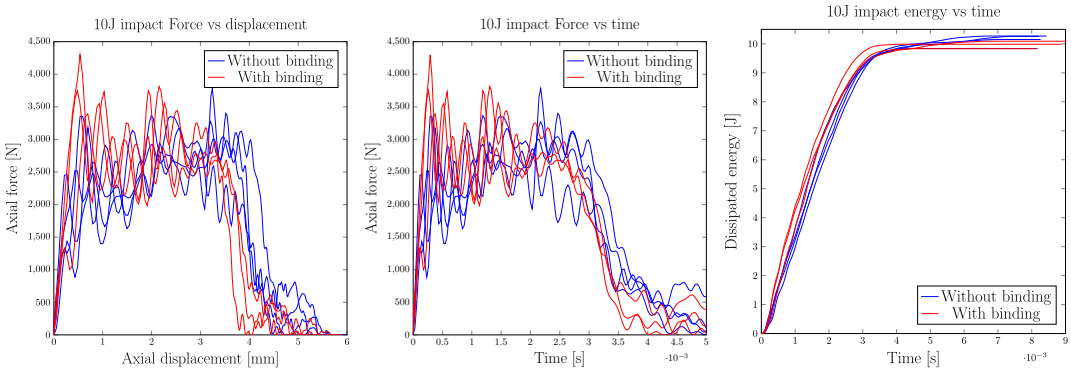

(a) **(b)** **(c)**

Figure 7.10: Experimental results for 10 J energy edge impact tests. (a) Vertical axial impact force versus vertical axial displacement. (b) Vertical axial impact force versus time. (c) Dissipated energy versus impact time.

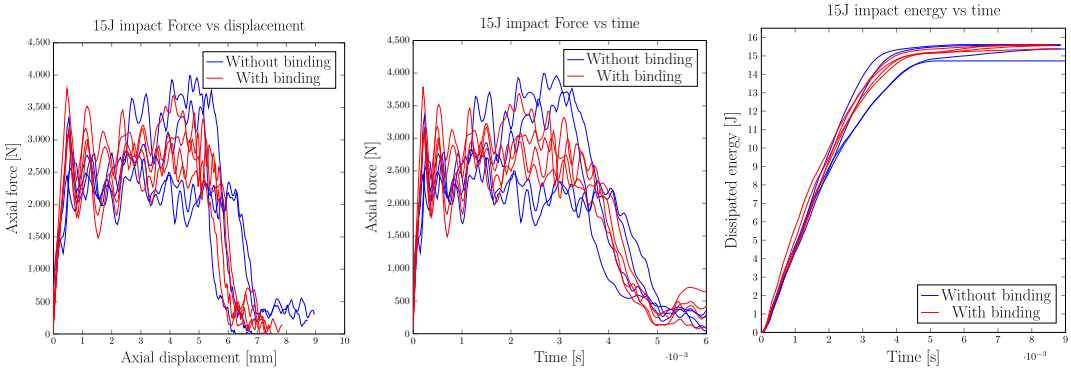

(a) **(b)** **(c)**

Figure 7.11: Experimental results for 15 J energy edge impact tests. (a) Vertical axial impact force versus vertical axial displacement. (b) Vertical axial impact force versus time. (c) Dissipated energy versus impact time.

For a clearer comparison of the experimental results reported, figure 7.12 displays the comparison of force-displacement graphs for different impact energies when no binding and binding is applied. Figure 7.12 displays the results from one typical specimen for each impact energy and not an average value. Additionally, table 7.1 presents the average maximum force and average maximum displacement for the three energy levels without and with binding.

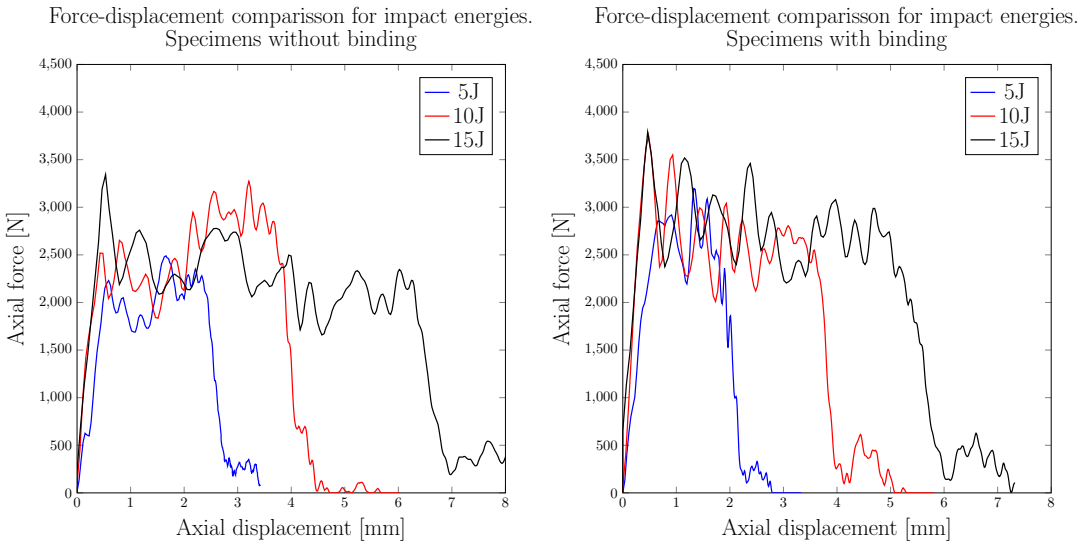

Figure 7.12: Comparison of experimental results of force-displacement graphs for different impact energies. (a) Cases without binding, (b) cases with binding.

As shown in figure 7.9, the axial force experienced a first peak load followed by a sharp decrease of load under the visible average plateau force. As damage occurred in the laminate, the load climbed again sharply, reaching values equal to or higher than the initial peak load. Soon after, the load started decreasing, indicating the end of the impact event. It is noticeable that the specimens with binding experience a higher peak load than those without binding. This higher load results from the specimens with the binding being stronger at the edge due to the additive binding.

The specimens without binding presented a maximum average first peak load for an energy impact of 5 J of about 2360 N, while the average first peak load of the specimens with binding was increased by 24.6% to 2943 N.

The maximum vertical displacement of the impactor was smaller in the specimens with binding, as displayed in figure 7.9a. The maximum average vertical displacement without binding was about 2.7 mm, and the maximum average axial displacement with binding was 2.4 mm, as shown in figure 7.9a. The average duration of the impact was between 3.0 and 3.5 ms, and it was similar in all cases, without and with binding. As visible in figure 7.9c, almost all the impact energy was dissipated.

Table 7.1: Comparison of maximum average axial force and vertical displacement for 5, 10 and 15 J energy impact specimens without and with binding.

Specimen	Average maximum force [kN] (CV%)	Average maximum displacement [mm] (CV%)
5 J specimen without binding	2360.29 (4.59)	2.71 (2.71)
5 J specimen with binding	2943.04 (2.79)	2.39 (3.46)
10 J specimen without binding	2882.15 (15.62)	4.56 (2.73)
10 J specimen with binding	3813.06 (11.97)	4.07 (4.31)
15 J specimen without binding	2842.06 (13.23)	6.48 (10.15)
15 J specimen with binding	3310.73 (9.70)	6.17 (3.12)

The slight differences in energy dissipated from the actual value of energy impact were due to inaccuracies at the time of setting up the height of the weight, the calibration of the optical light gate used for measuring the velocity of the impactor and the elastic energy dissipated in the rebound of the striker. Additionally, the slope of the dissipated energy for specimens with binding is steeper than the one for specimens without binding for the cases of 5 and 10 J. In this manner, specimens with binding dissipated the impact energy slightly faster than those without binding. This faster energy dissipation is also visible in figure 7.9b, as the load drops faster in the specimens with binding.

10 J energy impact specimens results are similar to the 5 J specimens but with a bigger scatter of the graphs due to the greater energy to dissipate and the greater extent of the damage. As shown in figure 7.10, the specimens with binding experience a higher peak load than those without binding, as in the case of the 5 J energy impact specimens. The first peak load of the specimens without binding for an energy impact of 10 J is about 2882 N, while the average first peak load of the specimens with binding was about 3813 N.

The maximum vertical displacement of the impactor was smaller in the specimens with binding, as displayed in figure 7.10a. The maximum average vertical displacement without binding was about 4.56 mm, and the maximum average axial displace-

ment with binding was about 4.07 mm. The average duration of the impact was between 3.5 and 4.0 ms, and it was similar in all cases, without and with binding. As visible in figure 7.10c, almost all the impact energy was dissipated. Additionally, similar to the 5 J energy impact specimens, the slope of the dissipated energy for specimens with binding is slightly steeper than the one for specimens without binding. In this manner, specimens with binding dissipated the impact energy slightly faster than those without binding. This faster energy dissipation is also visible in figure 7.10b, as the load drops faster in the specimens with binding.

The 15 J energy impact specimens without binding showed a considerable scatter in the value of force recorded, as displayed in figure 7.11. A total of four specimens were tested, and 2 of them followed the trend observed in the 5 and 10 J energy impact specimens, so the load followed the average force plateau. However, the other two specimens deviated from the trend, and the load kept growing after the load drop following the first peak. Moreover, these two deviated specimens present a closer average maximum vertical displacement to the case with binding than to the other two non-deviated specimens without binding.

The specimens with binding experience a higher peak load than those without binding, as shown in figure 7.11. The peak load of the specimens without binding was about 2842 N, whereas the peak load of the specimens with binding was about 3310 N.

The maximum vertical displacement of the impactor was smaller in the specimens with binding, as seen in figure 7.12. The maximum average vertical displacement without binding was about 6.48 mm, and the maximum average axial displacement with binding was about 6.17 mm. The average duration of the impact was about 5 ms, and it was similar in all cases, without and with binding. As visible in figure 7.11c, almost all the impact energy was dissipated. Additionally, similar to the 5 and 10 J energy impact specimens, the slope of the dissipated energy for specimens with binding is slightly steeper than the one for specimens without binding, which did not deviate from the trend seen for 5 J and 10 J impact energies. In this case, the difference in dissipated the impact energy is smaller than in the 5 and 10 J cases.

7.3.2 Edge impact X-ray computer tomography scan results

Impacted specimens, which represented the trend of the damage of each energy impact used, were scanned with an X-ray computer tomography scanner. Despite the damage in specimens without and with damage presenting a similar maximum depth of delamination (depth of the cracks), the extent of the cracks in the lengthwise direction (side with 130 mm length) was smaller in the case of the specimens with

binding.[1]. All the figures produced from the post-processing of the volumes of images scanned are presented below in the document. First, figures showing the extent of damage in specimens without and with binding for the same level of energy impact are shown. Then, a comparison of the cracks in the lengthwise direction in specimens without and with binding is presented in an extensive series of images, which display slices of the specimens at different vertical distances from the point of impact.

Figure 7.13 displays the cross-section and top view at the impact point of a 5 J energy impact specimen without binding. The initial thickness of the substrate laminate was 3.12 mm and after the impact, the final engrossment thickness is 4.31 mm, which is a 38% thickness engrossment increase. Relatively small energy of 5 J produced 6.24 mm depth cracks, as shown in figure 7.14. As a general trend for all the levels of energy tested, the longest delaminations in specimens without binding occurred at the exterior 45° layers, as the ones visible in figure 7.13 and measured in figure 7.14b. Figure 7.14a displays the projection of all the X-rayed slices in the $x-y$ (length-width) plane. The shadowed area in the frontal view of figure 7.14b indicates the 6.24 mm deep delamination pointed out, showing the 45° orientation of the delamination.

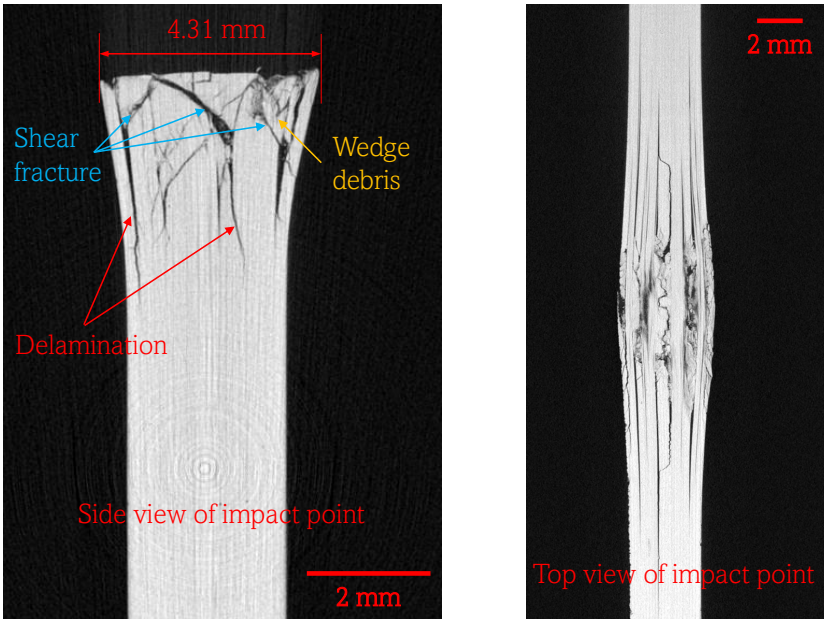

Figure 7.13: Cross-section and top view at the impact point of an edge impact specimen without binding impacted with 5 J energy. The final engrossed thickness after impact is 4.31 mm. The original substrate laminate thickness is 3.12 mm.

Figure 7.15 shows the cross-section and top view at the impact point of a 5 J energy impact specimen with binding. The thickness engrossment at the impact area is

[1]The reconstructed 3D volumes of the scans are included in this thesis as additional material, which can be found in section B.3

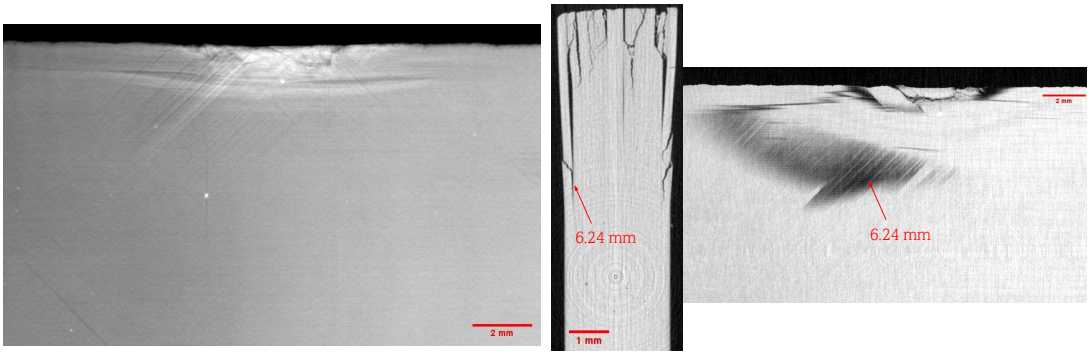

(a) **(b)**

Figure 7.14: Damage extent from a 5 J energy edge impact in a specimen without binding. (a) Front view projection of the summation of all slices through the thickness of the specimen. (b) Deepest cracks side view and front view at the deepest crack slice (6.24 mm). The dark lines in 45° represent the delamination at interface 1.

39% from a cured substrate laminate thickness of 3.12 mm, approximating the same engrossment as the case without binding. Relatively small energy of 5 J produced 6.17 mm depth cracks, as shown in figure 7.16. Unlike the specimen without binding, the deepest crack occurred at the 0/90 interface, as seen in figure 7.16b. Figure 7.16a displays the projection of all the X-rayed slices in the $x - y$ (length-width) plane. The shadowed area in the front view of figure 7.16b indicates the 6.17 mm delamination depth pointed out, showing the 90° orientation of the delamination. Additionally, the damage shown in the cross-section view of figure 7.15 displays the wedge damage effects described in section 2.3.1.

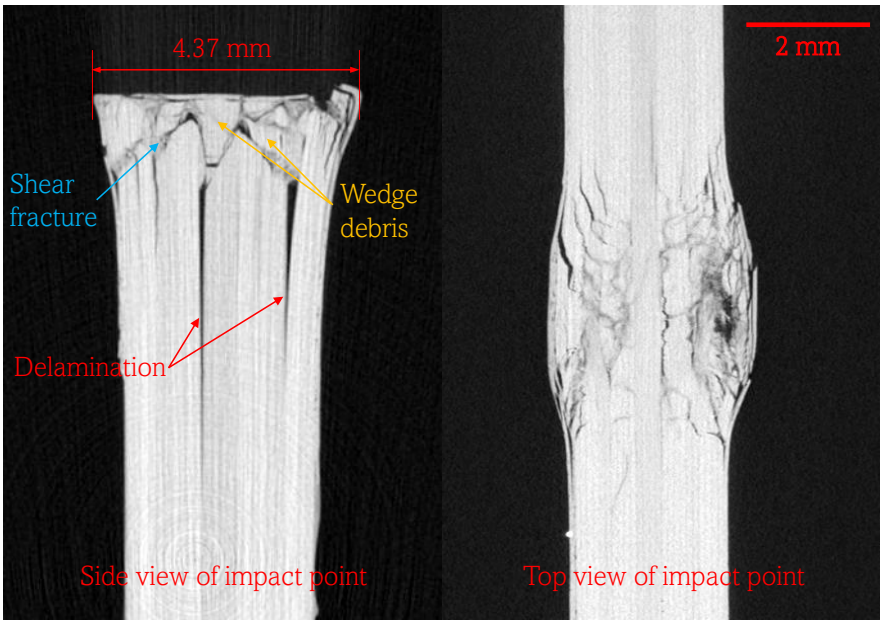

Figure 7.15: Cross-section and top view at the impact point of an edge impact specimen with binding impacted with 5 J energy. The final engrossed thickness after impact is 4.37 mm. The original substrate laminate thickness is 3.12 mm.

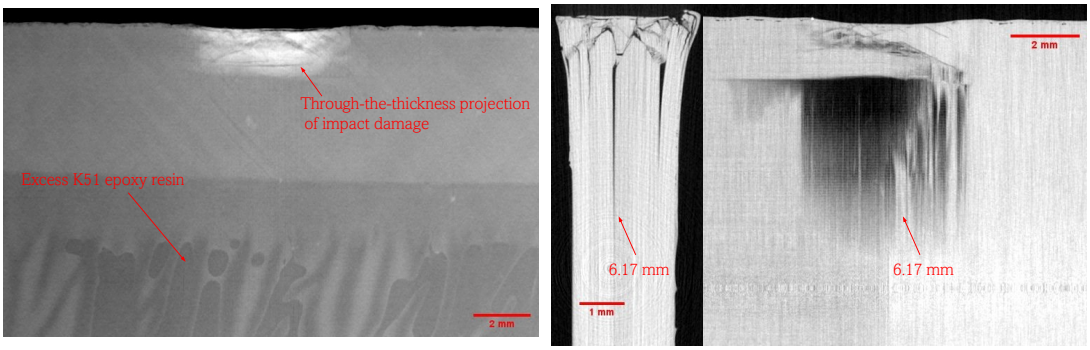

(a) **(b)**

Figure 7.16: Damage extent from a 5 J energy edge impact in a specimen with binding. (a) Front view projection of the summation of all slices through the thickness of the specimen. (b) Deepest cracks side view and front view at the deepest crack slice (6.17 mm). The dark lines in 90° represent the delamination at interface 4.

Figure 7.17 shows a comparison of the extent of the crack lengths in the x (length) direction of specimens without and with binding impacted with a 5 J impact energy. Different sliced cuts were made from the X-rayed scan to view the cracks at different depths (heights) from the top of the specimen, where the impact occurred. The extent of the cracks in the width of the specimens without binding and with binding are similar. However, the addition of the binding reduced the maximum length of the cracks. The different cracks are labelled in the comparison figure to be easier to track across the whole figure.

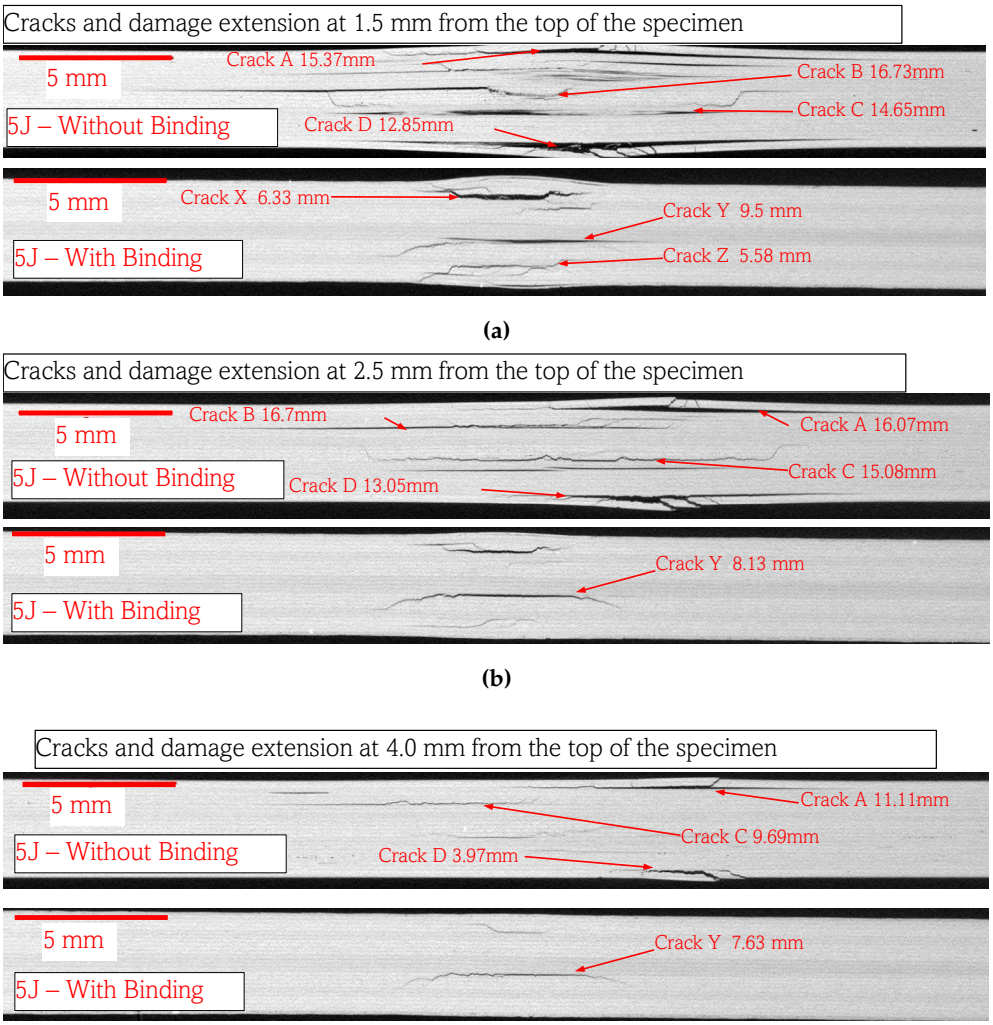

Figure 7.17: Comparison of crack lengths in the x (lengthwise) direction of specimens without and with binding for a 5 J impact energy. The images show the extent of the cracks at different distances from the impact point.

Figure 7.18 shows the cross-section and top view at the impact point of a 10 J energy impact specimen with binding. The thickness engrossment at the impact area is 2.33 times a cured laminate thickness of 3.12 mm. As in the case of the 5 J impact energy, the deepest cracks occurred at the 45° interfaces. Figure 7.19a displays the projection of all the X-rayed slices in the $x-y$ (length-width) plane. The shadowed area in the front view of figure 7.19b indicates the extent of the delamination of a crack in a 45/0 interface. The crack of 8.11 mm displayed in the cross-section view in figure 7.19b corresponds to the same crack displayed in the front view. The cross-section/front view displayed in figure 7.19b does not correspond to the exact deepest point of the crack, which is 10.05 mm, but the cross-section view and is only for indicating the location of the crack at interface 2.

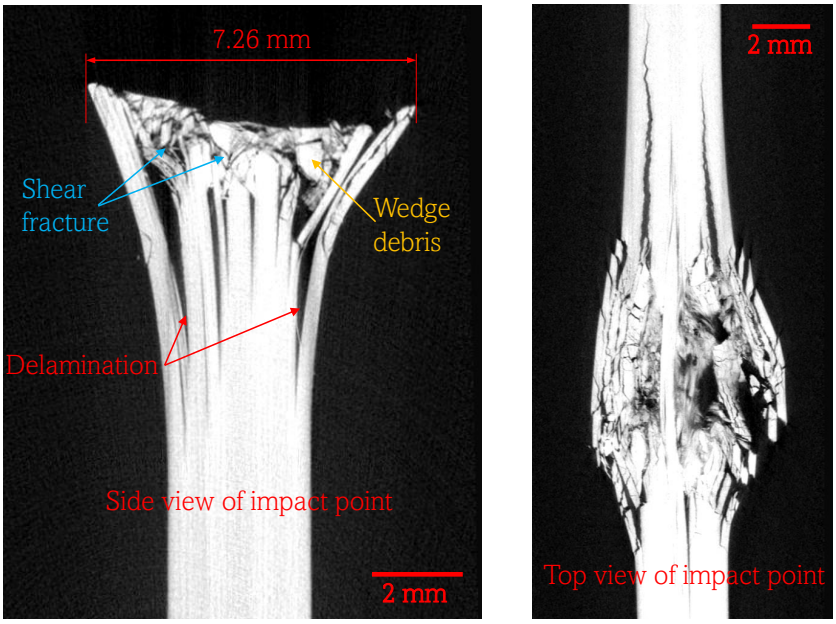

Figure 7.18: Cross-section and top view at the impact point of an edge impact specimen without binding impacted with 10 J energy. The final engrossed thickness after impact is 7.26 mm. The original substrate laminate thickness is 3.12 mm.

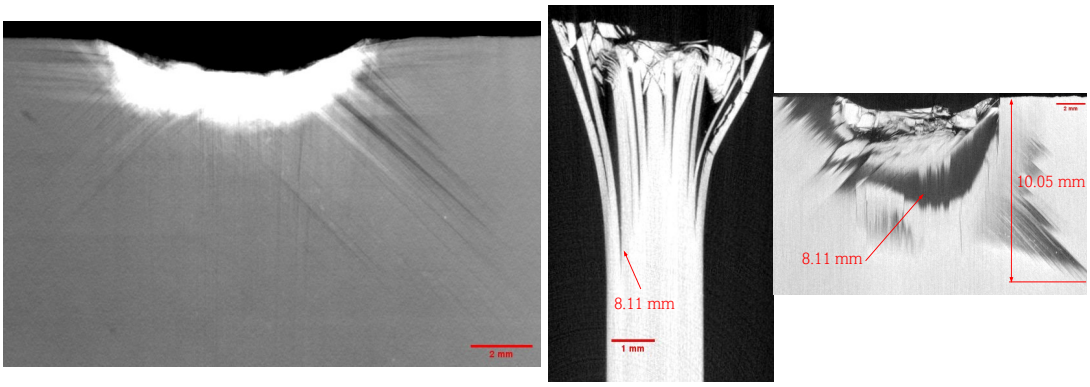

(a) **(b)**

Figure 7.19: Damage extent from a 10 J energy edge impact in a specimen without binding. (a) Front view projection of the summation of all slices through the thickness of the specimen. (b) Deepest cracks lateral view and interface view at the deepest crack slice.

Figure 7.20 shows the cross-section and top view at the impact point of a 10 J energy impact specimen with binding. The thickness engrossment at the impact area is 87% from a cured laminate thickness of 3.12 mm. Unlike in the 5 J impact energy case for the specimen with binding, the largest crack occurs at the 45/0 interfaces, as in the case of the specimens without binding. Figure 7.21a displays the projection of all the X-rayed slices in the $x-y$ (length-width) plane. The shadowed area in the frontal view of figure 7.21b indicates the extent of the delamination of a crack in a 45/0 interface, showing clearly the 45° orientation of the delamination. The crack of

7.14 mm displayed in the cross-section view in figure 7.21b corresponds to the same crack displayed in the front view. The cross-section view displayed in figure 7.21b does not correspond to the exact deepest point of the crack, which is 8.88 mm deep, but is only for indicating the location of the crack at interface 2.

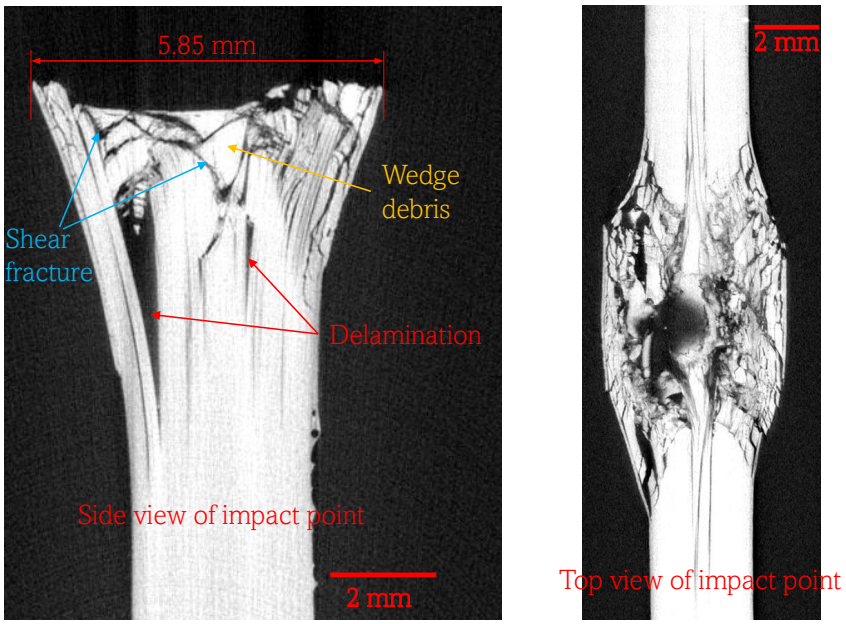

Figure 7.20: Cross-section and top view at the impact point of an edge impact specimen with binding impacted with 10J energy. The final engrossed thickness after impact is 5.85 mm. The original substrate laminate thickness is 3.12 mm.

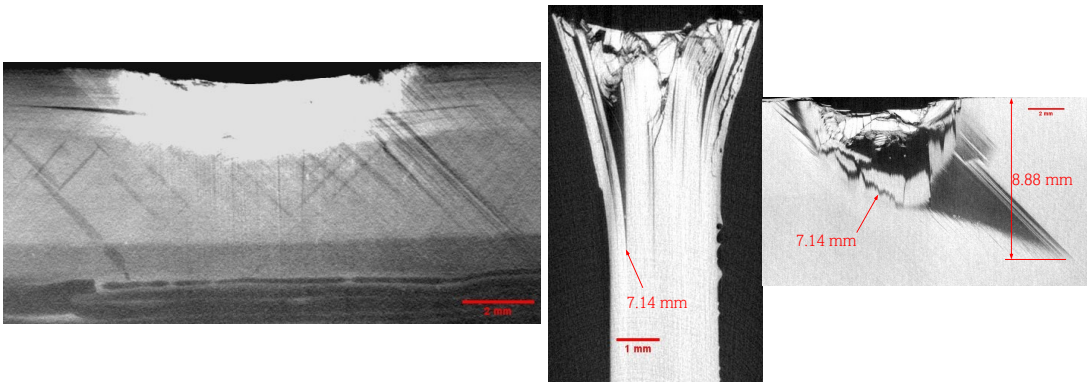

(a) **(b)**

Figure 7.21: Damage extent from a 10 J energy edge impact in a specimen with binding. (a) Front view projection of the summation of all slices through the thickness of the specimen. (b) Deepest cracks lateral view and interface view at the deepest crack slice.

Figure 7.22 shows a comparison of the extent of the crack lengths in the x (length) direction of specimens without and with binding impacted with a 10 J impact energy. Different sliced cuts were made from the X-ray scan to view the cracks at different depths from the top of the specimen, where the impact occurred. The extent of the cracks in the width of the specimens without binding and with binding are similar.

However, the addition of the binding reduced the maximum length of the cracks. Different cracks are pointed and labelled in the comparison figures to be easier to track across the whole figure.

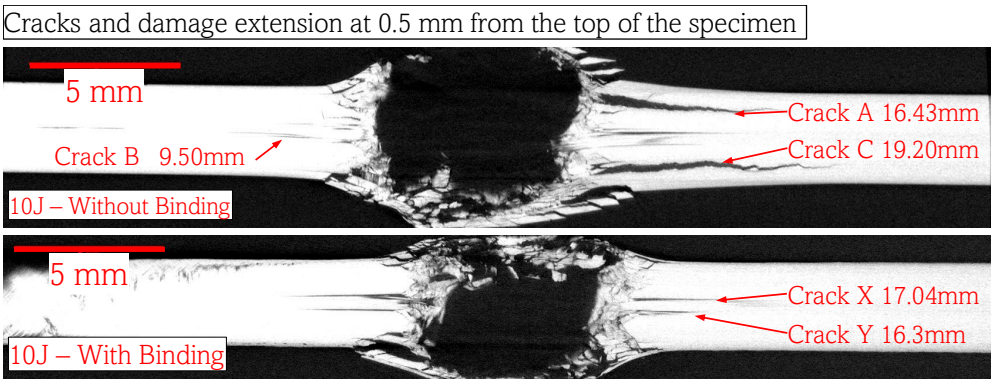

(a)

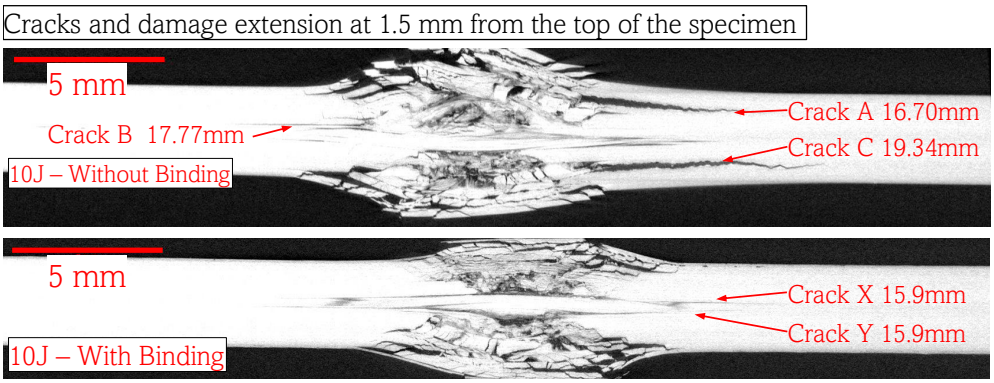

(b)

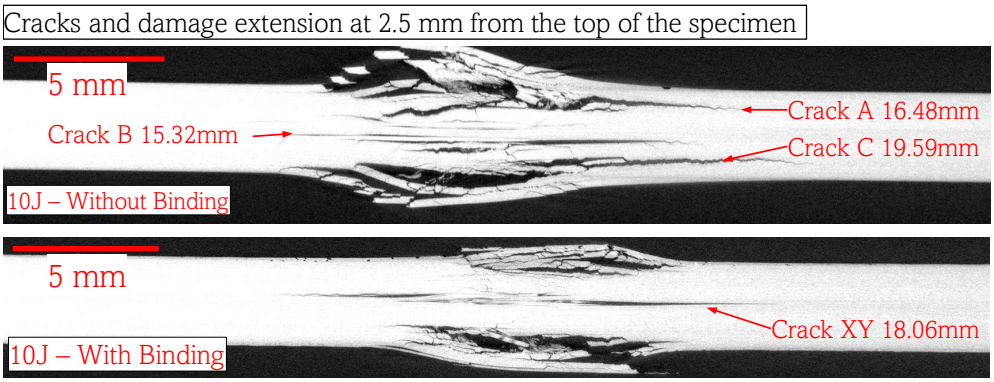

(c)

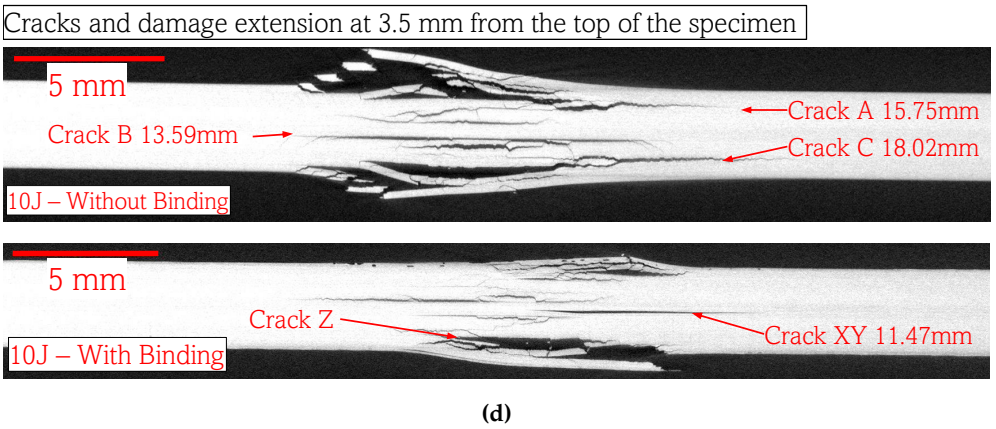
Cracks and damage extension at 3.5 mm from the top of the specimen
5 mm
Crack B 13.59mm
Crack A 15.75mm
Crack C 18.02mm
10J – Without Binding
5 mm
Crack Z
Crack XY 11.47mm
10J – With Binding

(d)

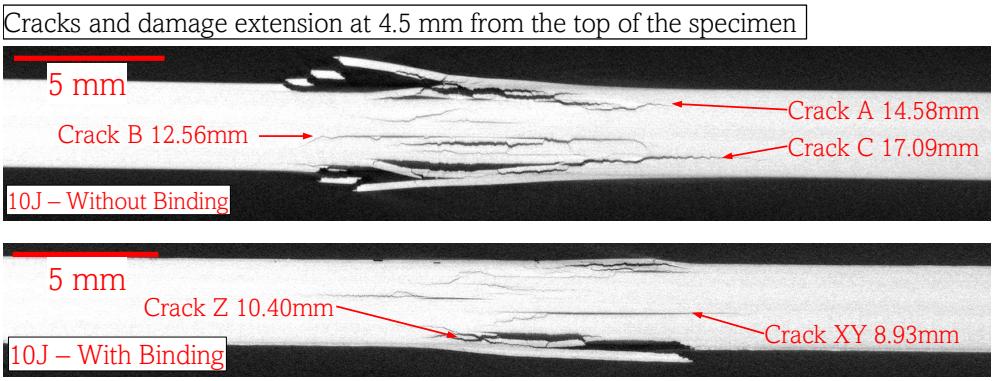
Cracks and damage extension at 4.5 mm from the top of the specimen
5 mm
Crack B 12.56mm
Crack A 14.58mm
Crack C 17.09mm
10J – Without Binding
5 mm
Crack Z 10.40mm
Crack XY 8.93mm
10J – With Binding

(e)

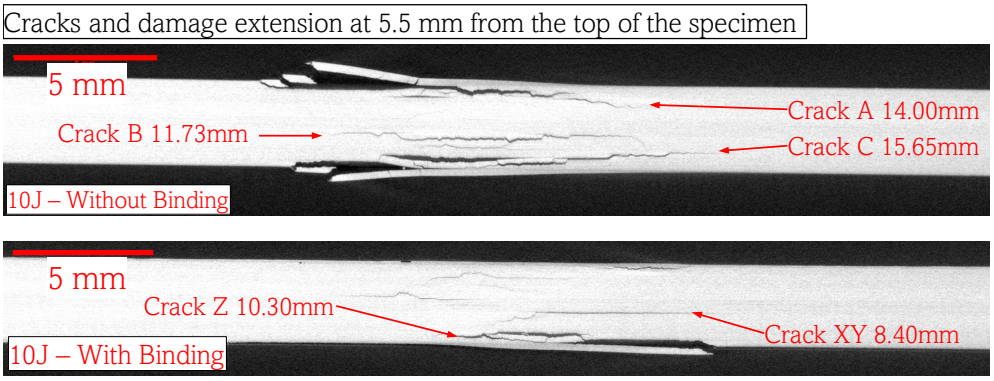
Cracks and damage extension at 5.5 mm from the top of the specimen
5 mm
Crack B 11.73mm
Crack A 14.00mm
Crack C 15.65mm
10J – Without Binding
5 mm
Crack Z 10.30mm
Crack XY 8.40mm
10J – With Binding

(f)

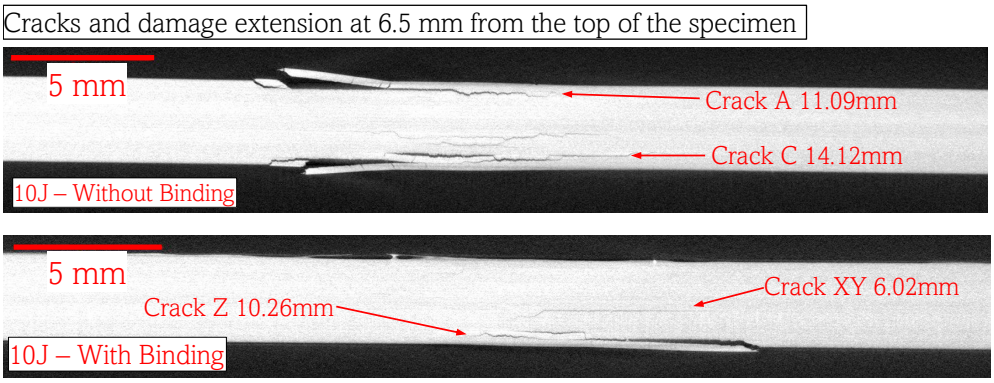
Cracks and damage extension at 6.5 mm from the top of the specimen
5 mm
Crack A 11.09mm
Crack C 14.12mm
10J – Without Binding
5 mm
Crack Z 10.26mm
Crack XY 6.02mm
10J – With Binding

(g)

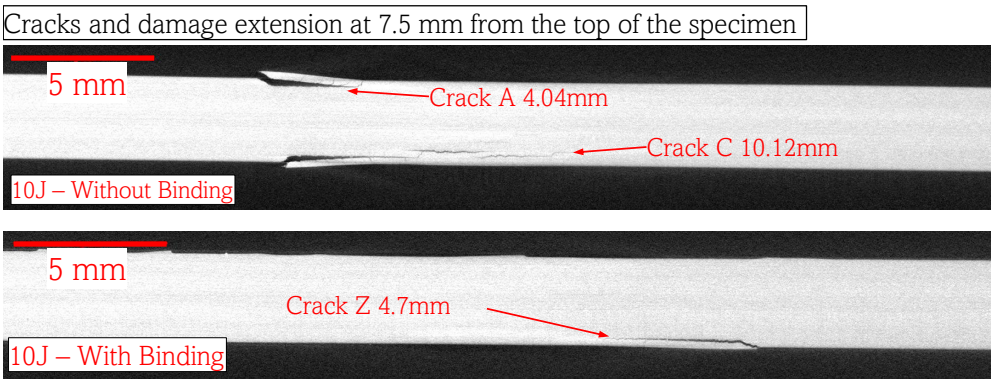

(h)

Figure 7.22: comparison of crack lengths in the x (lengthwise) direction of specimens without and with binding for a 10 J impact energy. The images show the extent of the cracks at different distances from the impact point.

Figure 7.23 shows the cross-section and top view at the impact point of a 15 J energy impact specimen without binding. The thickness engrossment at the impact area is 2.55 times from a cured laminate thickness of 3.12 mm. As in the case of the 5 J impact energy, the deepest cracks occurred at the $0/45°$ interfaces, and a great damage area was left after the impact. Figure 7.24a displays the projection of all the X-rayed slices in the $x - y$ (length-width) plane, showing the depth extent of the permanent indent at the impact point. The shadowed area in the frontal view of figure 7.24b indicates the extent of the delamination of a crack in a $45/0$ interface. Additionally, a significant crack is visible at the block of $90°$ plies in the centre of the laminate. The crack of 11.46 mm displayed in the cross-section view in figure 7.24b corresponds to the same crack displayed in the front view, albeit the cross-section view does not correspond to the exact point of the crack, which is 12.36 mm and is only for indicating the location of the crack.

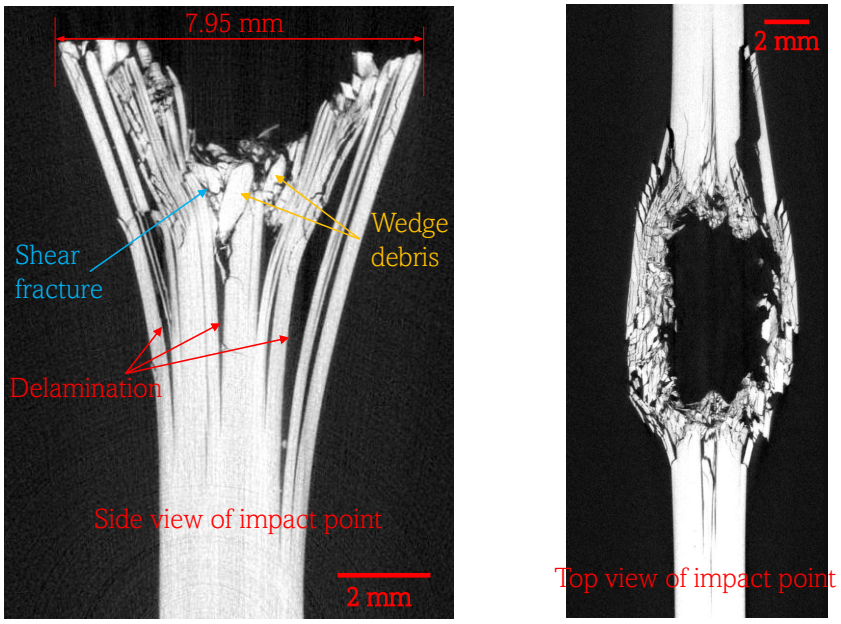

Figure 7.23: Cross-section and top view at the impact point of an edge impact specimen without binding impacted with 15 J energy. The final engrossed thickness after impact is 7.95 mm. The original substrate laminate thickness is 3.12 mm.

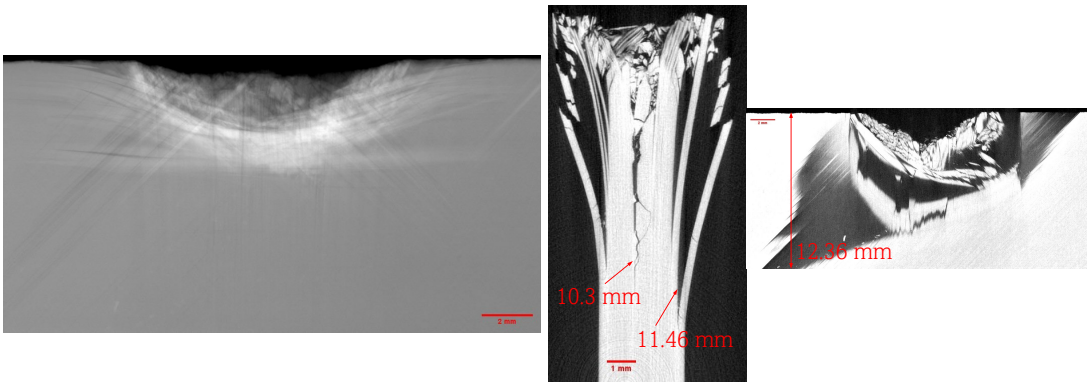

(a) **(b)**

Figure 7.24: Damage extent from a 15 J energy edge impact in a specimen without binding. (a) Front view projection of the summation of all slices through the thickness of the specimen. (b) Deepest cracks lateral view and interface view at the deepest crack slice.

Figure 7.25 shows the cross-section and top view at the impact point of a 15 J energy impact specimen with binding. The thickness engrossment at the impact area is 2.39 times from a cured laminate thickness of 3.12 mm. Unlike in the 5 J impact energy case for the specimen with binding, the largest crack occurs at the 45/0 interfaces, as in the case of the specimens without binding. Figure 7.26a displays the projection of all the X-ray slices in the $x-y$ (length-width) plane. The shadowed area in the frontal view of figure 7.26b indicates the extent of the delamination of a crack in a 45/0 interface, showing clearly the 45° orientation of the delamination. The crack of

10.13 mm displayed in the cross-section view in figure 7.26b corresponds to the same crack displayed in the front view, albeit the cross-section view does not correspond to the exact point of the crack, which is 13.17 mm deep and is only for indicating the location of the crack.

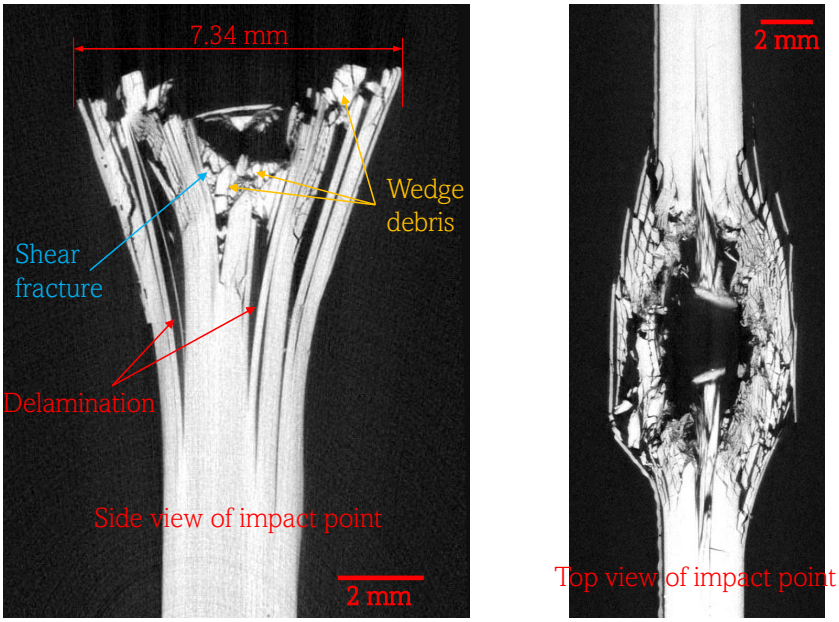

Figure 7.25: Cross-section and top view at the impact point of an edge impact specimen with binding impacted with 15 J energy. The final engrossed thickness after impact is 7.45 mm. The original substrate laminate thickness is 3.12 mm.

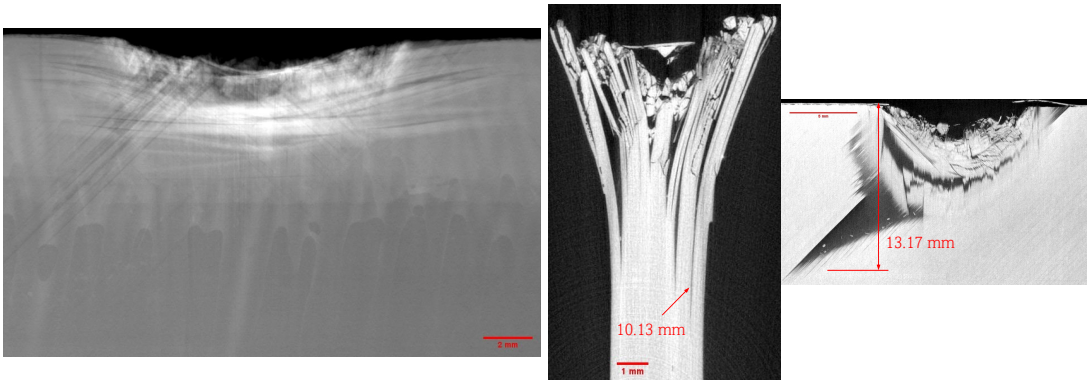

(a) **(b)**

Figure 7.26: Damage extent from a 15 J energy edge impact in a specimen with binding. (a) Front view projection of the summation of all slices through the thickness of the specimen. (b) Deepest cracks lateral view and interface view at the deepest crack slice.

Figure 7.27 shows a comparison of the extent of the crack lengths in the x (length) direction of specimens without and with binding impacted with a 15 J impact energy. Different sliced cuts were made from the X-ray scan to view the cracks at different depths from the top of the specimen, where the impact occurred. The extent of the cracks in the width of the specimens without binding and with binding are similar.

As in the previous cases of 5 and 10 J impact energy, adding the additive binding reduced the length of the cracks. The different cracks are pointed and labelled in the comparison figure to be easier to track across the whole figure.

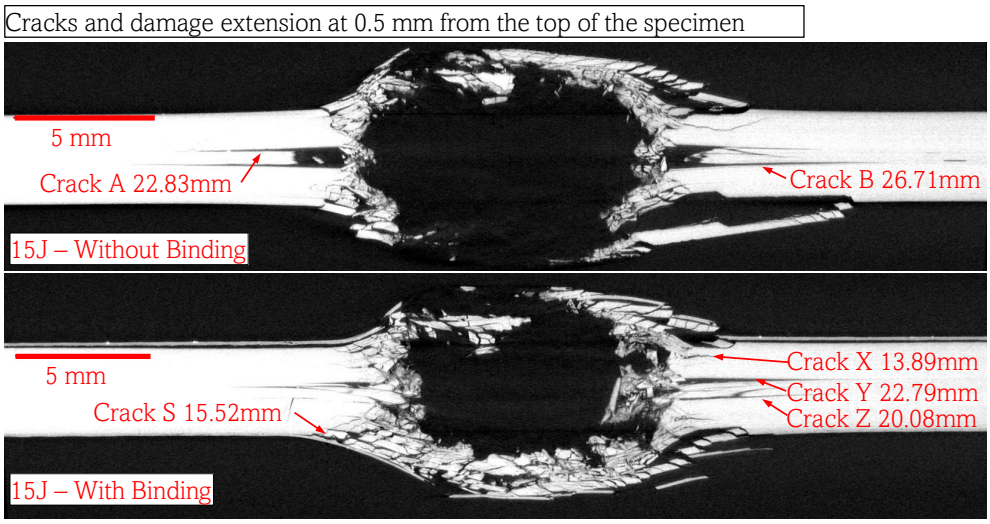

(a)

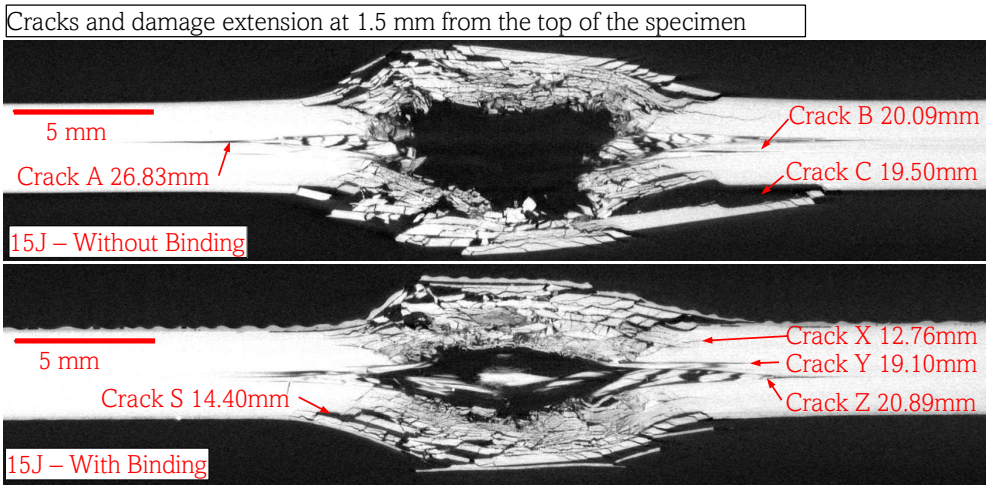

(b)

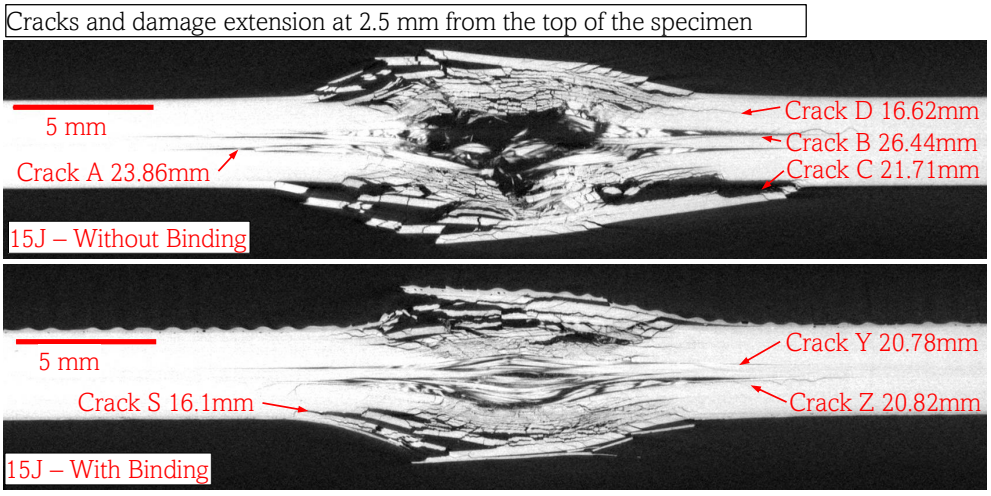

(c)

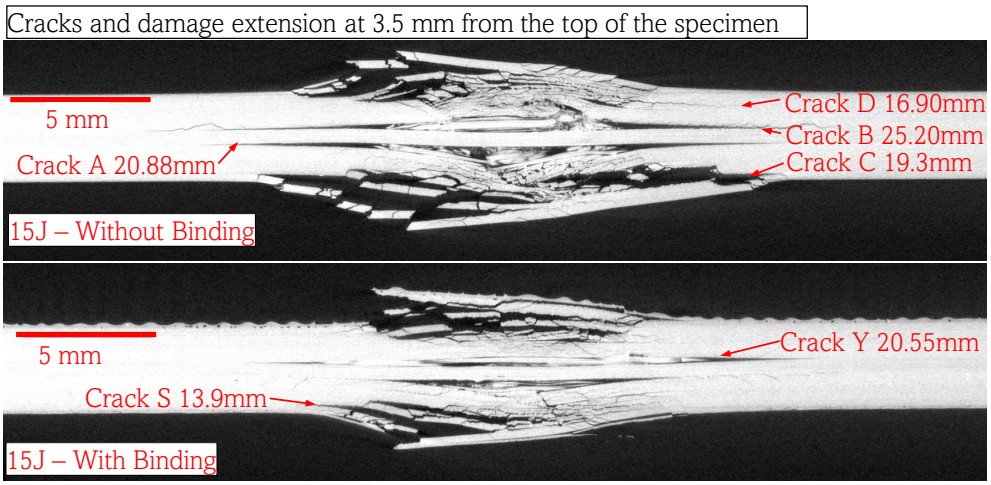
Cracks and damage extension at 3.5 mm from the top of the specimen
5 mm
Crack A 20.88mm
Crack D 16.90mm
Crack B 25.20mm
Crack C 19.3mm
15J – Without Binding
5 mm
Crack S 13.9mm
Crack Y 20.55mm
15J – With Binding

(d)

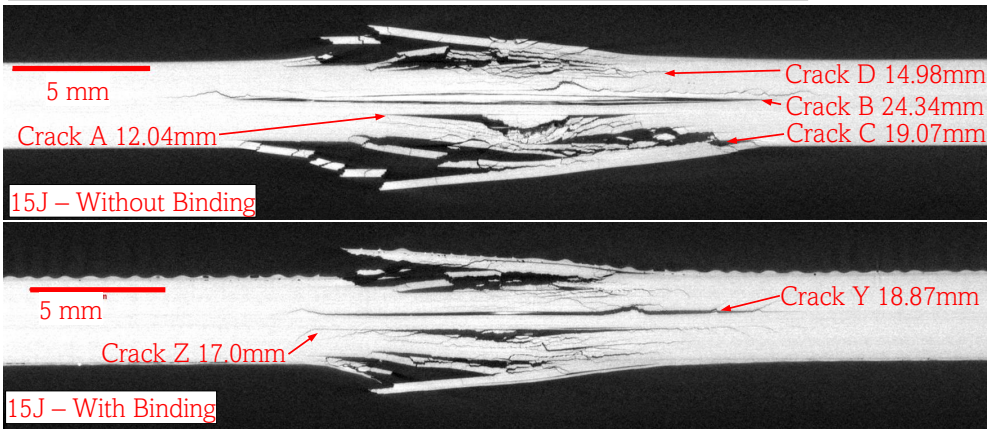
Cracks and damage extension at 4.5 mm from the top of the specimen
5 mm
Crack A 12.04mm
Crack D 14.98mm
Crack B 24.34mm
Crack C 19.07mm
15J – Without Binding
5 mm
Crack Z 17.0mm
Crack Y 18.87mm
15J – With Binding

(e)

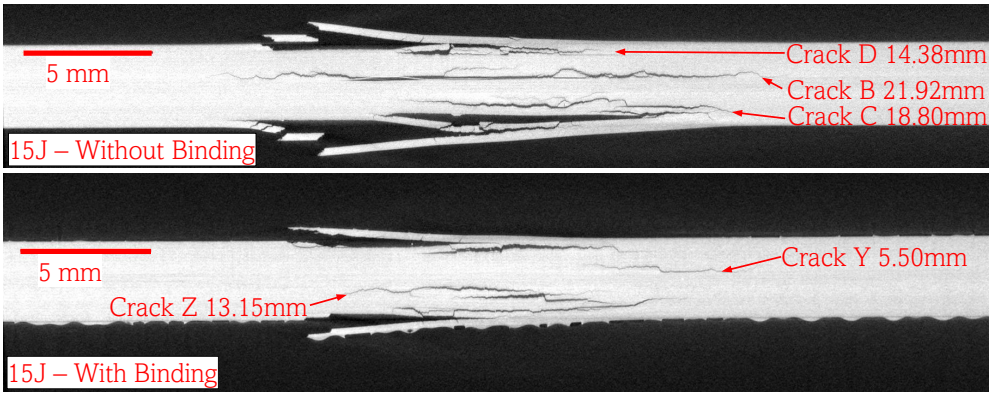
Cracks and damage extension at 7.0 mm from the top of the specimen
5 mm
Crack D 14.38mm
Crack B 21.92mm
Crack C 18.80mm
15J – Without Binding
5 mm
Crack Z 13.15mm
Crack Y 5.50mm
15J – With Binding

(f)

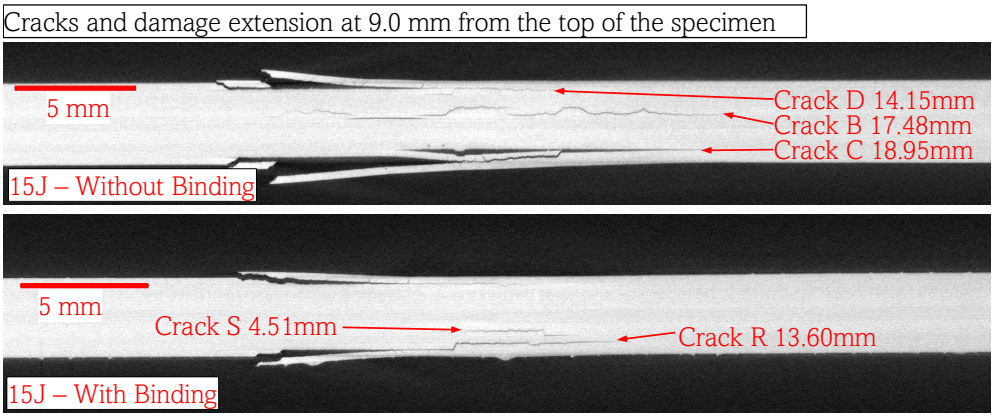

(g)

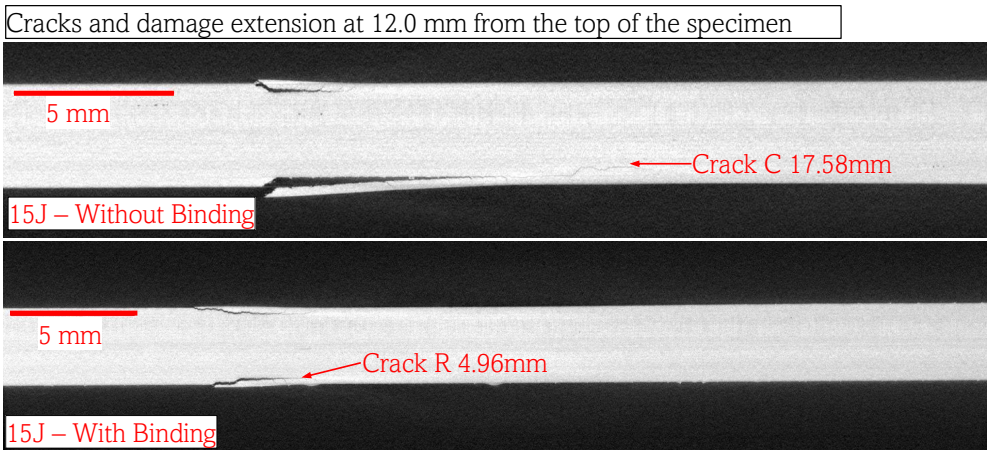

(h)

Figure 7.27: comparison of crack lengths in the x (lengthwise) direction of specimens without and with binding for a 15 J impact energy. The images show the extent of the cracks at different distances from the impact point.

Figure 7.28 shows a comparison of the dimensions of the longest cracks in the lengthwise direction (x) for the three levels of energy shown in figures 7.17, 7.22 and 7.27 as a function of the distance to the impact point. It is interesting to note that the lengths of the cracks for specimens with binding seem to be similar to the size of the cracks from lower impact energy of specimens without binding.

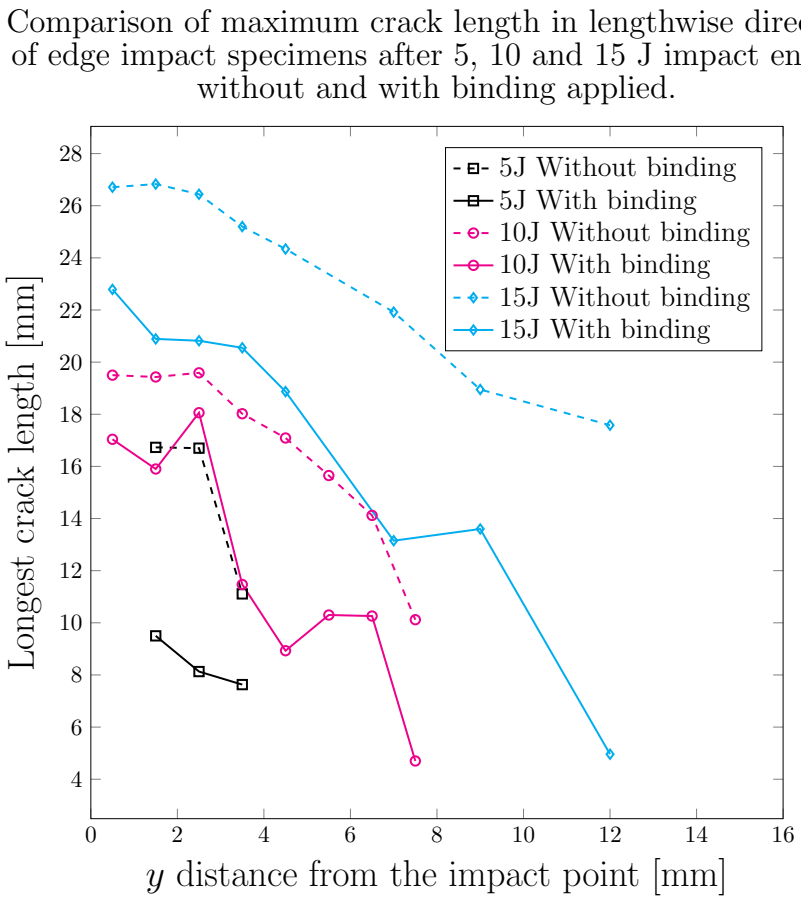

Figure 7.28: Comparison of maximum crack length in the x direction of edge impact specimens after 5, 10 and 15 J impact energy without and with binding applied.

7.4 Discussion

The edge impact caused delamination in all interfaces. As reported in the FE results, the value of $\mathcal{G}$ at all interfaces presented high enough values for the crack to develop. The FE results indicated a significant reduction of $\mathcal{G}$ at the different interfaces when the additive binding was added. However, the values of $\mathcal{G}$ were not small enough for arresting delamination, not even for the longest pre-crack lengths.

As in the case of section 6.5, no data was found for the fracture toughness values of the IM7/913, so the value of fracture toughness $\mathcal{G}_{Ic}$ and $\mathcal{G}_{IIc}$, which are known to be mostly matrix dependant, were taken as $\mathcal{G}_{Ic}$=0.25 N/mm and $\mathcal{G}_{IIc}$=1.08 N/mm, estimated from E-Glass/913 prepreg in [267]. Additionally, $\mathcal{G}_{IIIc}$ was assumed equal to $\mathcal{G}_{IIc}$ as per the common practice [280]. For a pre-crack length of 0.25 mm and an applied impactor vertical displacement of 0.5 mm, the values of $\mathcal{G}$ at interfaces 1, 2 and 3 are much higher than any of the $\mathcal{G}_{ic}$ (i = I, II, III). Moreover, it is for a pre-crack of 1.5 mm that the value of $\mathcal{G}$ is high enough at interface 4 for it to delaminate.

The load-displacement curves presented are similar to those presented in [167]. First,

a peak load was reached, after which a sudden drop in the load placed the axial force in a plateau which extended for several ms and in which crushing of the laminate occurred. Finally, a drop in load determined the maximum permanent indentation created on the edge of the specimen. Interestingly, the peak force reached in the specimens with binding is higher than the peak force in the cases without binding. Thus, the plateau load value observed in the cases with binding is also higher than the plateau load value in the cases without binding. This phenomenon could be explained as the addition of the binding is providing extra support to the fibres so they do not break under compression, strengthening the edge and the fibres finishing at the edge. As the initial moments of the damage are ruled by the strength of the fibres in the direction of the impact, the support given by the binding pushes the fibre compression failure load higher, which conduces to a higher peak load.

As shown in the XCT scannings of figures 7.13, 7.15, 7.18, 7.20, 7.23 and 7.25, cracks of 1.5 mm are easily originated from the crack impact in the form of kink bands and wedge effects, and hence the interface 4 (0/90) also delaminate. In this manner, the model predicted correctly that all interfaces would delaminate.

The specimens with additive binding presented shorter cracks in the length direction after the impact. However, the additive bindings did not seem to have a significant impact on the vertical extent of the damage for the different impact energy tested (5, 10 and 15 J). For instance, only in the 10 J impact energy case, the extent of the cracks in the width direction (y direction) was less in the case with binding. Furthermore, the deepest cracks for the case of the 5 J specimens were almost of the same dimensions for both cases, without and with binding, as seen in figures 7.14b and 7.16b. On the other hand, in the case of the 10 J specimens, cracks were 11.6% less deep in the specimen with binding, as shown in figures 7.19b and 7.21b. Furthermore, for the 15 J specimen, the specimens with binding presented a very similar value of crack depth to those of specimens without binding.

On the other side, as shown in figure 7.28, the additive bindings reduced the extent of the delaminations occurring in the length direction. For example, at a depth of 3.5 mm from the impact point, the crack length extension was reduced by 31.3% for the 5 J specimens, 36.3% for the 10 J specimens and 18.5% for the 15 J specimens.

It is to be noted that the total thickness of the substrate laminate is thinner than those laminates studied by Ostre et al. in [167], although the impact energies used in [167] were higher than the ones used in this study.

7.5 Conclusion

The use of additive bindings in the form of thin laminates bonded to the edge of a composite laminate have been studied to enhance the damage tolerance of composite laminates under edge impact. Furthermore, a FE numerical analysis has been conducted to study the feasibility of such a solution in arresting or suppressing delamination from the event of an edge-on impact. Additionally, experimental testing was carried out to determine the enhancement achieved in the damage tolerance of edge-impacted specimens when the additive binding was in place. Finally, the concluding points of this study are mentioned below:

- The use of additive bindings reduced the extent of the crack lengths in the lengthwise direction by about 31%, 36% and 19% for the specimens impacted with 5 J, 10 J and 15 J, respectively.
- The presence of the additive bindings strengthened the edge of the laminate, and a higher average peak load and plateau load were observed for specimens with binding.
- Despite the presence of the additive binding, the edge-on impact produced delamination in all the interfaces as predicted by the VCCT model and reported in the FE results.
- Further investigations should be carried out with thicker substrate laminates for studying if the additive bindings perform better in thicker substrate laminates, e.g., Ostre et al. [167] laminate thickness.

Chapter 8

Results on suppressing delamination in composite laminates with open holes

This chapter presents the numerical and experimental results for the third research question. FE analyses have been conducted to determine an appropriate additive binding configuration for suppressing delamination from the edge of the hole in the centre of the laminate. Then, experimental testing as described in section 5.6 was carried out to study the effectiveness of the solution. Some experimental specimens were XCT scanned, and clear damage profiles after impact were shown. The results are presented, discussed, and finally, conclusions are drawn.

8.1 Substrate laminate selection

An industry-used stacking sequence was selected for the composite laminates with open holes. Based on the work carried in [21, 205, 211, 212, 216], a quasi-isotropic laminate was selected with a stacking sequence of $[45_m/0_m/-45_m/90_m]_n s$. A stacking sequence with $m = 4$ and $n = 1$ was selected, as this configuration was specified to fail by delamination, as shown in figure 2.28. As the purpose of the additive binding is to stop delamination or enhance the response of composite laminates with open holes to delamination, a layup highly susceptible to failure due to delamination was selected.

A diameter of 6 mm was decided for the hole, and hence based on figure 5.7, the total length of specimens was 200 mm, the free length between end-tabs was 120 mm, and the width was 30 mm. The total laminate thickness was 4.16 mm.

8.2 FE results

Different crack lengths at three interfaces between layer blocks with different fibre orientations were modelled due to the symmetry of the laminate from its through-the-thickness mid-plane, as explained in section 4.4. The bonded nodes extended across the laminate from the crack tip nodes, schematically shown in figure 8.1.

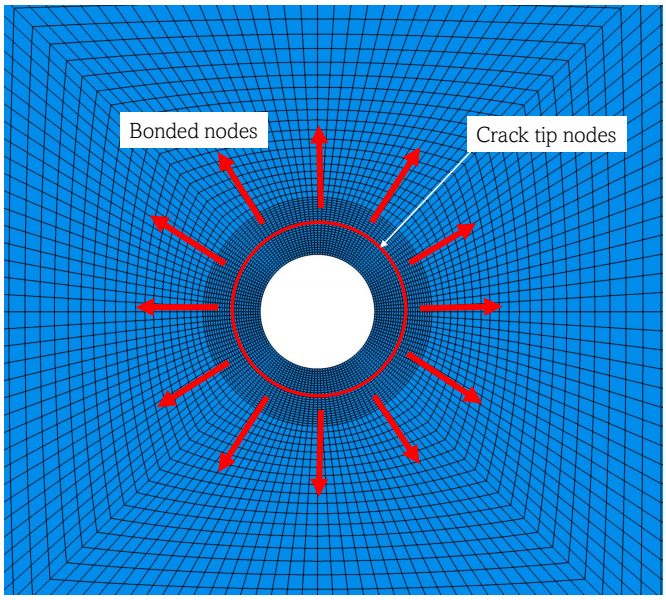

Figure 8.1: Definition of the crack tip nodes between interfaces at the fine mesh area. The red arrows indicate the perpendicular direction to the delamination tip, needed for the FE modelling and definition of the crack in Abaqus.

The crack tip bonded nodes were defined around the whole circumference of the

hole, so the crack tip node has a circular shape. For this reason, a blended method between the ones used in 6.2 and 7.2 for the display of $\mathcal{G}$ at the crack tip was used. In this way, a bubble chart was used to represent the value of the energy release rate around the crack tip. Figure 8.2 shows the normalised energy release rate $\mathcal{G}/\mathcal{G}_{max}$ variation for different pre-crack lengths at different interfaces. The values of $\mathcal{G}/\mathcal{G}_{max}$ are arranged around the deformed shape of the hole after loading (ellipsoidal shape) and are represented by the diameter/radius of the bubble printed at the coordinates of each crack tip node, as shown in figure 8.2. Hence, the larger the diameter of the circle in figure 8.2, the larger the energy release rate at that node. The maximum value $\mathcal{G}_{max}$ occurs for a delamination length of 0.125 mm at interface 1. For reference, $\mathcal{G}_{max} = 3.664 N/mm$. The coordinates x and y are referenced from the centre of the hole and refer to the position of the nodes in the deformed shape of the hole. Additionally, for a clearer understanding of the variation of $\mathcal{G}/\mathcal{G}_{max}$ around the hole, figure 8.3 displays the variation of $\mathcal{G}/\mathcal{G}_{max}$ around the crack tip with respect to the 0° fibre orientation. The location of the crack tip is varied with angle increments of 2.5° (α angle) from 0° to 360°.

The values of $\mathcal{G}/\mathcal{G}_{max}$ displayed in figure 8.2 show how the highest value of energy release rate changes as the delamination size increases for the three interfaces when an axial strain of 1% is applied. It is visible how interfaces 1 and 2 present higher values of $\mathcal{G}$ than interface 3. In particular, the values of $\mathcal{G}$ at both interfaces 1 and 2 are very close, indicating that both interfaces could have the same probabilities of delaminating. In reality it is known that all interfaces delaminate, as recollected in [21, 205, 211, 212, 216], and visualised in the experimental results shown in section 8.3.

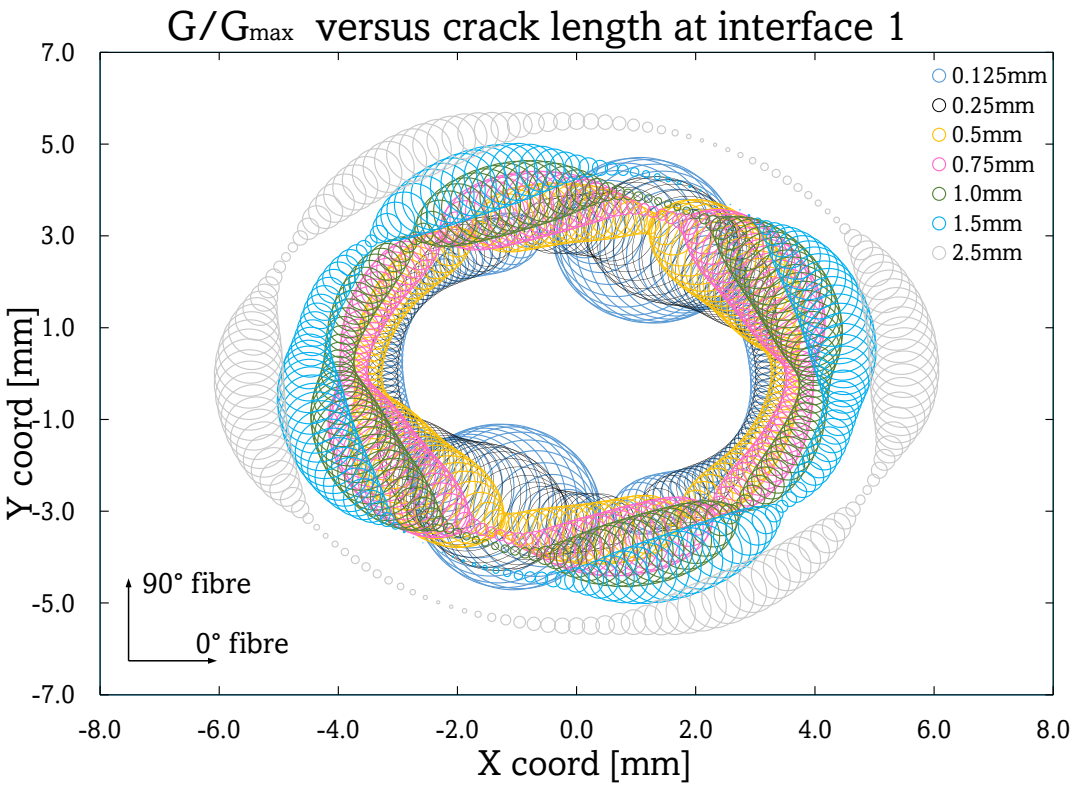
G/Gmax versus crack length at interface 1
0.125mm
0.25mm
0.5mm
0.75mm
1.0mm
1.5mm
2.5mm
90° fibre
0° fibre
Y coord [mm]
X coord [mm]
7.0
5.0
3.0
1.0
-1.0
-3.0
-5.0
-7.0
-8.0
-6.0
-4.0
-2.0
0.0
2.0
4.0
6.0
8.0

(a)

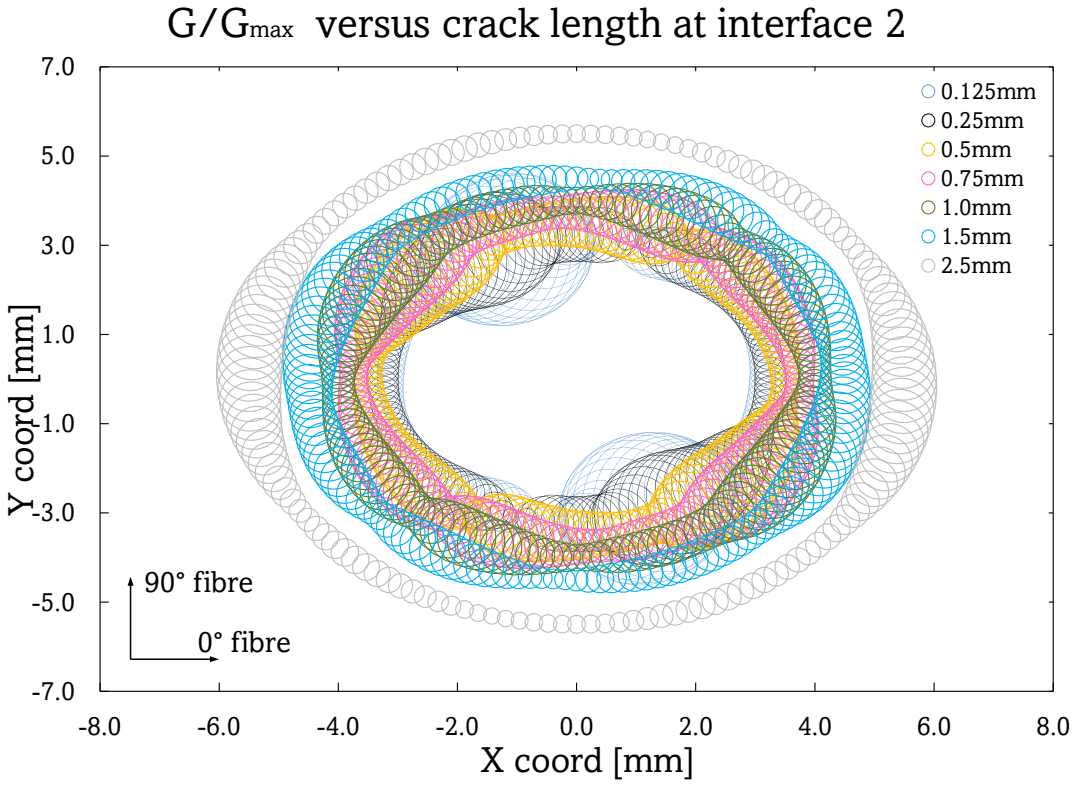
G/Gmax versus crack length at interface 2
0.125mm
0.25mm
0.5mm
0.75mm
1.0mm
1.5mm
2.5mm
90° fibre
0° fibre
Y coord [mm]
X coord [mm]
7.0
5.0
3.0
1.0
-1.0
-3.0
-5.0
-7.0
-8.0
-6.0
-4.0
-2.0
0.0
2.0
4.0
6.0
8.0

(b)

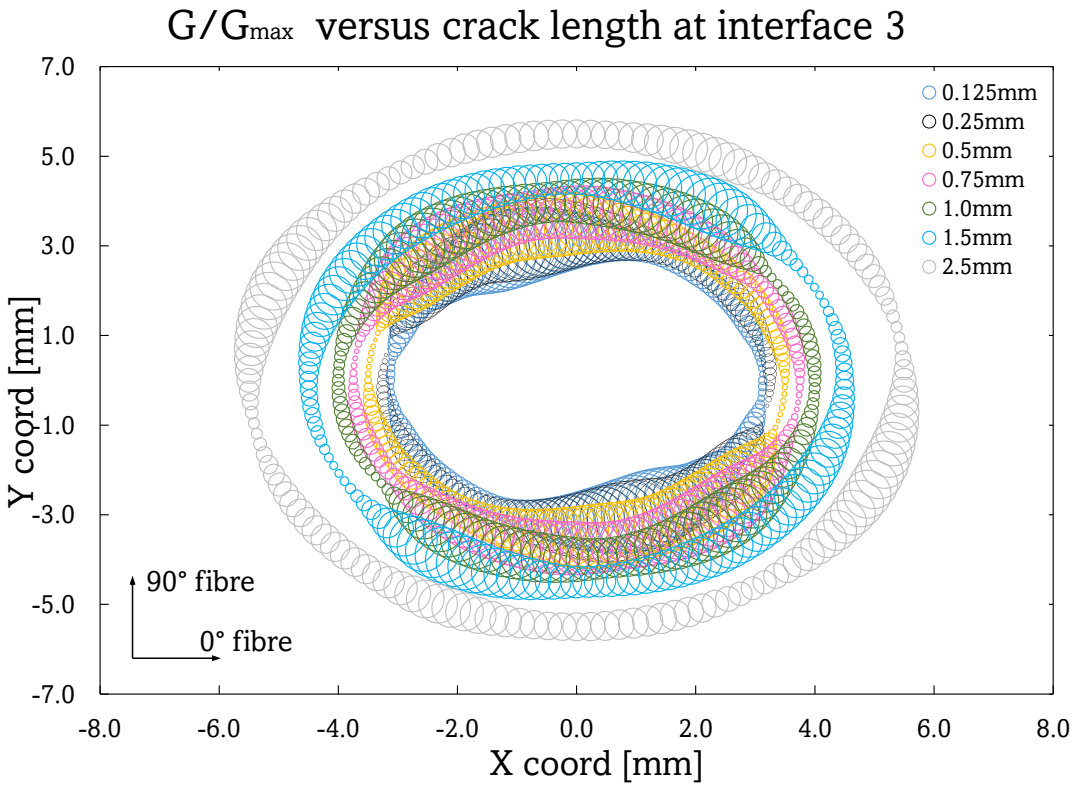

(c)

Figure 8.2: Normalised energy release rate $\mathcal{G}/\mathcal{G}_{max}$ around the crack tip of the open hole for different crack lengths. (a) Interface 1, (b) interface 2, (c) interface 3.

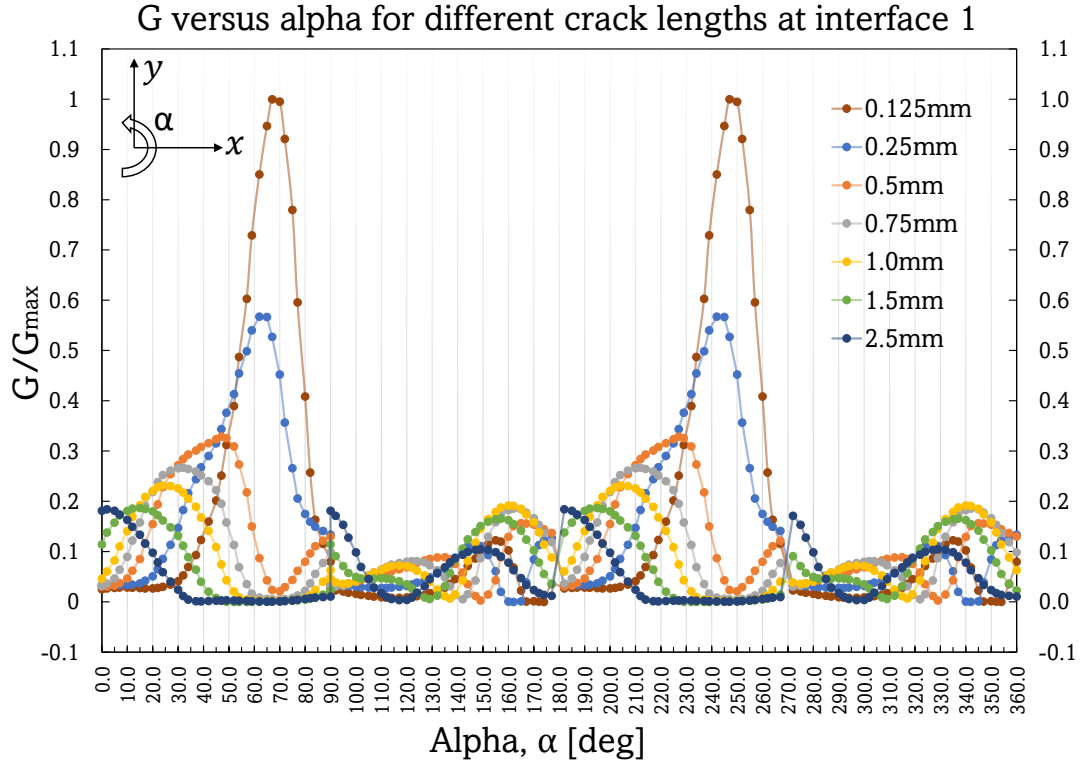

(a)

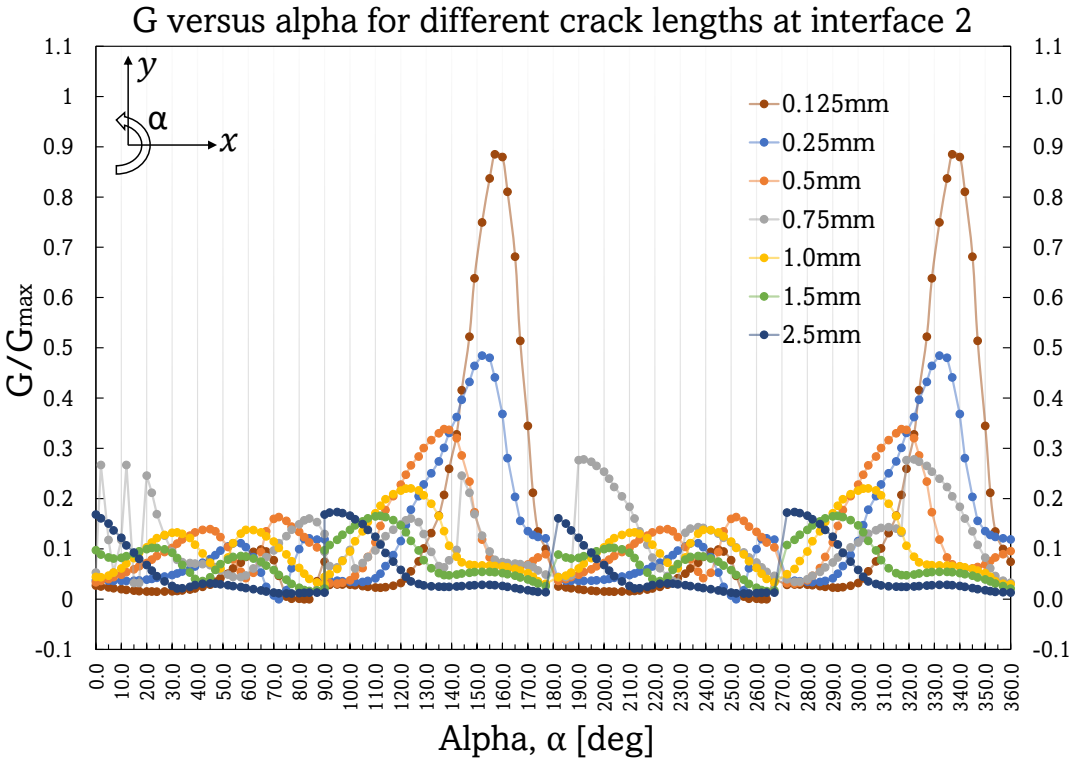

(b)

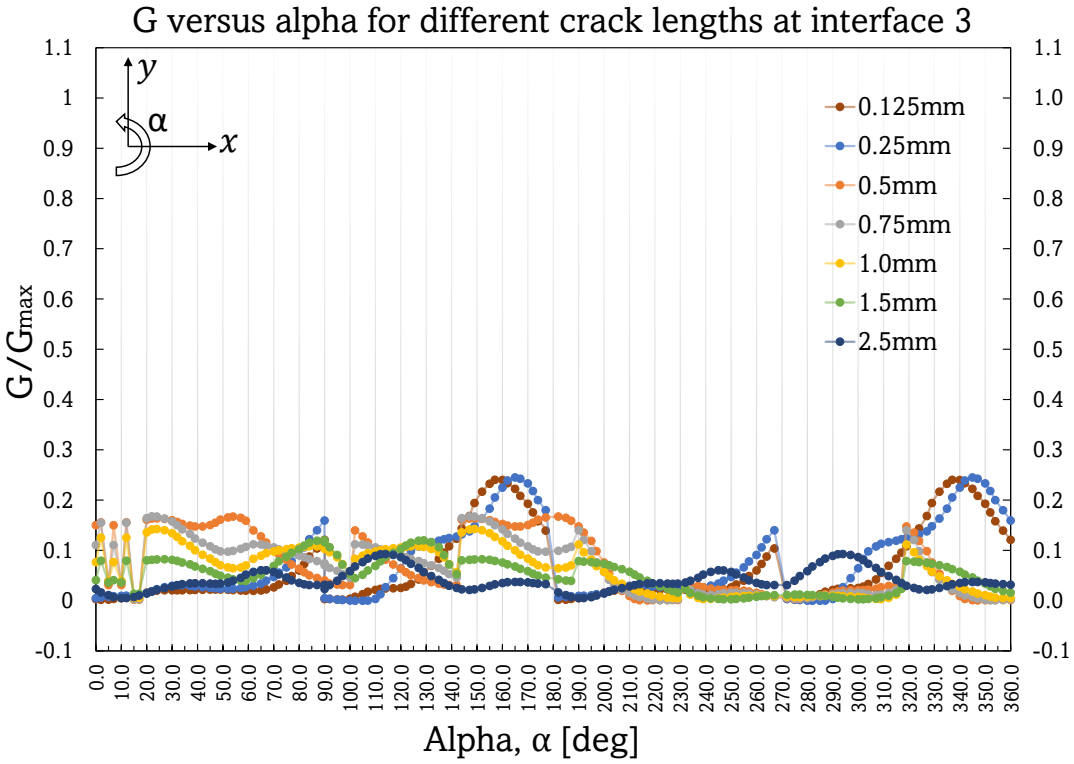

(c)

Figure 8.3: Normalised energy release rate $\mathcal{G}/\mathcal{G}_{max}$ around the crack tip of the open hole for different crack lengths with their location respect the 0° fibre orientation. (a) Interface 1, (b) interface 2, (c) interface 3.

As shown in figures 8.2 and 8.3, the minimum and maximum delamination lengths simulated were 0.125 and 2.5 mm. For a clearer visualisation of the magnitude of $\mathcal{G}$ at each interface, figure 8.4 compares the value of $\mathcal{G}/\mathcal{G}_{max}$ between the three interfaces at crack lengths of 0.125 and 2.5 mm. As logically expected, due to the ± 45 layers, interfaces 1 and 2 experience the highest values of $\mathcal{G}$ at symmetrically opposite points from the centre of the hole. The FE model is linearly elastic, and for ease of analysis and comparison, all simulations were performed with 1% applied strain.

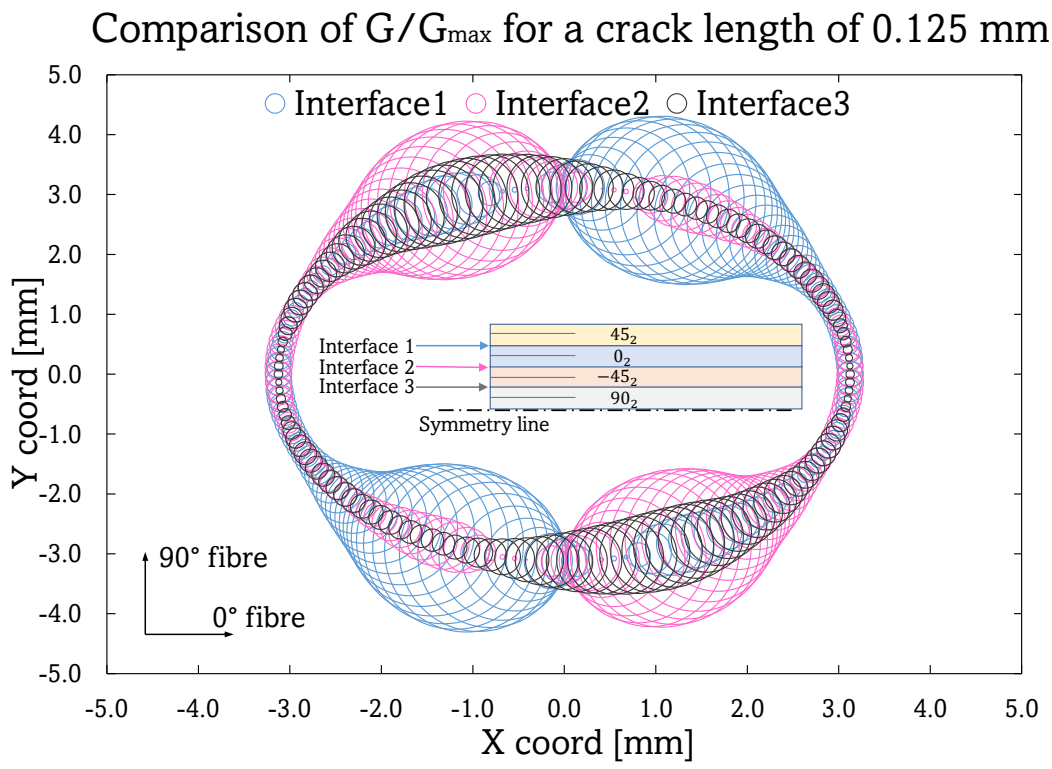

(a)

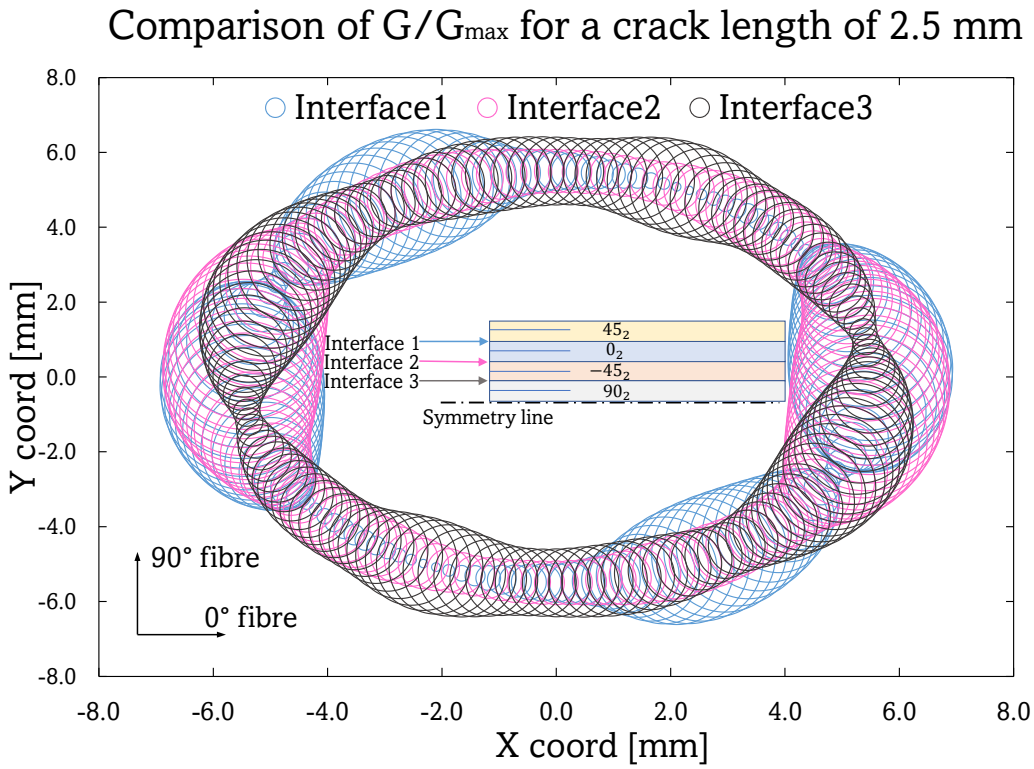
Comparison of G/Gmax for a crack length of 2.5 mm
Interface1
Interface2
Interface3
Interface 1
Interface 2
Interface 3
45₂
0₂
−45₂
90₂
Symmetry line
90° fibre
0° fibre
Y coord [mm]
X coord [mm]

(b)

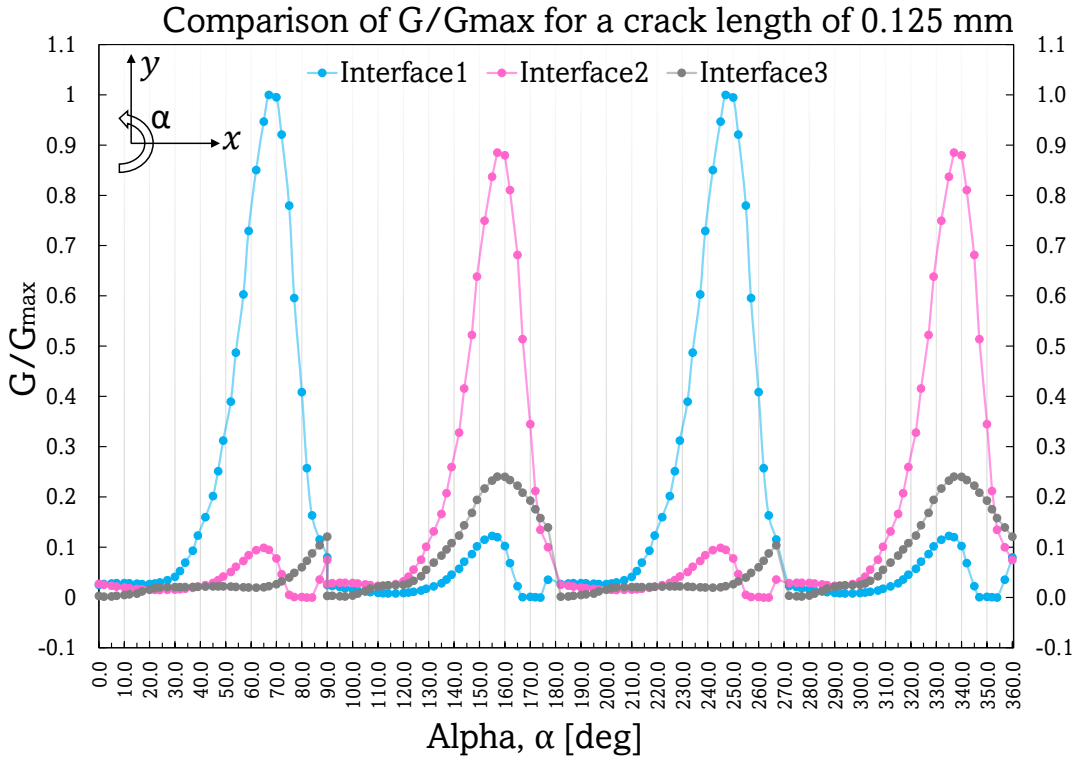
Comparison of G/Gmax for a crack length of 0.125 mm
Interface1
Interface2
Interface3
y
α
x
G/Gmax
Alpha, α [deg]

(c)

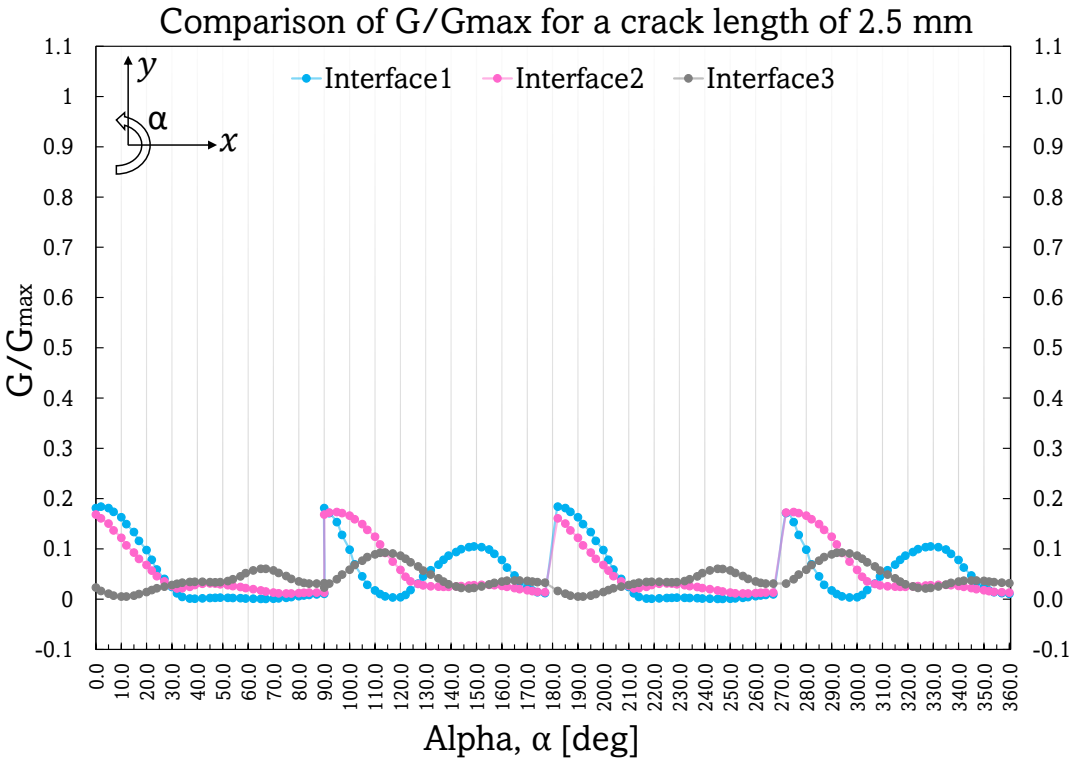

(d)

Figure 8.4: comparison of normalised energy release rate $\mathcal{G}/\mathcal{G}_{max}$ around the crack tip of the open hole for the different interfaces modelled. (a), (c) Crack length of 0.125 mm, (b)(d) crack length of 2.5 mm.

8.2.1 Binding design

Narrow and thin additive binding laminates were added to the substrate laminate in the form of stripes. Although from the edge of the hole the binding layup is $[\pm\theta]_s$, contrary to the case of the free-edge delamination specimens, the additive binding stripes are unidirectional narrow composite laminates. were unidirectional. For varying the angle of the additive binding, they were bent with an angle through the hole of the substrate laminate, as shown in figure 5.9a.

Due to the more challenging design of the additive binding stripes than the additive binding for the free-edge delamination and edge impact specimens, it was not possible to carry out automatised simulations. First, four different additive bindings with the layup of $[90]_4$, $[\pm75]_s$, $[\pm60]_s$ and $[\pm45]_s$ were modelled and simulated. These bindings were named "simplified bindings" as they did not entirely represent how the additive binding stripes bent over the edge of the hole. These simplified bindings had a "V" shaped geometry. As was explained in section 5.4, the bindings were applied as unidirectional stripes, and hence, strictly speaking, focusing only on one

stripe, this binding would be providing a layup of $+\theta_4$ on one surface of the substrate laminate and a layup of $-\theta_4$ on the other opposite surface. For this reason, strictly speaking, they were not $[\pm\theta]_s$ additive bindings, with θ = 45, 60, 75, 90.

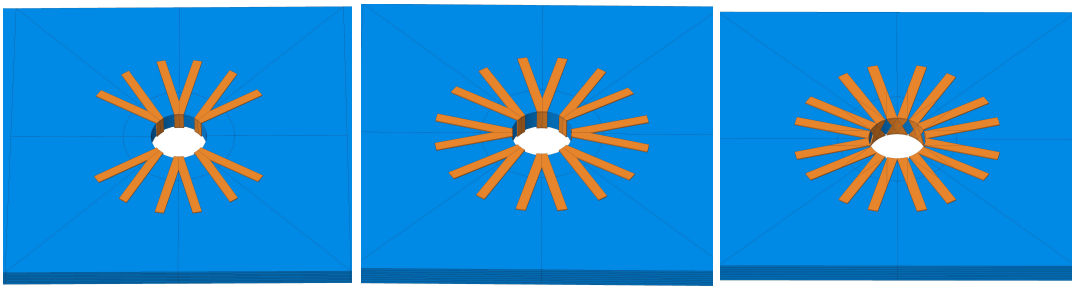

(a) **(b)** **(c)**

Figure 8.5: Simplified and realistic bindings placed over the edge of the hole. (a) 6 simplified bindings, (b) 8 simplified bindings and (c) 8 realistic bindings. All bindings shown are $[\pm 75]_s$.

These simplified additive bindings were placed over six edge points, as shown in figure 8.5a and simulated. Later, as shown in figure 8.5b the simplified bindings were placed over eight points of the hole for comparison. As seen in figures 5.9a and 8.5b, it would have been very difficult to place additive bindings in more than eight points of the hole due to the reduced size of the hole. A second and more realistic additive binding stripe than the "simplified" shape was also modelled to mimic the actual shape of the additive binding around the edge of the hole. These second bindings were named "realistic bindings". The same $[90]_4$, $[\pm 75]_s$, $[\pm 60]_s$ and $[\pm 45]_s$ layups were modelled placing them in eight points of the edge of the hole, as shown in figure 8.5c.

Figure 8.6 shows a comparison of the maximum value of energy release rate $\mathcal{G}_{max}$ at interface 1 for each different binding, normalised with the maximum value of energy release rate $\mathcal{G}_{max,WithoutBinding}$ at interface 1 when no binding is applied. In addition, the three different bindings modelled, "6 simplified bindings", "8 simplified bindings" and "8 realistic bindings", were compared for crack lengths of 0.125 and 2.5 mm.

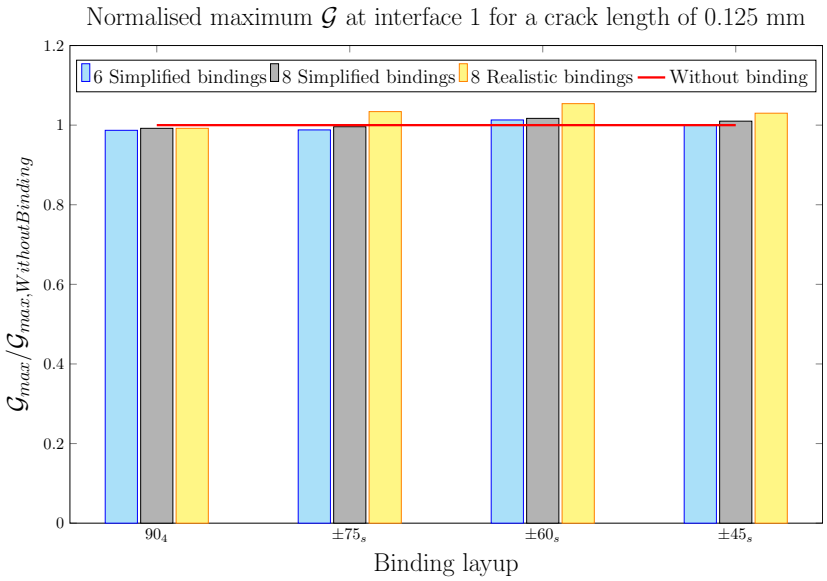

(a)

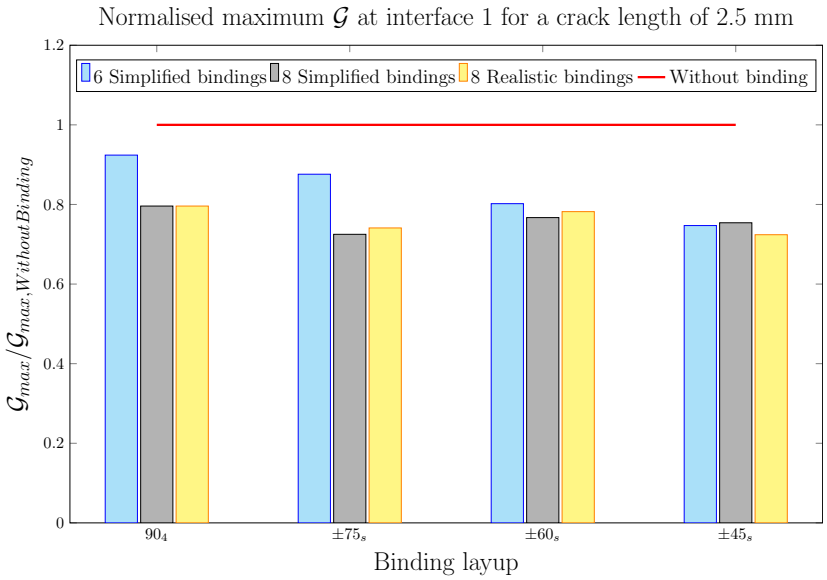

(b)

Figure 8.6: Comparison of normalised energy release rate $\mathcal{G}/\mathcal{G}_{max}$ around the crack tip of interface 1. (a) Crack length of 0.125 mm, (b) crack length of 2.5 mm.

As shown in figure 8.6a, for small crack lengths as 0.125 mm, the value of $\mathcal{G}_{max}$ does not decrease from the case without binding, and for some additive binding layups, it did increase from the case without binding. However, as delamination length grows, the $\mathcal{G}_{max}$ does decrease with the addition of additive bindings. As shown in figure 8.6b, the "realistic" additive binding generally obtained lower values of $\mathcal{G}_{max}$ than the "simplified" bindings, and the lowest value of $\mathcal{G}_{max}$ is obtained with a $[\pm 45]_s$ "realistic" binding, which reduced the $\mathcal{G}_{max}$ by 27.6% from the case without binding. Hence, $[\pm 45]_s$ additive bindings were experimentally tested to study their effect. Section 8.3 presents the experimental results obtained.

8.3 Experimental results

Both quasi-static and fatigue testing were performed in open-hole specimens to study the effect of the additive binding.

8.3.1 Quasi-static tensile results

The quasi-static tests were conducted as explained in section 5.6.2. As mentioned in section 5.4, the placement of the additive binding over the hole reduced the actual hole diameter compared with the case without binding. The reduction in diameter was approximately 1 mm, so the specimens with binding presented average measurable diameters of 5 mm, while the specimens without binding presented diameters of 6 mm. Although the additive binding should ideally only reduce the hole diameter size by 0.48 mm, the manufacturing difficulties and the flow of K51 epoxy resin made that the average measured diameter for the specimens with binding was 5 mm. For this reason, additional specimens were manufactured and tested to evaluate the effect of the change in diameter. Specimens without binding and with a hole diameter of 5 mm were manufactured to see if the results obtained would be closer to the specimens with the binding whose drilled hole was 6 mm diameter but whose final diameter was 5 mm. Additionally, specimens with a drilled hole of 7 mm were also manufactured for testing them with additive binding, so their final diameter would be 6 mm. Table 8.1 shows the summary of the open-hole specimens manufactured and quasi-statically tested. All open-hole specimens were manufactured with a width of 30 mm and a free length between end-tabs of 120 mm. End-tabs of 40x30 mm were water-jet cut from a glass-epoxy panel and glued on the specimens.

Table 8.1: Initial and final hole diameter for all open hole specimens tested without and with additive binding.

Specimen designation	Type of Binding	Initial diameter, D_i [mm]	Final diameter, D_f [mm]
OHNB6	No binding	6	6
OHB6	$[\pm 45]_s$	6	5
OHNB5	No binding	5	5
OHB7	$[\pm 45]_s$	7	6

For calculating the average applied stress to the specimens, the force measured by the load cell was divided by the cross-section area of each specimen's substrate laminate, defined as the thickness times the width of the specimen, as in [215]. The IM7/913

nominal ply thickness of 0.13 mm was used for calculating the total thickness of the substrate laminates.

All specimens were tested until final failure or until the testing machine detected a load drop higher than 40%. In each specimen tested, failure was defined as when load dropped by 5% or more in the load-displacement curve, even though the laminate would still withhold load and would even support higher loads, as similar as in [205].

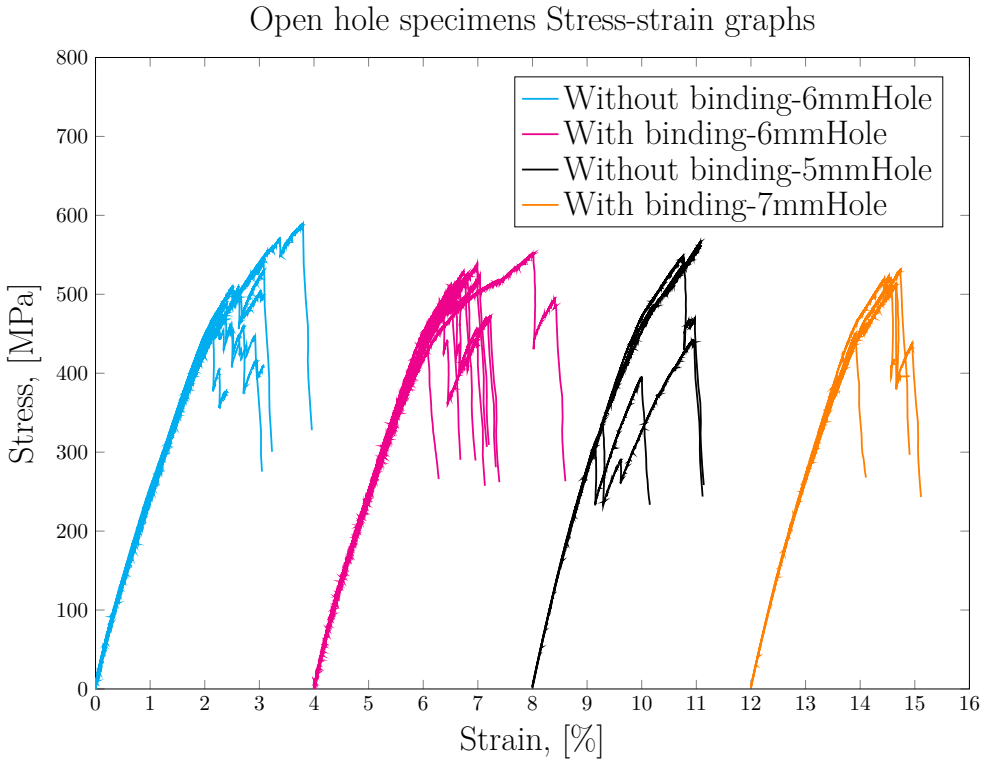

Figure 8.7: Stress-strain experimental results for the open-hole specimens without any binding and with a $[\pm 45]_s$ binding. Specimens with drilled hole diameters of 5, 6 and 7 mm were tested.

The stress-strain results for the samples without and with binding are shown in figure 8.7. All four specimens configurations shown in table 8.1 are presented in figure 8.7. To make the comparsion clearer, each of the cases has been plotted displaced an offset of 4% between different specimen configurations. Hence, the results of specimens without binding and drilled diameter of 6 mm are plotted starting from 0% strain, the specimens with binding and drilled diameter of 6 mm are plotted starting from 4% strain, specimens without binding and drilled diameter of 5 mm are plotted to start from 8% strain and specimens without binding and drilled diameter of 7 mm are plotted to start from 12% strain.

Table 8.2 presents the load direction engineering modulus, maximum force, stress and strain at failure for specimens without and with binding. The strain and force at failure are taken as the points where the load dropped by 5% or more. For calculating

the engineering modulus of the laminates, the slope of a straight line between two points on the stress-strain graphs at 0.2% and 0.4% strain was used for each specimen and then averaged for each group.

Table 8.2: Maximum force, stress and strain at failure for open-hole specimens without and with binding.

	Specimen			
Property	OHNB6	OHB6	OHNB5	OHB7
Load direction engineering modulus [GPa] (CV%)	26.03 (4.03)	25.85 (1.34)	29.76 (1.23)	28.50 (1.00)
Maximum force [kN] (CV%)	64.48 (9.52)	64.23 (5.76)	65.07 (19.05)	63.07 (6.55)
Force at 5% load drop [kN] (CV%)	63.71 (9.20)	64.23 (5.76)	60.32 (30.83)	63.07 (6.55)
Stress at 5% load drop [MPa] (CV%)	507.81 (9.31)	512.47 (5.76)	483.31 (30.83)	505.37 (6.55)
strain at maximum force [abs.%] (CV%)	2.94 (21.84)	2.78 (17.62)	3.01 (23.73)	2.5 (13.29)
strain at 5% load drop [abs.%] (CV%)	2.83 (22.66)	2.78 (17.62)	2.51 (49.49)	2.5 (13.29)

As shown in figure 8.7, all specimens tested present similar stress-strain graphs. For the specimens without binding, the OHNB6 specimens present an average value of 2.83%, 507.81 MPa and 63.71 kN for strain, stress and load at the failure point, respectively. The OHNB5 specimens present an average value of 2.51%, 483.31 MPa and 64.23 kN for strain, stress and load at the failure point, respectively. It is to be noted that the engineering modulus of the OHNB5 specimens is slightly higher than the one for the OHNB6 specimens due mainly to the difference in hole size.

The OHB6 specimens present an average value of 2.78%, 512.47 MPa and 64.23 kN for strain, stress and load at the failure point, respectively. Moreover, the OHB7 specimens present an average value of 2.5%, 505.37 MPa and 63.07 kN for , stress and load at the failure point, respectively.

It is noteworthy that the specimens without binding presented a higher coefficient of variation than the specimen with binding. This is better seen for the stress value at 5% load drop, where the specimens OHNB5 present a coefficient of variation of

about 5 times the coefficient of variation of the specimens with binding. On the other hand, the specimens OHNB6 present almost double the value of the coefficient of variation than the OHB6 specimens.

Interrupted tests were taken for XCT scanning to study the strain of the damage in both cases, without and with binding. The tests were interrupted after the first load drop of 5% occurred, so the specimens had technically failed but could have withheld higher loads. The XCT scan images are presented following.

Figure 8.8 displays an XCT scan projection of an open-hole specimen at the hole area. This projection is the average of the sum of all the slices from the XCT scan viewed from the top. The figure shows a specimen tested until the first load drop of 5% was recorded (see table 8.2). Different damages are visible as the 0°, 90° and ±45° delaminations originating from the hole edge. Free-edge delamination damage origination is also visible in the form of white parts at the free edges.

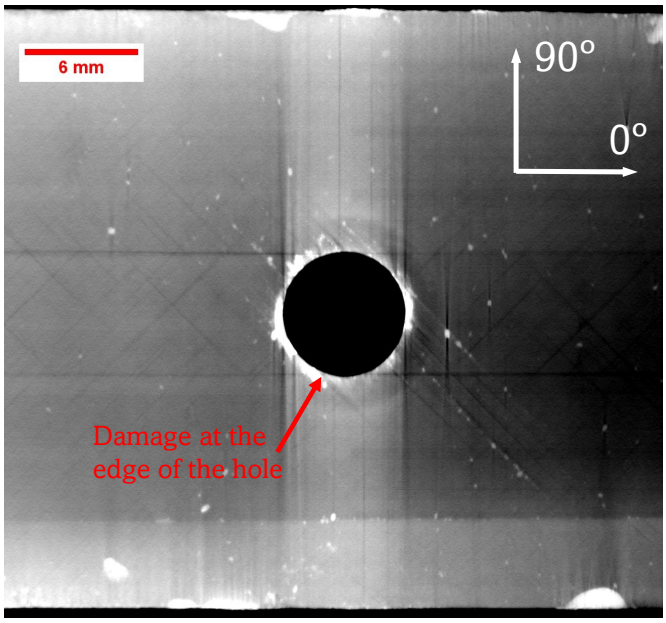

Figure 8.8: XCT scan projection of the average of the sum of all the scans showing the damage through-the-thickness at the hole area from an open-hole specimen OHNB6 tested until first load drop of 5% (see table 8.2). The white area around the hole indicates the damage area at the edge of the hole. Faint lines of different plies orientations are visible.

Figure 8.9 shows different cross-sections of a OHNB6 specimen. As seen in figure 8.9a free-edge delaminations spread across the whole width of the specimen from both free edges between the -45/90 interface. In the cross-section view AA' shown in figure 8.9a it is visible how different interlaminar delaminations are joining through-the-thickness, and in the cross-section view BB' it is seen how these delaminations are

starting from the edge of the hole. The cross-section view CC' in figure 8.9b shows how these interlaminar delaminations, which occur at all interfaces and join through-the-thickness originate as well from the edge of the hole and spread along the whole length of the specimen in the loading direction. These interlaminar delaminations originating from the edge of the hole in cross-section view CC' are the same as the ones seen in the cross-section view AA'. The cross-section view DD' shows the delamination running between the -45/90 interfaces and joining through the 90° layers block at the very free edge of the sample. These -45/90 interface delaminations are visible in the transverse lines (90°) of the left-side image of figure 8.9b. Additionally, the -45/90 delaminations do not completely join across the width of the laminate, as seen in the left-side image of figure 8.9b, and hence they are not visible in the CC' cross-section view.

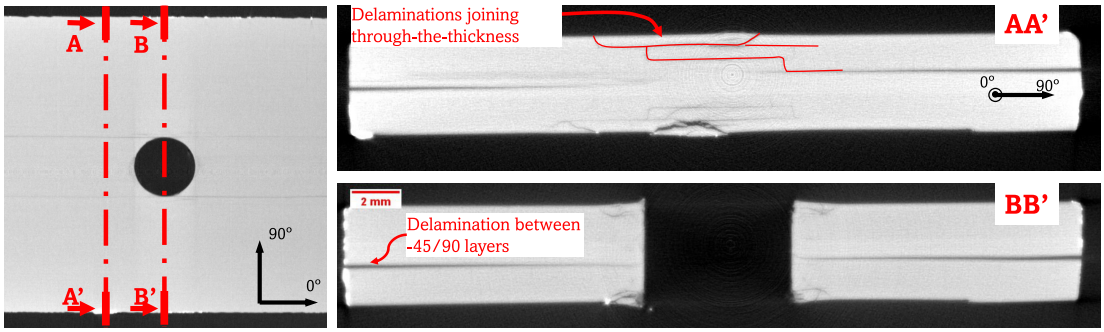

(a)

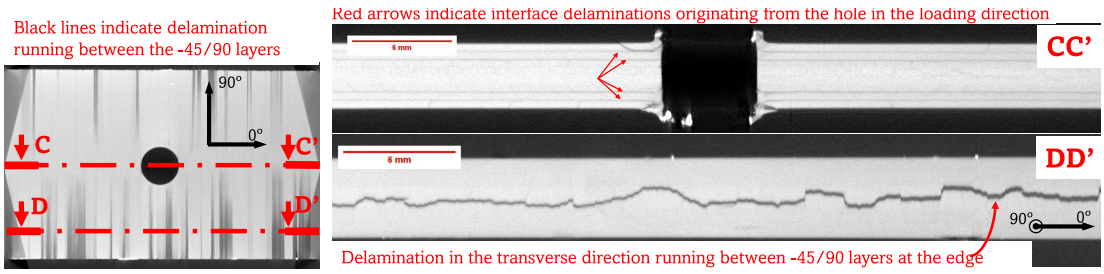

(b)

Figure 8.9: XCT scans of the cross-sections of an open-hole specimen OHNB6 tested until first load drop of 5% (see table 8.2). (a) Left figure is a top view of the specimen at the hole area. Right views are cross-sectional views of the width of the specimen. (b) Left view is a top view of the specimen between 0/90 interfaces, so the delamination running between 0/90 layers is visible. Right views are cross-sectional views of the length of the specimen.

Figure 8.10 displays an XCT scan projection of an open-hole specimen with a $[\pm 45]$ binding at the hole area. The figure shows a specimen tested until the first load drop of 5% was recorded (see table 8.2). The different ply orientations are visible as in the case of figure 8.8, but the most prominent damage visible in figure 8.10 is the delaminations occurring between the 0/-45 interfaces in the form of straight black

lines in the 0° direction. These 0/-45 delaminations are clearly visible in figure 8.11b and pointed out in figure 8.11c.

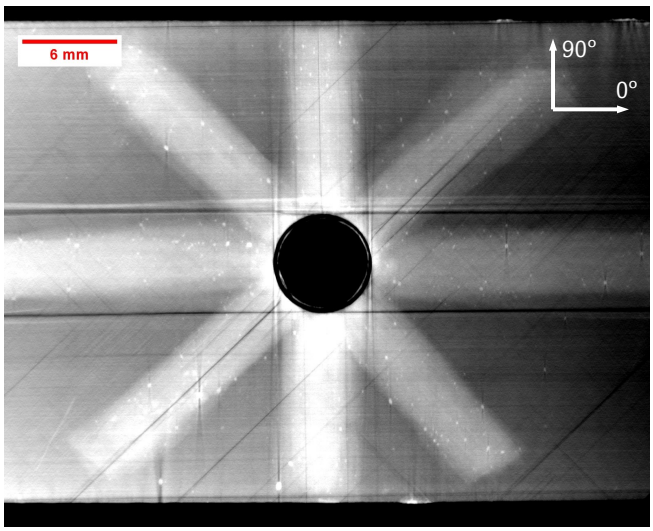

Figure 8.10: XCT scan projection the average of the sum of all the scans showing the damage through-the-thickness at the hole area from an open-hole specimen OHB6 with a $[\pm 45]$ binding tested until first load drop of 5% (see table 8.2). The visible black lines in the 0° direction, which are tangent to the hole are the 45/0 layers delaminations visible in the right view of figure 8.11a. Lines of different plies orientations are visible.

Figure 8.11 shows different cross-sections a OHB6 specimen. As seen in the cross-section view AA' of figure 8.11a free-edge delaminations spread across the whole width of the specimen from both free edges and between the 45/0, 0/-45 and -45/90 interfaces. In the left image of figure 8.11a a top through-the-thickness view shows the area of the hole, and the 0/-45 interface delamination is visible as the black area running in the 0° direction. In the cross-section view BB' it is seen how the binding placed through the hole was debonded from the edge of the hole and how the interlaminar delamination of the 45/0 interfaces reached the edge of the hole. Figure 8.11b shows a close view of the cross-section view AA'.

The cross-section view CC' in figure 8.11c shows how these interlaminar delaminations, which occur at all interfaces, reach the edge of the hole completely delaminating the 45/0 and 0/-45 interfaces along the whole length of the specimen. These interlaminar delaminations cross-section view CC' are the same as the ones seen in the cross-section view AA'. The cross-section view DD' shows the delaminations running between 45/0, 0/-45 and the -45/90 interfaces at the very free edge of the sample. The -45/90 interface delamination is visible in the transverse lines (90°) of the left-side image of figure 8.9b. As in the case without binding (figure 8.9b), the -45/90 delaminations do not join across the width of the laminate, as seen in the left-side image of figure 8.11c, and hence they are not visible in the CC' cross-section view. The 45/0 and 0/-45 interfaces delaminations do join across the width of the specimen

and hence are visible in both cross-section views CC′ and DD′ of figure 8.11c.

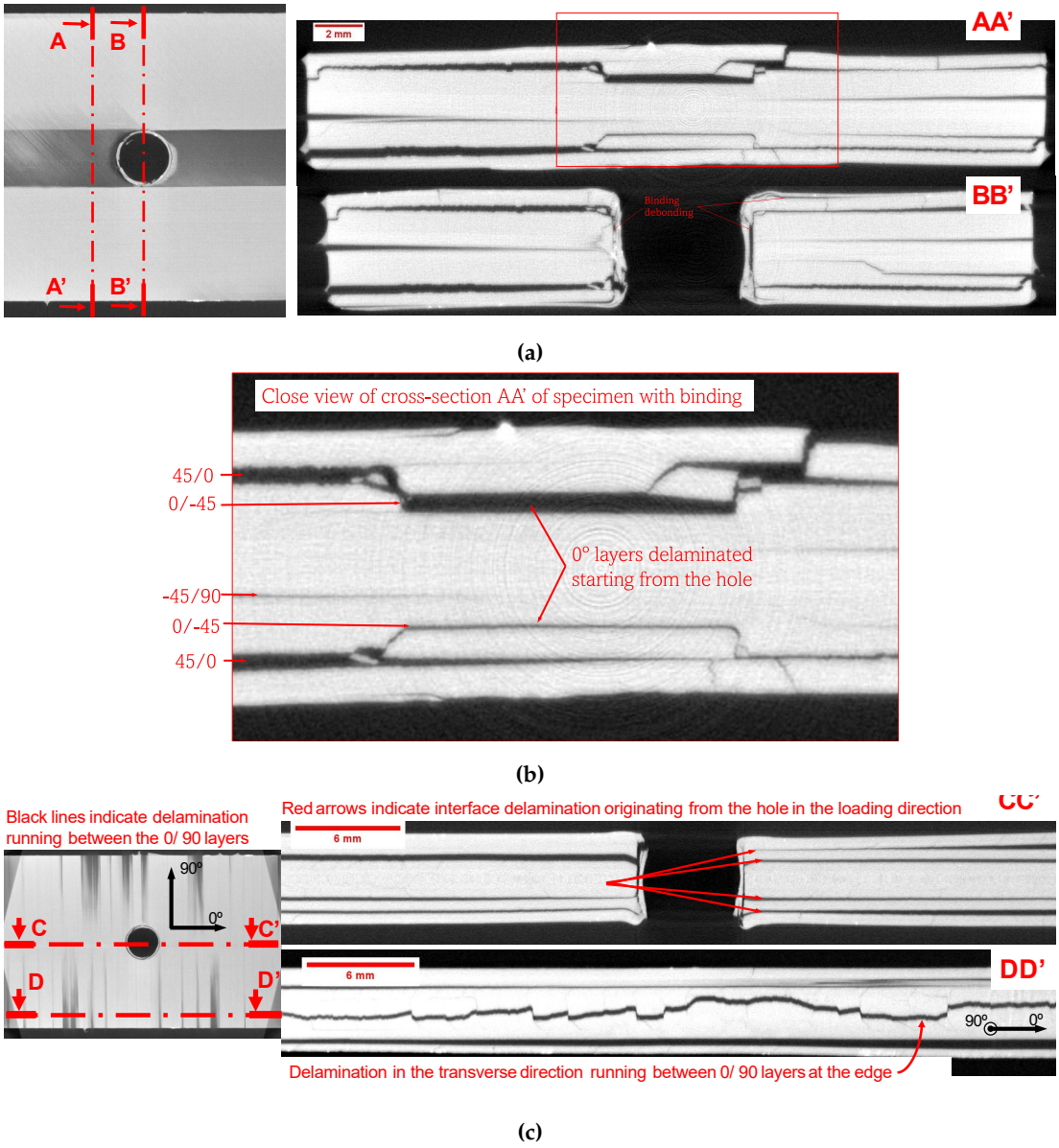

Figure 8.11: XCT scans of the cross-sections of an open-hole specimen OHB6 with a $[\pm 45]$ binding tested until first load drop of 5% (see table 8.2). (a) Left figure is a top view of the specimen at the hole area. Right wiews are cross-sectional views of the width of the specimen. (b) Close view of cross-sectional cut AA′. (c) Left view is a top view of the specimen between 0/90 interfaces, so the delamination running between 0/90 layers is visible. Right views are cross-sectional views of the length of the specimen.

It is worth mentioning that in the post-morten inspection of the specimens without binding, it was visible that they also delaminated in between the 45/0 and 0/-45 interfaces, as in the XCT images of the case of the specimen with binding showed. Additionally, during the tensile testing, it was observed that the specimens with binding failed more violently and abruptly than those without binding.

8.3.2 Tension-tension fatigue results

The fatigue tests were conducted under load-control tension-tension loading at a 5 Hz frequency. A loading R-ratio of 0.1 and severity of 65%, from the defined failure load in section 8.3.1, were used. As per equations (8.1) and (8.2) the maximum load applied (F_{max}) was 42 kN, which is 65% of the failure load of OHNB6 specimens (see table 8.2), and the minimum load (F_{min}) was of 4.2 kN. Hence the load amplitude (F_a) was 18.9 kN, and the mean force (F_m) was 23.1 kN. All tests were conducted using an Instron Servo-hydraulic 8801 testing machine with mechanical wedge grips. The cross-head displacement was measured with the vertical displacement of the grips. One specimen without additive binding was tested, and four specimens with additive binding were tested.

$$F_a = \frac{F_{max} - F_{min}}{2} \tag{8.1}$$

$$F_m = \frac{F_{max} + F_{min}}{2} \tag{8.2}$$

Figure 8.12 shows the normalised effective engineering modulus against the number of cycles elapsed. The normalised effective modulus was calculated as defined in [287], and it was reported every 10 cycles between 10 and 100 cycles, every 100 cycles between 100 and 1000 cycles, every 10^3 cycles between 10^3 and 10^4 cycles, and every 10^4 between 10^4 and 10^5 cycles. As visible in figure 8.12, specimens with binding performed worse than those without binding. This behaviour will be explained in more detail in section 8.4.

All tests were run until 10^5 cycles (run-out) or until failure of the specimen, but for one specimen without binding which was stopped at 60x10^3 cycles due to testing facility restrictions. If the specimen had been left, it is thought that it would have run-out.

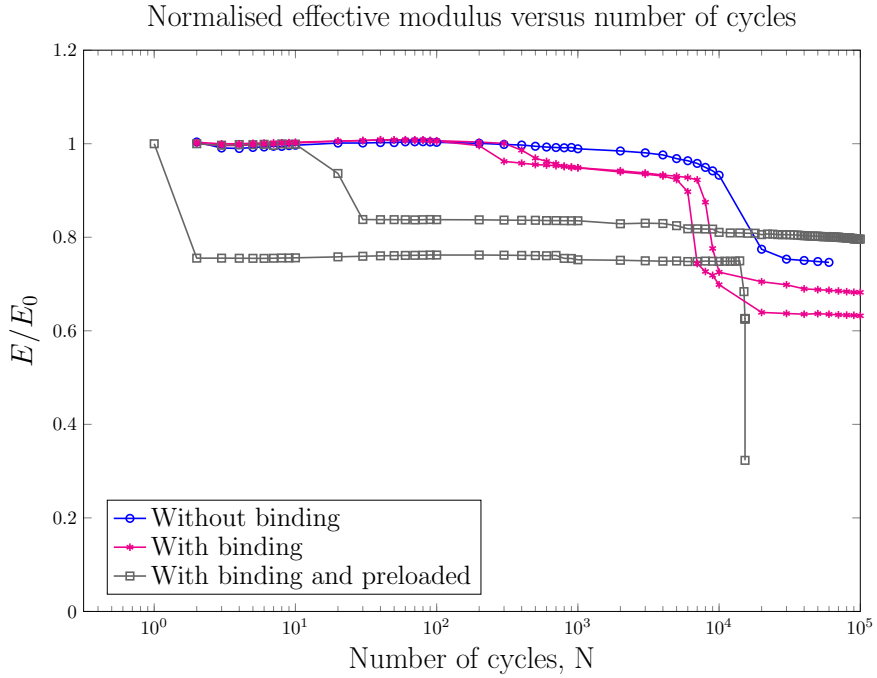

Figure 8.12: Normalised effective modulus of open-hole fatigue specimens versus the number of cycles.

8.4 Discussion

8.4.1 Quasi-static tensile specimens discussion

For the open-hole specimens, the values of $\mathcal{G}$ were higher for smaller delamination lengths than for larger delamination lengths. A reduction of $\mathcal{G}$ of 27.6% was achieved for a crack length of 2.5 mm with a $[\pm 45]_s$ additive binding. However, the FE results indicated that the use of $[\pm 45]_s$ additive bindings would give a higher value of $\mathcal{G}$ for small crack lengths (0.125 mm) than when no binding was used, as shown in figure 8.6a. This could indicate that the additive binding could potentially promote the development of small cracks but arresting them when growing after a certain length. It could be that the experimentally viewed phenomenon of higher concentration of damage in specimens with binding than in specimens without binding is directly related to this "crack promoting behaviour" shown in the FE results for small pre-crack lengths when additive bindings are applied figure 8.6.

It has been experimentally shown that these thin additive binding stripes did not perform any visible improvement in the suppression of delamination. However, the addition of the additive bindings did not harm the performance of the specimens with binding compared with the specimens without binding. On the basis of the results shown in section 8.3.1, it was concluded that the selection of the substrate laminate layup or testing and design process was not appropriate for studying the

effect of the additive binding for suppressing delamination in composite laminates with open holes. The substrate laminate layup was selected based on the results reported in [216]. A 6 mm hole diameter was the minimum feasible size for the hole for manufacturing the specimens with binding, and a layup of $[45_m/0_m/-45_m/90_m]_n s$ with $m = 4$ and $n = 1$ fails due to delamination. Thus, a $[45_4/0_4/-45_4/90_4]_s$ layup was selected. However, free-edge delamination was not taken into account to occur at the time of substrate laminate selection.

The purpose of the additive binding was to stop delamination originating from the edge of the hole; hence, the free-edge delamination originating from both sides of the width of the substrate was not considered. However, this free-edge delamination was observed when conducting the experimental testing, as shown in figure 8.13.

In this way, the results obtained for the solution tested indicate that the additive bindings studied do not help the improvement of the delamination resistance for composite laminates with open holes. However, it is believed that if other layups not so-susceptible to delamination had been used for the substrate laminate, the results obtained could have indicated that the additive bindings do help for stopping delamination originating from the edge of the hole. For instance, a laminate with sub-laminate scaling ($[(45/0/-45/90)_4]_s$) rather than ply scaling ($[45_4/0_4/-45_4/90_4]_s$) could have been used. Moreover, this $[45_4/0_4/-45_4/90_4]_s$ layup could have been tested with the use of additive bindings for suppressing free-edge edge delamination in chapter 6. In this manner, delamination originating from all edges of the substrate laminate would have been suppressed.

Nevertheless, the results obtained still do present promising results. As shown in table 8.2, the use of additive bindings reduced the coefficient of variation for all the results reported. Both specimens OHNB6 and OHB6 presented similar force at a 5% load drop. For the case of the specimens without binding, they reported slightly higher maximum force, as they could still withhold load after having failed technically. However, for the specimens OHB6, the failure load corresponded with the maximum load, meaning that the specimens with binding failed more catastrophically than those without binding. This higher coefficient of variation is believed to be due to the presence of manufacturing defects in the samples when drilling the holes. The presence of the additive binding reduced the influence of those manufacturing damages.

As shown in figures 8.9 and 8.11, the specimens with binding were more severely damage than the specimens without binding, as they present bigger delaminations. As mentioned before, the specimens with binding failed more abruptly and explosively than specimens without binding. Figure 8.13 shows the free-edge delamination damage progress for an OHB7 specimen at different strain rates (ϵ was used to rep-

resent strain in figure 8.13). Free-edge delamination between the 0/90 interfaces is visible at an strain of 0.84%, and for an strain of 2.29%, the free-edge delamination has wholly separated the 0/90 interfaces. For about an strain of 2.6%, the laminate splinters and fails but still could withhold more displacement. Finally, for an strain of 3%, the laminate cannot withhold any more load.

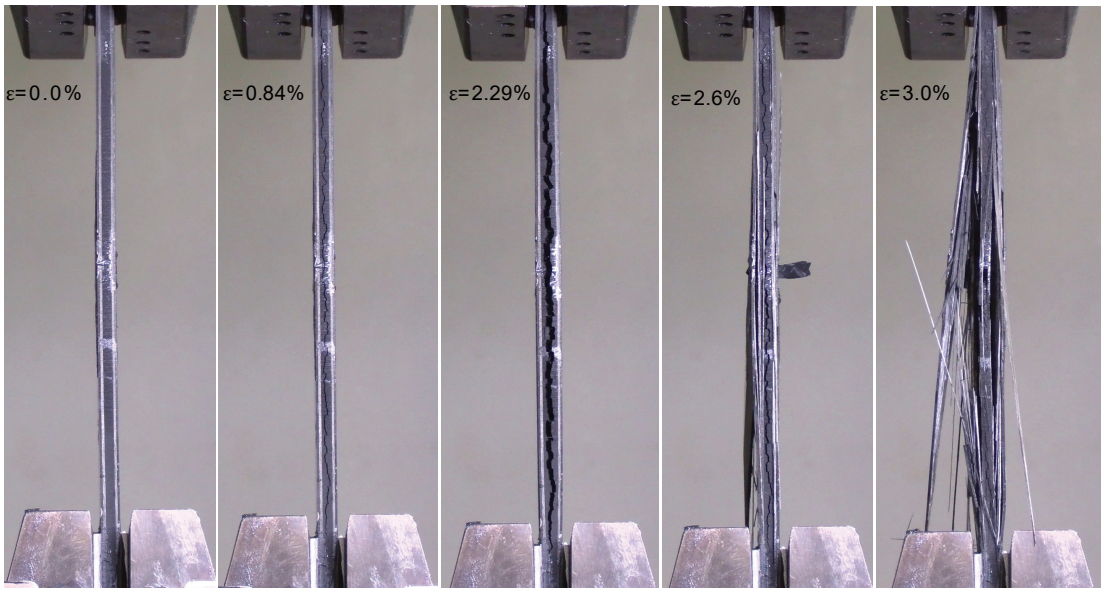

Figure 8.13: OHB7 specimens tensile loading failure process. Great free edge delamination occurred between the 0/90 interfaces

8.4.2 Tension-tension fatigue specimens discussion

Due to testing restrictions, achieving a complete set of testing results for fatigue testing of open-hole specimens was impossible. For instance, the only open-hole specimen without binding had to be stopped at $60x10^4$ cycles. Additionally, only four specimens with binding were tested. As shown in figure 8.12 two of the specimens with binding suffered a considerable drop in stiffness within the first 10 cycles. This drop in stiffness was due to the preloading of the specimens to characterise the initial stiffness of the specimens. However, the pretension was not calibrated appropriately, and a relatively high load was applied, incurring premature damage to these two specimens. One of these preloaded specimens reached the 10^5 run-out number of cycles as the other two specimens with binding. The other preloaded specimen failed around 15200 cycles. After these two preloaded specimens' early stiffness loss, two other specimens with binding were tested without preloading.

The specimens without binding and with binding (which had not been preloaded) presented very similar behaviour. However, the specimens with binding suffered a stiffness loss at around 6000 cycles, which was 4000 cycles before the specimens with-

out binding. The use of additive bindings for suppressing free edge delamination, as the one shown in figure 8.13 could have prevented the earlier drop of stiffness of the specimens with binding (6000 cycles) compared to the specimen without binding (10^4 cycles).

It is to be noted that the fatigue tests were started different than the procedure explained in [287]. The specimens were loaded slowly to the mean load value (F_m), then loaded rapidly to the maximum load and then the fatigue cycles started. It is thought that this first rapid loading of the specimens from F_a to F_{max} was too abrupt to the specimens, and potential damage occurred.

Due to the small set of results, the fatigue tests are not conclusive to indicate the positive or negative effect of the binding on the damage tolerance of composite laminates with open holes under tension-tension fatigue loads.

8.5 Conclusions

The use of thin additive binding stripes, which are bonded to the edge of the hole of composite laminates with open holes, has been studied for suppressing the damage originating from the edge of the hole. In particular, it was intended that these additive bindings would suppress delamination arising from the damage occurring at the edge of the hole. A FE numerical analysis has been conducted to study the feasibility of such a solution and determine the effect of different additive binding layups on the value of $\mathcal{G}$ for different crack lengths. Moreover, experimental testing was conducted to determine the enhancement achieved when the additive binding was in place. The concluding points of this study are recollected below:

- The FE results indicated that the use of additive bindings around the hole only produced significant improvements in the value of $\mathcal{G}$ for large pre-crack lengths, i.e., for a delamination length of 2.5 mm, a reduction of 27.6% was achieved at interface 1 with a $[\pm 45]_s$ binding layup.

- The layup utilised for the substrate laminate was not adequate for studying the effect of additive bindings around the edge of the hole of composite laminates with open holes. Therefore, a layup not so susceptible to free-edge delamination is recommended for future works. Additionally, the use of additive bindings for suppressing free-edge delamination is recommended in both specimens without and with binding around the edge of the hole. In this way, the effect of the binding over the edge of the hole is not affected by free-edge delamination.

- The use of additive bindings around the open hole did not affect the maximum

load or strain before failure of the selected substrate layup. However, the presence of the additive binding significantly reduced the coefficient of variance of the experimental results.

- The fatigue test results were not conclusive, and further work is needed to determine the effect of the additive bindings. Additionally, no preloading of the specimens is recommended for fatigue testing unless it is a low loading.

Chapter 9

Results on enhancing the bearing response of pin-loaded composite laminates

This chapter presents the numerical and experimental results for the fourth research question. Numerical results indicate that the constraint that the additive binding places at the edge of the substrate laminate enhance the damage tolerance of the substrate laminate for small cracks at the edge of the hole. Experimental testing as described in section 5.8 was carried out to study the effectiveness of the solution. Some experimental specimens were XCT scanned, and clear damage profiles after loading were shown. The use of additive bindings at the edge of the hole of pin load laminates improved the offset bearing strength of laminates with binding by about 37.5%. The results are exposed, discussed, and finally, conclusions are drawn.

9.1 Substrate laminate selection

A quasi-isotropic laminate, like the one used for the open-hole specimens, was selected for the pin load specimens. The layup had a stacking sequence of $[45_m/0_m/-45_m/90_m]_{ns}$, with $m = 4$ and $n = 1$.

Similar to the open hole case, a diameter of 6 mm was decided for the hole and hence based on figure 5.11, the total length of specimens was 200 mm, the distance between the edge and the centre of the hole was 18 mm, and the width was 30 mm. The total laminate thickness was 4.16 mm.

9.2 FE results

Different delamination lengths at all interfaces between layer blocks with different fibre orientations were modelled, as explained in section 4.5. The bonded nodes extended across the laminate from the crack tip nodes, similar to the case of the open hole specimens FE. Figure 8.1 schematically shows the location of the bonded nodes of the FE model. It is important to remember that differently from the open hole FE model, cracks were modelled in all interfaces of the substrate laminate at the same time as this helped to reduce the simulation time.

The pin size used for simulations was 6 mm diameter for the cases without binding and 5.76 mm for the case with binding, as the nominal ply thickness of the additive binding is 0.03 mm and the additive binding stripes overlap over the hole, as explained in section 4.5.

The crack tip bonded nodes were defined around the whole circumference of the hole, so the crack tip node has a circular shape. For this reason, for the display of $\mathcal{G}$ at the crack tip, a similar method as in section 8.2 was used. In this way, a bubble chart was used to represent the value of the energy release rate around the crack tip. Figure 9.1 shows the normalised energy release rate $\mathcal{G}/\mathcal{G}_{max}$ variation for different pre-crack lengths at different interfaces. The values of $\mathcal{G}/\mathcal{G}_{max}$ are arranged around the deformed shape of the hole after loading (ellipsoidal shape) and are represented by the size of the bubble printed at the coordinates of each crack tip node, as shown in figure 9.1. The larger the diameter of the circle in figure 9.1, the larger the energy release rate at that node is. The maximum value $\mathcal{G}_{max}$ occurs for a delamination length of 0.125 mm at interface 1. The coordinates x and y are referenced from the centre of the hole and refer to the position of the nodes in the deformed shape of the hole. Additionally, for a clearer understanding of the variation of $\mathcal{G}/\mathcal{G}_{max}$ around the hole, figure 9.2 displays the variation of $\mathcal{G}/\mathcal{G}_{max}$ around the crack tip with respect to

the 0° fibre orientation. The location of the crack tip is varied with angle increments of 2.5° (α angle) from 0° to 360°.

The values of $\mathcal{G}/\mathcal{G}_{max}$ displayed in figure 9.1 show how the highest value of energy release rate changes as the delamination size increases for the three interfaces when an axial strain of 1% is applied[1]. It is visible how interfaces 1 and 2 present higher values of $\mathcal{G}$ than interface 3. In particular, the values of $\mathcal{G}$ at both interfaces 1 and 2 are very close, indicating that both interfaces could have the same probabilities of delaminating.

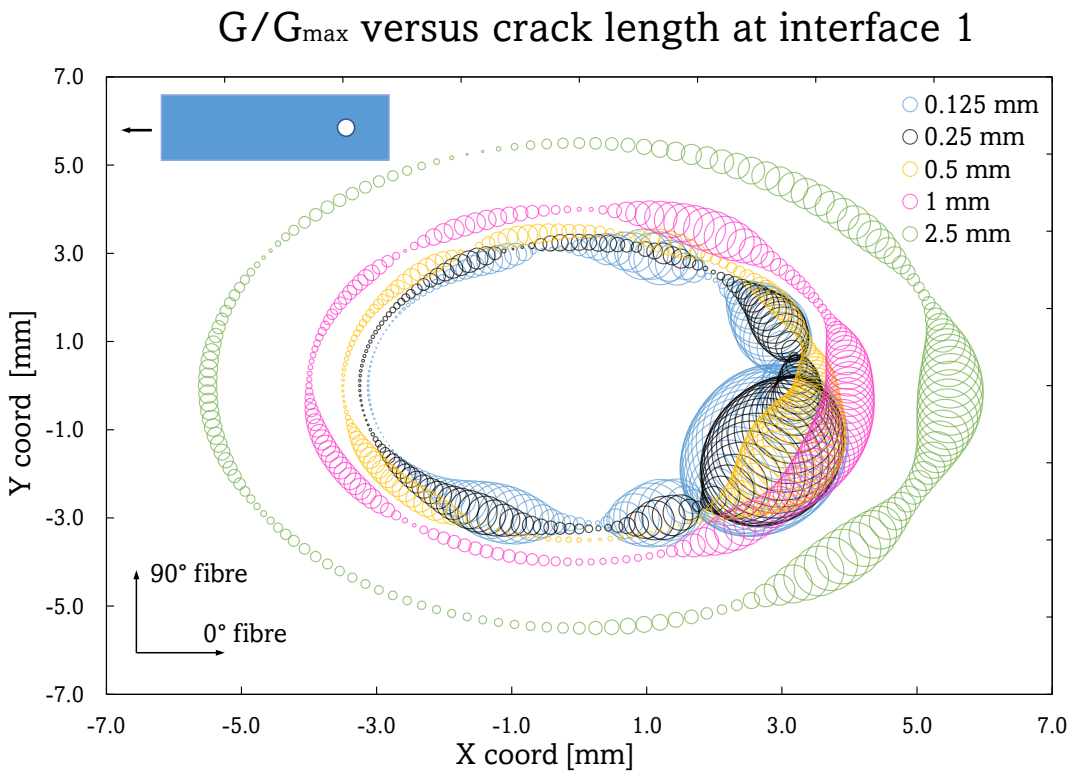

(a)

[1]Do not mistake with bearing strain. A displacement of 1% of its length (200 mm) was imposed on the laminate.

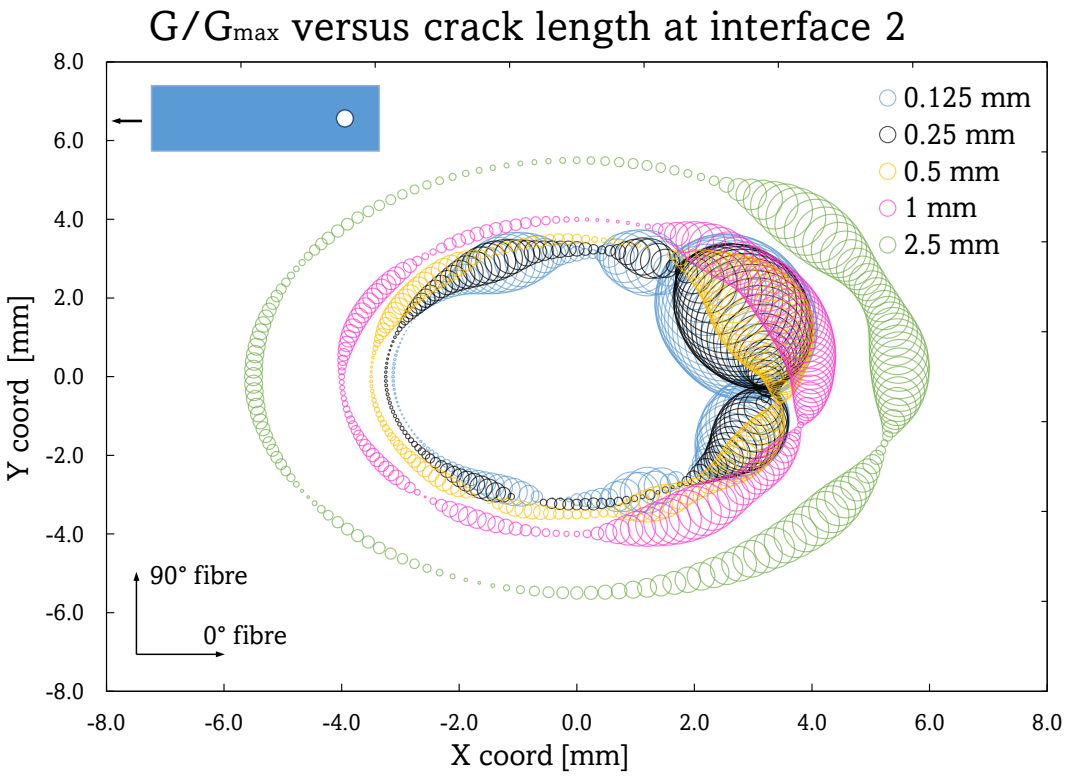

(b)

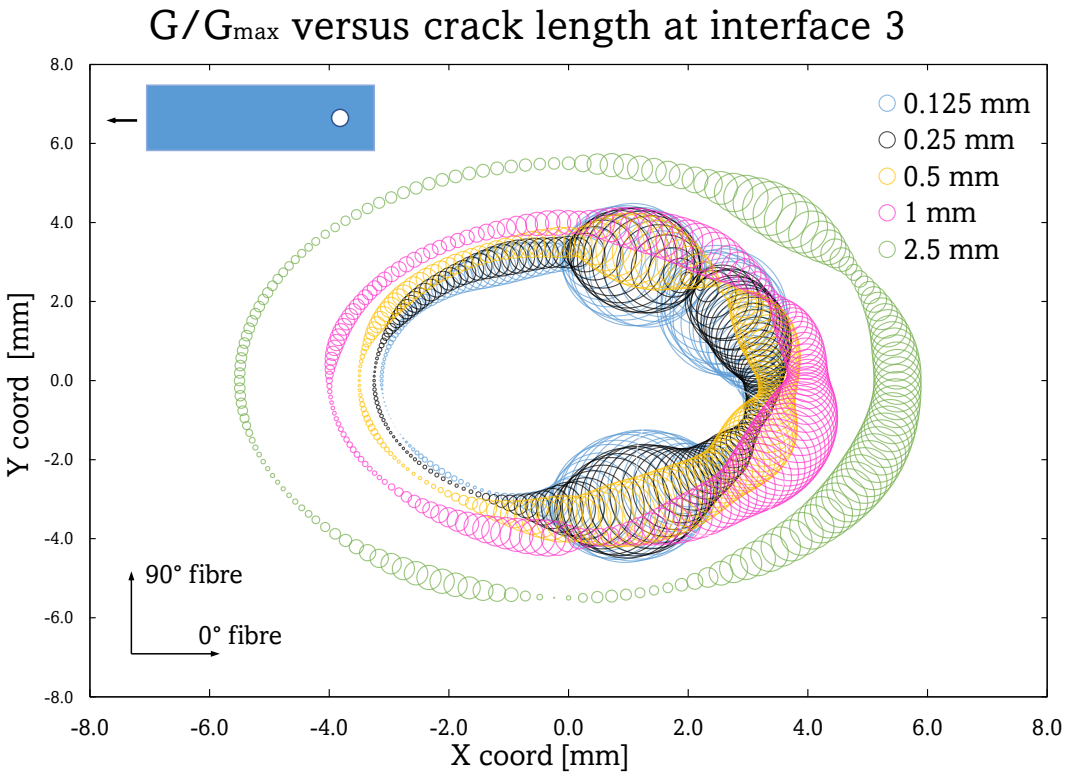

(c)

Figure 9.1: Normalised energy release rate $\mathcal{G}/\mathcal{G}_{max}$ around the crack tip of the hole of pin-loaded specimens for different crack lengths. (a) Interface 1, (b) interface 2, (c) interface 3.

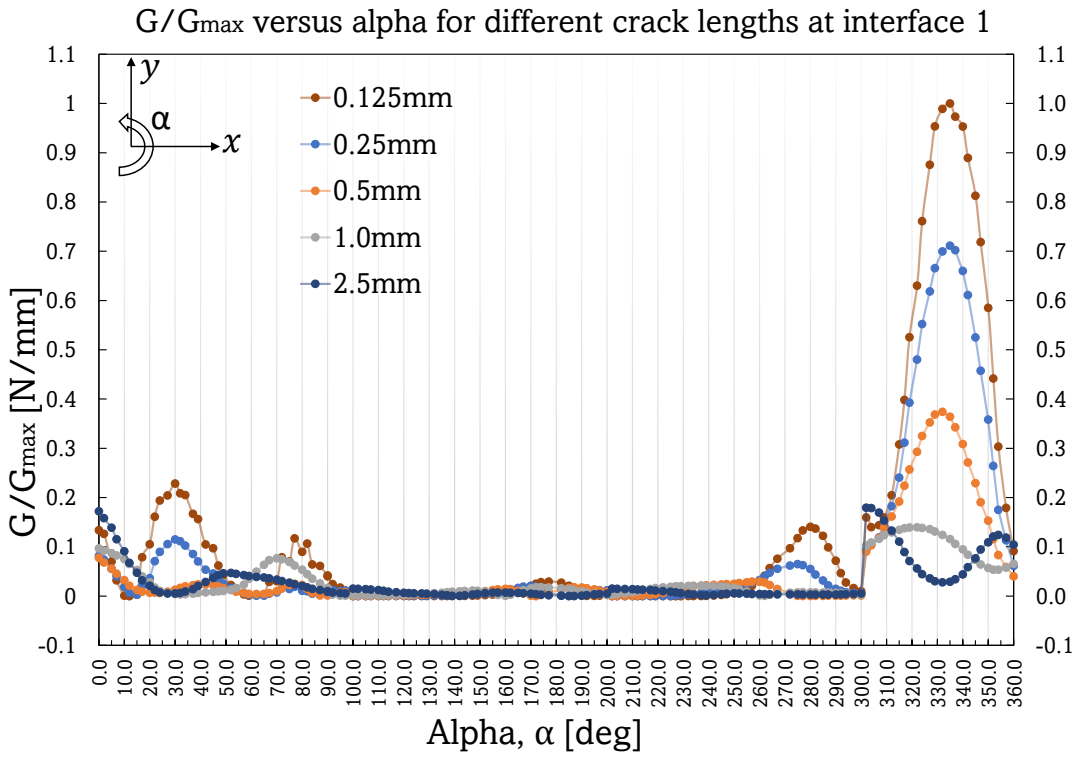
G/Gmax versus alpha for different crack lengths at interface 1
y
α
x
0.125mm
0.25mm
0.5mm
1.0mm
2.5mm
G/Gmax [N/mm]
Alpha, α [deg]

(a)

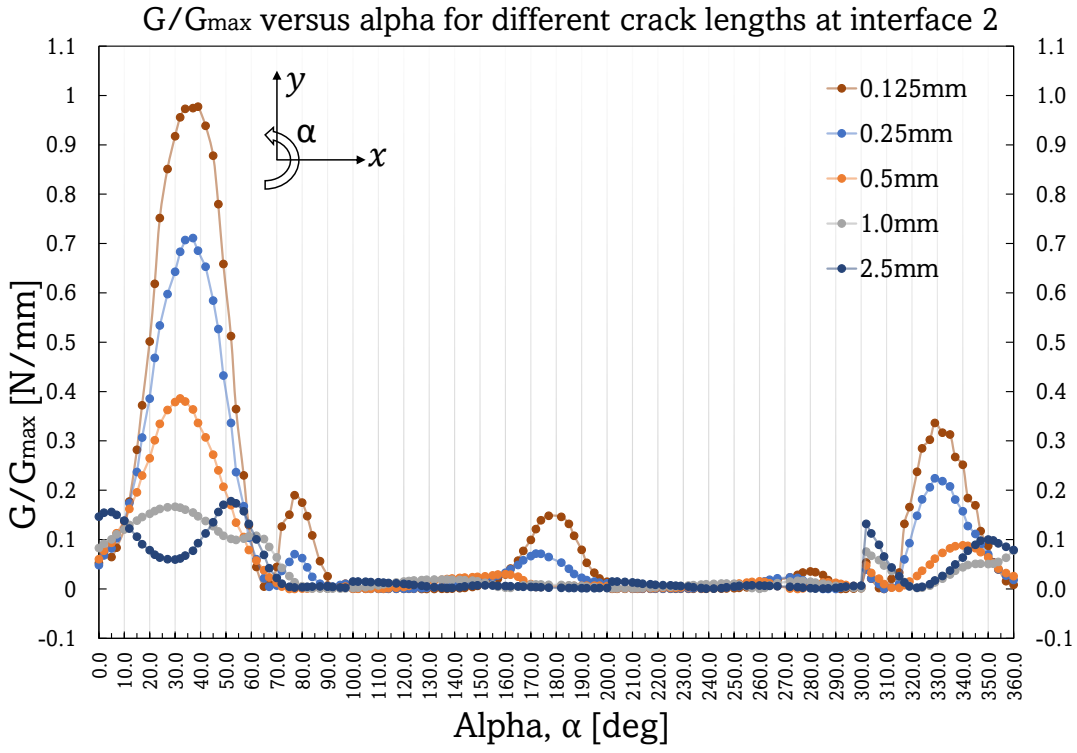
G/Gmax versus alpha for different crack lengths at interface 2
y
α
x
0.125mm
0.25mm
0.5mm
1.0mm
2.5mm
G/Gmax [N/mm]
Alpha, α [deg]

(b)

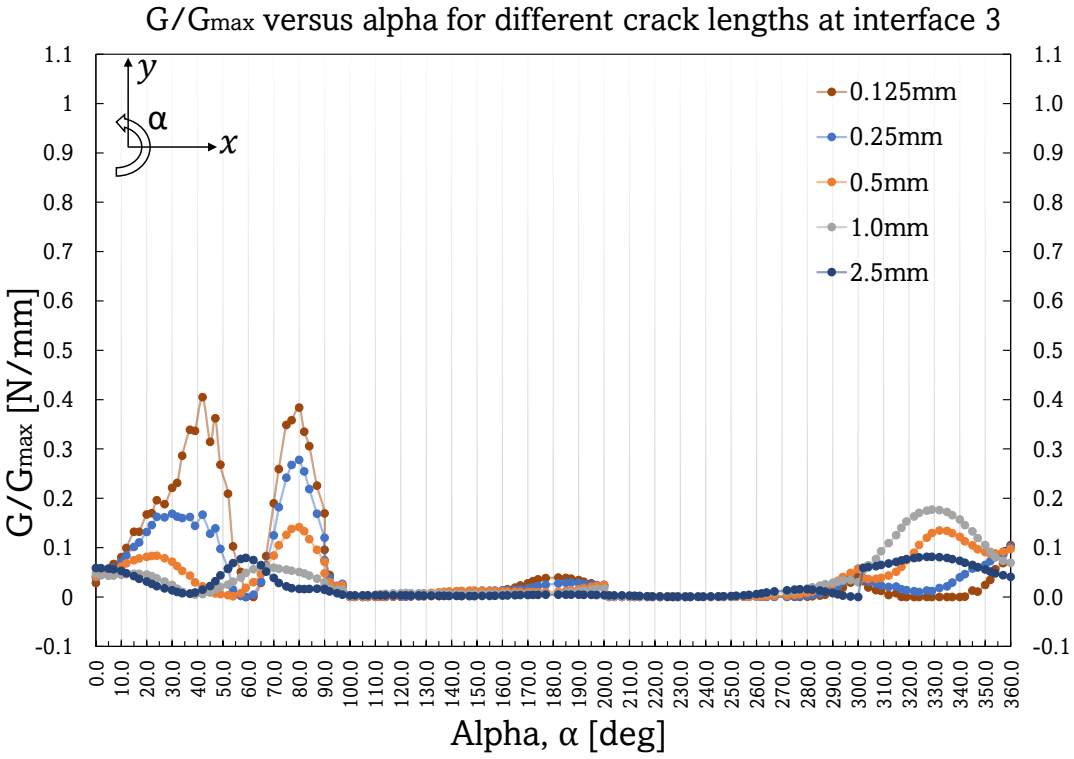

(c)

Figure 9.2: Normalised energy release rate $\mathcal{G}/\mathcal{G}_{max}$ around the crack tip of the open hole for different crack lengths with their location respect the 0° fibre orientation. (a) Interface 1, (b) interface 2, (c) interface 3.

As shown in figure 9.1 the minimum and maximum delamination lengths simulated were 0.125 and 2.5 mm. For a clearer visualisation of the magnitude of $\mathcal{G}$ at each interface, figure 9.3 compares the value of $\mathcal{G}/\mathcal{G}_{max}$ between the three interfaces at crack lengths of 0.125 and 2.5 mm. As logically expected, due to the ± 45 layers, interfaces 1 and 2 experience the highest values of $\mathcal{G}$ at symmetrically opposite points from the centre of the hole. The FE model is linear elastic, and for ease of analysis and comparison, all simulations were performed with 1% applied strain.

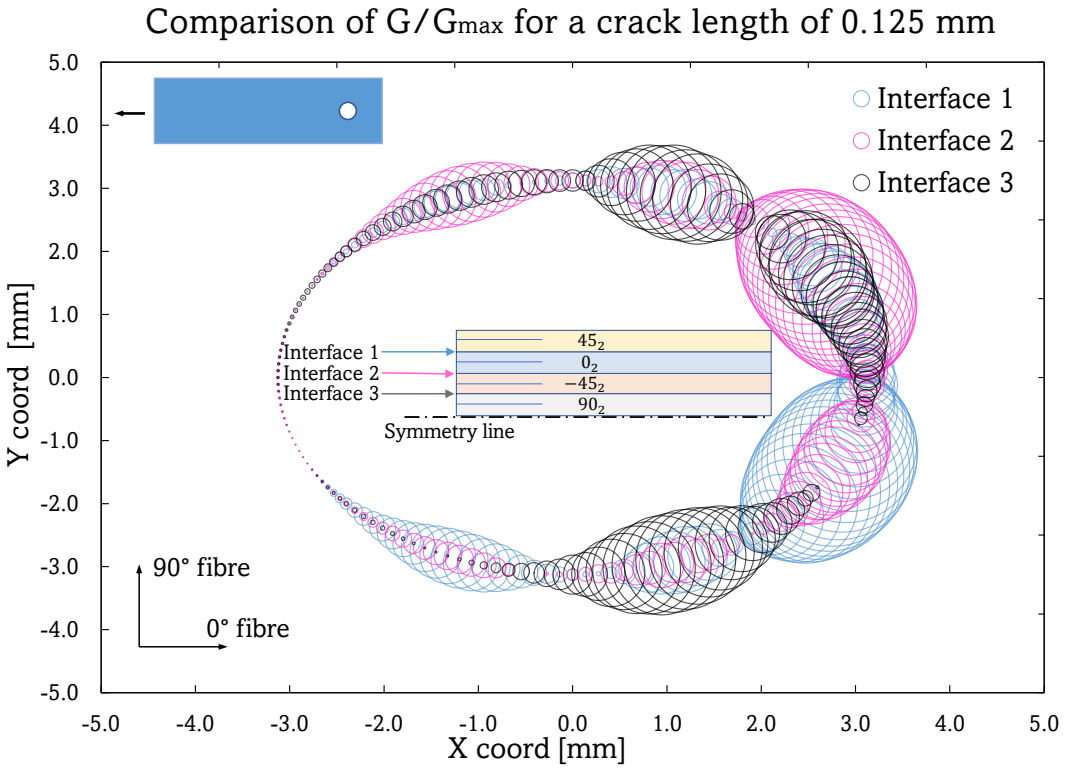
Comparison of G/Gmax for a crack length of 0.125 mm
Interface 1
Interface 2
Interface 3
Interface 1
Interface 2
Interface 3
45_2
0_2
-45_2
90_2
Symmetry line
90° fibre
0° fibre
Y coord [mm]
X coord [mm]
5.0
4.0
3.0
2.0
1.0
0.0
-1.0
-2.0
-3.0
-4.0
-5.0
-5.0
-4.0
-3.0
-2.0
-1.0
0.0
1.0
2.0
3.0
4.0
5.0

(a)

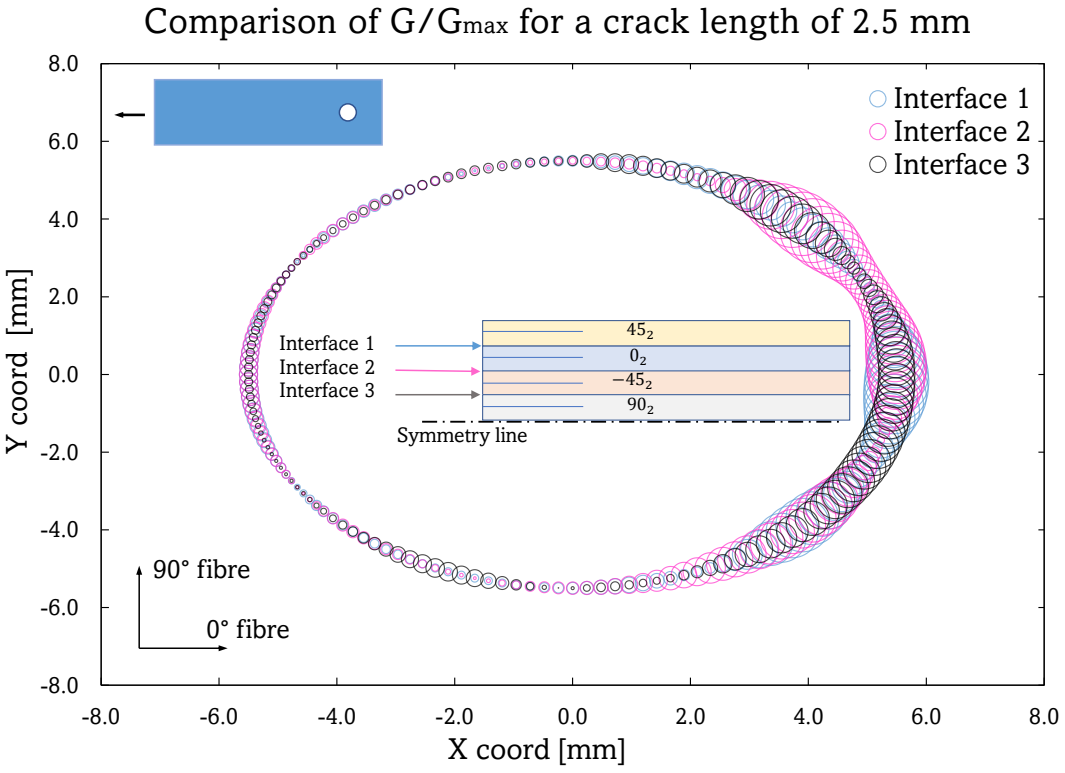
Comparison of G/Gmax for a crack length of 2.5 mm
Interface 1
Interface 2
Interface 3
Interface 1
Interface 2
Interface 3
45_2
0_2
-45_2
90_2
Symmetry line
90° fibre
0° fibre
Y coord [mm]
X coord [mm]
8.0
6.0
4.0
2.0
0.0
-2.0
-4.0
-6.0
-8.0
-8.0
-6.0
-4.0
-2.0
0.0
2.0
4.0
6.0
8.0

(b)

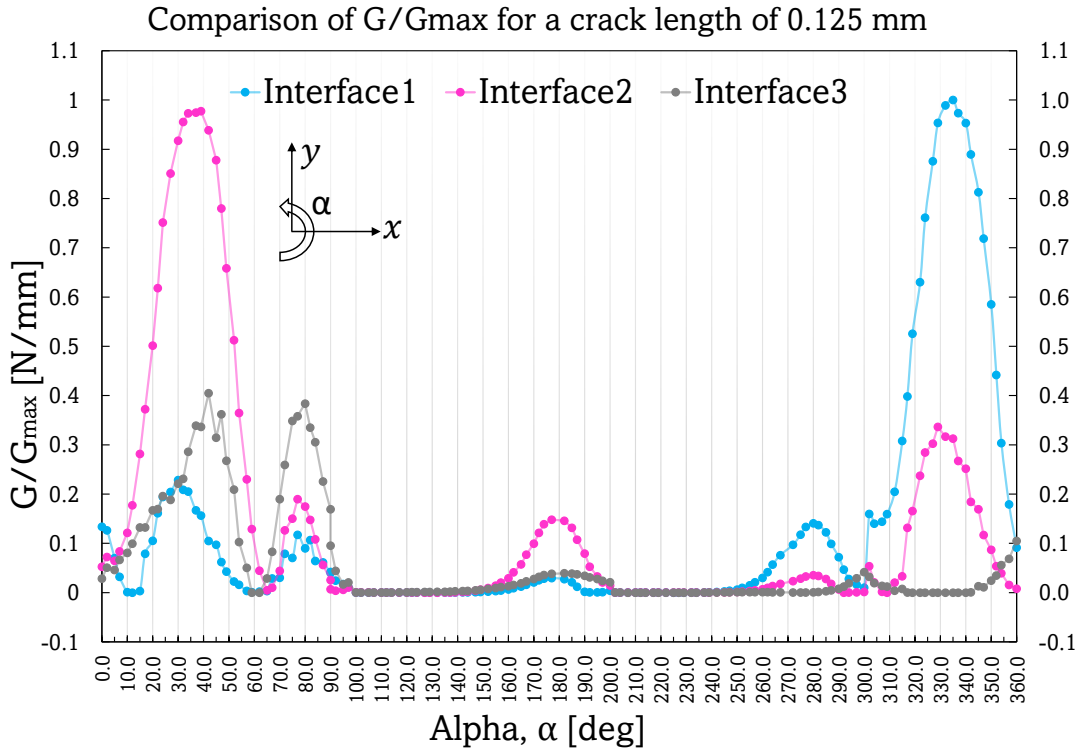

(c)

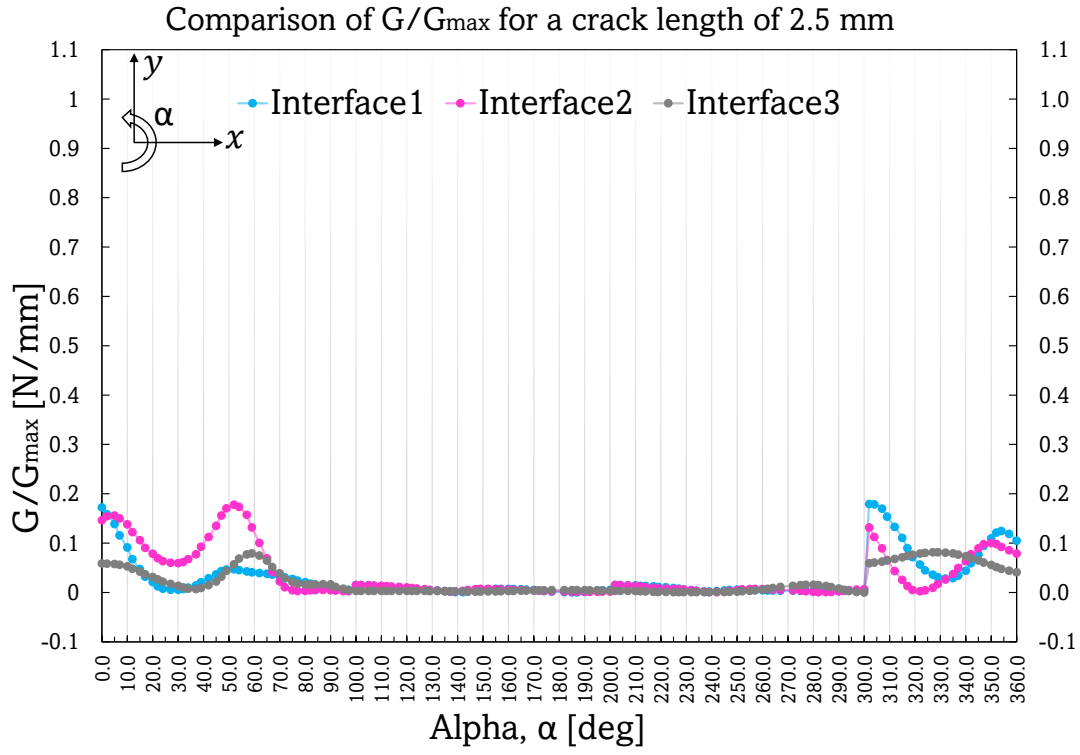

(d)

Figure 9.3: comparison of normalised energy release rate $\mathcal{G}/\mathcal{G}_{max}$ around the crack tip of the open hole for the different interfaces modelled. (a), (c) Crack length of 0.125 mm, (b)(d) crack length of 2.5 mm.

9.2.1 Binding design

Narrow and thin additive binding laminates were added to the substrate laminate in the form of stripes. Although from the edge of the hole the binding layup is $[\pm\theta]_s$, contrary to the case of the free-edge delamination specimens, the additive binding stripes are unidirectional narrow composite laminates. were unidirectional. For varying the angle of the additive binding, they were bent with an angle through the hole of the substrate laminate, as shown in figure 5.9a.

As in the case of the open-hole specimens, due to the more challenging design of the additive binding stripes than the additive binding for the free-edge delamination and edge impact specimens, it was not possible to carry out automatised simulations. For the case of the pin-loaded FE models, only realistic bindings (see figure 4.10) were used. Moreover, based on the results obtained for the open-hole specimens and due to computational time (see section 4.5), only two different "realistic bindings" additive binding layups were simulated. Figure 8.5 shows the different additive binding placements and types, i.e., simplified and realistic. Additive bindings with $[90]_4$ and $[\pm 45]_s$ layups were modelled and simulated. Again, as in the case of the open hole simulations and as explained in section 5.4, the bindings were applied as unidirectional stripes. In this way, strictly speaking, focusing only on one stripe, this binding would be providing a layup of $+\theta_4$ on one surface of the substrate laminate, and a layup of $-\theta_4$ on the other opposite surface. For this reason, strictly speaking, they were not $[\pm\theta]_s$ additive bindings, with θ = 45 and 90.

These "realistic bindings" were compared for three different crack lengths: 0.125 mm, 1.0 mm and 2.5 mm. The bindings were modelled by placing them in eight points on the edge of the hole, as in the open hole case and shown in figure 8.5c. Figure 9.4 shows a comparison of the normalised maximum value of energy release rate $\mathcal{G}_{max}$ at interface 1 and the three crack lengths for each different binding. The values of figure 9.4 are normalised with the maximum value of energy release rate $\mathcal{G}_{max,WithoutBinding}$, which occurs for a pre-crack of 0.125 mm at interface 1 when no binding is applied. For reference, $\mathcal{G}_{max,WithoutBinding}$ = 95.42 N/mm.

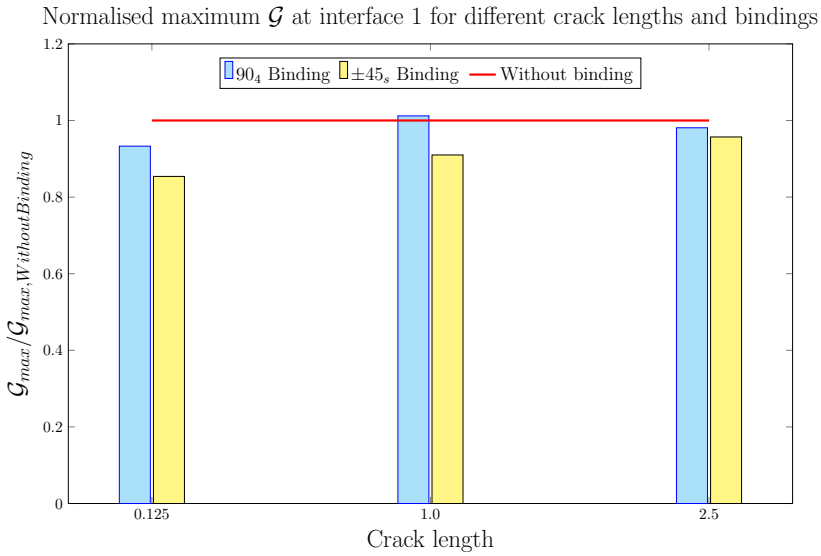

Figure 9.4: Comparison of normalised energy release rate $\mathcal{G}/\mathcal{G}_{max}$ around the crack tip at interface 1.

As shown in figure 9.4, the $[\pm 45]_s$ binding reduced $\mathcal{G}_{max}$ more than the $[90]_4$ binding. The lowest value of $\mathcal{G}_{max}$ for both $[\pm 45]_s$ and $[90]_4$ bindings was obtained for a crack length of 0.125 mm and reported a reduction of $\mathcal{G}_{max}$ of 14.6% and 6.7% from the case without binding, respectively. Hence, $[\pm 45]_s$ additive bindings were experimentally tested for studying their effect, and section 9.3 presents the experimental results obtained. It is also visible that the value of $\mathcal{G}_{max}$ was reduced the most for very small pre-crack lengths, but it was not reduced so much for bigger delamination lengths, i.e., 2.5 mm cracks. It is also interesting to note that the value of $\mathcal{G}_{max}$ was reported bigger for a pre-crack of 1 mm than for a 2.5 mm.

9.3 Experimental results

Pin load specimens were tested under quasi-static tensile and fatigue loading to study the effect of the additive binding.

9.3.1 Quasi-static tensile results

The quasi-static tests were conducted under displacement-control tensile loading at 1 mm/min rate.

As mentioned in section 5.5, the placement of the additive binding over the hole reduced the actual hole diameter compared with the case without binding. The reduction in diameter was approximately 1 mm, so the specimens with binding presented average measurable diameters of 5 mm, while the specimens without binding pre-

sented diameters of 6 mm. Although the additive binding should ideally only reduce the hole diameter size by 0.48 mm, the manufacturing difficulties and the flow of K51 epoxy resin caused the average measured diameter for the specimens with binding to be about 5 mm. For this reason, additional specimens were manufactured and tested to evaluate the effect of the change in diameter. Specimens without binding and with a hole diameter of 5 mm were manufactured to see if the results obtained would be closer to the specimens with the binding which drilled hole was 6 mm diameter but which final diameter was about 5 mm. Table 9.1 shows the resume of the open-hole specimens manufactured and quasi-statically tested. It is to be noted that the pin diameter for specimens with binding and drilled hole of 6 mm, the pin diameter used was 4.76 mm. This was because some of the PLB6 specimens had slightly smaller diameter, so it was decided to reduce the diameter of the pin to 4.76 mm, which fitted all PLB6 specimens. In this way, all PLB6 specimens were tested with the same pin size, but this meant that some samples had less tight fitting.

End-tabs of 40x30 mm were water-jet cut from a glass-epoxy panel and glued to one end of the specimens. All specimens were tested until final failure or until the testing machine detected a load drop higher than 40%.

The bearing stress at i-th data point (σ_i^{br}) was calculated as per equation 9.1, as defined in ASTM D5961 [244]. The force measured by the load at i-th data point (P_i) was divided by the product of the diameter (D), the nominal thickness of the sample (h) and a load constant per hole factor (k), where k = 2 for a single-fastener or pin test. The nominal ply thickness of 0.13 mm was used for all calculations.

$$\sigma_i^{br} = \frac{P_i}{k \cdot D \cdot h} \tag{9.1}$$

Table 9.1: Initial and final hole diameter for all open hole specimens tested without and with additive binding.

Specimen designation	Type of Binding	Initial diameter, D_i [mm]	Final diameter, D_f [mm]	Pin diameter, d_p [mm]
PLNB6	No binding	6	6	6
PLB6	$[\pm 45]_s$	6	5	4.76
PLNB5	No binding	5	5	5

The ultimate bearing strength (σ^{bru}) was calculated as per equation 9.2, where P^{max} is the maximum load,

$$\sigma^{bru} = \frac{P^{max}}{k \cdot D \cdot h} \tag{9.2}$$

And the bearing strain at the i-th data point (ϵ_i^{br}) was calculated as per equation 9.3, where δ_{1i} and δ_{2i} are the displacements of each grip, K is a load constant equal to 1 for double-shear tests, and D is the diameter of the specimen.

$$\epsilon_i^{br} = \frac{\frac{\delta_{1i}+\delta_{2i}}{2}}{K \cdot D} \tag{9.3}$$

It is worth mentioning that when recording the displacements of each grip, the stiffness of the machine would cause inaccuracies from the real displacement value. However, all samples were measured in the same way, and the measurement uncertainty would be the same for all of them.

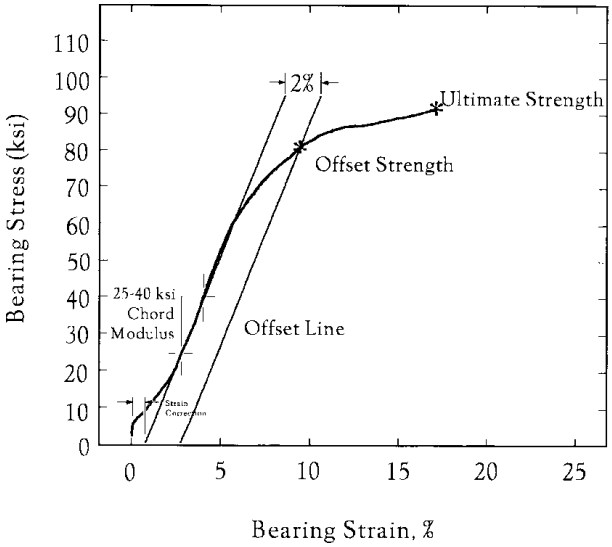

Figure 9.5: Example of bearing stress-strain curve - Reproduced from [244].

In order to calculate the offset strength (σ^{bro}), a bearing chord stiffness line offset along the strain axis by 2% was intersected with the stress-strain curve. The use of 2% as offset is indicated in the ASTM procedure in [244], as shown in figure 9.5. For calculating the bearing chord stiffness, the slope of a straight line between two points on the stress-extension graphs at 2% and 4% extension was used for each specimen and then averaged for each group.

The stress-extension results for samples without and with binding are shown in figure 9.6. All three specimens configurations shown in table 9.1 are presented in figure 9.6. Table 9.2 presents the bearing chord stiffness modulus, maximum load, ultimate bearing strength, ultimate bearing strain and offset bearing strength for specimens without and with binding.

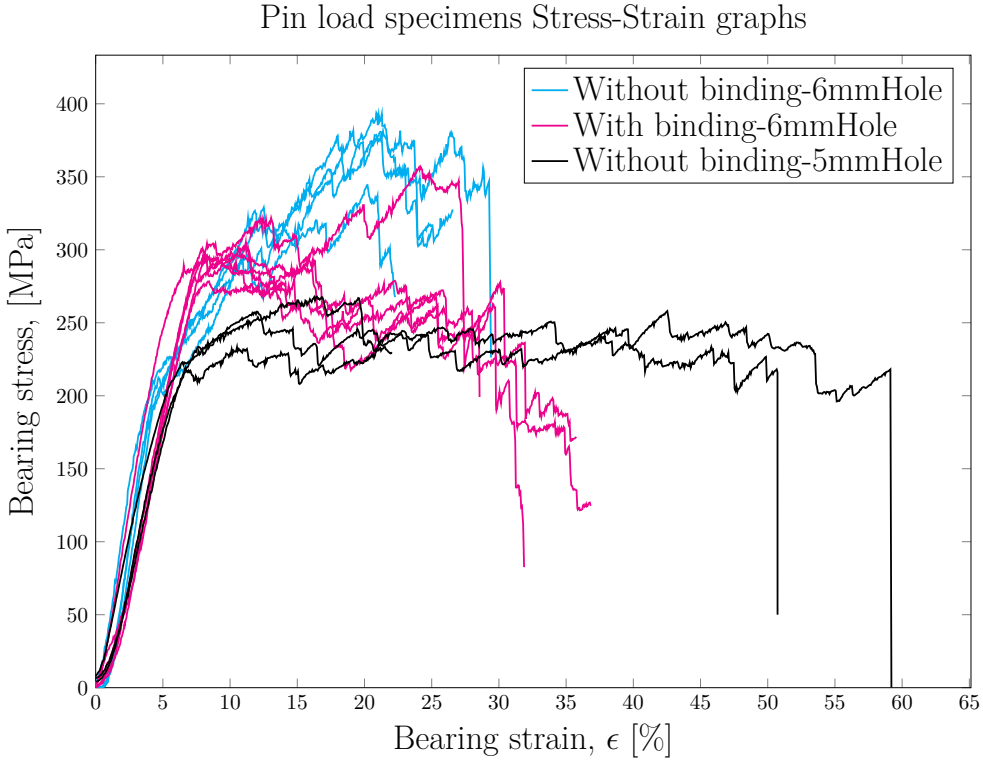

Figure 9.6: Stress-Strain experimental results for the pin load specimens without any binding and with a $[\pm 45]_s$ binding. Specimens with drilled hole diameters of 5 and 6 mm were tested. All specimens shown were tested until final failure or until the testing machine detected a load drop higher than 40%.

Table 9.2: Bearing chord stiffness, maximum force, ultimate stress and strain, and offset strength for pin load specimens without and with binding.

	Specimen		
Property	PLNB6	PLB6	PLNB5
Bearing chord stiffness [GPa] (CV%)	61.6 (4.3)	49.07 (9.64)	44.58 (7.78)
Maximum load [kN] (CV%)	9.4 (5.78)	7.64 (8.58)	6.34 (7.09)
Ultimate bearing strength [kN] (CV%)	376.62 (5.78)	306.14 (8.58)	254.03 (7.09)
Ultimate bearing strain [abs.%] (CV%)	20.47 (4.83)	12.13 (49.76)	12.96 (24.16)
Offset bearing strength [MPa] (CV%)	207.25 (7.13)	285 (7.75)	223.33 (4.93)

For the specimens without binding, the PLNB6 specimens present an average value of 20.47%, 376.62 MPa and 9.4 kN for ultimate bearing strain and bearing stress, and maximum load, respectively; and the offset bearing strength is 207.25 MPa. The PLNB5 specimens present an average value of 12.96%, 254.03 MPa and 6.34 kN for ultimate bearing strain and bearing stress, and maximum load, respectively, and their offset bearing strength is 233.33 MPa. It is to be noted that the bearing chord stiffness of PLNB6 specimens is higher than the one for the PLB6 and PLNB5 specimens, as will be discussed in section 9.4.

The PLB6 specimens present an average value of 12.13%, 306.14 MPa and 7.64 kN for ultimate bearing strain, bearing stress, and maximum load, respectively. The specimens with binding have an offset bearing strength of 285 MPa. It is interesting to note that the offset bearing strength of PLB6 specimens is much higher than for PLNB6 and PLNB5 specimens.

Notably, the specimens without binding presented a smaller coefficient of variation than those with binding in all properties but the offset strength. This is contrary to what has been reported for the free-edge delamination and open-hole specimens, where the addition of the additive bindings reduced the coefficient of variation. This phenomenon is further discussed in section 9.4.

Failed specimens were taken for XCT scanning to study the extension of the damage in both cases, without and with binding. The XCT scan images are presented below.

Figure 9.7 displays an XCT scan projection of the average sum of a PLNB6 specimen tested until failure at the hole area. Different damages are visible across the 0°, 90° and ±45° layers, as shown in the top projection of figure 9.7a. The most prominent damage visible is the transverse intralaminar matrix cracking at the 90° layers, as pointed out with red arrows. The pushing of the pin made the 90° layers separate, promoting delamination between the 0/-45 and -45/90 interfaces and pushing out the 90° plies block out of the laminate at the end of the specimen, as shown in figure 9.7 and as will be discussed in section 9.4. Additionally, a peel off of some fibres of the 45° layers are also visible in figure 9.7b and should not be interpreted as 45° delamination. This peel off is also shown in pictures of the failed specimens, as figure 9.14a.

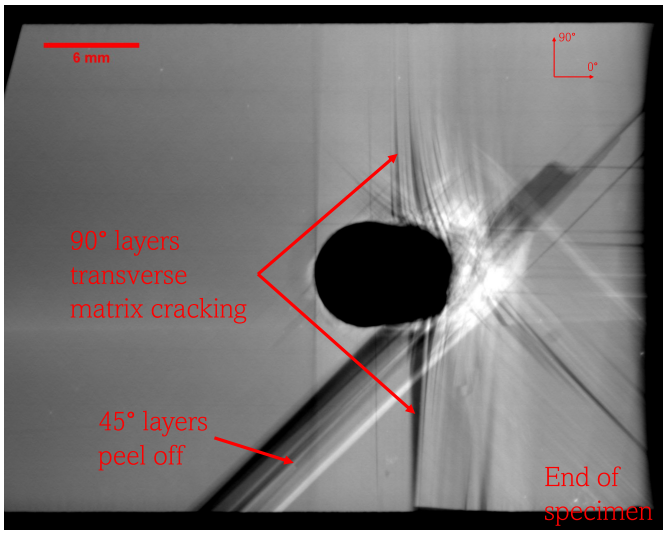

(a)

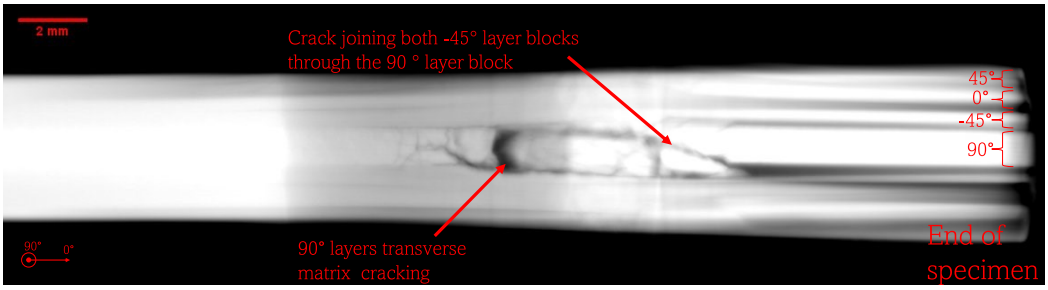

(b)

Figure 9.7: XCT scan projections of the damage at the hole area from a pin load specimen without binding tested until failure. Transverse intralaminar matrix cracking between the 90° plies is visible. Lines of different plies orientations are also visible. (a) Top view projection. (b) Side view projection.

Figure 9.8 shows different XCT image cross-sections of a PLNB6 specimen tested until failure at the hole area. Both left images of figures 9.8a and 9.8b show a top cross-section view of the 90° layers where transverse intralaminar matrix cracking of the 90° layers is clearly visible. Figure 9.8a displays three different cross-section views along the width of the specimen, e.g., AA', BB' and CC', which show how damage propagates from the centre of the hole (AA') towards the edge of the hole in contact with the pin (BB') and towards the extreme of the sample (CC'). The top left parts visible at cross-section AA' are the parts of the top $+45$ layers which peeled off as a result of the extension of the specimen from damage originating at the hole edge. On the right side of cross-section AA' it is visible how the matrix and fibres of the -45 layers broke at the vicinity of the edge of the hole. This fibre breakage is extended to all layers at the contact point of the edge of the hole and the pin, as shown in cross-section BB'. At cross-sections BB' and CC', it is visible how the 90° block of layers has delaminated. Figure 9.8b displays three different cross-section views along the

length of the specimen, e.g., DD', EE' and FF', which show how damage propagates from the right side of the laminate (DD'), towards the centre of the laminate (EE') and the left side of the laminate (FF'). It is visible between views DD' and FF' how the cracks separating the 90° layers migrated to the 0/-45 interface. At cross-section EE' great damage at the hole edge is visible, plus delaminations across all interfaces.

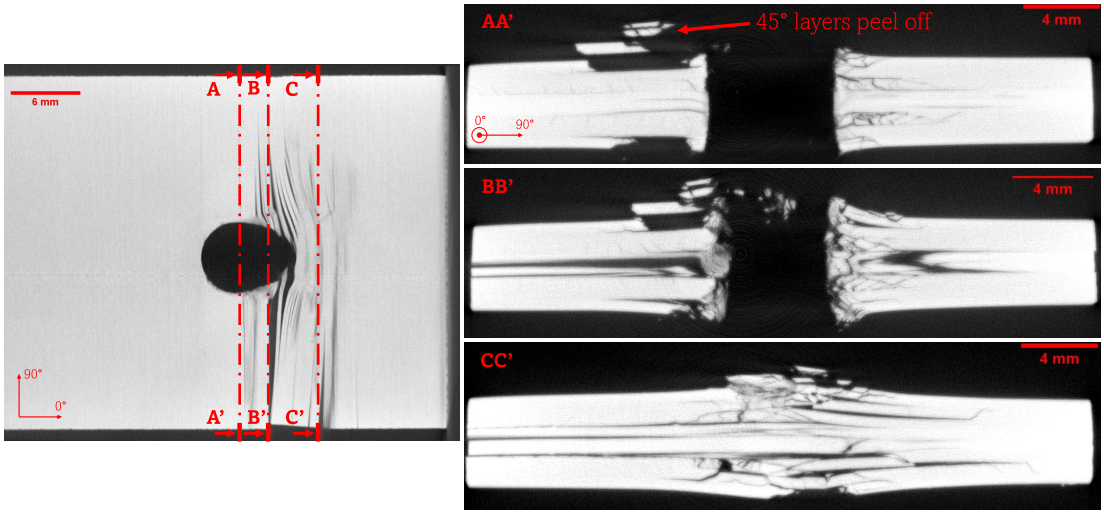

(a)

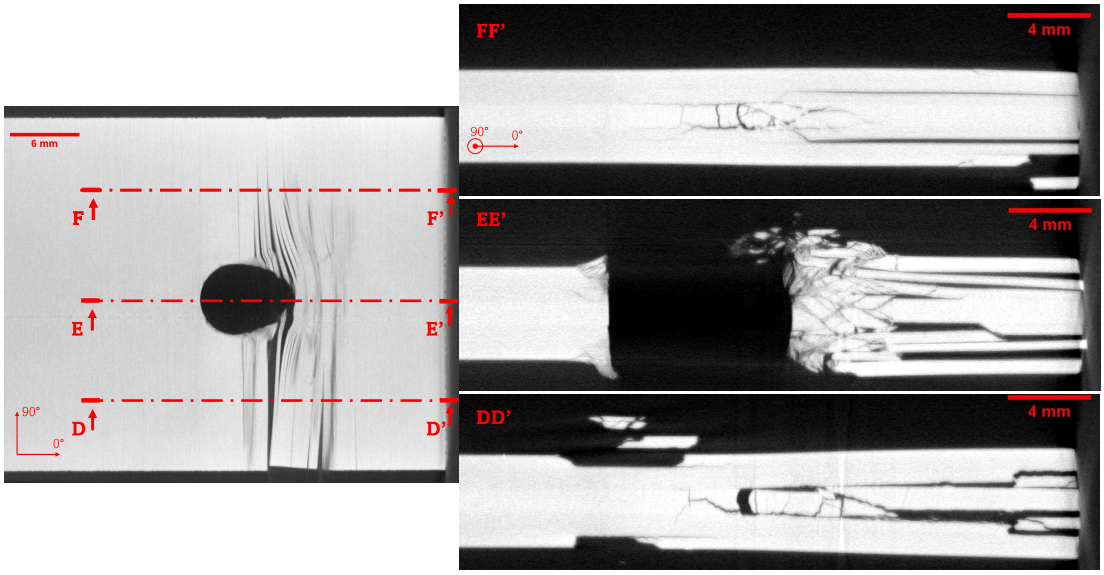

(b)

Figure 9.8: XCT scans of a pin load specimen cross-sections without binding tested until failure. (a) Cross-sectional view of the width of the specimen. (b) Cross-sectional view of the length of the specimen.

Figure 9.9 displays an XCT scan projection of a PLB6 specimen tested until failure at the hole area. Different damages are visible across the 0°, 90° and ±45° layers, as shown in the top projection of figure 9.9a. As in the case of the PLNB6 specimen, the most apparent damage visible is the transverse intralaminar matrix cracking occur-

ring at the 90° layers. The pushing of the pin made the 90° layers separate, promoting delamination between the 0/-45 and -45/90 interfaces and pushing out the 90° plies block out of the laminate at the extreme of the specimen, as shown in figure 9.10 and as will be discussed in section 9.4. Additionally, as in the PLNB6 specimen, a peel off of some fibres of the 45° layers is also visible, as shown in figure 9.9b.

As shown in figure 9.9a, the deformed shape of the hole is more in the form of a pear, whereas, in the case of the PLNB6 specimens, the deformed shape of the hole is more ellipsoidal. Nevertheless, as shown in figure 9.6, the total hole deformation was similar in both cases.

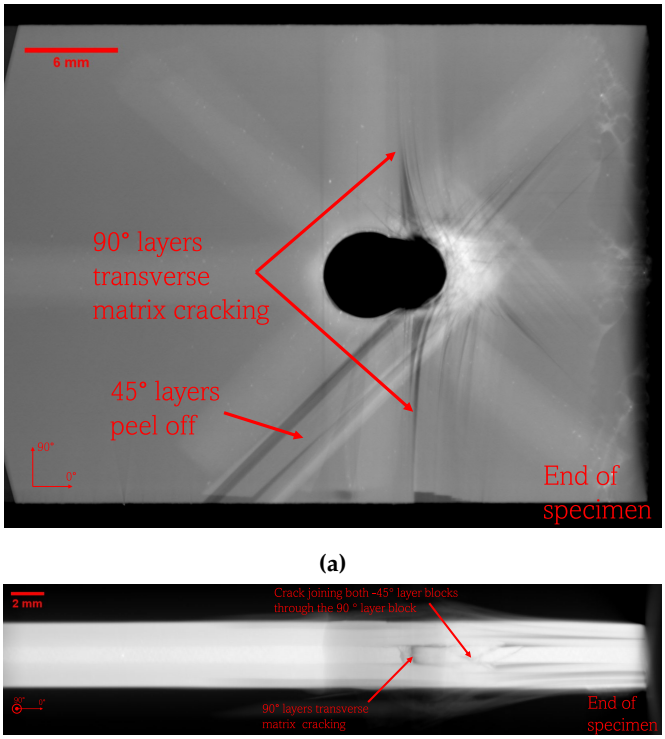

Figure 9.9: XCT scan projections of the damage at the hole area from a pin load specimen with a $[\pm 45]_s$ binding tested until failure. Transverse intralaminar matrix cracking between the 90° plies is visible. Lines of different plies orientations are also visible. (a) Top view projection. (b) Side view projection.

Figure 9.10 shows different XCT image cross-sections of a PLB6 specimen tested until failure at the hole area. Both left images of figures 9.10a and 9.10b show a top cross-section view of the 90° layers where transverse intralaminar matrix cracking of the 90° layers is clearly visible. Three different cross-section views, e.g., AA', BB' and CC', show how damage propagates from the centre of the hole (AA') towards the edge of the hole in contact with the pin (BB') and towards the extreme of the sample (CC').

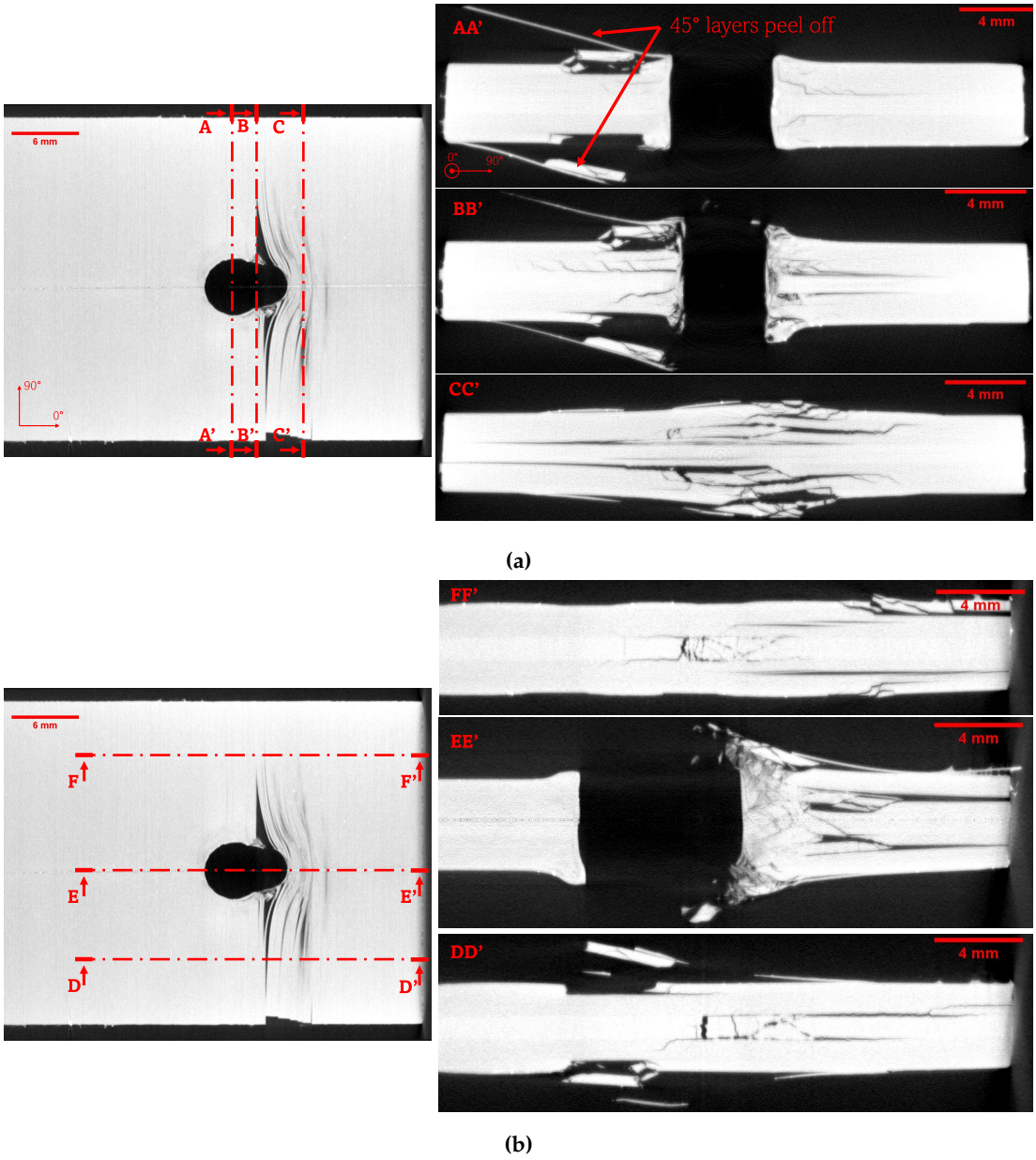

Figure 9.10: XCT scans of the cross-sections of a pin load specimen with a $[\pm 45]_s$ binding tested until failure. (a) Cross-sectional view of the width of the specimen. (b) Cross-sectional view of the length of the specimen.

Similar damage is visible in the case of the PLB6 specimens, which is seen in the PLNB6 specimens at the top left point of cross-section AA'. Parts of the top +45 layers, which peeled off as a result of the extension of the specimen, are visible. Additionally, a peeled-off binding stripe due to the peeling off of the +45 layers is also visible. However, less damage at the -45° layers is observed on the right side of cross-section AA', compared to that one seen in cross-section AA' of in figure 9.8a. Nevertheless, similar damage as that one shown in cross-sections BB' and CC' of figure 9.8a is view in cross-sections BB' and CC' of figure 9.10a.

Moreover, the damage visible in cross-sections DD', EE' and FF' of figure 9.10b is similar to that one of the same cross-sections of figure 9.8b. It is visible how delamination cut through the -45° layers from the -45/90 interfaces to the 0/-45 interfaces, from the DD' cross-section view to the FF' cross-section view.

9.3.2 Tension-tension fatigue results

The fatigue tests were conducted under load-control tension-tension loading at a 5 Hz frequency. A loading R-ratio of 0.1 and severity between 60 to 65%, from the defined failure load in section 9.3.1, were used. Hence, as per equations (8.1) and (8.2) the maximum load applied (F_{max}) was 6 kN (63% of the failure load without binding), and the minimum load (F_{min}) was of 0.6 kN. Hence the load amplitude (F_a) was 2.7 kN, and the mean force (F_m) was 3.3 kN. All tests were conducted in an Instron Servo-hydraulic 8801 testing machine with mechanical wedge grips. The cross-head displacement was measured with the vertical displacement of the grips. Two specimens without additive binding were tested, and five specimens with additive binding were tested.

Figure 9.11 shows the normalised joint stiffness of pin load fatigue specimens against the number of cycles. The normalised joint stiffness was calculated as defined in [289], and it was reported every 10 cycles between 10 and 100 cycles, every 100 cycles between 100 and 1000 cycles, every 10^3 cycles between 10^3 and 10^4 cycles, and every 10^4 between 10^4 and 10^5 cycles.

Figure 9.12 shows the hole elongation against the number of cycles. Figures 9.12b shows the detail of the hole elongation for $20x10^3$ cycles and 10^3, respectively.

All tests were run until 10^5 cycles (run-out) or until failure of the specimen. It is to be noted that all the pins used for the specimens with binding broke due to shear during the development of the tests. The pins broke in a way that the shear-broken faces got locked inside the hole, making the pin as two joined/tied smaller pins at the centre of the pin. In this way, the fatigue tests could keep on until run out without the machine detecting the pin breakage. This phenomenon will be analysed in section 9.4.

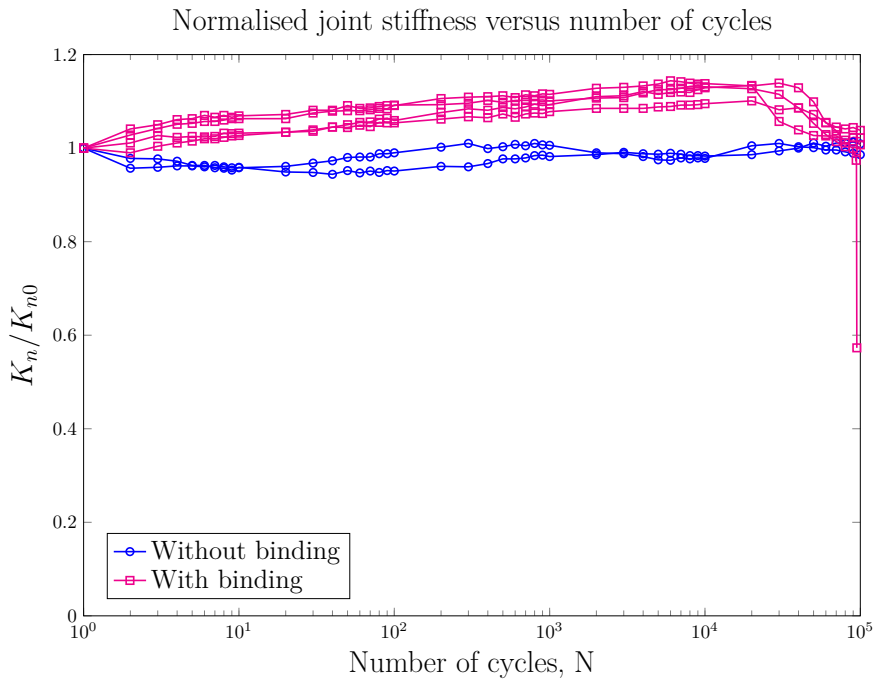

Figure 9.11: Normalised joint stiffness of pin load fatigue specimens versus the number of cycles.

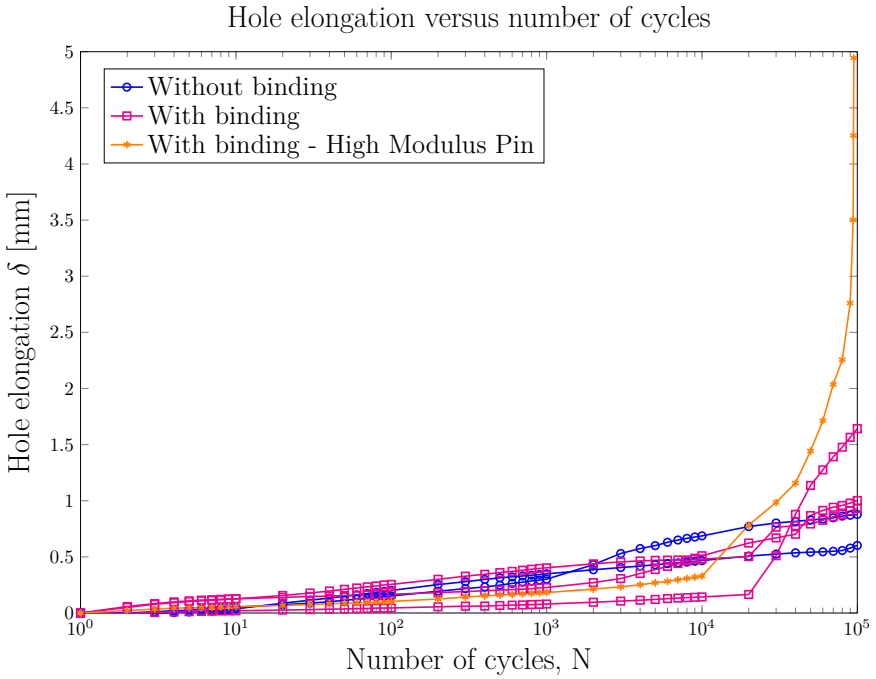

(a)

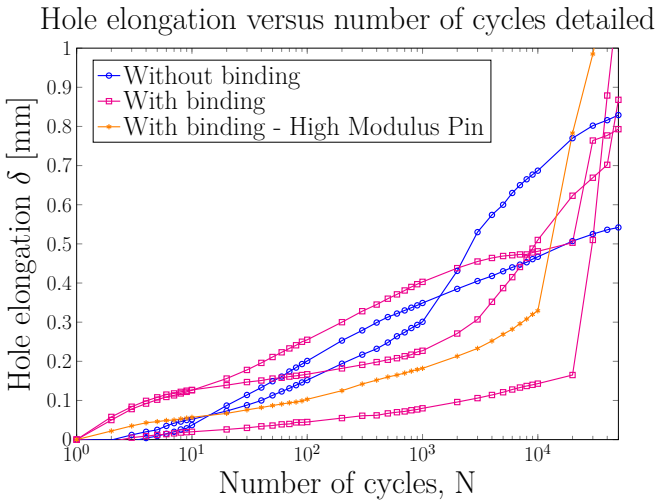

(b)

Figure 9.12: Hole elongation of pin load fatigue specimens versus the number of cycles. (a) Full testing, (b) detail before $50x10^4$ cycles.

9.4 Discussion

9.4.1 Quasi-static tensile specimens discussion

The reduction in the diameter of the PLB6 specimens to diameters of about 5 mm or less made it challenging to make a direct comparison of the results. A steel pin of 6 mm was reduced to a diameter of 4.76 mm, which fit all the holes of the specimens with binding in a tight or close fit. It was decided that all tests would be done with a tight fit between the pin and the hole; hence, the specimens PLNB6 were tested with a 6 mm diameter pin. The PLNB5 specimens were tested with a 5 mm pin. As mentioned before, all the PLB6 specimens did not have all the same diameter, and hence they were tested with a pin of 4.76 mm diameter. Hence, some PLB6 specimens had a sligth less tight fit than others. Both PLNB6 and PLNB5 specimens had tight pin-hole fit with their corresponding 6 and 5 mm diameter pins.

This difference in tightness and the presence of K51 excess resin around the hole is visible in the start of the stress-strain graphs (figure 9.6), where the PLB6 specimens had a slower start of taking the load before the 5% bearing strain approximately. This slower start is due to the clearance between the 4.76 mm pin and the hole of the specimen and the pin crushing the resin residue until it settled properly over the binding. This behaviour is more clearly visible in figure 9.13, as the PLNB6 specimen tested with a 4.76 mm pin had a even larger delay to start taking the load than the PLB6 specimen.

Additional PLNB6 specimens were also tested with a 4.76 mm diameter and, as expected [237, 241], the offset strength and ultimate damage values are much smaller than the ones for the PLNB6 specimens tested with a 6 mm diameter pin. Clearance between the pin and the hole changes the location and direction of the maximum tensile stresses, obtaining smaller strengths for higher clearances [237, 241]. Figure 9.13 compares a representative PLNB6 specimen tested with a 4.76 mm pin, a PLNB6 specimen tested with a 6 mm diameter pin and a PLB6 specimen tested with a 4.76 mm diameter pin. Based on these results, it was concluded then that a tight fit was needed for all tests, and it was a good decision to test the samples with different pin diameters.

As shown in figure 9.13 and recollected in table 9.2, the PLB6 specimens present a 37.5% higher offset strength than the PLNB6 specimens. As explained in [296], the stiffness of the joint is governed by the in-plane compressive modulus and the through-the-thickness tensile modulus in the vicinity of the hole. Hence, the bindings increase the through-the-thickness strength and allow for better resistance to outward displacement or bulging of the laminate. Additionally, the addition of the bindings

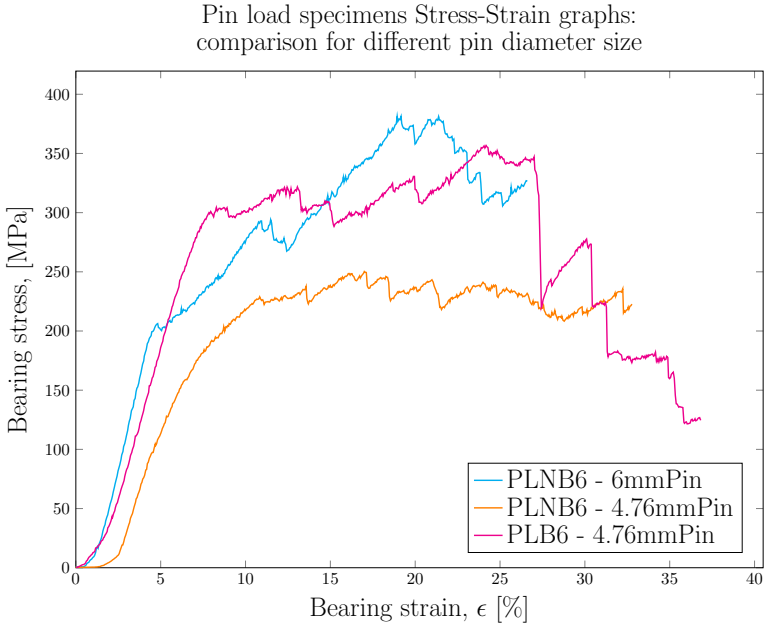

Figure 9.13: Stress-strain curves for a representative PLNB6 specimen tested with a 4.76 mm diameter pin and a representative PLB6 specimen.

reinforces and enhances the in-plane compressive stiffness and allows the joint to resist the compression of the material ahead of the hole for higher strains.

The higher values of offset strength in specimens with binding could also be deduced from the FE results. For small delaminations (0.125 mm), or when the damage is initiated, the effect of the binding in strengthening the hole is visible in figure 9.4, as the value of $\mathcal{G}$ is reduced by 14.6% from the case without binding. As the delamination length grows, approximately after the bearing strain for which the offset strength is measured, the effect of the binding is nullified by the extent of the damage at the hole.

The PLNB6 specimens present a higher average maximum stress than the PLB6 specimens. This is due to increased stress concentration for using a smaller pin in the PLB6 specimens, as explained in [237, 241]. When using a smaller pin diameter, the pin-hole clearance affects the location and direction of the peak stresses as well as the magnitude [237]. Using a 4.76 mm diameter pin for the PLB6 specimens permitted a tight fit at the beginning of the testing. However, once the pin was accommodated over the binding and the initial crushing of the matrix of the pin had been finalised, the use of a smaller pin generated a higher stress concentration factor than a 6 mm pin. As a result, the maximum compressive stress between the pin and the hole edge was higher in the PLB6 specimens. Kelly and Hallstrom [232] found that the hole deformation was found to be slightly larger for clearance fit laminates in comparison to neat fit laminates for a given load level. This larger hole deformation and smaller contact area between the pin and the hole showed a decrease in the stiffness of the

joint. In this way, it is justified that the PLB6 specimens presented smaller chord stiffnes than the PLNB6 specimens.

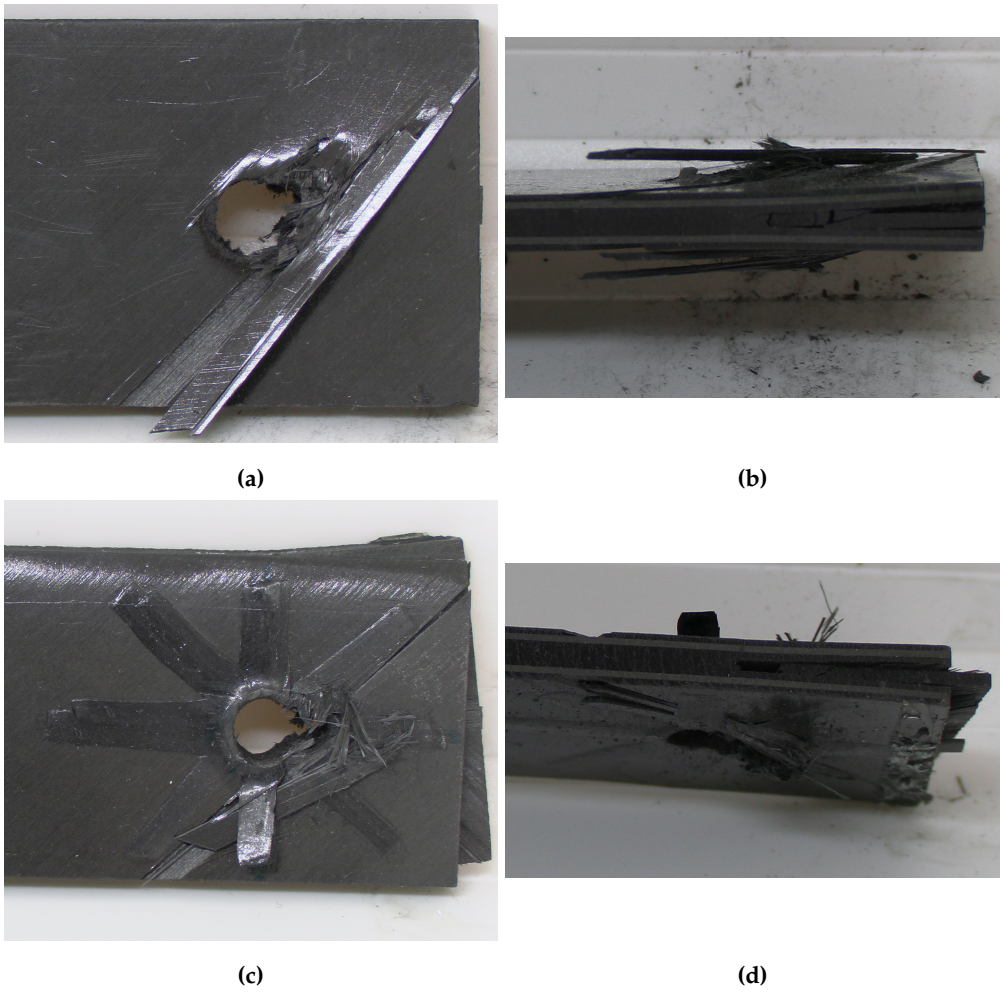

Figure 9.14: Top and side views of failed specimens where the extent of damage at the hole area (hole deformation) and the separation of the 90° are visible.

From the XCT scan images, it is visible that after the nucleation of damage process at the hole edge (matrix cracking, fibre breakage, wedge effect as seen in cross-sections EE' of figures 9.8b and 9.10b), the 90° layers separated via transverse intralaminar matrix cracking. Figure 9.14 displays the top and side views of PLNB6 and PLB6 specimens, where it is viewed how the 90° layers separated and were being pulled out of the specimen. Additionally, it is visible how the top and bottom +45 layers suffered peeling from the fibres that touched the pin tangentially.

Further research is needed to determine the best approach for solving the mismatch in pin diameter between the specimens without and with binding. The use of smaller diameters for the cases without binding undermines their performance significantly and would not give a realistic representation of the joint behaviour. However, the necessity of a smaller diameter for specimens with binding for an initial tight fit

infers the same problem. Figure 9.15 shows the deformed hole of a PLNB5 specimen, which resembles the pear-like shape of the deformed holes of PLB6 specimens. In this way, it is deduced that the PLB6 presented lower maximum stress than the PLNB6 specimens due to the smaller pin diameter.

Figure 9.15: Top view of a failed PLNB5 specimen. The deformed shape of the hole presents a pear-like shape similar to that of the PLB6 specimens.

A possible solution to this obstacle could be preloading the specimens slightly with binding so the appropriate crushing of the binding matrix is done. Then, once the stiff part of the graph starts, stop the loading, unload the test, remove the pin and fit a new pin closer to the one used in the case without binding. For example, applied to the testing done in this research, the PLB6 specimens would have been preloaded between a 3% and a 5% bearing strain with a 4.76 mm diameter pin, unloaded, and tested with a pin diameter which would have given a tight fit for the slightly deformed hole, e.g., a pin diameter of 5.5 mm.

Moreover, regarding solutions to the geometry of the specimen, a possible solution for this problem would be the manufacture of specimens with bigger hole diameters. In this way, the aspect ratio between the pin used of the specimens without and with binding would be smaller, reducing the influence of the stress concentration at the hole edge due to different pin diameters.

The comparison of PLB6 and PLNB5 specimens present similar problems as the PLB6 and PLNB6 specimens comparison. The use of a 4.76 mm pin for the PLB6 produces a high pin-hole clearance, which is not directly comparable to the tight fit of the PLNB5 specimens with their 5 mm pins. In this way, it is interesting to note that PLNB5 specimens have a 18.13% smaller offset bearing strength than the PLB6, but have a 6.8% higher ultimate bearing strength (see table 9.2).

9.4.2 Tension-tension fatigue specimens discussion

All fatigue tests of pin load specimens with binding were inconclusive, as the pin broke due to bending stress. As in the case of the quasi-static loading, a smaller pin was used for the specimens with binding. Although the pin did not break in the quasi-static tests, the bending stress value was very high and close to the bending strength of the pin material used. This situation was not contemplated when starting the fatigue experiments, and should have been taken into account.

As in the research conducted by Sola et al. [297], the residual stiffness did not change significantly with increasing cycle count and was determined not to be a good damage metric for fatigue bearing life. Moreover, in the case of the specimens with binding, as the initial stiffness is smaller than the real one due to the settlement and crushing period of the pin over on the binding, the value of residual stiffness is higher than the initial one throughout the testing. Furthermore, the breakage of the pins for the specimens with binding reduces the stiffness of the pin compared to the laminate.

A pin diameter of 5 mm was used for specimens with binding, and a pin diameter of 6 mm was used for the specimens without binding. As a result, the bending stress at the surface of the specimen is proportional to the cube of the radius, as defined in equation 9.4. In this manner, the difference in maximum bending stress value from a 6 mm pin to a 5 mm pin is almost 73%.

$$\sigma_B = \frac{P_B \cdot L}{\pi \cdot r^3} \tag{9.4}$$

Different materials combined with appropriate thermal treatments were used for the 5 mm diameter pins. Annealed silver steel [298] was used originally for the pins, but as they broke during the testing, a stronger material was sought. A heat-treated high modulus H13 tool steel [299] was also used for manufacturing one of the 5 mm diameter pins, which strength was between 1.2 and 1.5 GPa[1] (High modulus pin referenced in figure 9.12). However, all 5 mm diameter pins broke during the fatigue testing. The failure of the pins did not stop the fatigue testing, as the pins broke brittlely at the centre of the specimen, deflected slightly and were kept "locked" throughout all the testing. As shown in figure 9.12a, approximately after $20x10^3$ cycles, all specimens with binding had presented a deflection of the hole elongation value, which is deemed to be related to the point where the 5 mm pins broke. Thus, a closer look out is shown in figures 9.12b, where it is visible how the specimens with binding did present smaller hole elongations than the specimens without binding until 10^4 cycles.

[1] Average according to different manufacturers when following heat treatment specifications, which indeed were followed.

As in the case of the quasi-static loading, it is thought that if the hole diameter had been larger, these hole effects of high bending stresses and stress concentration points would have had a secondary role compared with the benefits of the additive binding.

Further research is needed where better material and dimensions of the pin are used in the experimental testing. Furthermore, if specimens with a diameter of 6 mm are mandatory, thinner laminates would reduce the maximum load, and hence, maybe, a 5 mm diameter pin would withstand the fatigue testing without breaking.

9.5 Conclusion

The use of thin-ply additive binding stripes, which are bonded to the edge of the hole of pin-loaded composite laminates, has been studied for suppressing the damage originating from the edge of the hole. In particular, it was intended that these additive bindings would enhance the damage tolerance of the pin-loaded laminates and potentially suppress delamination extent when the damage was already present. A FE numerical analysis has been conducted to study the feasibility of such a solution and determine the effect of different additive binding layups on the value of $\mathcal{G}$ for different crack lengths. Moreover, experimental testing was conducted to determine the damage tolerance enhancement achieved when the additive binding was in place. The concluding points of this study are recollected below:

- The FE results indicated that the use of additive bindings around the hole only produced significant improvements in the value of $\mathcal{G}$ for small pre-crack lengths, increasing the through-the-thickness and in-plane strength around the hole area. For a delamination length of 0.125 mm, a reduction of $\mathcal{G}$ of 14.6% was achieved at interface 1 with a $[\pm 45]_s$ binding layup. As the value of delamination length increases, the value of $\mathcal{G}$ does not significantly reduce compared to a laminate without binding.

- The use of additive bindings around the hole improved the offset bearing strength of the pin-loaded laminates with binding by about 37.5% from the specimens without binding.

- Different approaches can be taken for better designs of the quasi-static experiment. It is suggested the design of laminates with larger hole diameters as a viable solution for avoiding the effect of stress concentrators when using different diameter pins for specimens without and with binding. Additionally, carrying out the quasi-static tests in 2 steps is also suggested for fitting a larger diameter pin once the binding has been crushed.

- The presence of the additive binding increased the coefficient of variance of the experimental results.

- The use of normalised hole elongation versus the number of cycles is defined as a much more representative damage parameter than the loss in stiffness for the pin-loaded laminates tested in this study.

- The fatigue test results were not conclusive as the pins used broke during testing. In this way, further work is needed to determine the effect of the additive bindings. However, until 10^4 cycles, the specimens with binding presented smaller hole elongations than those without binding. Hence it is suspected that having the pins not failed for the specimens with binding, smaller hole elongations would have been achieved after the fatigue testing.

Chapter 10

Conclusions and future works

This final chapter presents the recollection of conclusions obtained from the use of additive binding layers for suppressing delamination and enhancing damage tolerance of composite laminates in the four loading scenarios studied in this thesis. It also introduces future works which have been outlined in the previous chapters. This chapter is also intended as a reflection of what could have been done differently and justifies the decisions taken throughout the development of this work.

The use of additive binding layers has been explored for suppressing or stopping delamination originating from the edges of composite laminates in four different loading scenarios. Additionally, the possibility of using the additive binding for enhancing the damage tolerance of composite laminates was studied. First, the application of the additive bindings was tailored for each loading scenario with the help of FE modelling and simulation, and then experimental work was carried out to verify the effect of the additive bindings.

The use of the VCCT as the tool for developing the FE simulations kept the simulations simple and computationally light[1], while achieving satisfactory results for the simulations. It is to be noted that the FE modelling was used as a design tool for verifying the effectiveness of the additive binding to stop delamination originating from the edges of composite laminates. These simulations computed the value of energy release rate $\mathcal{G}$ at the tip of modelled cracks. The comparison of the values of $\mathcal{G}$ between the cases without and with additive binding showed to be an effective method for determining the influence of the binding on the substrate laminate.

The results obtained differ for each loading scenario. The most important benefit is that the used of additive binding managed to enhance the strength of the samples in which cases delamination was a key damage mode, as in research question 1. Additionally, a generally observed benefit from using the additive bindings in three of the four loading scenarios is the reduction in the coefficient of variance in the experimental results. Although common conclusions could be withdrawn from the four loading scenarios, each presented characteristics unique to it. Therefore, different conclusions gathered from each loading scenario are presented below.

The use of additive binding in composite laminates under tension satisfactorily stopped delamination in layups susceptible to free-edge delamination without affecting other failure modes. As a result, the load and strain at failure were significantly increased. However, further work is needed to explore new design ideas that could help remove the stress concentration at the joining point between the end-tabs and the additive bindings. The main conclusions obtained from the use of additive bindings for suppressing delamination in unnotched samples under tension and possible future works are presented following:

- Using additive bindings at the free edges on laminates susceptible to free-edge delamination under axial loading can significantly enhance their failure load and strain. For example, in the angle-ply laminate $[(20_2/-20_2)_2]_s$ studied in this paper, the failure load and strain were increased by 47% and 49%, respectively.

- The use of this technique can suppress other modes of damage arising at the free

[1] Lighter than if compared to cohesive elements.

edges, e.g. matrix cracking. For example, in the quasi-isotropic layup studied in this paper, the nonlinearity of the stress-extension curve was eliminated, indicating that the matrix cracking and free-edge delamination in the off-axis layers were successfully suppressed.

- The $[\pm 45]_s$ additive bindings do not affect other failure modes as shear or tensile strength of the composite. This is deemed to be because of their small quantity compared to the main substrate and relatively low stiffness in the load direction. For instance, the final failure stress stayed almost unchanged in the quasi-isotropic substrate, indicating that the final failure process dominated by 0-degree layer fibre failure was not affected by the bindings. This is excellent news for testing and characterisation purposes, suggesting that binding mainly eliminates the damages initiated by the free-edges, and other failure modes are not affected.

- The suppression of free-edge delamination could lead to the testing and use of different laminate layups in the industry, which as of now are not viable, as when testing coupons of those layups, they fail due to free-edge delamination.

- Improvement of the binding manufacturing methods could be further explored to avoid introducing stress concentration at the binding termination point. For example, longer bindings covered by the end-tab could potentially resolve this issue.

- This technique could be used to suppress free-edge delamination in actual structures or composite laminate coupon samples for material characterisation testing.

- It is to be noted that the selection of a $[\pm 45]_s$ binding layup indicated by the FE modelling did stop the free-edge delamination. This shows the capabilities of the FE modelling approach for choosing an appropriate binding layup. Further experiments on other binding layups can help to build a richer set of experimental results and are suggested by the authors as interesting future research. Additionally, the FE modelling allows for a better informed choosing on the binding material. For this thesis only one material was studied, but the effect of the Young's modulus of the fibre could have a great impact.

The use of additive bindings for enhancing the damage tolerance of composites under edge impact satisfactorily reduced the lengthwise extension of the delamination occurring at all interfaces of the laminates. The main conclusions extracted from the work carried out, and possible future works are mentioned below:

- The use of additive bindings reduced the extent of the crack lengths in the lengthwise direction by about 31%, 36% and 19% for the specimens impacted with 5 J, 10 J and 15 J, respectively.

- The presence of the additive bindings strengthened the edge of the laminate, and a higher average peak load and plateau load were observed for specimens with binding.

- Despite the presence of the additive binding, the edge-on impact produced delamination in all the interfaces between layers wit different fibre orientations, as predicted by the VCCT model and reported in the FE results.

- A higher number of additive binding layups could have been simulated and tested if the computational cost of the simulation could have been reduced or higher performance computers were available. This includes not only bindings in the form of layers. For example, a protection layer in the form of a lightweight layer off resin or semi-hard foam could be studied as a sacrificial part in the event of edge impact.

- The additive binding could potentially be a lightweight and inexpensive method to protect stiffeners from low energy edge impacts.

- Further investigations should be carried out with thicker substrate laminates for studying if the additive bindings perform better in thicker substrate laminates, e.g., Ostre et al. [167] laminate thickness.

For both cases of composite laminates with open holes and pin-loaded laminates, the placement of the additive bindings was in the form of narrow stripes threaded through the hole and bent over the edge of the hole for forming the desired additive binding layup.

In the case of the laminates with open holes studied in this thesis, it was mainly concluded that another substrate layup should have been selected for this type of study rather than the one utilised. It is expected that delamination from free edges would be the main cause of failure. It is usual that this free-edge delamination would occur in laminates with holes, and the development of delamination actually helps to dissipate energy during the load and allows for the laminate to withhold higher loads. In this way, the suppression of delamination arising from the edge of the hole provokes a more sudden failure of the laminate, as the energy is not dissipated slowly, but the delamination occurs abruptly and faster than when no binding is applied. The concluding point of the use of additive bindings in composite laminates with open holes in this thesis and possible future works are recollected below:

- The FE results indicated that the use of additive bindings around the hole only produced significant reduction in the value of energy release rate $\mathcal{G}$ for large pre-crack lengths, i.e., for a delamination length of 2.5 mm, a reduction of 27.6% was achieved at interface 1 with a $[\pm 45]_s$ binding layup.

- The layup utilised for the substrate laminate was not adequate for studying the effect of additive bindings around the edge of the hole of composite laminates with open holes. Therefore, a layup not so susceptible to free-edge delamination is recommended for future works. Additionally, the use of additive bindings for suppressing free-edge delamination is recommended in both specimens without and with binding around the edge of the hole. In this way, the effect of the binding over the edge of the hole is not affected by free-edge delamination.

- The presence of the additive binding significantly reduced the coefficient of variance of the experimental results.

- The fatigue test results were not conclusive, and further work is needed to determine the effect of the additive bindings. Additionally, no preloading of the specimens is recommended for fatigue testing unless it is a low loading. Furthermore, it is recommended to follow the ASTM procedure for the fatigue testing of the samples and start the cyclic loading after a full specimen load and not from the mean load (F_m) as was done in this study.

On the use of additive narrow binding stripes for enhancing the damage tolerance of pin load laminates, the main conclusion was that the pin diameter ratio between the pin used for the specimens without and with binding should not influence the development of the experiments. The preferred solution would be to manufacture laminates with larger holes, so the reduction in diameter due to adding the bindings has a secondary role. The main conclusions and possible future works for pin load laminates are presented following:

- The FE results indicated that the use of additive bindings around the hole only produced significant improvements in the value of $\mathcal{G}$ for small pre-crack lengths, increasing the through-the-thickness and in-plane strength around the hole area. For the $[45_4/0_4/-45_4/90_4]_s$ studied, when small pre-cracks of 0.125 mm were simulated, a reduction of $\mathcal{G}$ of 14.6% was achieved at interface 1 ($[45_4//0_4/-45_4/90_4]_s$) with a $[\pm 45]_s$ binding layup. As the value of delamination length increases, the value of $\mathcal{G}$ does not significantly reduce compared to a laminate without binding.

- The use of additive bindings around the hole improved the offset bearing strength of the pin-loaded laminates with binding by about 37.5% from the specimens without binding.

- Different approaches can be taken for better designs of the quasi-static experiment. It is suggested the design of laminates with larger hole diameters a viable solution for avoiding the effect of stress concentrators when using different diameter pins for specimens without and with binding. Additionally, carrying out the quasi-static

tests in 2 steps is also suggested for fitting a larger diameter pin once the binding has been crushed.

- The presence of the additive binding increased the coefficient of variance of the experimental results.

- The use of normalised hole elongation versus the number of cycles was defined as a more representative damage parameter than the loss in stiffness for the pin-loaded laminates tested in this study.

- The fatigue test results were not conclusive as the pins used broke during testing. In this way, further work is needed to determine the effect of the additive bindings. However, until 10^4 cycles, the specimens with binding presented smaller hole elongations than those without binding. Hence it is suspected that having the pins not failed for the specimens with binding, smaller hole elongations would have been achieved after the fatigue testing.

The use of additive bindings has been presented as a lightweight, cheap and efficient method for suppressing delamination originating from the edges of composite laminates. In this way, the primary purpose of this thesis was achieved by giving a response to the four questions or loading scenarios envisioned. The additive binding solution was first studied for suppressing free-edge delamination in laminates under tension, then edge impact, open hole and last pin-loaded laminates.

It was concluded that the use of additive bindings was a good solution for research questions one and two, but did not particularly affect the results from the cases without binding in research questions three and four. In the cases where free-edge delamination was a key failure mechanism (research question one), free-edge lamination was successfully suppressed, increasing the final maximum load and strain of unnotched specimens under tension. In the case of composite laminates under edge impact (research question two), the use of additive bindings on the impacted edge reduced the extent of delamination in the perpendicular direction to the impact and enhanced the transverse strength of the laminates. When using additive bindings in notched specimens under tension (research question three), the failure load and extension remained almost unchanged due to the appearance of free-edge delamination which ruled the failure of the specimens. Last, the use of additive bindings in pin-loaded laminates (research question four) is still to be decided based on further investigations, as the use of smaller pins for the specimens with binding increased the stress at contact point between the pin and the laminate, reducing the ultimate bearing strength of the specimens with binding. However, higher significant higher offset bearing strength were obtained for the specimens with binding.

List of References

[1] Adrian P. Mouritz. **Materials selection for aerospace**. In Adrian P Mouritz, editor, *Introduction to Aerospace Materials*, pages 569–600. Elsevier, 2012. doi:10.1533/9780857095152.569.

[2] Ted L. Anderson. *Fracture Mechanics: Fundamentals and Applications*. CRC Press, third edit edition, jun 2005. doi:10.1201/9781420058215.

[3] S. L. Ogin, P. Brøndsted, and J. Zangenberg. **Composite materials: Constituents, architecture, and generic damage**. In *Modeling Damage, Fatigue and Failure of Composite Materials*, pages 3–23. Elsevier Inc., jan 2016. doi:10.1016/B978-1-78242-286-0.00001-7.

[4] Ismail Hakki Hacialioglu. **A review of the Global Composites Market and Turkish Composites Market**, 2018.

[5] Zdenek P. Bazant, Isaac M. Daniel, and Zhengzhi Li. **Size Effect and Fracture Characteristics of Composite Laminates**. *Journal of Engineering Materials and Technology*, **118**(3):317–324, jul 1996. doi:10.1115/1.2806812.

[6] M. R. Wisnom and J. W. Atkinson. **Reduction in tensile and flexural strength of unidirectional glass fibre-epoxy with increasing specimen size**. *Composite Structures*, **38**(1-4):405–411, may 1997. doi:10.1016/S0263-8223(97)00075-5.

[7] M. R. Wisnom. **Size effects in the testing of fibre-composite materials**. *Composites Science and Technology*, **59**(13):1937–1957, oct 1999. doi:10.1016/S0266-3538(99)00053-6.

[8] P. P. Camanho, P. Maimí, and C. G. Dávila. **Prediction of size effects in notched laminates using continuum damage mechanics**. *Composites Science and Technology*, **67**(13):2715–2727, oct 2007. doi:10.1016/j.compscitech.2007.02.005.

[9] J Lee and C Soutis. **Measuring the notched compressive strength of composite laminates: Specimen size effects**. *Composites Science and Technology*, **68**(12):2359–2366, 2008. doi:https://doi.org/10.1016/j.compscitech.2007.09.003.

[10] M.R. Wisnom, B. Khan, and S.R. Hallett. **Size effects in unnotched tensile strength of unidirectional and quasi-isotropic carbon/epoxy composites**. *Composite Structures*, **84**(1):21–28, jun 2008. doi:10.1016/j.compstruct.2007.06.002.

[11] B. Y. Chen, T. E. Tay, P. M. Baiz, and S. T. Pinho. **Numerical analysis of size effects on open-hole tensile composite laminates**. *Composites Part A: Applied Science and Manufacturing*, **47**(1):52–62, 2013. doi:10.1016/j.compositesa.2012.12.001.

[12] G.H. Erçin, P.P. Camanho, J. Xavier, G. Catalanotti, S. Mahdi, and P. Linde. **Size effects on the tensile and compressive failure of notched composite laminates**. *Composite Structures*, **96**:736–744, feb 2013. doi:10.1016/j.compstruct.2012.10.004.

[13] R Byron Pipes and N.J. Pagano. **Interlaminar Stresses in Composite Laminates Under Uniform Axial Extension**. *Journal of Composite Materials*, **4**(4):538–548, oct 1970. doi:10.1177/002199837000400409.

[14] A.H. Puppo and H.A. Evensen. **Interlaminar Shear in Laminated Composites Under Generalized Plane Stress**. *Journal of Composite Materials*, **4**(2):204–220, feb 1970. doi:10.1177/002199837000400206.

[15] James T.S. Wang and John N Dickson. **Interlaminar Stresses in Symmetric Composite Laminates**. *Journal of Composite Materials*, **12**(4):390–402, dec 1978. doi:10.1177/002199837801200404.

[16] Erik A Phillips, Carl T Herakovich, and Lori L Graham. **Damage development in composites with large stress gradients**. *Composites Science and Technology*, **61**(15):2169–2182, nov 2001. doi:10.1016/S0266-3538(01)00112-9.

[17] N.J. Pagano and R. Byron Pipes. **The Influence of Stacking Sequence on Laminate Strength**. *Journal of Composite Materials*, **5**(1):50–57, jan 1971. doi:10.1177/002199837100500105.

[18] Carl-Gustaf Aronsson. **Stacking sequence effects on fracture of notched carbon fibre/epoxy composites**. *Composites Science and Technology*, **24**(3):179–198, jan 1985. doi:10.1016/0266-3538(85)90072-7.

[19] P.A. Smith and K.J. Pascoe. **The effect of stacking sequence on the bearing strengths of quasi-isotropic composite laminates**. *Composite Structures*, **6**(1-3):1–20, jan 1986. doi:10.1016/0263-8223(86)90065-6.

[20] Edgar Fuoss, Paul V. Straznicky, and Cheung Poon. **Effects of stacking sequence on the impact resistance in composite laminates — Part 1: parametric study**. *Composite Structures*, **41**(1):67–77, jan 1998. doi:10.1016/S0263-8223(98)00036-1.

[21] Stephen R. Hallett and Michael R. Wisnom. **Numerical investigation of progressive damage and the effect of layup in notched tensile tests**. *Journal of Composite Materials*, **40**(14):1229–1245, jul 2006. doi:10.1177/0021998305057432.

[22] Richard M. Christensen. **Effective properties of composite materials containing voids**. *Proceedings of the Royal Society of London. Series A: Mathematical and Physical Sciences*, **440**(1909):461–473, feb 1993. doi:10.1098/rspa.1993.0027.

[23] Mahoor Mehdikhani, Larissa Gorbatikh, Ignaas Verpoest, and Stepan V Lomov. **Voids in fiber-reinforced polymer composites: A review on their formation, characteristics, and effects on mechanical performance**. *Journal of Composite Materials*, **53**(12):1579–1669, may 2019. doi:10.1177/0021998318772152.

[24] BN Fedulov, FK Antonov, AA Safonov, AE Ushakov, and SV Lomov. **Influence of fibre misalignment and voids on composite laminate strength**. *Journal of Composite Materials*, **49**(23):2887–2896, sep 2015. doi:10.1177/0021998314557533.

[25] Robert M. Jones. *Mechanics of Composite Materials*. CRC Press, oct 1999. doi:10.1201/9781498711067.

[26] J.M. Whitney and C.E. Browning. **Free-Edge Delamination of Tensile Coupons**. *Journal of Composite Materials*, **6**(2):300–303, apr 1972. doi:10.1177/002199837200600211.

[27] N. J. PAGANO and L. M. LACKMAN. **Prevention of Delamination of Composite Laminates**. *AIAA Journal*, **13**(3):399–401, mar 1975. doi:10.2514/3.49713.

[28] Alexander Harris and Oscar Orringer. **Investigation of Angle-Ply Delamination Specimen For Interlaminar Strength Test**. *Journal of Composite Materials*, **12**(3):285–299, oct 1978. doi:10.1177/002199837801200306.

[29] S.S. Wang. **Edge delamination in angle-ply composite laminates**. In *22nd Structures, Structural Dynamics and Materials Conference*, number Pt 1, pages 473–484, Reston, Virigina, apr 1981. American Institute of Aeronautics and Astronautics. doi:10.2514/6.1981-578.

[30] S.S. Wang and I. Choi. **The mechanics of delamination in fibre-reinforced composite materials**. Technical report, NASA, 1983.

[31] S.S. Wang. **Fracture Mechanics for Delamination Problems in Composite Materials**. In George J. Dvorak and Richard T. Shield, editors, *Mechanics of Material Behavior*, **6** of *Studies in Applied Mechanics*, pages 369–383. Elsevier, 1984. doi:https://doi.org/10.1016/B978-0-444-42169-2.50029-2.

[32] Donald F. Adams and Jayant M. Mahishi. **DELAMINATION MICROMECHANICS ANALYSIS**. Technical report, NASA, Laramie, Wyoming, 1985.

[33] K. S. Kim and C. S. Hong. **Delamination Growth in Angle-Ply Laminated Composites**. *Journal of Composite Materials*, **20**(5):423–438, 1986. doi:10.1177/002199838602000502.

[34] Amar C. Garg. **Delamination—a damage mode in composite structures**. *Engineering Fracture Mechanics*, **29**(5):557–584, jan 1988. doi:10.1016/0013-7944(88)90181-6.

[35] A. S.D. Wang. **Overview of the delamination problem in structural composites**. *Mechanical and corrosion properties. Series A, Key engineering materials*, **37**:1–19, jan 1989. doi:10.4028/www.scientific.net/kem.37.1.

[36] D Daniewicz and G Frantziskonis. **Edge delamination in laminated composites**. *Composite Structures*, **21**(3):141–153, jan 1992. doi:10.1016/0263-8223(92)90014-4.

[37] Vladimir V. Bolotin. **Delaminations in composite structures: Its origin, buckling, growth and stability**. *Composites Part B: Engineering*, **27**(2 PART B):129–145, jan 1996. doi:10.1016/1359-8368(95)00035-6.

[38] M. R. Wisnom. **The role of delamination in failure of fibre-reinforced composites**. *Philosophical Transactions of the Royal Society A: Mathematical, Physical and Engineering Sciences*, **370**(1965):1850–1870, apr 2012. doi:10.1098/rsta.2011.0441.

[39] W.S. Chan and A.S.D. Wang. **Effects of a 90° ply on matrix cracks and edge delamination in composite laminates**. *Composites Science and Technology*, **38**(2):143–157, jan 1990. doi:10.1016/0266-3538(90)90003-N.

[40] Raymond B Krieger. **An Adhesive Interleaf to Reduce Stress Concentrations Between Plys of Structural Composites**. In *Adhesion 12*, **32**, pages 159–165. Springer Netherlands, Dordrecht, 1988. doi:10.1007/978-94-009-1349-3_10.

[41] W. CHAN and O. OCHOA. **Suppression of edge delamination in composite laminates by terminating a critical ply near the edges**. In *29th Structures, Structural Dynamics and Materials Conference*, Reston, Virginia, apr 1988. American Institute of Aeronautics and Astronautics. doi:10.2514/6.1988-2257.

[42] LA Mignery, TM Tan, and CT Sun. **The Use of Stitching to Suppress Delamination in Laminated Composites**. In *Delamination and Debonding of Materials*, pages 371–371–15. ASTM International, 100 Barr Harbor Drive, PO Box C700, West Conshohocken, PA 19428-2959, 1985. doi:10.1520/STP36315S.

[43] Ronald Krueger. **Virtual crack closure technique: History, approach, and applications**. *Applied Mechanics Reviews*, **57**(2):109–143, mar 2004. doi:10.1115/1.1595677.

[44] V. D. Azzi and S. W. Tsai. **Anisotropic strength of composites**. *Experimental Mechanics*, **5**(9):283–288, 1965. doi:10.1007/bf02326292.

[45] Stephen W. Tsai and Edward M. Wu. **A General Theory of Strength for Anisotropic Materials**. *Journal of Composite Materials*, **5**(1):58–80, jul 1971. doi:10.1177/002199837100500106.

[46] M.W. Hyer. **Laminated Plate and Shell Theory**. In *Comprehensive Composite Materials*, pages 479–510. Elsevier, jan 2000. doi:10.1016/B0-08-042993-9/00054-1.

[47] M.W. Hyer and A.M. Waas. **Micromechanics of Linear Elastic Continuous Fiber Composites**. In *Comprehensive Composite Materials*, pages 345–375. Elsevier, jan 2000. doi:10.1016/b0-08-042993-9/00049-8.

[48] Jack R. Vinson and Robert L. Sierakowski, editors. *The Behavior Of Structures Composed Of Composite Materials*, **105** of *Solid Mechanics And Its Applications*. Springer Netherlands, Dordrecht, 2002. doi:10.1007/0-306-48414-5.

[49] M. W. Hyer and Scott R. White. *Stress Analysis of Fiber-reinforced Composite Materials*. DEStech Publications, Inc., 2009.

[50] Carl T. Herakovich. **Mechanics of composites: A historical review**, apr 2012. doi:10.1016/j.mechrescom.2012.01.006.

[51] Sérgio Frascino Müller de Almeida and Zabulon dos Santos Nogueira Neto. **Effect of void content on the strength of composite laminates**. *Composite Structures*, **28**(2):139–148, jan 1994. doi:10.1016/0263-8223(94)90044-2.

[52] M.E. Waddoups, J.R. Eisenmann, and B.E. Kaminski. **Macroscopic Fracture Mechanics of Advanced Composite Materials**. *Journal of Composite Materials*, **5**(4):446–454, apr 1971. doi:10.1177/002199837100500402.

[53] G. Caprino, J.C. Halpin, and L. Nicolais. **Fracture mechanics in composite materials**. *Composites*, **10**(4):223–227, 1979. doi:https://doi.org/10.1016/0010-4361(79)90023-5.

[54] Richard M Christensen. **Why progress on the failure of fiber composite materials has been so retarded**, nov 2017. doi:10.1177/0731684417733550.

[55] M. J. Hinton, A. S. Kaddour, and P. D. Soden. **A comparison of the predictive capabilities of current failure theories for composite laminates, judged against experimental evidence**. *Composites Science and Technology*, **62**(12-13 SPECIAL ISSUE):1725–1797, sep 2002. doi:10.1016/S0266-3538(02)00125-2.

[56] M. J. Hinton and A. S. Kaddour. **The background to the Second World-Wide Failure Exercise**. *Journal of Composite Materials*, **46**(19-20):2283–2294, sep 2012. doi:10.1177/0021998312449885.

[57] A. S. Kaddour and M. J. Hinton. **Maturity of 3D failure criteria for fibre-reinforced composites: Comparison between theories and experiments: Part B of WWFE-II**. *Journal of Composite Materials*, **47**(6-7):925–966, mar 2013. doi:10.1177/0021998313478710.

[58] N.J. Pagano and G.A. Schoeppner. **Delamination of Polymer Matrix Composites: Problems and Assessment**. *Comprehensive Composite Materials*, pages 433–528, 2000. doi:10.1016/b0-08-042993-9/00073-5.

[59] M.J. Laffan. **Testing the toughness of polymer matrix composites**. In *Failure Mechanisms in Polymer Matrix Composites*, pages 110–128. Elsevier, jan 2012. doi:10.1533/9780857095329.1.110.

[60] **18 - Fracture processes of aerospace materials**. In Adrian P Mouritz, editor, *Introduction to Aerospace Materials*, pages 428–453. Elsevier, 2012. doi:10.1533/9780857095152.428.

[61] N. Sato, M. Hojo, and M. Nishikawa. **Intralaminar fatigue crack growth properties of conventional and interlayer toughened CFRP laminate under mode I loading**. *Composites Part A: Applied Science and Manufacturing*, **68**:202–211, jan 2015. doi:10.1016/j.compositesa.2014.09.031.

[62] Robert L. Crane. **Nondestructive Inspection of Composites**. In *Comprehensive Composite Materials*, pages 227–233. Elsevier, jan 2000. doi:10.1016/B0-08-042993-9/00075-9.

[63] Bernhard R. Tittmann and Robert L. Crane. **Ultrasonic Inspection of Composites**. In *Comprehensive Composite Materials*, pages 259–320. Elsevier, jan 2000. doi:10.1016/B0-08-042993-9/00201-1.

[64] Robert Crane, Donald Hagemaier, and Robert Fassbender. **Radiographic Inspection of Composites**. In *Comprehensive Composite Materials*, pages 321–344. Elsevier, jan 2000. doi:10.1016/B0-08-042993-9/00078-4.

[65] R.L. Thomas, L.D. Favro, X. Han, and Z. Ouyang. **Thermal Methods Used in Composite Inspection**. In *Comprehensive Composite Materials*, pages 427–446. Elsevier, jan 2000. doi:10.1016/B0-08-042993-9/00082-6.

[66] Sridhar Krishnaswamy. **Optical Methods of Inspecting Composites (Holography and Shearography)**. In *Comprehensive Composite Materials*, pages 447–468. Elsevier, jan 2000. doi:10.1016/B0-08-042993-9/00083-8.

[67] Nagaraja Shetty, S. M. Shahabaz, S. S. Sharma, and S. Divakara Shetty. **A review on finite element method for machining of composite materials**, sep 2017. doi:10.1016/j.compstruct.2017.06.012.

[68] R Foye and D Baker. **Design of orthotropic laminates, presented at the 11th annual AIAA structures**. In *Structural dynamics and materials conference, Denver, Colorado*, 1970.

[69] F. W. Crossman, W. J. Warren, A. S.D. Wang, and G. E. Law. **Initiation and Growth of Transverse Cracks and Edge Delamination in Composite Laminates Part 2. Experimental Correlation**. *Journal of Composite Materials*, **14**(1):88–108, jul 1980. doi:10.1177/002199838001400107.

[70] C T Herakovich. **Edge effects and delamination failures**. *The Journal of Strain Analysis for Engineering Design*, **24**(4):245–252, oct 1989. doi:10.1243/03093247V244245.

[71] JM Whitney and RY Kim. **Effect of Stacking Sequence on the Notched Strength of Laminated Composites**. In *Composite Materials: Testing and Design (Fourth Conference)*, number 617, pages 229–229–14. ASTM International, 100 Barr Harbor Drive, PO Box C700, West Conshohocken, PA 19428-2959, 1977. doi:10.1520/STP26946S.

[72] MM Ratwani and HP Kan. **Effect of Stacking Sequence on Damage Propagation and Failure Modes in Composite Laminates**. In *Damage in Composite Materials: Basic Mechanisms, Accumulation, Tolerance, and Characterization*, pages 211–211–18. ASTM International, 100 Barr Harbor Drive, PO Box C700, West Conshohocken, PA 19428-2959, 1982. doi:10.1520/STP34328S.

[73] N. Hongkarnjanakul, C. Bouvet, and S. Rivallant. **Validation of low velocity impact modelling on different stacking sequences of CFRP laminates and influence of fibre failure**. *Composite Structures*, **106**:549–559, dec 2013. doi:https://doi.org/10.1016/j.compstruct.2013.07.008.

[74] Alaattin Aktas and M.Husnu Dirikolu. **The effect of stacking sequence of carbon epoxy composite laminates on pinned-joint strength**. *Composite Structures*, **62**(1):107–111, oct 2003. doi:10.1016/S0263-8223(03)00096-5.

[75] J.M. Whitney and R.J. Nuismer. **Stress Fracture Criteria for Laminated Composites Containing Stress Concentrations**. *Journal of Composite Materials*, **8**(3):253–265, jul 1974. doi:10.1177/002199837400800303.

[76] John C Brewer and Paul A Lagace. **Quadratic Stress Criterion for Initiation of Delamination**. *Journal of Composite Materials*, **22**(12):1141–1155, dec 1988. doi:10.1177/002199838802201205.

[77] Matthew T. Fenske and Anthony J. Vizzini. **The inclusion of in-plane stresses in delamination criteria**. *Journal of Composite Materials*, **35**(15):1325–1342, 2001. doi:10.1106/VB89-LW8A-9H32-2TN3.

[78] Z. Hashin. **Failure Criteria for Unidirectional Fiber Composites**. *Journal of Applied Mechanics*, **47**(2):329–334, jun 1980. doi:10.1115/1.3153664.

[79] M.R. Wisnom, G.F.J. Hill, and M. I. Jones. **Through thickness failure prediction of composite structural elements**. In *13th ICCM International Conferences on Composite Materials*, Beijing, China, 2001.

[80] A.C. Orifici, I. Herszberg, and R.S. Thomson. **Review of methodologies for composite material modelling incorporating failure**. *Composite Structures*, **86**(1-3):194–210, nov 2008. doi:10.1016/j.compstruct.2008.03.007.

[81] Alan Arnold Griffith. **VI. The phenomena of rupture and flow in solids**. *Philosophical Transactions of the Royal Society of London. Series A, Containing Papers of a Mathematical or Physical Character*, **221**(582-593):163–198, jan 1920. doi:10.1098/rsta.1921.0006.

[82] George R. Irwin. **Fracture**. **970**, pages 551–590. Springer, Berlin, Heidelberg, 1958. doi:10.1007/978-3-642-45887-3_5.

[83] TK O'Brien. **Characterization of Delamination Onset and Growth in a Composite Laminate**. In *Damage in Composite Materials: Basic Mechanisms, Accumulation, Tolerance, and Characterization*, pages 140–167. ASTM International, 100 Barr Harbor Drive, PO Box C700, West Conshohocken, PA 19428-2959, 1982. doi:10.1520/STP34325S.

[84] E.F. Rybicki and M.F. Kanninen. **A finite element calculation of stress intensity factors by a modified crack closure integral**. *Engineering Fracture Mechanics*, **9**(4):931–938, jan 1977. doi:10.1016/0013-7944(77)90013-3.

[85] E.F. Rybicki, D.W. Schmueser, and J Fox. **An Energy Release Rate Approach For Stable Crack Growth in the Free-Edge Delamination Problem**. *Journal of Composite Materials*, **11**(4):470–487, oct 1977. doi:10.1177/002199837701100409.

[86] Andreas J. Brunner. **Fracture mechanics of polymer composites in aerospace applications**. In *Polymer Composites in the Aerospace Industry*, pages 195–252. Elsevier, jan 2020. doi:10.1016/B978-0-08-102679-3.00008-3.

[87] Rafiullah Khan. **Fiber bridging in composite laminates: A literature review**, dec 2019. doi:10.1016/j.compstruct.2019.111418.

[88] W.V. Liebig, C. Leopold, and K. Schulte. **Photoelastic study of stresses in the vicinity of a unique void in a fibre-reinforced model composite under compression**. *Composites Science and Technology*, **84**:72–77, jul 2013. doi:10.1016/j.compscitech.2013.04.011.

[89] F. Paris, E. Correa, and J. Cañas. **Micromechanical view of failure of the matrix in fibrous composite materials**. *Composites Science and Technology*, **63**(7):1041–1052, may 2003. doi:10.1016/S0266-3538(03)00017-4.

[90] E. K. Gamstedt, S. I. Andersen, and Roskilde (DK). Materials Research Department. Risø National Lab. *Fatigue degradation and failure of rotating composite structures - Materials characterisation and underlying mechanisms.* Risø National Laboratory, 2001.

[91] Patrick Johnson and Fu-Kuo Chang. **Characterization of Matrix Crack-Induced Laminate Failure—Part II: Analysis and Verifications**. *Journal of Composite Materials*, **35**(22):2037–2074, nov 2001. doi:10.1106/VTQ8-TXDY-72Q6-677V.

[92] Luo-Yu Xu. **Interaction between matrix cracking and edge delamination in composite laminates**. *Composites Science and Technology*, **50**(4):469–478, jan 1994. doi:10.1016/0266-3538(94)90055-8.

[93] F. Bassam, L. Boniface, K. Jones, and S.L. Ogin. **On the behaviour of the residual strain produced by matrix cracking in cross-ply laminates**. *Composites Part A: Applied Science and Manufacturing*, **29**(11):1425–1432, nov 1998. doi:10.1016/S1359-835X(98)00037-2.

[94] J. E. Bailey, P. T. Curtis, and A. Parvizi. **On the transverse cracking and longitudinal splitting behaviour of glass and carbon fibre reinforced epoxy cross ply laminates and the effect of Poisson and thermally generated strain**. *Proceedings of the Royal Society of London. A. Mathematical and Physical Sciences*, **366**(1727):599–623, jul 1979. doi:10.1098/rspa.1979.0071.

[95] Stephen Tsai, Sangwook Sihn, and Ran Kim. **Thin Ply Composites**. In *46th AIAA/ASME/ASCE/AHS/ASC Structures, Structural Dynamics and Materials Conference*, **4**, pages 2555–2559, Reston, Virigina, apr 2005. American Institute of Aeronautics and Astronautics. doi:10.2514/6.2005-2005.

[96] Serge Abrate. **Matrix cracking in laminated composites: A review**. *Composites Engineering*, **1**(6):337–353, jan 1991. doi:10.1016/0961-9526(91)90039-U.

[97] Z. Hashin and A. Rotem. **A Fatigue Failure Criterion for Fiber Reinforced Materials**. *Journal of Composite Materials*, **7**(4):448–464, oct 1973. doi:10.1177/002199837300700404.

[98] A. Puck. **FAILURE ANALYSIS OF FRP LAMINATES BY MEANS OF PHYSICALLY BASED PHENOMENOLOGICAL MODELS**. *Composites Science and Technology*, **58**(7):1045–1067, jul 1998. doi:10.1016/S0266-3538(96)00140-6.

[99] A. Puck and H. Schürmann. **Failure analysis of FRP laminates by means of physically based phenomenological models**. *Composites Science and Technology*, **62**(12-13):1633–1662, sep 2002. doi:10.1016/S0266-3538(01)00208-1.

[100] Masaharu Iwamoto, Qing Qing Ni, Teruhiko Fujiwara, and Ken Kurashiki. **Intralaminar fracture mechanism in unidirectional CFRP composites: Part I: Intralaminar toughness and AE characteristics**. *Engineering Fracture Mechanics*, **64**(6):721–745, dec 1999. doi:10.1016/s0013-7944(99)00096-x.

[101] DE McCabe, editor. *Fracture Toughness Evaluation by R-Curve Methods*. Number 527. ASTM International, 100 Barr Harbor Drive, PO Box C700, West Conshohocken, PA 19428-2959, jan 1973. doi:10.1520/STP527-EB.

[102] R. D. Jamison. **On the Interrelationship Between Fiber Fracture and Ply Cracking in Graphite/Epoxy Laminates**. In H. Thomas Hahn, editor, *Composite Materials: Fatigue and Fracture*, chapter On the Int, pages 252–273. ASTM International, 100 Barr Harbor Drive, PO Box C700, West Conshohocken, PA 19428-2959, 1986. doi:10.1520/STP19990S.

[103] Jens Zangenberg, Povl Brøndsted, and John W Gillespie. **Fatigue damage propagation in unidirectional glass fibre reinforced composites made of a non-crimp fabric**. *Journal of Composite Materials*, **48**(22):2711–2727, sep 2014. doi:10.1177/0021998313502062.

[104] Serra Topal, Luca Baiocchi, Andrew D. Crocombe, Stephen L. Ogin, Prasad Potluri, Philip J. Withers, Marino Quaresimin, Paul A. Smith, Matthew C. Poole, and Alexander E. Bogdanovich. **Late-stage fatigue damage in a 3D orthogonal non-crimp woven composite: An experimental and numerical study**. *Composites Part A: Applied Science and Manufacturing*, **79**:155–163, dec 2015. doi:10.1016/j.compositesa.2015.08.020.

[105] P. D. Edwins and R. T. Potter. **Some observations on the nature of fibre reinforced plastics and the implications for structural design**. *Philosophical Transactions of the Royal Society of London. Series A, Mathematical and Physical Sciences*, **294**(1411):507–517, jan 1980. doi:10.1098/rsta.1980.0060.

[106] R. Gutkin, S.T. Pinho, P. Robinson, and P.T. Curtis. **On the transition from shear-driven fibre compressive failure to fibre kinking in notched CFRP laminates under longitudinal compression**. *Composites Science and Technology*, **70**(8):1223–1231, aug 2010. doi:10.1016/j.compscitech.2010.03.010.

[107] S.T. Pinho, P. Robinson, and L. Iannucci. **Fracture toughness of the tensile and compressive fibre failure modes in laminated composites**. *Composites Science and Technology*, **66**(13):2069–2079, oct 2006. doi:10.1016/j.compscitech.2005.12.023.

[108] R.R. Effendi, J.-J. Barrau, and D. Guedra-Degeorges. **Failure mechanism analysis under compression loading of unidirectional carbon/epoxy composites using micromechanical modelling**. *Composite Structures*, **31**(2):87–98, jan 1995. doi:10.1016/0263-8223(94)00060-3.

[109] S.T. Pinho, R. Gutkin, S. Pimenta, N.V. De Carvalho, and P. Robinson. **Fibre-dominated compressive failure in polymer matrix composites**. In *Failure Mechanisms in Polymer Matrix Composites*, pages 183–223. Elsevier, jan 2012. doi:10.1533/9780857095329.1.183.

[110] E.F. Rybicki. **Approximate Three-Dimensional Solutions for Symmetric Laminates Under Inplane Loading**. *Journal of Composite Materials*, **5**(3):354–360, mar 1971. doi:10.1177/002199837100500305.

[111] G Isakson and A Levy. **Finite-Element Analysis of Interlaminar Shear in Fibrous Composites**. *Journal of Composite Materials*, **5**(2):273–276, feb 1971. doi:10.1177/002199837100500215.

[112] R. Byron Pipes. **Moiré Analysis of the Interlaminar Shear Edge Effect in Laminated Composites**. *Journal of Composite Materials*, **5**(2):255–259, feb 1971. doi:10.1177/002199837100500211.

[113] A.S.D. Wang and Frank W Crossman. **Some New Results on Edge Effect in Symmetric Composite Laminates**. *Journal of Composite Materials*, **11**(1):92–106, jan 1977. doi:10.1177/002199837701100110.

[114] Peter W Hsu and Carl T Herakovich. **Edge Effects in Angle-Ply Composite Laminates***. *Journal of Composite Materials*, **11**(4):422–428, oct 1977. doi:10.1177/002199837701100405.

[115] Carl T. Herakovich. **On the Relationship between Engineering Properties and Delamination of Composite Materials**. *Journal of Composite Materials*, **15**(4):336–348, jul 1981. doi:10.1177/002199838101500404.

[116] B. T. Rodini and J. R. Eisenmann. **An Analytical and Experimental Investigation of Edge Delamination in Composite Laminates**. In *Fibrous Composites in Structural Design*, pages 441–457. Springer US, Boston, MA, 1980. doi:10.1007/978-1-4684-1033-4_25.

[117] A.S.D. Wang and F.W. Crossman. **Initiation and Growth of Transverse Cracks and Edge Delamination in Composite Laminates Part 1. An Energy Method**. *Journal of Composite Materials*, **14**(1):71–87, jan 1980. doi:10.1177/002199838001400106.

[118] Edward M Wu and R C Reuter Jr. **Crack extension in fiberglass reinforced plastics**. Technical report, ILLINOIS UNIV AT URBANA DEPT OF THEORETICAL AND APPLIED MECHANICS, 1965.

[119] M.L. Benzeggagh and M. Kenane. **Measurement of mixed-mode delamination fracture toughness of unidirectional glass/epoxy composites with mixed-mode bending apparatus**. *Composites Science and Technology*, **56**(4):439–449, 1996. doi:10.1016/0266-3538(96)00005-X.

[120] J.R. Reeder. **A Bilinear Failure Criterion for Mixed-Mode Delamination**. In *Eleventh Volume: Composite Materials—Testing and Design*, number 1206, pages 303–303–20. ASTM International, 100 Barr Harbor Drive, PO Box C700, West Conshohocken, PA 19428-2959, 1993. doi:10.1520/STP12636S.

[121] Reeder J.R. **3D Mixed-Mode Delamination Fracture Criteria–An Experimentalist's Perspective James R. Reeder**. *21st Anual Technical Conference*, pages 1–19, 2006.

[122] S. S. Wang. **Fracture Mechanics for Delamination Problems in Composite Materials**. *Journal of Composite Materials*, **17**(3):210–223, may 1983. doi:10.1177/002199838301700302.

[123] ASD Wang, M. Slomiana, and RB Bucinell. **Delamination Crack Growth in Composite Laminates**. In *Delamination and Debonding of Materials*, pages 135–135–33. ASTM International, 100 Barr Harbor Drive, PO Box C700, West Conshohocken, PA 19428-2959, 1985. doi:10.1520/STP36303S.

[124] J.C.J. Schellekens and R. de Borst. **A non-linear finite element approach for the analysis of mode-I free edge delamination in composites**. *International Journal of Solids and Structures*, **30**(9):1239–1253, jan 1993. doi:10.1016/0020-7683(93)90014-X.

[125] Carl T Herakovich. **Influence of Layer Thickness on the Strength of Angle-Ply Laminates**. *Journal of Composite Materials*, **16**(3):216–227, may 1982. doi:10.1177/002199838201600305.

[126] WS Chan, C Rogers, and S Aker. **Improvement of Edge Delamination Strength of Composite Laminates Using Adhesive Layers**. In *Composite Materials: Testing and Design (Seventh Conference)*, pages 266–266–20. ASTM International, 100 Barr Harbor Drive, PO Box C700, West Conshohocken, PA 19428-2959, 1986. doi:10.1520/STP35353S.

[127] W. CHAN and A.S. WANG. **A study on the effects of the 90 deg ply on matrix cracks in composite laminates**. In *27th Structures, Structural Dynamics and Materials Conference*, Reston, Virigina, may 1986. American Institute of Aeronautics and Astronautics. doi:10.2514/6.1986-1018.

[128] Edward W. Y. Lee and Wen S. Chan. **Delamination arrestment by discretizing the critical ply in a laminate**. In *30th Structures, Structural Dynamics and Materials Conference*, Reston, Virigina, apr 1989. American Institute of Aeronautics and Astronautics. doi:10.2514/6.1989-1403.

[129] A.P. Mouritz, K.H. Leong, and I. Herszberg. **A review of the effect of stitching on the in-plane mechanical properties of fibre-reinforced polymer composites**. *Composites Part A: Applied Science and Manufacturing*, **28**(12):979–991, jan 1997. doi:10.1016/S1359-835X(97)00057-2.

[130] Daniel A Drake, Rani W Sullivan, Andrew E Lovejoy, Stephen B Clay, and Dawn C Jegley. **Influence of stitching on the out-of-plane behavior of composite materials – A mechanistic review**. *Journal of Composite Materials*, **55**(23):3307–3321, sep 2021. doi:10.1177/00219983211009290.

[131] T.R.C. Chuaqui, E. Sebastian, V. Sahadevan, A.T. Rhead, and R. Butler. **Edge treatment of short beam shear tests for improved assessment of structural strength**. *Composites Part A: Applied Science and Manufacturing*, **137**:105991, oct 2020. doi:10.1016/j.compositesa.2020.105991.

[132] T.R.C. Chuaqui, M.W.D. Nielsen, J. Colton, R. Butler, and A.T. Rhead. **Effects of ply angle and blocking on open-hole tensile strength of composite laminates: A design and certification perspective**. *Composites Part B: Engineering*, **207**:108582, feb 2021. doi:10.1016/j.compositesb.2020.108582.

[133] W. E. Howard, Terry Gossard, and Robert M. Jones. **Composite laminate free-edge reinforcement with U-shaped caps. Part I - Stress analysis.** *AIAA Journal*, **27**(5):610–616, may 1989. doi:10.2514/3.10152.

[134] W. E. Howard, Terry Gossard, and Robert M. Jones. **Composite Laminate Free-Edge Reinforcement with U-Shaped Caps Part 11: Theoretical-Experimental Correlation**. *AIAA Journal*, **27**(5):617–623, may 1989. doi:10.2514/3.48818.

[135] Roland Kim. **A Study in the Prevention of Free-Edge Delamination for Fiber-Reinforced Composite Materials**. *Senior Project Report (Robert M. Jones, superviser), ESM Department, Virginia Tech, Blacksburg, Virginia*, 1988.

[136] Joel Galos. **Thin-ply composite laminates: a review**, mar 2020. doi:10.1016/j.compstruct.2020.111920.

[137] Christian Mittelstedt and Wilfried Becker. **Free-Edge Effects in Composite Laminates**. *Applied Mechanics Reviews*, **60**(5):217–245, sep 2007. doi:10.1115/1.2777169.

[138] M. de Freitas and L. Reis. **Failure mechanisms on composite specimens subjected to compression after impact**. *Composite Structures*, **42**(4):365–373, aug 1998. doi:10.1016/S0263-8223(98)00081-6.

[139] A. Malhotra, F. J. Guild, and M. J. Pavier. **Edge impact to composite laminates: experiments and simulations**. *Journal of Materials Science*, **43**(20):6661–6667, oct 2008. doi:10.1007/s10853-008-2863-z.

[140] L.Gunnar Melin and Joakim Schön. **Buckling behaviour and delamination growth in impacted composite specimens under fatigue load: an experimental study**. *Composites Science and Technology*, **61**(13):1841–1852, oct 2001. doi:10.1016/S0266-3538(01)00085-9.

[141] Solver I. Thorsson, Sunil P. Sringeri, Anthony M. Waas, Brian P. Justusson, and Mostafa Rassaian. **Experimental investigation of composite laminates subject to low-velocity edge-on impact and compression after impact**. *Composite Structures*, **186**:335–346, feb 2018. doi:10.1016/j.compstruct.2017.11.084.

[142] Andrew T. Rhead, David Marchant, and Richard Butler. **Compressive strength of composite laminates following free edge impact**. *Composites Part A: Applied Science and Manufacturing*, **41**(9):1056–1065, sep 2010. doi:10.1016/j.compositesa.2009.10.024.

[143] Serge Abrate. **Modeling of impacts on composite structures**. *Composite Structures*, **51**(2):129–138, feb 2001. doi:10.1016/S0263-8223(00)00138-0.

[144] W.J. Cantwell and J. Morton. **The impact resistance of composite materials — a review**. *Composites*, **22**(5):347–362, sep 1991. doi:10.1016/0010-4361(91)90549-V.

[145] Serge Abrate. **Impact on Laminated Composite Materials**. *Applied Mechanics Reviews*, **44**(4):155–190, apr 1991. doi:10.1115/1.3119500.

[146] Andrew T. Rhead, Richard Butler, and Giles W. Hunt. **Post-buckled propagation model for compressive fatigue of impact damaged laminates**. *International Journal of Solids and Structures*, **45**(16):4349–4361, aug 2008. doi:10.1016/j.ijsolstr.2008.03.014.

[147] Andrew T. Rhead and Richard Butler. **Compressive static strength model for impact damaged laminates**. *Composites Science and Technology*, **69**(14):2301–2307, nov 2009. doi:10.1016/j.compscitech.2009.01.010.

[148] C. Bouvet, S. Rivallant, and J.J. Barrau. **Low velocity impact modeling in composite laminates capturing permanent indentation**. *Composites Science and Technology*, **72**(16):1977–1988, nov 2012. doi:10.1016/j.compscitech.2012.08.019.

[149] Y. Shi, T. Swait, and C. Soutis. **Modelling damage evolution in composite laminates subjected to low velocity impact**. *Composite Structures*, **94**(9):2902–2913, sep 2012. doi:10.1016/j.compstruct.2012.03.039.

[150] Wei Tan, Brian G. Falzon, Louis N.S. Chiu, and Mark Price. **Predicting low velocity impact damage and Compression-After-Impact (CAI) behaviour of composite laminates**. *Composites Part A: Applied Science and Manufacturing*, **71**:212–226, apr 2015. doi:10.1016/j.compositesa.2015.01.025.

[151] C.S. Lopes, S. Sádaba, C. González, J. Llorca, and P.P. Camanho. **Physically-sound simulation of low-velocity impact on fiber reinforced laminates**. *International Journal of Impact Engineering*, **92**:3–17, jun 2016. doi:10.1016/j.ijimpeng.2015.05.014.

[152] X.C. Sun, M.R. Wisnom, and S.R. Hallett. **Interaction of inter- and intralaminar damage in scaled quasi-static indentation tests: Part 2 – Numerical simulation**. *Composite Structures*, **136**:727–742, feb 2016. doi:10.1016/j.compstruct.2015.09.062.

[153] E. Abisset, F. Daghia, X.C. Sun, M.R. Wisnom, and S.R. Hallett. **Interaction of inter- and intralaminar damage in scaled quasi-static indentation tests: Part 1 – Experiments**. *Composite Structures*, **136**:712–726, feb 2016. doi:10.1016/j.compstruct.2015.09.061.

[154] M.R. Abir, T.E. Tay, M. Ridha, and H.P. Lee. **Modelling damage growth in composites subjected to impact and compression after impact**. *Composite Structures*, **168**:13–25, may 2017. doi:10.1016/j.compstruct.2017.02.018.

[155] A. Soto, E.V. González, P. Maimí, J.A. Mayugo, P.R. Pasquali, and P.P. Camanho. **A methodology to simulate low velocity impact and compression after impact in large composite stiffened panels**. *Composite Structures*, **204**:223–238, nov 2018. doi:10.1016/j.compstruct.2018.07.081.

[156] Raffael Bogenfeld, Janko Kreikemeier, and Tobias Wille. **Review and benchmark study on the analysis of low-velocity impact on composite laminates**. *Engineering Failure Analysis*, **86**:72–99, apr 2018. doi:10.1016/j.engfailanal.2017.12.019.

[157] Masaya Ebina, Akinori Yoshimura, Kenichi Sakaue, and Anthony M. Waas. **High fidelity simulation of low velocity impact behavior of CFRP laminate**. *Composites Part A: Applied Science and Manufacturing*, **113**:166–179, oct 2018. doi:10.1016/j.compositesa.2018.07.022.

[158] E.V. González, P. Maimí, P.P. Camanho, A. Turon, and J.A. Mayugo. **Simulation of drop-weight impact and compression after impact tests on composite laminates**. *Composite Structures*, **94**(11):3364–3378, nov 2012. doi:10.1016/j.compstruct.2012.05.015.

[159] Solver I. Thorsson, Anthony M. Waas, and Mostafa Rassaian. **Low-velocity impact predictions of composite laminates using a continuum shell based modeling approach part A: Impact study**. *International Journal of Solids and Structures*, **155**:185–200, dec 2018. doi:10.1016/j.ijsolstr.2018.07.020.

[160] Solver I. Thorsson, Anthony M. Waas, and Mostafa Rassaian. **Low-velocity impact predictions of composite laminates using a continuum shell based modeling approach Part b: BVID impact and compression after impact**. *International Journal of Solids and Structures*, **155**:201–212, dec 2018. doi:10.1016/j.ijsolstr.2018.07.018.

[161] Kangkang Wang, Libin Zhao, Haiming Hong, and Jianyu Zhang. **A strain-rate-dependent damage model for evaluating the low velocity impact induced damage of composite laminates**. *Composite Structures*, **201**:995–1003, oct 2018. doi:10.1016/j.compstruct.2018.06.046.

[162] Hongliang Tuo, Zhixian Lu, Xiaoping Ma, Chao Zhang, and Shuwen Chen. **An experimental and numerical investigation on low-velocity impact damage and compression-after-impact behavior of composite laminates**. *Composites Part B: Engineering*, **167**:329–341, jun 2019. doi:10.1016/j.compositesb.2018.12.043.

[163] Nian. Li and P.H. Chen. **Experimental investigation on edge impact damage and Compression-After-Impact (CAI) behavior of stiffened composite panels**. *Composite Structures*, **138**:134–150, mar 2016. doi:10.1016/j.compstruct.2015.11.060.

[164] Nian Li and Puhui Chen. **Failure prediction of T-stiffened composite panels subjected to compression after edge impact**. *Composite Structures*, **162**:210–226, feb 2017. doi:10.1016/j.compstruct.2016.12.004.

[165] A. Arteiro, P.J. Gray, and P.P. Camanho. **Simulation of edge impact and compression after edge impact in CFRP laminates**. *Composite Structures*, **240**:112018, may 2020. doi:10.1016/j.compstruct.2020.112018.

[166] Benjamin Ostré, Christophe Bouvet, Frédéric Lachaud, Clément Minot, and Jacky Aboissière. **Edge impact damage scenario on stiffened composite structure**. *Journal of Composite Materials*, **49**(13):1599–1612, jun 2015. doi:10.1177/0021998314537325.

[167] Benjamin Ostré, Christophe Bouvet, Clément Minot, and Jacky Aboissière. **Edge impact modeling on stiffened composite structures**. *Composite Structures*, **126**:314–328, aug 2015. doi:10.1016/j.compstruct.2015.02.020.

[168] Benjamin Ostré, Christophe Bouvet, Clément Minot, and Jacky Aboissière. **Experimental analysis of CFRP laminates subjected to compression after edge impact**. *Composite Structures*, **152**:767–778, sep 2016. doi:10.1016/j.compstruct.2016.05.068.

[169] Benjamin Ostré, Christophe Bouvet, Clément Minot, and Jacky Aboissière. **Finite element analysis of CFRP laminates subjected to compression after edge impact**. *Composite Structures*, **153**:478–489, oct 2016. doi:10.1016/j.compstruct.2016.06.041.

[170] Samuel Rivallant, Christophe Bouvet, and Natthawat Hongkarnjanakul. **Failure analysis of CFRP laminates subjected to compression after impact: FE simulation using discrete interface elements**. *Composites Part A: Applied Science and Manufacturing*, **55**:83–93, dec 2013. doi:10.1016/j.compositesa.2013.08.003.

[171] S. Murakami. **Notion of Continuum Damage Mechanics and its Application to Anisotropic Creep Damage Theory**. *Journal of Engineering Materials and Technology*, **105**(2):99–105, apr 1983. doi:10.1115/1.3225633.

[172] Solver I. Thorsson, Anthony M. Waas, and Mostafa Rassaian. **Numerical investigation of composite laminates subject to low-velocity edge-on impact and compression after impact**. *Composite Structures*, **203**:648–658, nov 2018. doi:10.1016/j.compstruct.2018.06.094.

[173] D. Hull. **A unified approach to progressive crushing of fibre-reinforced composite tubes**. *Composites Science and Technology*, **40**(4):377–421, jan 1991. doi:10.1016/0266-3538(91)90031-J.

[174] L. Daniel, P.J Hogg, and P.T Curtis. **The crush behaviour of carbon fibre angle-ply reinforcement and the effect of interlaminar shear strength on energy absorption capability**. *Composites Part B: Engineering*, **31**(5):435–440, jul 2000. doi:10.1016/S1359-8368(00)00026-3.

[175] Z.E.C. Hall, J. Liu, R.A. Brooks, H. Liu, J.W.M. Crocker, A.M. Joesbury, L.T. Harper, B.R.K. Blackman, A.J. Kinloch, and J.P. Dear. **The effectiveness of patch repairs to restore the impact properties of carbon-fibre reinforced-plastic composites**. *Engineering Fracture Mechanics*, **270**:108570, jul 2022. doi:10.1016/j.engfracmech.2022.108570.

[176] S. A. Hitchen and R. M.J. Kemp. **The effect of stacking sequence on impact damage in a carbon fibre/epoxy composite**. *Composites*, **26**(3):207–214, mar 1995. doi:10.1016/0010-4361(95)91384-H.

[177] C. Soutis and P.T. Curtis. **Prediction of the post-impact compressive strength of cfrp laminated composites**. *Composites Science and Technology*, **56**(6):677–684, jan 1996. doi:10.1016/0266-3538(96)00050-4.

[178] M.V. Hosur, C.R.L. Murthy, T.S. Ramamurthy, and Anita Shet. **Estimation of impact-induced damage in CFRR laminates through ultrasonic imaging**. *NDT & E International*, **31**(5):359–374, oct 1998. doi:10.1016/S0963-8695(97)00053-4.

[179] F. Mili and B. Necib. **The effect of stacking sequence on the impact-induced damage in cross-ply E-glass/epoxy composite plates**. *Archive of Applied Mechanics*, **79**(11):1019–1031, nov 2009. doi:10.1007/s00419-008-0272-z.

[180] C.S. Lopes, P.P. Camanho, Z. Gürdal, P. Maimí, and E.V. González. **Low-velocity impact damage on dispersed stacking sequence laminates. Part II: Numerical simulations**. *Composites Science and Technology*, **69**(7-8):937–947, jun 2009. doi:10.1016/j.compscitech.2009.02.015.

[181] T.A. Sebaey, E.V. González, C.S. Lopes, N. Blanco, P. Maimí, and J. Costa. **Damage resistance and damage tolerance of dispersed CFRP laminates: Effect of the mismatch angle between plies**. *Composite Structures*, **101**:255–264, jul 2013. doi:10.1016/j.compstruct.2013.01.026.

[182] T. Apichattrabrut and K. Ravi-Chandar. **Helicoidal Composites**. *Mechanics of Advanced Materials and Structures*, **13**(1):61–76, jan 2006. doi:10.1080/15376490500343808.

[183] L.K. Grunenfelder, N. Suksangpanya, C. Salinas, G. Milliron, N. Yaraghi, S. Herrera, K. Evans-Lutterodt, S.R. Nutt, P. Zavattieri, and D. Kisailus. **Bio-inspired impact-resistant composites**. *Acta Biomaterialia*, **10**(9):3997–4008, 2014. Biomineralization. doi:https://doi.org/10.1016/j.actbio.2014.03.022.

[184] J.S. Shang, Nigel H.H. Ngern, and Vincent B.C. Tan. **Crustacean-inspired helicoidal laminates**. *Composites Science and Technology*, **128**:222–232, 2016. doi:https://doi.org/10.1016/j.compscitech.2016.04.007.

[185] D. Ginzburg, F. Pinto, O. Iervolino, and M. Meo. **Damage tolerance of bio-inspired helicoidal composites under low velocity impact**. *Composite Structures*, **161**:187–203, 2017. doi:https://doi.org/10.1016/j.compstruct.2016.10.097.

[186] M.R. Abir, T.E. Tay, and H.P. Lee. **On the improved ballistic performance of bio-inspired composites**. *Composites Part A: Applied Science and Manufacturing*, **123**:59–70, 2019. doi:https://doi.org/10.1016/j.compositesa.2019.04.021.

[187] Lorenzo Mencattelli and Silvestre T. Pinho. **Ultra-thin-ply CFRP Bouligand bio-inspired structures with enhanced load-bearing capacity, delayed catastrophic failure and high energy dissipation capability**. *Composites Part A: Applied Science and Manufacturing*, **129**:105655, feb 2020. doi:10.1016/j.compositesa.2019.105655.

[188] Lorenzo Mencattelli and Silvestre T. Pinho. **Herringbone-Bouligand CFRP structures: A new tailorable damage-tolerant solution for damage containment and reduced delaminations**. *Composites Science and Technology*, **190**:108047, apr 2020. doi:10.1016/j.compscitech.2020.108047.

[189] Qigang Han, Hanlin Qin, Zhiwu Han, Lin Li, Wenqiang Zhang, Yanbiao Sun, and Shaoqian Shi. **Mechanical properties of a novel dactyl-inspired green-composite sandwich structures with basalt fiber**. *Journal of Sandwich Structures and Materials*, **23**(3):803–813, mar 2021. doi:10.1177/1099636219846646.

[190] James C. Weaver, Garrett W. Milliron, Ali Miserez, Kenneth Evans-Lutterodt, Steven Herrera, Isaias Gallana, William J. Mershon, Brook Swanson, Pablo Zavattieri, Elaine DiMasi, and David Kisailus. **The Stomatopod Dactyl Club: A Formidable Damage-Tolerant Biological Hammer**. *Science*, **336**(6086):1275–1280, jun 2012. doi:10.1126/science.1218764.

[191] Lorenzo Mencattelli and Silvestre T. Pinho. **Realising bio-inspired impact damage-tolerant thin-ply CFRP Bouligand structures via promoting diffused sub-critical helicoidal damage**. *Composites Science and Technology*, **182**:107684, 2019. doi:https://doi.org/10.1016/j.compscitech.2019.107684.

[192] Mohamad Fotouhi, Mahdi Damghani, Mun Choong Leong, Sakineh Fotouhi, Meisam Jalalvand, and Michael R. Wisnom. **A comparative study on glass and carbon fibre reinforced laminated composites in scaled quasi-static indentation tests**. *Composite Structures*, **245**:112327, aug 2020. doi:10.1016/j.compstruct.2020.112327.

[193] K. Saka and J. Harding. **A simple laminate theory approach to the prediction of the tensile impact strength of woven hybrid composites**. *Composites*, **21**(5):439–447, sep 1990. doi:10.1016/0010-4361(90)90444-2.

[194] A. Wagih, P. Maimí, N. Blanco, S.M. García-Rodríguez, G. Guillamet, R.P. Issac, A. Turon, and J. Costa. **Improving damage resistance and load capacity of thin-ply laminates using ply clustering and small mismatch angles**. *Composites Part A: Applied Science and Manufacturing*, **117**:76–91, feb 2019. doi:10.1016/j.compositesa.2018.11.008.

[195] N.K Naik, R. Ramasimha, H. Arya, S.V Prabhu, and N. ShamaRao. **Impact response and damage tolerance characteristics of glass–carbon/epoxy hybrid composite plates**. *Composites Part B: Engineering*, **32**(7):565–574, oct 2001. doi:10.1016/S1359-8368(01)00036-1.

[196] M.V. Hosur, M. Adbullah, and S. Jeelani. **Studies on the low-velocity impact response of woven hybrid composites**. *Composite Structures*, **67**(3):253–262, mar 2005. doi:10.1016/j.compstruct.2004.07.024.

[197] D.D.R. Cartié and P.E. Irving. **Effect of resin and fibre properties on impact and compression after impact performance of CFRP**. *Composites Part A: Applied Science and Manufacturing*, **33**(4):483–493, 2002. doi:https://doi.org/10.1016/S1359-835X(01)00141-5.

[198] S. K. Sharma and B. V. Sankar. **Effect of Stitching on Impact and Interlaminar Properties of Graphite/Epoxy Laminates**. *Journal of Thermoplastic Composite Materials*, **10**(3):241–253, may 1997. doi:10.1177/089270579701000302.

[199] Miguel Ubago Torres and Meisam Jalalvand. **Additive binding layers to suppress free edge delamination in composite laminates under tension**. *Composites Part A: Applied Science and Manufacturing*, **156**:106902, May 2022. doi:10.1016/j.compositesa.2022.106902.

[200] O L Bowie. **Analysis of an Infinite Plate Containing Radial Cracks Originating at the Boundary of an Internal Circular Hole**. *Journal of Mathematics and Physics*, **35**(1-4):60–71, apr 1956. doi:10.1002/sapm195635160.

[201] R Byron Pipes, Robert C Wetherhold, and John W Gillespie. **Notched Strength of Composite Materials**. *Journal of Composite Materials*, **13**(2):148–160, apr 1979. doi:10.1177/002199837901300206.

[202] Thomas A. Cruse. **Tensile Strength of Notched Composites**. *Journal of Composite Materials*, **7**(2):218–229, feb 1973. doi:10.1177/002199837300700206.

[203] R J Nuismer and Jm Whitney. **Uniaxial Failure of Composite Laminates Containing Stress Concentrations**. *ASTM special technical publications*, pages 117–142, 1975.

[204] Rajesh S. Vaidya and C. T. Sun. **Fracture Criterion for Notched Thin Composite Laminates**. *AIAA Journal*, **35**(2):311–316, feb 1997. doi:10.2514/2.93.

[205] S.R. R. Hallett, B.G. G. Green, W.G. G. Jiang, and M.R. R. Wisnom. **An experimental and numerical investigation into the damage mechanisms in notched composites**. *Composites Part A: Applied Science and Manufacturing*, **40**(5):613–624, may 2009. doi:10.1016/j.compositesa.2009.02.021.

[206] Rajesh S. Vaidya, J. C. Klug, and C. T. Sun. **Effect of Ply Thickness on Fracture of Notched Composite Laminates**. *AIAA Journal*, **36**(1):81–88, jan 1998. doi:10.2514/2.355.

[207] P.P. Camanho, G.H. Erçin, G. Catalanotti, S. Mahdi, and P. Linde. **A finite fracture mechanics model for the prediction of the open-hole strength of composite laminates**. *Composites Part A: Applied Science and Manufacturing*, **43**(8):1219–1225, aug 2012. doi:10.1016/j.compositesa.2012.03.004.

[208] A. Parvizi, K. W. Garrett, and J. E. Bailey. **Constrained cracking in glass fibre-reinforced epoxy cross-ply laminates**. *Journal of Materials Science*, **13**(1):195–201, jan 1978. doi:10.1007/BF00739291.

[209] Pedro P. Camanho, Carlos G. Dávila, Silvestre T. Pinho, Lorenzo Iannucci, and Paul Robinson. **Prediction of in situ strengths and matrix cracking in composites under transverse tension and in-plane shear**. *Composites Part A: Applied Science and Manufacturing*, **37**(2):165–176, feb 2006. doi:10.1016/j.compositesa.2005.04.023.

[210] George J. Dvorak and Norman Laws. **Analysis of Progressive Matrix Cracking In Composite Laminates II. First Ply Failure**. *Journal of Composite Materials*, **21**(4):309–329, apr 1987. doi:10.1177/002199838702100402.

[211] B.G. Green, M.R. Wisnom, and S.R. Hallett. **An experimental investigation into the tensile strength scaling of notched composites**. *Composites Part A: Applied Science and Manufacturing*, **38**(3):867–878, mar 2007. doi:10.1016/j.compositesa.2006.07.008.

[212] M.R. Wisnom, S.R. Hallett, and C. Soutis. **Scaling Effects in Notched Composites**. *Journal of Composite Materials*, **44**(2):195–210, jan 2010. doi:10.1177/0021998309339865.

[213] D. Mollenhauer, E.V. Iarve, R. Kim, and B. Langley. **Examination of ply cracking in composite laminates with open holes: A moiré interferometric and numerical study**. *Composites Part A: Applied Science and Manufacturing*, **37**(2):282–294, feb 2006. doi:10.1016/j.compositesa.2005.06.004.

[214] Paul A Lagace. *Notch sensitivity and stacking sequence of laminated composites*. ASTM International, 1986.

[215] ASTM D5766/D5766M-11. **Standard Test Method for Open-Hole Tensile Strangth of Polymer Matrix Composite Laminates**, 2011. doi:10.1520/D5766.

[216] Michael R. Wisnom and Stephen R. Hallett. **The role of delamination in strength, failure mechanism and hole size effect in open hole tensile tests on quasi-isotropic laminates**. *Composites Part A: Applied Science and Manufacturing*, **40**(4):335–342, apr 2009. doi:10.1016/j.compositesa.2008.12.013.

[217] M. Ridha, C.H. Wang, B.Y. Chen, and T.E. Tay. **Modelling complex progressive failure in notched composite laminates with varying sizes and stacking sequences**. *Composites Part A: Applied Science and Manufacturing*, **58**:16–23, mar 2014. doi:10.1016/j.compositesa.2013.11.012.

[218] M.M. Moure, F. Otero, S.K. García-Castillo, S. Sánchez-Sáez, E.J. Barbero, and E.J. Barbero. **Damage evolution in open-hole laminated composite plates subjected to in-plane loads**. *Composite Structures*, **133**:1048–1057, dec 2015. doi:10.1016/j.compstruct.2015.08.045.

[219] Vishwas Divse, Deepak Marla, and Suhas S. Joshi. **Finite element analysis of tensile notched strength of composite laminates**. *Composite Structures*, **255**:112880, jan 2021. doi:10.1016/j.compstruct.2020.112880.

[220] Stephen R. Hallett, Ben G. Green, Wen-Guang Jiang, Kin Hei Cheung, and Michael R. Wisnom. **The open hole tensile test: a challenge for virtual testing of composites**. *International Journal of Fracture*, **158**(2):169–181, aug 2009. doi:10.1007/s10704-009-9333-8.

[221] C. S. Lopes, C. González, O. Falcó, F. Naya, J. LLorca, and B. Tijs. **Multiscale virtual testing: the roadmap to efficient design of composites for damage resistance and tolerance**. *CEAS Aeronautical Journal*, **7**(4):607–619, dec 2016. doi:10.1007/s13272-016-0210-7.

[222] O. Falcó, R.L. Ávila, B. Tijs, and C.S. Lopes. **Modelling and simulation methodology for unidirectional composite laminates in a Virtual Test Lab framework**. *Composite Structures*, **190**:137–159, apr 2018. doi:10.1016/j.compstruct.2018.02.016.

[223] Benjamin George Green. *The effect of size on the tensile strength of composite laminates containing circular holes*. PhD thesis, University of Bristol, 2006.

[224] J Görlich. **Experimental and numerical analysis of size effects in notched composite specimens–report**. *Technical University of Dresden Institute for Lightweight Structures*, 2008.

[225] M Cheung and SR Hallett. **Investigation of the effect of specimen width on open hole tensile strength**. In *Composites Testing for Model Identification (CompTest), Dayton*, 2008. Name and Venue of Event: CompTest, Dayton, USA.

[226] Ingvar Eriksson. **On the Bearing Strength of Bolted Graphite/Epoxy Laminates**. *Journal of Composite Materials*, **24**(12):1246–1269, dec 1990. doi:10.1177/002199839002401201.

[227] X Wu, M. Fotouhi, J D Fuller, and M R Wisnom. **Bearing failure of pseudo-ductile thin ply angle-ply laminates**. In *ECCM 2018 - 18th European Conference on Composite Materials*, 2018.

[228] T.A. Collings. **On the bearing strengths of cfrp laminates**. *Composites*, **13**(3):241–252, jul 1982. doi:10.1016/0010-4361(82)90006-4.

[229] J.H. Stockdale and F.L. Matthews. **The effect of clamping pressure on bolt bearing loads in glass fibre-reinforced plastics**. *Composites*, **7**(1):34–38, 1976. doi:https://doi.org/10.1016/0010-4361(76)90279-2.

[230] JH Crews. **Bolt-Bearing Fatigue of a Graphite/Epoxy Laminate**. In *Joining of Composite Materials*, pages 131–131–14. ASTM International, 100 Barr Harbor Drive, PO Box C700, West Conshohocken, PA 19428-2959. doi:10.1520/STP33478S.

[231] Hong Sheng Wang, Chang Li Hung, and Fu Kuo Chang. **Bearing failure of bolted composite joints. Part I: Experimental characterization**. *Journal of Composite Materials*, **30**(12):1284–1313, 1996. doi:10.1177/002199839603001201.

[232] Gordon Kelly and Stefan Hallström. **Bearing strength of carbon fibre/epoxy laminates: Effects of bolt-hole clearance**. *Composites Part B: Engineering*, **35**(4):331–343, jan 2004. doi:10.1016/j.compositesb.2003.11.001.

[233] W.J. Quinn and F.L. Matthews. **The Effect of Stacking Sequence on the Pin-Bearing Strength in Glass Fibre Reinforced Plastic**. *Journal of Composite Materials*, **11**(2):139–145, apr 1977. doi:10.1177/002199837701100202.

[234] C.T. McCarthy and M.A. McCarthy. **Design and failure analysis of composite bolted joints for aerospace composites**. In *Polymer Composites in the Aerospace Industry*, pages 331–369. Elsevier, jan 2020. doi:10.1016/B978-0-08-102679-3.00012-5.

[235] P. P. Camanho, S. Bowron, and F. L. Matthews. **Failure Mechanisms in Bolted CFRP**. *Journal of Reinforced Plastics and Composites*, **17**(3):205–233, feb 1998. doi:10.1177/073168449801700302.

[236] RA Naik and JH Crews Jr. **Stress analysis method for a clearance-fit bolt under bearing loads**. *AIAA journal*, **24**(8):1348–1353, 1986.

[237] M.W. Hyer, E.C. Klang, and D.E. Cooper. **The Effects of Pin Elasticity, Clearance, and Friction on the Stresses in a Pin-Loaded Orthotropic Plate**. *Journal of Composite Materials*, **21**(3):190–206, mar 1987. doi:10.1177/002199838702100301.

[238] Albert J DiNicola and Steven C Fantle. **Bearing strength behavior of clearance-fit fastener holes in toughened graphite/epoxy laminates**. *ASTM Special Technical Publication*, **1206**:220–220, 1993.

[239] F. Lanza Di Scalea, F. Cappello, and G. L. Cloudt. **On the Elastic Behavior of a Cross-Ply Composite Pin-Joint with Clearance Fits**. *Journal of Thermoplastic Composite Materials*, **12**(1):13–22, jan 1999. doi:10.1177/089270579901200102.

[240] F. Pierron, F. Cerisier, and M. Grediac. **A Numerical and Experimental Study of Woven Composite Pin-Joints**. *Journal of Composite Materials*, **34**(12):1028–1054, jun 2000. doi:10.1177/002199830003401204.

[241] M.A McCarthy, V.P Lawlor, W.F Stanley, and C.T McCarthy. **Bolt-hole clearance effects and strength criteria in single-bolt, single-lap, composite bolted joints**. *Composites Science and Technology*, **62**(10-11):1415–1431, aug 2002. doi:10.1016/S0266-3538(02)00088-X.

[242] UA Khashaba, TA Sebaey, and KA Alnefaie. **Failure and reliability analysis of pinned-joint composite laminates: Effects of pin–hole clearance**. *Journal of Composite Materials*, **47**(18):2287–2298, aug 2013. doi:10.1177/0021998312457196.

[243] Francesco Ascione, Luciano Feo, and Franco Maceri. **On the pin-bearing failure load of GFRP bolted laminates: An experimental analysis on the influence of bolt diameter**. *Composites Part B: Engineering*, **41**(6):482–490, sep 2010. doi:10.1016/j.compositesb.2010.04.001.

[244] ASTM D5961/D5961M-01. **Standard Test Method for Bearing Response of Polymer Matrix Composite Laminates**. *American Standard of Testing Methods*, page 26, 2003.

[245] Peter Shyprykevich. **Characterization of bolted joint behavior: MIL-HDBK-17 accomplishments at standardization**. *Journal of Composites, Technology and Research*, **17**(3):260–270, 1995.

[246] P.D. Herrington and M. Sabbaghian. **Effect of Radial Clearance between Bolt and Washer on the Bearing Strength of Composite Bolted Joints**. *Journal of Composite Materials*, **26**(12):1826–1843, dec 1992. doi:10.1177/002199839202601208.

[247] Rajiv A Naik and JH Crews Jr. **Ply-level failure analysis of a graphite/epoxy laminate under bearing-bypass loading**. Technical report, 1988.

[248] Yi Xiao and Takashi Ishikawa. **Bearing strength and failure behavior of bolted composite joints (part I: Experimental investigation)**. *Composites Science and Technology*, **65**(7-8):1022–1031, jun 2005. doi:10.1016/j.compscitech.2005.02.011.

[249] Yuejie Cao, Duquan Zuo, Y. Zhao, Zengqiang Cao, Jie Zhi, Guo Zheng, and T.E. Tay. **Experimental investigation on bearing behavior and failure mechanism of double-lap thin-ply composite bolted joints**. *Composite Structures*, **261**:113565, apr 2021. doi:10.1016/j.compstruct.2021.113565.

[250] A. Fink and P.P. Camanho. **Reinforcement of composite bolted joints by means of local metal hybridization**. In *Composite Joints and Connections*, pages 3–34. Elsevier, jan 2011. doi:10.1533/9780857094926.1.3.

[251] S E Jones and M. J. Platts. **Using internal fibre geometry to improve the performance of pin-loaded holes in composite materials**. *Applied Composite Materials*, **3**(2):117–134, 1996. doi:10.1007/BF00158997.

[252] B. Kolesnikov, L. Herbeck, and A. Fink. **CFRP/titanium hybrid material for improving composite bolted joints**. *Composite Structures*, **83**(4):368–380, jun 2008. doi:10.1016/j.compstruct.2007.05.010.

[253] P.P. Camanho, A. Fink, A. Obst, and S. Pimenta. **Hybrid titanium–CFRP laminates for high-performance bolted joints**. *Composites Part A: Applied Science and Manufacturing*, **40**(12):1826–1837, dec 2009. doi:10.1016/j.compositesa.2009.02.010.

[254] A. Fink, P.P. Camanho, J.M. Andrés, E. Pfeiffer, and A. Obst. **Hybrid CFRP/titanium bolted joints: Performance assessment and application to a spacecraft payload adaptor**. *Composites Science and Technology*, **70**(2):305–317, feb 2010. doi:10.1016/j.compscitech.2009.11.002.

[255] S. Akbarpour and S. Hallström. **Reinforcement around holes in composite materials by use of patched metal inserts**. *Composite Structures*, **225**:111084, oct 2019. doi:10.1016/j.compstruct.2019.111084.

[256] A. Fink, B. Kolesnikov, and H. Wilmes. **CFRP/titanium hybrid: Improving composite structure coupling**. *JEC Composites Magazine*, (7):64–67, 2004. cited By 6.

[257] J. Troschitz, R. Kupfer, and M. Gude. **Process-integrated embedding of metal inserts in continuous fibre reinforced thermoplastics**. *Procedia CIRP*, **85**:84–89, jan 2019. doi:10.1016/j.procir.2019.09.039.

[258] Christopher J. Cameron, Johan Larsson, Mohamed Sahbi Loukil, Timothy Murtagh, and Per Wennhage. **Bearing strength performance of mixed thin/thick-ply, quasi-isotropic composite laminates**. *Composite Structures*, **261**:113312, apr 2021. doi:10.1016/j.compstruct.2020.113312.

[259] Ever J. Barbero. *Finite Element Analysis of Composite Materials using Abaqus™*. CRC Press, second edition, apr 2013. doi:10.1201/b14788.

[260] DS Simulia. **Abaqus/CAE User's Manual**.

[261] G. Alfano and M. A. Crisfield. **Finite element interface models for the delamination analysis of laminated composites: mechanical and computational issues**. *International Journal for Numerical Methods in Engineering*, **50**(7):1701–1736, mar 2001. doi:10.1002/nme.93.

[262] P P Camanho, C. G. Davila, and M. F. de Moura. **Numerical Simulation of Mixed-Mode Progressive Delamination in Composite Materials**. *Journal of Composite Materials*, **37**(16):1415–1438, aug 2003. doi:10.1177/0021998303034505.

[263] Yuichiro Aoki and Hiroshi Suemasu. **Damage analysis in composite laminates by using an interface element**. *Advanced Composite Materials*, **12**(1):13–21, jan 2003. doi:10.1163/156855103322320347.

[264] Z Zou, S.R Reid, and S Li. **A continuum damage model for delaminations in laminated composites**. *Journal of the Mechanics and Physics of Solids*, **51**(2):333–356, 2003. doi:https://doi.org/10.1016/S0022-5096(02)00075-3.

[265] DS Simulia. **Abaqus Analysis User's Guide (6.14) Chapter 32.5, Cohesive elements**.

[266] S.R. Hallett and P.W. Harper. **Modelling delamination with cohesive interface elements**. In *Numerical Modelling of Failure in Advanced Composite Materials*, pages 55–72. Elsevier, 2015. doi:10.1016/B978-0-08-100332-9.00002-5.

[267] Z. Petrossian and Michael R Wisnom. **Prediction of delamination initiation and growth from discontinuous plies using interface elements**. *Composites Part A: Applied Science and Manufacturing*, **29**(5-6):503–515, jan 1998. doi:10.1016/S1359-835X(97)00134-6.

[268] A. Turon, P.P. Camanho, J. Costa, and C.G. Dávila. **A damage model for the simulation of delamination in advanced composites under variable-mode loading**. *Mechanics of Materials*, **38**(11):1072–1089, nov 2006. doi:10.1016/j.mechmat.2005.10.003.

[269] Paul W. Harper and Stephen R. Hallett. **Cohesive zone length in numerical simulations of composite delamination**. *Engineering Fracture Mechanics*, **75**(16):4774–4792, nov 2008. doi:10.1016/j.engfracmech.2008.06.004.

[270] E. V. González, P. Maimí, A. Turon, P. P. Camanho, and J. Renart. **Simulation of delamination by means of cohesive elements using an explicit finite element code**. *Computers, Materials and Continua*, **9**(1):51–92, jan 2009. doi:10.3970/CMC.2009.009.051.

[271] Paul W. Harper and Stephen R. Hallett. **A fatigue degradation law for cohesive interface elements – Development and application to composite materials**. *International Journal of Fatigue*, **32**(11):1774–1787, nov 2010. doi:10.1016/j.ijfatigue.2010.04.006.

[272] Carlos Davila, Pedro Camanho, and Marcelo de Moura. **Mixed-mode decohesion elements for analyses of progressive delamination**. In *19th AIAA Applied Aerodynamics Conference*, Reston, Virigina, jun 2001. American Institute of Aeronautics and Astronautics. doi:10.2514/6.2001-1486.

[273] DS Simulia. **Abaqus Analysis User's Guide - 11.4.3 Crack propagation analysis**.

[274] Wen-guang Jiang and John L. Henshall. **Analysis of composite laminate beams using coupling cross-section finite element method**. *Applied Mathematics and Mechanics*, **27**(12):1709–1718, dec 2006. doi:10.1007/s10483-006-1213-z.

[275] Hexcel. **HexTow® IM7 Carbon Fiber**. *Hexcel Corporation, Accessed: 20 November 2018*, **000**:1–2, 2020.

[276] Hexcel Corporation. **HexPly ® 913 125°C curing epoxy matrix**. pages 1–5, 2020.

[277] SK Chemicals. **SKYFLEX Team Materials Selection Guide SKYFLEX Prepreg**, 2014.

[278] Tairyfil Formosa. **TC33 carbon fibre selection data sheet**, 2012.

[279] SK Chemicals. **Skyflex K51**. pages 1–8, 2013.

[280] Ronald Krueger. **Development and Application of benchmark examples for mode II static delamination propagation and fatigue growth predictions**. Technical report, 2011.

[281] Tamas Rev. *Exploiting thin-ply materials to establish controlled failure in carbon composites*. PhD thesis, University of Bristol, 2020.

[282] ASTM Committee D30. **D3039/D3039M: Standard Test Method for Tensile Properties of Polymer Matrix Composite Materials**. *Annual Book of ASTM Standards*, **15**:1–13, 2017.

[283] **Instron 5969 50 kN**.

[284] **Floor standing Fatigue Testing Systems - 8801 +-100kN**, 2022.

[285] Bin Liu, Richard Villavicencio, and Carlos Guedes Soares. **Failure characteristics of strength-equivalent aluminium and steel plates in impact conditions**. 03 2013. doi:10.1201/b15120-25.

[286] Calum Harker. *Improving aircraft composite Wing stiffeners with novel additive layers for suppressing delamination under edge*. Master thesis, University of Strathclyde, 2019.

[287] ASTM D7615/D7615M-19. **Standard Practice for Open-Hole Fatigue Response of Polymer Matrix Composite Laminates**, 2013. doi:10.1520/D7615.

[288] O.J. J. Nixon-Pearson, S.R. R. Hallett, P.J. J. Withers, and J. Rouse. **Damage development in open-hole composite specimens in fatigue. Part 1: Experimental investigation**. *Composite Structures*, **106**:882–889, dec 2013. doi:10.1016/j.compstruct.2013.05.033.

[289] ASTM D6873/D6873M-19. **Standard Practice for Bearing Fatigue Response of Polymer Matrix Composite Laminates**. *American Standard of Testing Methods*, page 10, 2019.

[290] Srinivasa D. Thoppul, Joana Finegan, and Ronald F. Gibson. **Mechanics of mechanically fastened joints in polymer–matrix composite structures – A review**. *Composites Science and Technology*, **69**(3-4):301–329, mar 2009. doi:10.1016/j.compscitech.2008.09.037.

[291] X Xu and M R Wisnom. **An experimental and numerical investigation of the interaction between splits and edge delaminations in [+20m/-20m] ns carbon/epoxy laminates**. In *ECCM 2012 - Composites at Venice, Proceedings of the 15th European Conference on Composite Materials*, 2012.

[292] TK O'Brien. **Mixed-Mode Strain-Energy-Release Rate Effects on Edge Delamination of Composites**. In *Effects of Defects in Composite Materials*, pages 125–125–18. ASTM International, 100 Barr Harbor Drive, PO Box C700, West Conshohocken, PA 19428-2959, 1983. doi:10.1520/STP30201S.

[293] Ronald Krueger. **Finite Element Analysis of Composite Joint Configurations With Gaps and Overlaps, NASA/CR-2014-218284**. Technical Report 2014, 2014.

[294] Brian P. Justusson, Matthew J. Molitor, Jeff S. Iqbal, Mostafa Rassaian, Trenton M. Ricks, and Robert K. Goldberg. **Overview of Coupon Testing of an IM7/8552 Composite Required to Characterize High-Energy Impact Dynamic Material Models**. Technical Memorandum (TM) NASA/TM-2020-220498, NASA, 2020.

[295] Michael R Wisnom and M I. Jones. **A Comparison between Interlaminar and In-plane Shear Strength of Unidirectional Glass Fibre-epoxy**. *Advanced Composites Letters*, **3**(2):096369359400300, mar 1994. doi:10.1177/096369359400300205.

[296] R. Li, N. Huong, A. Crosky, A.P. Mouritz, D. Kelly, and P. Chang. **Improving bearing performance of composite bolted joints using z-pins**. *Composites Science and Technology*, **69**(7-8):883–889, jun 2009. doi:10.1016/j.compscitech.2008.12.005.

[297] Cyril Sola, Bruno Castanié, Laurent Michel, Frédéric Lachaud, Arnaud Delabie, and Emmanuel Mermoz. **Bearing fatigue of composite laminates: Damage monitoring and fatigue life prediction**. *Composites Part B: Engineering*, **110**:487–496, feb 2017. doi:10.1016/j.compositesb.2016.11.031.

[298] **Silver Steel**.

[299] Azo Materials. **H13 Tool Steel**, 2013.

Appendix A

Numerical simulations additional information

A.1 Specifications of computer used for simulations

The computer used for all simulations was a Dell OptiPlex 7060 with the following specifications: Intel Core i7-8700 CPU processor with 6 cores and 12 logical processors at a maximum frequency of 3.20 GHz and a cache memory of 14 MB, 64 GB memory RAM installed, no graphics card and a HDD hard drive of 1 TB.

A.2 Generalised plane strain

The generalised plane strain, as proposed by Pipes and Pagano [13], is applied under the assumption that the stress field in a composite laminate under section is distributed so that the stress at points far from the loading points does not vary along the length of the specimen.

The strain along the x axis is not zero but constant for all slice points. The slice model [274] mimics the displacement field far away from the end-tabs, replicating what would be the displacement in the centre of an entire laminate.

Considering a symmetric composite laminate loaded by tractions applied only on its ends, such that the stress components are independent of the axial coordinate x. The equations at which Pipes and Pagano arrive for the displacement field of each node of the laminate are:

$$u = C_6 x' + U(y', z') \tag{A.1a}$$

$$v = V(y', z') \tag{A.1b}$$

$$w = W(y', z') \tag{A.1c}$$

Where x', y', z' are the coordinates of the node; U, V and W are the stress components in each node (dependent only on y' and z' coordinates), and C_6 is a constant depending on the axial force applied to the laminate.

Every node can move in x, y and z when the load is applied. The displacement (u, v, w) of each node depends on the coordinates (x', y', z') of the node.

The equation $u = C_6 x' + U(y', z')$ shows that it is possible to have different displacements in a slice or a cross-section where x' is constant. In that section, the term $C_6 x'$ stays constant but $U(y', z')$ will depend on the y' and z' coordinate. This means that we can expect different u displacement across a section. However, it is important to note that this displacement component, $U(y', z')$, is exactly the same in different slices far from the end-tabs.

A.3 Dependence of energy release rate with transverse shear modulus

At the time of performing the numerical simulations for validating the additive binding solution in the case of free-edge delamination (first research question), the input of material properties in Abaqus was by providing the "engineering constants" to the program. Unfortunately, the value of the transverse shear modulus through-the-thickness G_{23} was unavailable in the literature for the TC33/K51 prepreg carbon/epoxy material.

In a tensile loading scenario, the parameter G_{23} has a small influence on the proposed solution simulation. Several simulations were performed to calculate the value of $\mathcal{G}$ at the critical interface of the AP laminate for the verification of such independence of the results from the value of G_{23}. Figure A.1 shows the dependence of $\mathcal{G}$ with G_{23}.

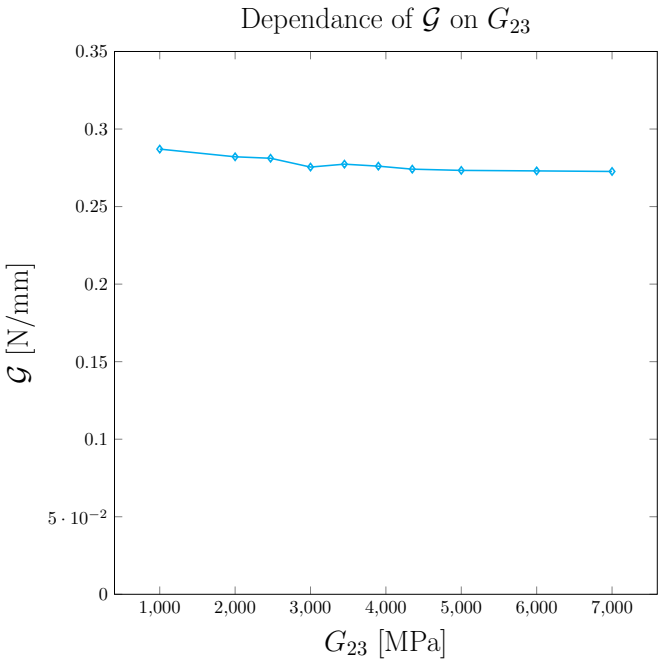

Figure A.1: Dependence of energy release rate with the transverse shear modulus through the thickness, G_{23}. Results for a crack of 4.5 mm at interface 1 in an AP laminate.

A.4 Edge impact finite elements modelling: lessons learned

The FE analysis of the composite laminates under edge impact resulted in the most challenging model of all the cases modelled in this thesis. The contact interactions and the restrictions of the VCCT made modelling the edge impact simulations challenging. Because of this, an intermediate agreement was made between performance and details to adhere the simulations to a real edge impact. Composite laminates under edge impact present severe and numerous failure mechanisms. The scope of the work carried out in this thesis was only concerning the influence of the additive bindings on the arrest of delamination in a composite laminate impacted edge-on. Furthermore, hence, delamination was the only failure mechanism modelled. The different aspects influencing the numerical cost of the simulations carried out for edge impact modelling are explained.

On the one hand, the VCCT presents handicaps and perks when simulating an impact scenario. Since only delamination was being modelled, there are cases in which, for the simulation, the 3D-8noded elements deformed more than expected, and excessive distortion and rotation happened in elements of the model. This kind of error is not always easy to solve, and one of the main mechanisms for solving it is to refine the mesh. However, due to the contact interactions, the mesh refinement increments the number of degrees of freedom to analyse exponentially (see Abaqus documentation). On the other hand, the mesh size used for the models found an agreement between

the accuracy of energy release rate values, the number of elements in the model and simulation time. Due to the element size selection, the model runs smoothly for small delamination crack lengths, such as 0.25 mm. However, as the delamination length increased, the elements between the impactor and the crack tip deformed more and more, and hence excessive element distortions occurred. This is seen in the increment of simulation time with the increment of delamination length and, finally the failure of the analysis, as mentioned in section 4.3.

Among different possibilities for solving these excessive distortions and rotations, the mesh refinement is the most common. Also, using higher stiffness values for the substrate laminate could solve the distortion problem. Additionally, configurations of the mesh element controls can be used; however, determining the proper parameters to use relies highly on the expertise of the user and the trial of different values for the parameters. Furthermore, other solutions are used in the discussions for solving this issue, such as using different types of elements, e.g., tetrahedral elements.

A.5 Finite element analysis Python codes.

The Python codes generated for each of the simulated loading scenarios can be found in the link below. The codes are compatible with Abaqus 2019, and some of them might not work for other versions of Abaqus. This is due to the indexing and naming procedure that Abaqus follows when internally storing the geometrical features of the models created.

Python codes for Abaqus 2019

Appendix B

Specimens manufacture and testing additional information

B.1 Lessons learned on the manufacture of composite laminates and specimens

Regarding the hand-layup of composite laminates, high precision is desired when cutting layers with angles different than 0° or 90° angles. Even maintaining an orthogonal cut throughout the cut of several plies of 0° or 90° layers is challenging. Hence, it is recommended that if the cutting is performed by hand-cutting, accuracy is maintained n the cut, and the angle of the cut is checked regularly to avoid incurring significant accumulated angle errors. Furthermore, a circular blade cutter, as shown in figure B.1, is recommended over the use of scalpels or blade-retractable knives for cutting the prepreg.

When laying up the different layers, it is recommended that different ply blocks are stacked together first. In this manner, if one ply does not get stacked together, wrinkles or twisting of the fibres occur, not the whole layup is faulty, and there is only a need to cut new plies of that specific orientation which was wrongly laid up.

Figure B.1: Rotatory circular blade cutter.

B.2 Edge impact cylindrical impactor plans

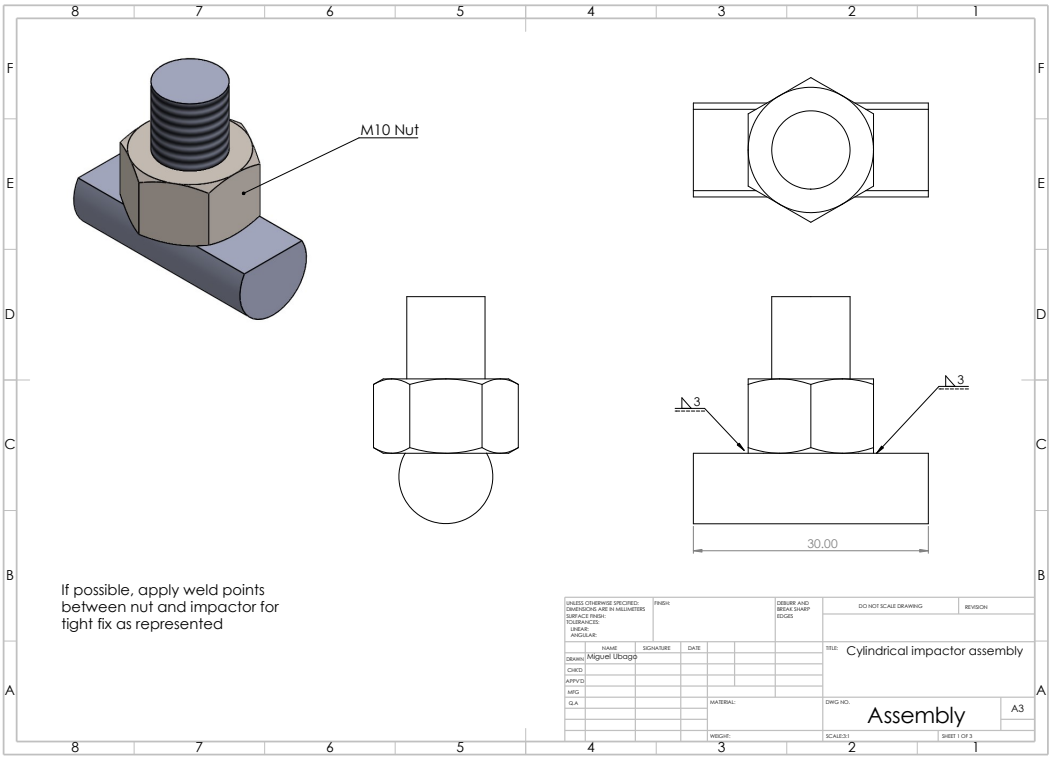
M10 Nut
3
3
30.00
If possible, apply weld points between nut and impactor for tight fix as represented
Miguel Ubaga
Cylindrical impactor assembly
Assembly
A3

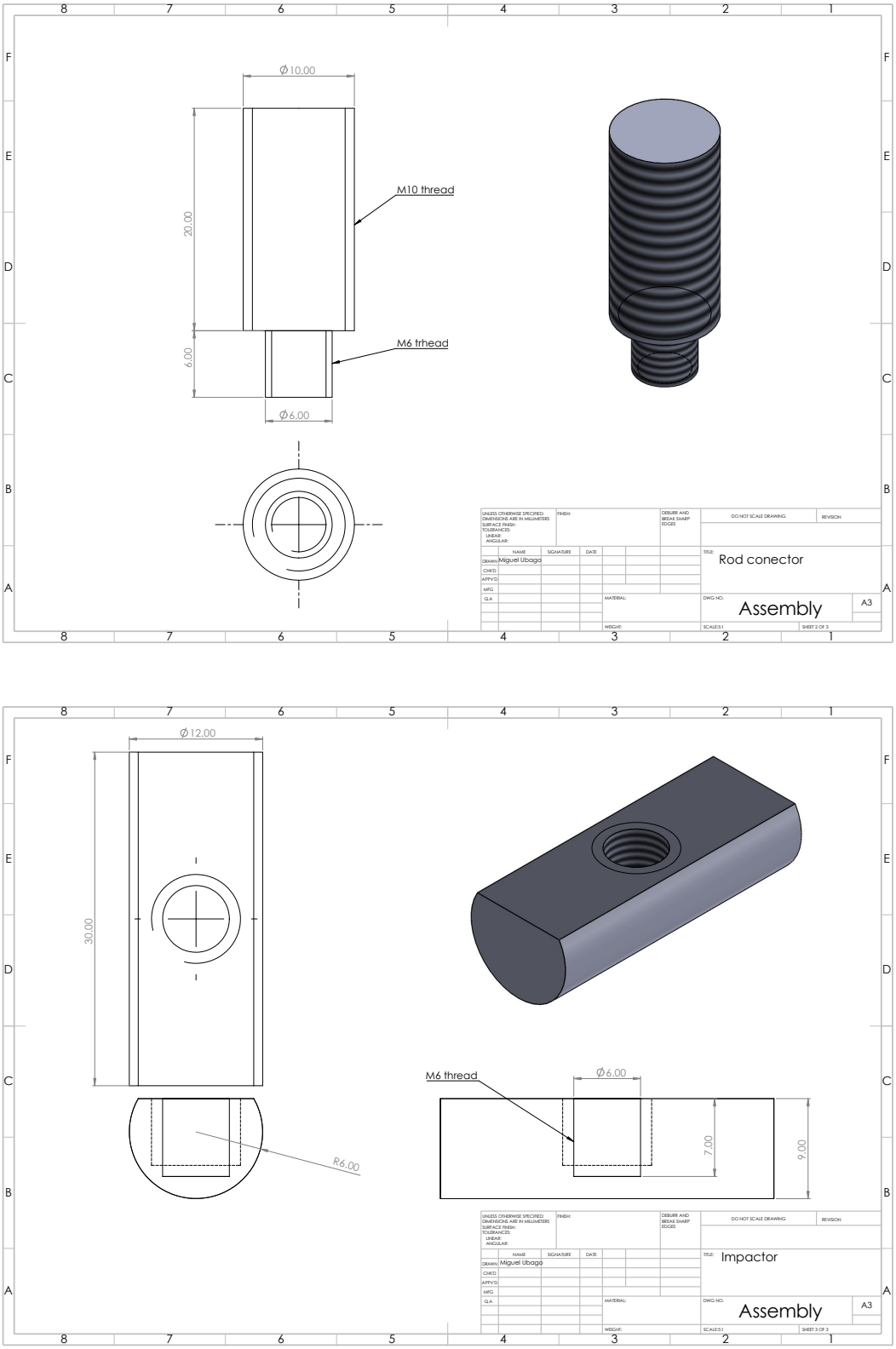

Figure B.2: Top and side views of failed specimens where the extent of damage at the hole area (hole deformation) and the separation of the 90° are visible.

B.3 XCT scan volume documents.

The reconstructed volumes of the XCT scans can be found following. Each reconstructed volume has independent parameters for appropriate viewing of the files when opened in a slice viewer. It is recommended to use ImageJ software for the manipulation of the images.

The following steps are Import-¿ Raw when opening the volumes in ImageJ. All volumes are to be opened as ”32-bit Real”, and the number of images is 2000. The width and height of the images is different for each volume of images and are specificied in the ”readme.txt” file which is located in the dataset.

The files can be found following the embedded link in the text of the specimens stated below[1]:

X-ray Computed Tomography scans

[1]Please note that all the additional content as X-ray computer tomography scans is available at the Pure Portal of University of Strathclyde.